

INTERPLAY OF CRYSTAL AND ELECTRONIC STRUCTURE IN BATTERY AND STRONGLY CORRELATED  
ELECTRON MATERIALS

By

Joshua D. Davis

A DISSERTATION

Submitted to  
Michigan State University  
in partial fulfillment of the requirements  
for the degree of

Chemistry—Doctor of Philosophy

2016

## ABSTRACT

### INTERPLAY OF CRYSTAL AND ELECTRONIC STRUCTURE IN BATTERY AND STRONGLY CORRELATED ELECTRON MATERIALS

By

Joshua D. Davis

Alkali and alkaline earth metal batteries, especially lithium-ion batteries, have had increased interest in the last decade. They offer higher energy density storage and quick discharge rates compared to other battery technologies. They power most of our portable electronics including phones and laptops. They have also been recently used more in consumer electric vehicles. Some of the other suggested applications include short term grid relief and storage for renewable energies from solar and wind sources. However, many lithium-ion batteries have poor thermal stability and are made from less abundant materials. Other derivatives of lithium-ion batteries based on magnesium and sodium have gained interest due to the potential increase in capacitance of bivalent magnesium and increased abundance of sodium. Even though sodium and magnesium-ion batteries could address some of the issues of lithium-ion batteries, they have their own issues to be considered.

Many of the lithium-ion cathode materials are transition metal oxides or transition metal polyoxoanions. The electronic structure of these materials typically has strongly correlated electron metal centers. The prospective compound of ordered  $\text{SrFeO}_2\text{F}$  has a similar two-dimension transition metal oxide layer to that of many copper oxyfluoride high temperature superconductors. The synthesis of  $\text{SrFeO}_2\text{F}$  for this study was compared to the synthetic method of Berry et al. in 2005 and 2008. While neither method produced the ordered  $\text{SrFeO}_2\text{F}$ , different magnetic data from each method suggests different localized order around the metal center. Density functional theory studies have predicted different bonding interactions between iron-oxygen bonds and iron-fluorine bonds in terms of both length and spin density. The studies also have suggested that a disordered  $\text{SrFeO}_2\text{F}$  structure would be the more thermodynamic stable structure. Future studies could involve looking at magnesium

derivatives for potentially new battery materials as the strontium cavities and the oxygen fluorine disorder could introduce large ion conduction pathways.

There are many  $\text{LiFeO}_2$  polymorphs that have been explored as potential lithium ion batteries. The one polymorph that has been the least studied has been that of the  $\text{T-LiFeO}_2$  structure. It was notable because it is synthesized from the  $\beta\text{-NaFeO}_2$  structure through ion exchange. The large cavities of  $\beta\text{-NaFeO}_2$  were hypothesized to allow for the intercalation of extra lithium for a multi-redox battery material,  $\text{T-Li}_{1+x}\text{FeO}_2$ . While the intercalation of extra lithium has been achieved, only the electrochemical cycling of iron II/III redox couple has been possible through cobalt doping. Room temperature ionic liquids were explored as alternative electrolytes to resist the high-voltage iron III/IV redox, but it proved ineffective. The electronic density of states for the  $\text{T-Li}_{0.5 < x < 1.5}\text{FeO}_2$  structures have shown that the iron II/III redox couple can access electrochemically active iron states at the Fermi level while the iron III/IV redox couple access inactive oxygen states. Other dopants of chromium, nickel, and vanadium were unsuccessful. Although the iron III/IV redox couple has proven ineffective, the  $\text{T-LiFeO}_2$  and  $\beta\text{-NaFeO}_2$  structure have shown interesting magnetic structures that warrant further investigations.

Magnesium offers increased charge capacity compared to lithium, but there have been reported issues of many electrolyte reactions in experimental magnesium-ion batteries. The  $\text{Mg}_{0.5}\text{B}_5\text{C}$  structure could potentially offer a solution as a solid state electrolyte for magnesium ion batteries. Conceptualized as a derivative structure to  $\text{NaB}_5\text{C}$ , nudged elastic band studies have predicted high ionic conductivity close to that of many lithium-ion solid state electrolytes. While the band gap calculated with hybrid density functionals have only shown a moderate band gap, the compound shows interesting prediction that warrants experimental study.

Copyright by  
JOSHUA D. DAVIS  
2016



This dissertation is dedicated to my wife, Emily Jean Davis, for giving me the support I needed, as well as to my parents and the rest of my family for believing in me and giving me their general support.

## ACKNOWLEDGEMENTS

Firstly, I would like to acknowledge Shannon S. Kraemer for her general professional and experimental support on many projects, most importantly for her support with scanning electronic microscopy. I would also like to thank Colin K. Blakely, PhD and Shaun R. Bruno, PhD for their introduction and training for the lab as well as their general professional guidance. Others I want to thank include Paul Reed, for his early computational support as I learned how to use a Linux system. I would like also to thank Richard J. Staples, PhD for his essential x-ray diffraction instrumental support. Michelle Johannes, PhD from the Navel Research Lab in Washington, DC has been vital for my understanding of Density Functional Theory and for a portion of my computational support. Also, a portion of this work was supported in part by Michigan State University through computational resources provided by the Institute for Cyber-Enabled Research. Finally, I would like to thank my advisor, Prof. Viktor V. Poltavets, PhD, for his experimental, scientific and professional support as well as my academic committee for their guidance. This research was supported in part by the National Science Foundation, Grant NSF DMR-1206718.

## TABLE OF CONTENTS

<b>LIST OF TABLES .....</b>	<b>x</b>
<b>LIST OF FIGURES.....</b>	<b>xiii</b>
<b>KEY TO ABBREVIATIONS .....</b>	<b>xx</b>
<b>1 Introduction.....</b>	<b>1</b>
1.1 <i>Energy Production and Storage</i> .....	1
1.1.1 Automobile Application .....	2
1.1.2 Pumped Hydro-Electric Storage (PHS) .....	3
1.1.3 Compressed Air Electric Storage (CAES) .....	3
1.1.4 Capacitors .....	4
1.1.5 Flywheels .....	4
1.1.6 Lead Acid Batteries .....	4
1.1.7 Nickel Cadmium and Nickel Metal Hydride Batteries.....	5
1.1.8 Lithium-ion, Sodium-ion, and Magnesium-ion batteries.....	6
1.1.10 Flow and Molten-Salt Batteries. ....	7
1.2 <i>Battery Technologies with Emphasis on Lithium-ion Technologies</i> .....	8
1.2.1 Energy Density and Other Considerations.....	11
1.2.2 The Solid Electrolyte Interface Layer .....	12
1.3 <i>Cathode Materials</i> .....	13
1.3.1 The Electrochemical Active Lithium Titanium Sulfide Structure .....	14
1.3.2 The Layered Lithium Cobalt Oxide Structure and Related Materials .....	16
1.3.3 The Lithium Iron Phosphate Structure and Related Compounds .....	18
1.3.4 The Spinel Lithium Manganate Structure .....	20
1.3.5 Lithium Vanadium Oxide Structures.....	22
1.3.6 Lithium-Sulfur Batteries.....	22
1.4 <i>Anode Materials</i> .....	23
1.4.1 Metal Anodes.....	24
1.4.2 The Lithium Metal Anode .....	24
1.4.3 The Lithium Aluminum Alloy.....	24
1.4.4 Magnesium and Sodium Metal Anodes.....	25
1.4.5 The Lithium Graphite Structure and Other Carbon Anodes .....	26
1.4.6 Lithium Silicon Anodes.....	27
1.4.7 Titanium Oxide Anodes.....	27
1.5 <i>Electrolytes for Alkali and Alkaline Earth Metal Batteries</i> .....	27
1.5.1 Organic Based Electrolytes .....	27
1.5.2 Room Temperature Ionic Liquids.....	28
1.5.3 Super Ionic Conductors.....	29
1.6 <i>Conclusion</i> .....	29
<b>2 A Discussion of the Experimental and Computational Methods .....</b>	<b>30</b>
2.1 <i>Synthetic Methods</i> .....	30
2.1.1 Ceramic Sintering.....	30

2.1.2 Soft Chemistry Methods .....	31
2.1.3 X-Ray Powder Diffraction.....	32
2.1.4 Scanning Electron Microscopy (SEM) .....	34
2.1.5 Inductively Coupled Plasma – Atomic Emission Spectroscopy .....	34
2.1.6 Cyclic Voltammetry .....	35
2.2 Computational Theory Methods .....	37
2.2.1 General Information on Density Functional Theory .....	37
2.2.2 Basis Sets.....	39
2.2.3 Potentials Used in Many Plane Wave Calculations.....	40
2.2.4 Density Functionals Used in Many Plane Wave Calculations .....	41
2.2.5 Geometry Optimization .....	42
2.2.6 Density of States and Band Structures .....	43
<b>3 Charge Transfer Semiconductor SrFeO<sub>2</sub>F .....</b>	<b>45</b>
3.1 Introduction to Metal Oxyfluorides.....	45
3.1.1 [CuO <sub>4</sub> ] <sup>2-</sup> Based Materials .....	46
3.1.2 Superconductivity .....	46
3.1.3 Charge Transfer Semiconductors.....	49
3.1.4 The FeOF Compound .....	49
3.1.5 Fluorinated Cathode Materials.....	50
3.1.6 The SrFeO <sub>2</sub> F compound .....	51
3.2 Experimental Details .....	54
3.2.1 Synthesis of the SrFeO <sub>3-δ</sub> Compound .....	54
3.2.2 Synthesis of the SrFeO <sub>2</sub> Infinite Layered Compound .....	54
3.2.3 Strontium Iron Oxyfluoride Synthesis.....	54
3.2.4 X-Ray Powder Diffraction Measurements .....	55
3.2.5 Mössbauer Measurements .....	55
3.2.6 Measurement of Magnetic Properties .....	55
3.2.7 Stoichiometry Characterization .....	56
3.2.8 Optimization of the A-C Parameter in Ordered SrFeO <sub>2</sub> F .....	56
3.2.9 Spin-Polarized SCF Calculations for Ordered and Disorder SrFeO <sub>2</sub> F Magnetic Structures.....	57
3.2.10 Relaxations of the Ordered and Disordered SrFeO <sub>2</sub> F Structure .....	57
3.2.11 Plotting of the Total and Spin Densities of the Ordered and Disordered SrFeO <sub>2</sub> F Structures .....	58
3.3 Results and Discussion .....	59
3.3.1 The Powder X-ray Diffraction Pattern of the Experimental SrFeO <sub>3</sub> Structure.....	59
3.3.2 The Powder X-ray Diffraction of the Experimental SrFeO <sub>2</sub> F Structure .....	60
3.3.3 Optimizations of Ordered SrFeO <sub>2</sub> F .....	62
3.3.4 Magnetization Data of SrFeO <sub>2</sub> F.....	67
3.3.5 Energetic Comparison of the Magnetic Structures of Order SrFeO <sub>2</sub> F .....	68
3.3.6 Density and Spin-Density of the Ordered SrFeO <sub>2</sub> F Magnetic Structures.....	72
3.3.10 Density and Spin-Density of the Disordered SrFeO <sub>2</sub> F structure .....	80
3.3.7 The Density of States for Ordered and Disordered SrFeO <sub>2</sub> F Structure.....	83
3.3.8 Mössbauer Parameter Calculations.....	87
3.4 Conclusion .....	89
<b>4 Analysis of the Iron II/III and the Iron III/IV Redox Couples in Iron-based Metal Oxides .....</b>	<b>91</b>
4.1 Introduction.....	91
4.2 Methods .....	93

4.2.1 Synthesis of 10% Doped $\beta$ -NaFeO <sub>2</sub> .....	93
4.2.2 Lithium Exchange of 10% Cobalt Doped $\beta$ -NaFeO <sub>2</sub> .....	93
4.2.3 Synthesis of Chromium, Nickel, and Vanadium Doped $\beta$ -NaFeO <sub>2</sub> .....	94
4.2.4 Powder X-Ray Diffraction Measurement and Scanning Electronic Microscopy .....	95
4.2.5 Cyclic Voltammetry .....	95
4.2.6 Surfaces of Bond Valance Analysis .....	96
4.2.7 Structure Relaxation of the T-Li <sub>x</sub> FeO <sub>2</sub> Structures .....	96
4.2.8 Magnetic Cell Relaxations of the T-LiFeO <sub>2</sub> and $\beta$ -NaFeO <sub>2</sub> Structures .....	97
4.3 <i>Electrochemical Investigation of the T-Li<sub>x</sub>FeO<sub>2</sub> System in Room Temperature Ionic Liquids</i> .....	98
4.3.1 Powder X-ray Diffraction Pattern of 10% Cobalt Doped $\beta$ -NaFeO <sub>2</sub> .....	98
4.3.2 Powder X-ray Diffraction Pattern of the Lithium Exchange of 10% Cobalt Doped $\beta$ -NaFeO <sub>2</sub> ..	99
4.3.3 Cyclic Voltammetry of the T-LiFe <sub>0.9</sub> Co <sub>0.1</sub> O <sub>2</sub> Compound .....	100
4.4 <i>Investigation of Chromium, Nickel, and Vanadium Doped <math>\beta</math>-NaFeO<sub>2</sub></i> .....	118
4.4.1 Chromium Doping of $\beta$ -NaFeO <sub>2</sub> .....	120
4.4.2 Nickel Doping of $\beta$ -NaFeO <sub>2</sub> .....	127
4.4.3 Vanadium Doping .....	134
4.5 <i>Bond Valance Analysis of <math>\beta</math>-NaFeO<sub>2</sub>, T-LiFeO<sub>2</sub>, CF-LiTiFeO<sub>4</sub>, and CF-Li<sub>2</sub>TiFeO<sub>4</sub></i> .....	135
4.5.1 Plotted Surfaces for the Bond Valance Analysis of $\beta$ -NaFeO <sub>2</sub> .....	135
4.5.2 Plotted Surfaces for the Bond Valance Analysis of T-LiFeO <sub>2</sub> .....	137
4.5.3 Plotted Surfaces for the Bond Valance Analysis of CF-LiFeTiO <sub>4</sub> .....	139
4.5.4 Plotted Surfaces of the Bond Valance Analysis of CF-Li <sub>2</sub> FeTiO <sub>4</sub> .....	141
4.6 <i>Computational Investigation of the T-Li<sub>x</sub>FeO<sub>2</sub> System as a Multi-Redox Lithium-ion Battery</i> .....	143
4.6.1 Dependence of Lithium Ion Position in the T-Li <sub>x</sub> FeO <sub>2</sub> Structures. ....	143
4.6.2 Calculated Electrochemical Potentials .....	146
4.6.3 Calculated Structural Parameters .....	148
4.6.4 Calculated Density of States for the T-Li <sub>x</sub> FeO <sub>2</sub> Structures with a Hubbard U <sub>eff</sub> of 4.0 eV .....	155
4.6.5 Calculated Density of States for the T-Li <sub>x</sub> FeO <sub>2</sub> Structures with the HSE06 Hybrid Functional	164
4.6.6 Calculated Magnetic Structures for T-LiFeO <sub>2</sub> and $\beta$ -NaFeO <sub>2</sub> with the PBE96 functional .....	167
4.6.7 Calculation of the Hubbard U through the Linear Response Approach .....	169
4.7 <i>Conclusion</i> .....	169
<b>5 Magnesium-ion Conductor Mg<sub>0.5</sub>B<sub>5</sub>C</b> .....	<b>173</b>
5.1 <i>Introduction</i> .....	173
5.2 <i>Computational Methods</i> .....	175
5.3 <i>Results &amp; Discussion</i> .....	177
5.4 <i>Conclusion</i> .....	185
<b>APPENDIX</b> .....	<b>186</b>
<b>REFERENCES</b> .....	<b>216</b>

## LIST OF TABLES

Table 3.1: Starting cell of $\text{SrFeO}_2\text{F}$ for optimization (listed atomic positions assume the lowest symmetry and no equivalent positions) .....	57
Table 3.2: Unit cell parameters for $\text{SrFeO}_{3-\delta}$ , $\text{SrFeO}_2$ , and $\text{SrFeO}_2\text{F}$ .....	61
Table 3.3: Refined structural data for the $\text{SrFeO}_2\text{F}$ structure .....	62
Table 3.4: $\text{SrFeO}_2\text{F}$ Mössbauer spectrum fitting parameters. ....	68
Table 3.5: Energetic analysis of the magnetic structures for $\text{SrFeO}_2\text{F}$ .....	70
Table 3.6: Calculated Mossbauer Parameters .....	89
Table 4.1: Final reaction temperatures for chromium, nickel, and vanadium dopings of $\beta\text{-NaFeO}_2$ .....	95
Table 4.2: Radius ratio for various oxidation states of transition metals coordinated to oxygen (CN = coordination number) Red highlighted cells have octahedral preference while green highlighted cell have tetrahedral preference. Blue are the Shannon Radii. ....	118
Table 4.3: Counted weights and ratio from Figure 4.29 .....	125
Table 4.4: Counted weights and ratio from Figure 4.30 .....	126
Table 4.5: Counted weights and ratio from Figure 4.37 .....	132
Table 4.6: Counted weights and ratio from Figure 4.38 .....	133
Table 4.7: PBE96 Calculated energies and magnetic moment of $\text{T-Li}_x\text{FeO}_2$ type structures calculated with PBE. Structures are described by Figure 4.48 and Figure 4.49. $\text{Li}_{1.5}\text{FeO}_2$ structures were based on structure 2 of $\text{Li}_2\text{FeO}_2$ . Bolded structures were chosen for further analysis. ....	145
Table 4.8: Absolute unit cell energies for the $\text{T-Li}_{0.5}\text{FeO}_2$ , $\text{T-LiFeO}_2$ , $\text{T-Li}_{1.5}\text{FeO}_2$ structures for the PBE96+U and HSE06 functionals .....	146
Table 4.9: Calculated open cell voltages with respect to lithium for the PBE96+U and HSE06 functionals .....	148
Table 4.10: Calculated cell parameters and volumes for the $\text{T-Li}_x\text{FeO}_2$ structures calculated at various levels of theory. (FM = Ferromagnetic, AFM = antiferromagnetic) .....	148
Table 4.11: Calculated Percent errors for the unit cell parameters and volumes for the $\text{T-Li}_x\text{FeO}_2$ structures at various levels of theory. ....	154
Table 5.1: Unit cell parameters and volumes for the $\text{NaB}_5\text{C}$ structures with different carbon/boron ordering patterns after the structure relaxations with Quantum Espresso or VASP. ....	178

Table 5.2: Calculated mass diffusivity and ionic conduction of $\text{Mg}_{0.5}\text{B}_5\text{C}$ .....	183
Table A.1: Muffin tin sphere orbital occupations for the ordered PBE96 $\text{SrFeO}_2\text{F}$ ferromagnetic structure. The muffin-tin size is listed next to each atomic symbol in atomic units.....	187
Table A.2: Muffin tin sphere orbital occupations for the ordered PBE96 $\text{SrFeO}_2\text{F}$ antiferromagnetic column structure. The muffin-tin size is listed next to each atomic symbol in atomic units. ....	188
Table A.3: Muffin tin sphere orbital occupations for the ordered PBE96 $\text{SrFeO}_2\text{F}$ antiferromagnetic sheet structure. The muffin-tin size is listed next to each atomic symbol in atomic units. ....	189
Table A.4: Muffin tin sphere orbital occupations for the ordered PBE96 $\text{SrFeO}_2\text{F}$ total antiferromagnetic structure. The muffin-tin size is listed next to each atomic symbol in atomic units. ....	190
Table A.5: Muffin tin sphere orbital occupations for the ordered PBE96+U $\text{SrFeO}_2\text{F}$ ferromagnetic structure. The muffin-tin size is listed next to each atomic symbol in atomic units. ....	191
Table A.6: Muffin tin sphere orbital occupations for the ordered PBE96+U $\text{SrFeO}_2\text{F}$ antiferromagnetic column structure. The muffin-tin size is listed next to each atomic symbol in atomic units. ....	192
Table A.7: Muffin tin sphere orbital occupations for the ordered PBE96+U $\text{SrFeO}_2\text{F}$ antiferromagnetic sheet structure. The muffin-tin size is listed next to each atomic symbol in atomic units. ....	193
Table A.8: Muffin tin sphere orbital occupations tables for the ordered PBE96+U $\text{SrFeO}_2\text{F}$ total antiferromagnetic sheet structure. The muffin-tin size is listed next to each atomic symbol in atomic units. ....	194
Table A.9: Muffin tin sphere orbital occupations for the disordered PBE96 $\text{SrFeO}_2\text{F}$ total antiferromagnetic structure. The muffin-tin size is listed next to each atomic symbol in atomic units. .	195
Table A.10: Muffin tin sphere orbital occupations for the disordered PBE96+U $\text{SrFeO}_2\text{F}$ total antiferromagnetic structure. The muffin-tin size is listed next to each atomic symbol in atomic units. .	196
Table A.11: Starting structure of ordered $\text{SrFeO}_2\text{F}$ relaxed in VASP .....	197
Table A.12: Starting structure of disordered $\text{SrFeO}_2\text{F}$ relaxed in VASP .....	198
Table A.13: Relaxed structure of disordered $\text{SrFeO}_2\text{F}$ relaxed in VASP .....	199
Table A.14: Crystal coordinates for the $\text{Na}_2\text{B}_{10}\text{C}_2$ super cell of $\text{NaB}_5\text{C}$ for the B/C ordered structure 1 (Figure 5.2) optimized by VASP.....	200
Table A.15: Crystal coordinates for the $\text{Na}_2\text{B}_{10}\text{C}_2$ super cell of $\text{NaB}_5\text{C}$ for the B/C ordered structure 2 (Figure 5.2) optimized by VASP.....	201
Table A.16: Crystal coordinates for the $\text{Na}_2\text{B}_{10}\text{C}_2$ super cell of $\text{NaB}_5\text{C}$ for the B/C ordered structure 3 (Figure 5.2) optimized by VASP.....	202
Table A.17: Crystal coordinates for the $\text{Na}_2\text{B}_{10}\text{C}_2$ super cell of $\text{NaB}_5\text{C}$ for the B/C ordered structure 4 (Figure 5.2) optimized by VASP.....	203

Table A18: Crystal coordinates for the $\text{Na}_2\text{B}_{10}\text{C}_2$ super cell of $\text{NaB}_5\text{C}$ for the B/C ordered structure 5 (Figure 5.2) optimized by VASP.....	204
Table A.19: Crystal coordinates for the $\text{Na}_2\text{B}_{10}\text{C}_2$ super cell of $\text{NaB}_5\text{C}$ for the B/C ordered structure 1 (Figure 5.2) optimized by Quantum Espresso.....	205
Table A.20: Crystal coordinates for the $\text{Na}_2\text{B}_{10}\text{C}_2$ super cell of $\text{NaB}_5\text{C}$ for the B/C ordered structure 2 (Figure 5.2) optimized by Quantum Espresso.....	206
Table A.21: Crystal coordinates for the $\text{Na}_2\text{B}_{10}\text{C}_2$ super cell of $\text{NaB}_5\text{C}$ for the B/C ordered structure 3 (Figure 5.1) optimized by Quantum Espresso.....	207
Table A.22: Crystal coordinates for the $\text{Na}_2\text{B}_{10}\text{C}_2$ super cell of $\text{NaB}_5\text{C}$ for the B/C ordered structure 4 (Figure 5.2) optimized by Quantum Espresso.....	208
Table A.23: Crystal coordinates for the $\text{Na}_2\text{B}_{10}\text{C}_2$ super cell of $\text{NaB}_5\text{C}$ for the B/C ordered structure 5 (Figure 5.2) optimized by Quantum Espresso.....	209
Table A.24: Crystal coordinates of the $\text{Mg}_4\text{B}_{10}\text{C}_8$ super cell of $\text{Mg}_{0.5}\text{B}_5\text{C}$ optimized by Quantum Espresso with the gamma point only. The structure was used as the starting point for the NEB calculations. ....	210
Table A.25: Crystal coordinates of the $\text{Mg}_4\text{B}_{10}\text{C}_8$ super cell of $\text{Mg}_{0.5}\text{B}_5\text{C}$ optimized by Quantum Espresso with 125 $k$ -points. The structure was used for electronic structure calculations. ....	211
Table A.26: Crystal coordinates of $\text{Mg}_4\text{B}_{10}\text{C}_8$ super cell of $\text{Mg}_{0.5}\text{B}_5\text{C}$ for the endpoint of the NEB calculation for the $\text{Mg}^{2+}$ diffusion in the [100] direction (optimized by Quantum Espresso with the gamma point only).....	212
Table A.27: Crystal coordinates of the $\text{Mg}_4\text{B}_{10}\text{C}_8$ super cell of $\text{Mg}_{0.5}\text{B}_5\text{C}$ for the endpoint of the NEB calculation for the $\text{Mg}^{2+}$ diffusion in the <b>[001]</b> direction (optimized by Quantum Espresso with the gamma point only).....	213



## LIST OF FIGURES

Figure 1.1: Diagram of a typical Lithium-ion battery .....	10
Figure 1.2: Crystal structure of lithium titanium sulfide ( $\text{LiTiS}_2$ ). Black dotted line denotes unit cell. ....	14
Figure 1.3: Crystal structure of lithium cobalt oxide ( $\text{LiCoO}_2$ ). Black dotted line denotes unit cell .....	16
Figure 1.4: Crystal structure of lithium iron phosphate ( $\text{LiFePO}_4$ ). Black box denotes unit cell. ....	18
Figure 1.5: Structures of sodium iron phosphate ( $\text{NaFePO}_4$ ); (a) Maricite (b) Triphylite. Black dotted box denotes the unit cell. ....	19
Figure 1.6: Structure of lithium manganese oxide ( $\text{LiMn}_2\text{O}_4$ ), showcasing tunnels for lithium-ion conduction .....	20
Figure 1.7: Structure of lithium graphite ( $\text{LiC}_6$ ) .....	26
Figure 2.1: Convention used for cyclic voltammograms of battery materials. <sup>155,157</sup> .....	36
Figure 3.1: Idealized structure of ordered $\text{SrFeO}_2\text{F}^{251}$ .....	52
Figure 3.2 Synthetic Routes for $\text{SrFeO}_2\text{F}$ .....	53
Figure 3.3: The powder XRD pattern of $\text{SrFeO}_{3-\delta}$ (WL = 1.5418 Å).....	59
Figure 3.4: The powder XRD pattern of $\text{SrFeO}_2\text{F}$ (WL = 1.5418 Å).....	60
Figure 3.5: PXD comparison of the patterns for $\text{SrFeO}_{3-\delta}$ , $\text{SrFeO}_2$ , and $\text{SrFeO}_2\text{F}$ .....	61
Figure 3.6: Optimization of $\text{SrFeO}_2\text{F}$ as a function of lattice parameter a and c from 3.876 to 3.995 Å. The colors highlight the energy levels in electron volts. ....	63
Figure 3.7: Optimization of $\text{SrFeO}_2\text{F}$ as a function of lattice parameter a and c from 3.758 to 4.114 Å. The colors highlight the energy levels in electron volts. ....	64
Figure 3.8: Optimization of $\text{SrFeO}_2\text{F}$ as a function of lattice parameter a and c from 3.542 to 4.1195 Å with LDA. The colors highlight the energy levels in electron volts. ....	65
Figure 3.9: Optimization of $\text{SrFeO}_2\text{F}$ from 3.35 to 4.00 Å for the a parameter, and 3.50 to 4.15 Å for the a parameter .....	66
Figure 3.10: Magnetic data of $\text{SrFeO}_2\text{F}$ (a) DC Magnetization at H=1000 Oe (b) Hysteresis at 10K and 300K from $\pm 10000$ Oe (c) AC susceptibility highlighted in (d) .....	67
Figure 3.11: Mössbauer spectrum of $\text{SrFeO}_2\text{F}$ at room temperature. It is fitted with three iron centers: Fe1 (blue line), Fe2 (red line), and Fe3 (green line). ....	68

Figure 3.12: Analyzed magnetic structures for the super cell $\text{SrFeO}_2\text{F}$ . Labeled structures match labels in Table 3.5. Strontium has been removed for clarity. ....	69
Figure 3.13: Total density calculated from the total AFM structure (d) calculated with PBE96. ....	73
Figure 3.14: Total density calculated from the total AFM structure (d) calculated with PBE96+U. ....	73
Figure 3.15: Spin density from the FM structure (a) calculated by PBE96. ....	74
Figure 3.16: Spin density from the AFM sheet structure (b) calculated by PBE96. ....	75
Figure 3.17: Spin density from the AFM column structure (c) calculated by PBE96. ....	76
Figure 3.18: Spin density from the AFM column structure (c) calculated by PBE96+U. ....	76
Figure 3.19: Spin density for the total AFM structure (d) calculated by PBE96. ....	77
Figure 3.20: Spin density from the FM structure (a) calculated by PBE96+U. ....	78
Figure 3.21: Spin density from the AFM Sheet structure (b) calculated by PBE96+U. ....	79
Figure 3.22: Spin density from the total AFM structure (d) calculated by PBE96+U. ....	80
Figure 3.23: Total density from the disordered $\text{SrFeO}_2\text{F}$ structure calculated by PBE96. ....	81
Figure 3.24: Total density from the disordered $\text{SrFeO}_2\text{F}$ calculated by PBE96+U. ....	82
Figure 3.25: Spin density from the disordered $\text{SrFeO}_2\text{F}$ calculated by PBE96. ....	82
Figure 3.26: Spin density from the disordered $\text{SrFeO}_2\text{F}$ structure calculated by PBE96+U. ....	83
Figure 3.28: Density of states for the total antiferromagnetic structure (d) calculated by PBE96. ....	84
Figure 3.29: Density of states for the total antiferromagnetic structure (d) calculated by PBE96+U. ....	85
Figure 3.30: Density of states for the total antiferromagnetic structure (d) calculated by PBE96. ....	85
Figure 3.31: Density of states for the disordered $\text{SrFeO}_2\text{F}$ structure calculated by PBE96+U. ....	86
Figure 3.32: Density of states for the total antiferromagnetic structure (d) PBE96 with mBJ ordered structure. ....	87
Figure 4.1: Powder x-ray diffraction of 10% cobalt doped $\beta\text{-NaFeO}_2$ . (WL=1.5418 Å). ....	98
Figure 4.2: Powder x-ray diffraction pattern of 10% cobalt doped $\text{T-LiFeO}_2$ . (WL=1.5418 Å). ....	99
Figure 4.3: Linear voltammetry with a pure aluminum cathode, a 1:9 electrolyte solution of $\text{LiTFSI}:\text{Pyr}_{13}\text{FSI}$ , and an anode of pure lithium. After a 10 second delay, the electrochemical split-cell was swept from 1 to 5 V at a rate of 1 mV/s. ....	100

Figure 4.4: Cyclic voltammetry with a lithium cobalt oxide (50 micron layer) cathode on a carbon paper current collector, a 1:9 electrolyte solution of LiTFSI:Pyr <sub>13</sub> FSI, and a lithium anode. After a 10 second delay, the electrochemical split-cell was swept from 3.1 to 4.1 V at a rate of 0.028 mV/s. ....	101
Figure 4.5: Cyclic voltammetry with a carbon paper cathode, a 1:9 electrolyte solution of LiTFSI:Pyr <sub>13</sub> FSI, and a lithium anode. The electrochemical split-cell was swept from 2 to 5 V at a rate of 0.083333 mV/s for three cycles/curves. ....	101
Figure 4.6: Cyclic voltammetry with a platinum cathode, a 1:9 electrolyte solution of LiTFSI: Pyr <sub>13</sub> FSI of 3 ml, and a lithium anode. The electrochemical beaker cell was swept from 2 to 5 V at a rate of 0.177778 mV/s for two cycles/curves.....	102
Figure 4.7: Cyclic voltammetry with a carbon paper cathode, a 1:9 electrolyte solution of LiTFSI: Pyr <sub>13</sub> FSI of 3 ml, and a lithium anode. The cell was swept from 2 to 5.2 V at a rate of 0.177778 mV/s for three cycles/curves.....	103
Figure 4.8: Cyclic voltammetry with a platinum cathode, a 1:9 electrolyte solution of LiTFSI:Pyr <sub>13</sub> FSI, and a lithium anode. The cell was swept from 2 to 5.2 V at a rate of 0.177778 mV/s for four cycles/curves. ....	104
Figure 4.9: Cyclic voltammetry with a platinum cathode, a 1:9 electrolyte solution of LiTFSI:Pyr <sub>13</sub> FSI, and an empty anode in a steel cell. After a 60 minute delay, the cell was swept from 2 to 5.2 V at a rate of 0.177778 mV/s for three cycles/curves. The measurement was stopped midway through the third cycle. ....	105
Figure 4.10: Pictures of the electrochemical cell after cyclic voltammetry with a lithium anode and a 1:9 electrolyte solution of LiTFSI:Pyr <sub>13</sub> FSI for a carbon paper cathode (left) or a platinum cathode (right)..	105
Figure 4.11: Cyclic voltammetry with a lithium cobalt oxide on a platinum cathode, a 1:9 electrolyte solution of LiTFSI:Pyr <sub>13</sub> FSI of 3 ml, and a lithium anode. After a 60 minute delay, the electrochemical beaker cell was swept from 3.1 to 4.1 V at a rate of 0.05556 mV/s for three cycles/curves. The test was stopped midway through the third cycle.....	106
Figure 4.12: Picture of the working modified split-cell design. All subsequent tests on T-LiFe <sub>0.9</sub> Co <sub>0.1</sub> O <sub>2</sub> were performed with on a modified split-cell set up pressed with a weight glass vile.....	107
Figure 4.13: Cyclic voltammetry with a lithium cobalt oxide on platinum cathode, a 1:9 electrolyte solution of LiTFSI:Pyr <sub>13</sub> FSI, and a lithium anode. After a 300 second delay, the modified split-cell was swept from 3.1 to 4.1V at a rate of 0.0925924 mV/s for three cycles/curves. ....	108
Figure 4.14: Example of short circuit. Effervescence is shown to form.....	109
Figure 4.15: Cyclic voltammetry with a 10% cobalt doped T-LiFeO <sub>2</sub> on platinum cathode, a 1:9 electrolyte solution of LiTFSI:Pyr <sub>13</sub> FSI of 800 microliters, and a lithium anode. After a 30 second delay, the modified split-cell was swept from 1 to 5 V at a rate of 0.37037 mV/s for three cycles/curves.....	110
Figure 4.16: Cyclic voltammetry with a 10% cobalt doped T-LiFeO <sub>2</sub> on platinum cathode, a 1:9 electrolyte solution of LiTFSI:Pyr <sub>13</sub> FSI of 800 microliters, and a lithium anode. After a 60 minute delay, the modified split-cell was swept from 1.4 to 5 V at a rate of 0.1 mV/s for three cycles/curves.....	111

Figure 4.17: Comparison of T-LiFe <sub>0.9</sub> Co <sub>0.1</sub> O <sub>2</sub> before and after the compound was cycled from 1.7 V to 4.6 V at a scan rate of 0.1 mV/s for six cycles/curves.....	112
Figure 4.18: Cyclic voltammetry with a 75 micron layer of 10% cobalt doped T-LiFeO <sub>2</sub> on platinum cathode, a 1:9 electrolyte solution of LiTFSI:Pyr <sub>13</sub> TFSI of 800 micro liters, and a lithium anode. After a 60 minute delay, the modified split-cell was swept from 3.0 to 4.3, 4.4, 4.5, 4.6 4.7, and 5.0 V at a rate of 0.0416669 mV/s for six cycles/curves. Curves 5 and 6 were performed at 50°C.....	113
Figure 4.19: Cyclic voltammetry with a 75 micron layer of 10% cobalt doped T-LiFeO <sub>2</sub> on platinum cathode, a 1:9 electrolyte solution of LiTFSI:Pyr <sub>13</sub> TFSI of 800 microliters, and a lithium anode. After a 60 seconds delay, the modified split-cell was swept from 3.0 to 4.6 V at a rate of 0.0416669 mV/s for three cycles/curves at a temperature of 75°C.....	114
Figure 4.20: Cyclic voltammetry with a 75 micron layer of 10% cobalt doped T-LiFeO <sub>2</sub> on platinum cathode, a 1:9 electrolyte solution of LiTFSI:Pyr <sub>13</sub> TFSI of 800 microliters, and a lithium anode. After a 60 minute delay, the modified split-cell was swept from 3.0 to 4.3, 4.4, 4.5, and 4.6 V at a rate of 0.0416669 mV/s for four cycles/curves at a temperature of 40°C.....	115
Figure 4.21: Cyclic voltammetry with a 75 micron layer of 10% cobalt doped T-LiFeO <sub>2</sub> on platinum cathode, a 1:9 electrolyte solution of LiTFSI:Pyr <sub>13</sub> TFSI of 800 microliters, and a lithium anode. After a 60 seconds delay, the modified split-cell was swept from 3.0 to 4.6 V at a rate of 0.0177778 mV/s for three cycles/curves at a temperature of 40°C.....	116
Figure 4.22: Cyclic voltammetry with a 75 micron layer of 10% cobalt doped T-LiFeO <sub>2</sub> on platinum cathode, a 1:9 electrolyte solution of LiTFSI:Pyr <sub>13</sub> TFSI of 800 microliters, and a lithium anode. After a 12 hour delay the cell was swept from 3.0 to 4.6 V at a rate of 0.008889 mV/s for five cycles/curves at a temperature of 40°C. ....	117
Figure 4.23: Powder x-ray diffraction patterns of $\beta$ -NaFeO <sub>2</sub> doped with different molar amounts of chromium (2.5, 5, 10, 15, and 25%). Mixtures were heated to a maximum value of 850°C for 48 hours. (WL = 1.5418 Å).....	120
Figure 4.24: Powder x-ray diffraction patterns of 10% molar chromium doped $\beta$ -NaFeO <sub>2</sub> fired at several temperature profiles. The bottom PXD pattern was heated for a total of 50 hours with an intermittent grinding at 48 hours. In comparison to Figure 4.25, the pattern was scanned for one hour. (WL = 1.5418 Å) .....	121
Figure 4.25: Powder x-ray diffraction patterns of 10% molar chromium doped $\beta$ -NaFeO <sub>2</sub> fired at several temperature profiles. In comparison of Figure 4.24, the pattern was scanned for two hours. (WL = 1.5418 Å) .....	122
Figure 4.26: Le Bail analysis of chromium doped $\beta$ -NaFeO <sub>2</sub> . (Reacted at 850°C for 48 hours) .....	122
Figure 4.27: SEM image of 2.5% chromium doped $\beta$ -NaFeO <sub>2</sub> .....	123
Figure 4.28: Back scatter SEM image of 2.5% chromium doped $\beta$ -NaFeO <sub>2</sub> with the measured EDX spectra at the designated selections. ....	124
Figure 4.29: EDX spectrum from labeled spectrum 6 in Figure 4.28 .....	125

Figure 4.30: EDX spectrum from labeled spectrum 7 in Figure 4.28 .....	126
Figure 4.31: Powder x-ray diffraction patterns of $\beta$ -NaFeO <sub>2</sub> doped with different molar amounts of nickel (2.5, 5, 10, 15, and 25%) Mixtures were heated to a maximum value of 1000°C for 72 hours (WL = 1.5418 Å) .....	127
Figure 4.32: Powder x-ray diffraction patterns of 2.5% molar nickel doped $\beta$ -NaFeO <sub>2</sub> fired at several temperature profiles. The PXD pattern, second from the bottom, was heated for a maximum of 120 hours with an intermittent grinding at 72 hours. (WL = 1.5418 Å) .....	129
Figure 4.33: Powder x-ray diffraction pattern of 5% molar nickel doped $\beta$ -NaFeO <sub>2</sub> fired at several temperature profiles. (WL = 1.5418 Å) .....	130
Figure 4.34: Le Bail analysis of nickel doped $\beta$ -NaFeO <sub>2</sub> . (Reacted at 1000°C for 72 hours) .....	130
Figure 4.35: SEM image of 2.5% nickel doped $\beta$ -NaFeO <sub>2</sub> .....	131
Figure 4.36: Back scatter SEM image of 2.5% nickel doped $\beta$ -NaFeO <sub>2</sub> with EDX spectra at the designated selections. ....	132
Figure 4.37: EDX spectrum from labeled spectrum 11 in Figure 4.36 .....	132
Figure 4.38: EDX spectrum from labeled spectrum 12 in Figure 4.36 .....	133
Figure 4.39: Powder x-ray diffraction patterns of $\beta$ -NaFeO <sub>2</sub> doped with a variety of different vanadium compositions at a variety of different temperature profiles. (WL = 1.5418 Å) .....	134
Figure 4.40: Surface of the bond valance sum analysis for sodium-oxygen bonds in $\beta$ -NaFeO <sub>2</sub> . The surface is plotted for a bond valance sum value of 1.1. ....	136
Figure 4.41: Surface of the bond valance mismatch analysis for sodium-oxygen bonds in $\beta$ -NaFeO <sub>2</sub> . The surface is plotted for a bond valance surface mismatch threshold of $\pm 0.15$ . ....	136
Figure 4.42: Surface of the bond valance sum analysis for lithium-oxygen bonds in T-LiFeO <sub>2</sub> . The surface was plotted for a bond valance sum value of 1.1. ....	138
Figure 4.43: Surface of the bond valance mismatch analysis for lithium-oxygen bonds in T-LiFeO <sub>2</sub> . The surface is plotted for a bond valance mismatch threshold of $\pm 0.15$ . ....	138
Figure 4.44: Surface of the bond valance sum analysis of lithium-oxygen bonds in CF-LiFeTiO <sub>4</sub> . The surface is plotted for a bond valance sum value of 1.0. ....	140
Figure 4.45: Surface of the bond valance mismatch analysis for lithium-oxygen bonds in CF-LiFeTiO <sub>4</sub> . The surface is plotted for mismatch threshold of $\pm 0.05$ . ....	140
Figure 4.46: Surface of the bond valance sum analysis for lithium-oxygen bonds in CF-Li <sub>2</sub> FeTiO <sub>4</sub> . The surface was plotted for a bond valance sum value of 1.0. ....	141
Figure 4.47: Surface of the bond valance mismatch analysis for lithium-oxygen bonds in CF-Li <sub>2</sub> FeTiO <sub>4</sub> . The surface was plotted for a mismatch threshold of $\pm 0.05$ . ....	142

Figure 4.48: General crystal structures of $T-Li_xFeO_2$ . A) Denotes the lithium ion arrangement of the $T-Li_{0.5}FeO_2$ structures calculated in Table 4.7 and the size of the cells used in the calculations B) General scheme of $T-Li_xFeO_2$ electrochemical cycling.....	143
Figure 4.49: Different arrangements of the added lithium-ions in the $T-Li_2FeO_2$ structures reported in Table 4.7. The unit cell is highlighted with the black outline .....	144
Figure 4.50: Comparison of different $T-Li_xFeO_2$ unit cell volumes at different levels of electronic structure theory (PBE96, PBE96+U) and magnetic arrangement. (FM = ferromagnetic, AFM = antiferromagnetic) .....	149
Figure 4.51: Comparison of the $T-Li_xFeO_2$ unit cell parameters A at different levels of electronic structure theory (PBE96, PBE96+U) and magnetic arrangement. (FM = ferromagnetic, AFM = antiferromagnetic) .....	151
Figure 4.52: Comparison of the $T-Li_xFeO_2$ unit cell parameters B at different levels of electronic structure theory (PBE96, PBE96+U) and magnetic arrangement. (FM = ferromagnetic, AFM = antiferromagnetic) .....	152
Figure 4.53: Comparison of the $T-Li_xFeO_2$ unit cell parameters C at different levels of electronic structure theory (PBE96, PBE96+U) and magnetic arrangement. (FM = ferromagnetic, AFM = antiferromagnetic) .....	153
Figure 4.54: Density of states for the ferromagnetic $T-LiFeO_2$ structure calculated with the PBE96+U functional after being relaxed with the PBE96 functional for a $U_{eff}$ value of 4.0 eV. ....	155
Figure 4.55: Density of states for ferromagnetic $T-LiFeO_2$ structure calculated with the PBE96+U functional after being relaxed with the PBE96+U functional for a $U_{eff}$ value of 4.0 eV.....	156
Figure 4.56: Density of states for C-type antiferromagnetic $T-LiFeO_2$ structure calculated with the PBE96+U functional after being relaxed with the PBE96+U functional for a $U_{eff}$ value of 4.0 eV. ....	157
Figure 4.57: Density of states for the initially ferromagnetic $T-Li_{0.5}FeO_2$ structure calculated with the PBE96+U functional after being relaxed with the PBE96 functional for a $U_{eff}$ value of 4.0 V.....	158
Figure 4.58: Density of states for the initially ferromagnetic $T-Li_{0.5}FeO_2$ structure calculated with the PBE96+U functional after being relaxed with the PBE96+U functional for a $U_{eff}$ value of 4.0 eV. ....	159
Figure 4.59: Density of states for the C-type antiferromagnetic $T-Li_{0.5}FeO_2$ structure calculated with the PBE96+U functional after being relaxed with the PBE96+U functional for a $U_{eff}$ value of 4.0 eV. ....	160
Figure 4.60: Density of states for ferromagnetic $T-Li_{1.5}FeO_2$ structure calculated with the PBE96+U functional after being relaxed with the PBE96 functional for a $U_{eff}$ value of 4.0 eV. ....	161
Figure 4.61: Density of states for the ferromagnetic $T-Li_{1.5}FeO_2$ structure calculated with the PBE96+U functional after being relaxed with the PBE96+U functional for a $U_{eff}$ value of 4.0 eV.....	162
Figure 4.62: Density of states for the C-type antiferromagnetic $T-Li_{1.5}FeO_2$ structure calculated with the PBE96+U functional with the PBE96+U functional for a $U_{eff}$ value of 4.0 eV. ....	163

Figure 4.63: Density of States for the ferromagnetic T-LiFeO <sub>2</sub> structure calculated with the HSE06 hybrid functional after being relaxed with the PBE96 functional.....	164
Figure 4.64: Density of states for the ferromagnetic T-Li <sub>0.5</sub> FeO <sub>2</sub> structure calculated with the PBE96 function after being relaxed with the PBE96 functional.....	165
Figure 4.65: Density of states for the ferromagnetic T-Li <sub>1.5</sub> FeO <sub>2</sub> structure calculated with the HSE06 functional after being relaxed with the PBE96 functional.....	166
Figure 4.66: Relative energies of different magnetic unit cells of T-LiFeO <sub>2</sub> relaxed with the PBE96 functional. The designation -1 stands for spin down and the designation 1 stand for spin up. The unit cell is shown with the labeled iron positions. Green is the lithium ion positions and red is the oxygen ion positions.....	167
Figure 4.67: Relative energies of different magnetic unit cells for $\beta$ -NaFeO <sub>2</sub> relaxed with the PBE96 functional. The designation -1 stands for spin down and the designation 1 stand for spin up. The unit cell is shown with labeled iron positions. Yellow is the lithium ion positions and red is the oxygen ion positions.....	168
Figure 5.1: Crystal structure models of (a) calcium hexaboride, CaB <sub>6</sub> , and (b-c) Mg <sub>0.5</sub> B <sub>5</sub> C for Mg ion diffusion in [100] and [001]. Mg ions in the initial and the final positions are shown as blue spheres, while grey spheres represent Mg atoms in the intermediate positions. Grey arrows indicate ion movements during the diffusion process. ....	173
Figure 5.2: Relative energies for NaB <sub>5</sub> C structures with different boron and carbon ordering patterns. Carbon atoms are oversized for clarity.....	177
Figure 5.3: Energy barriers for magnesium ion diffusion in the [100] and [001] direction for Mg <sub>0.5</sub> B <sub>5</sub> C.	179
Figure 5.4: The charge density isosurfaces for MgB <sub>5</sub> C: (a) a 3D view of the isosurface at 0.115 e/Å <sup>3</sup> , (b) the charge density section along the plane shown in (a) in values of e/Å <sup>3</sup> .....	180
Figure 5.5: Electron density isosurface (0.115 e/Å <sup>3</sup> ) of the optimized Mg <sub>0.5</sub> B <sub>5</sub> C structure. Section (a) is a view in the [100] direction; (b) is a view in the [010] direction; (c) is a view in the [001] direction. Magnesium, boron and carbon atoms have been represented by blue, green, and orange spheres, respectively.....	181
Figure 5.6: Calculated electronic band structure for the Mg <sub>0.5</sub> B <sub>5</sub> C structure. K-points have been given for an orthorhombic symmetry of the Brillion zone. The Fermi energy has been set to an energy of zero. ....	184

## KEY TO ABBREVIATIONS

2c-2e	2-center-2-electron
AC	Alternating current
AFM	Antiferromagnetic
B3LYP	The hybrid density functional by Becke, Lee, Yang, and Parr
BCS	Bardeen, Cooper, and Schrieffer of the superconductivity Theory
BVS	Bond valance sum
CAES	Compressed air electric storage
CCD	Charged coupled device
CN	Coordination number
DC	Direct current
DFT	Density functional theory
DFT+U	The general DFT method corrected with an on-site Hubbard $U_{\text{eff}}$ Value
DOS	Density of states
EDX	Energy dispersed x-ray spectroscopy
EFG	Electric Field Gradient
FC	Field cooling
FM	Ferromagnetic
GGA	General gradient approximation
$G_{\text{max}}$	Density cut-off parameter used by the Wien2k program
HOMO	Highest occupied molecular orbital
HSE06	The 2006 hybrid functional by Heyd, Scuseria, and Ernzerhof
IBZ	Irreducible Brillion zone
ICP	Induced coupled plasma



ICP-AES	Induced coupled plasma - atomic emission spectroscopy
ICP-OES	Induced coupled plasma - optical emission spectroscopy
IPD	Image plate device
ISE	Ion selective electrode
LAPW	Linearized augmented plane wave method
LDA	Local density approximation
LiTFSI	Lithium bis(trifluoromethane)sulfonamide
LUMO	Lowest unoccupied molecular orbital
mBJ	The modified Becke-Johnson potential
NEB	Nudged elastic band
OCV	Open cell voltage
PAW	Projector augmented wave method
PBE96	The Perdew-Burke-Ernzerhof 1996 density functional
PBe96+U	The PBE96 functional corrected with an on-site Hubbard Ueff Value
PE	Potential energy
PES	Potential energy surface
PHES	Pumped hydro storage
PPMS	Physical Property Measurement System
PSD	Position sensitive device
PVDF	Poly(vinylidene fluoride)
PW91	The Perdew-Wang 1991 density functional
PXD	Powder x-ray diffraction
Pyr13FSI	N-Propyl-N-methylpyrrolidinium bis(fluorosulfonyl)imide
Pyr13TFSI	N-Propyl-N-methylpyrrolidinium bis(trifluoromethanesulfonyl)imide
RK <sub>max</sub>	Wave function cut-off parameter used by the Wien2k program

RTIL	Room temperature ionic liquid
SEI	Solid electrolyte interface
SEM	Scanning electron Microscope
SCF	Self consistent field
SLI	Starting lighting ignition
SQUID	Superconducting quantum interference device
TISAB II	Total ionic strength adjustment buffer II solution
Ueff	Corrective parameter used in the general Hubbard U scheme
UPS	Uninterruptable power supply
VASP	Vienna Ab initio simulation package
WL	Wave length
XRD	X-ray diffraction
ZFC	Zero field cooling

# ***1 Introduction***

## **1.1 Energy Production and Storage**

With the ever increasing threat of global warming and environmental destruction, many in the world have been looking to find new ways to live sustainably.<sup>1</sup> The development of solar and wind energy has been on a steady rise. Much of these technologies offer a large amount of potential sources for renewable energy. While solar and wind energies at the moment still have issues with efficiency and inconsistent sources, many are working to improve these problems.<sup>2</sup> One of the largest accepted ways to manage the inconsistent sources has been to utilize storage devices like batteries. Because of the intermittency of the sun and the wind, it can be difficult for power service companies to deliver a constant source of energy to their customers. Because of this, the attachment of large scale batteries has been added to many parts of the grid with any excess energy to be released at a deficit.<sup>2</sup> Many different technologies are suited for different parts in the grid. Some technologies have been used for the simple purpose of storing mass amounts of energy for an extended period of time. Other technologies have been better suited for load shifting, power quality, and shorter grid storage. Load shifting has been related to smoothly adjusting the energy requirement of different sectors along the grid.<sup>3,4</sup> For example, toward the end of the day many industrial sites have closed down for the day leading to many people commuting home. In that time, much of the energy would be moved from the industrial sector to the private sector. Battery technologies can act as a buffer if located strategically. A battery center could store an excess of energy for the industrial sector when workers have traveled home, while a battery center located closer to the residential area could aide in power quality until the grid has adjusted. The battery stations in both areas could potentially allow energy production for both areas to run more consistently and efficiently.<sup>5,6</sup>

Power efficiency has always been important to the environment and economics. Electricity

delivered through the lines experience a loss and any technology that allows the power company lessen the loss is attributed to better cost and efficiency.<sup>6</sup> Battery grid storage in Alaska and Puerto Rico has been used to maintain stable power to many people.

Where grid storage technology exists on its pathway to the consumer depends on what it can be used for. An efficient grid needs storage for all practicalities. The closer the storage technologies have been placed near the energy production facility the more it should be used for raw energy storage. For example the technologies of Pumped hydro-electric storage (PHS) and compressed-air energy storages (CAES) have been the technologies for long-term storage for ancillary services.<sup>7</sup> The closer the technology has been place toward the consumer the more it should be directed for power quality and load leveling. Locating the storage technology more in the middle of power generation and consumer delivery has been better suited for transmission support.<sup>7,8</sup> While batteries are designed to store electrical energy for certain period of time, it has shown to been best for storing energy on the length of days or hours for load leveling and power quality.<sup>6</sup> Lithium-ion batteries and its derivatives could be used for energy storage in a wide variety of application due to their high energy density and discharge rate compared to other battery technologies.<sup>9-11</sup> Before discussing the specifics of lithium-ion battery operation, other comparable energy storage methods have been mentioned and compared in the following text.

#### **1.1.1 Automobile Application**

Portable electronics have grown to be a major aspect in many people's lives and many rely on their portable phones and computers. However, sustainable grid energy and environmentally friendly automobiles have shown to be a more pressing avenue for battery innovation.<sup>12,13</sup> While consumer devices have been important in out every day lives, their low energy cost coupled with their poor recycling programs have made them fairly inconsequential when it comes to future sustainability. Consumer electronics should be recycled, but the problems with recycling consumer electronics has

been a distribution and communication one, not a chemical one.<sup>14</sup> According to the National Academies of Sciences-Engineering-Medicine, the United States has used almost a third of the energy we produce used on transportation with 86% of that coming from petroleum and diesel sources.<sup>13</sup> Personal vehicles use 60% of that energy. Working toward changing automobiles to more of a sustainable technology would definitely have a great impact on that factor.

### **1.1.2 Pumped Hydro-Electric Storage (PHS)**

Although automobiles and personal electronics have been widely associated with newer battery technologies, grid storage has been a major practicality to consider, as well. Framing how newer battery technologies can compare to other storage technologies has been important. Pumped hydro electric storage has been one of the oldest forms of storing energy for the grid, but it has primarily been used to store mass quantities of energy to be used for later unexpected times. To store the energy this way a large amount of water would be pumped into an elevated reservoir from a lower one. At a later time when the energy would be needed, the water from the elevated reservoir would be deposited back to the lower reservoir as it passes through a hydroelectric pump to power the grid.<sup>7</sup> This type of function has only been good for storing energy for an extended period of time and not for immediate support. This method requires a large amount of land and a specific type of terrain to set up. It requires two large reservoirs to hold a massive amount of water, and for one of the reservoirs to be elevated in relation to the other.<sup>3,8</sup> A deep valley or a dried up lake would be desired for each reservoir. It has been the most utilized in terms of grid storage and has a generation capacity of 127GW for the entire grid storage in the U.S.<sup>15</sup> Even though it has been one of the cheapest methods of energy storage, it only has a specific energy of 0.028 Wh/kg.<sup>16</sup>

### **1.1.3 Compressed Air Electric Storage (CAES)**

Compressed Air Electric Storage (CAES) has been another means of long term energy storage and also requires a specific land structure to be utilized. To function, CAES requires the utilization of a

deep cavity within the earth similar to an old mine or cave. The energy produced would be stored as compressed air inside the cave or mine to be used latter. As with PHS, this method has not been suited for immediate grid relief and has been used only primarily for long term energy storage.<sup>7,17</sup> There have not been many in use because of the necessity for a specific geological structure.<sup>17</sup>

#### **1.1.4 Capacitors**

Capacitors store electrical energy directly without conversion.<sup>3</sup> In a capacitor, energy is stored as an electric gradient in polar material between two charged sheets of metal. As the device is charged, one sheet begins to accumulate a negative charge while the other sheet gains a positive charge which produces an electric gradient.<sup>18</sup> Capacitors have been primarily used for immediate grid relief and not for long term storage as they can easily leak charge.<sup>19</sup>

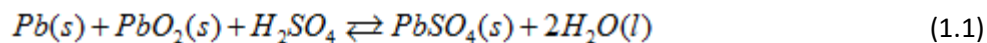
#### **1.1.5 Flywheels**

Flywheels have been more designed as power quality response and load leveling even though they can store energy for an extended period of time. They work by storing the energy in a continuous spinning wheel that can speed up when energy is needed to be stored and slow down when the energy would be released. The exchange of energy to and from the flywheel would occur through the use of a motor or generator. One of the downsides to this technology would be the moving parts and magnetic fields required to support the spinning wheels and minimize friction.<sup>7</sup> They have been used on many NASA satellites because of their long-term storage.<sup>20</sup>

#### **1.1.6 Lead Acid Batteries**

Compared to lithium-ion battery technologies, lead acid batteries have been one of the older batteries with low voltage and energy density, but it has been an inexpensive option and is well matured. The technology has been used in UPS devices for power quality in grid storage, early hybrid electric vehicles, and SLI batteries.<sup>21</sup> Some have suggested its use for wind and solar storages, as well. In general, all batteries utilize a redox reaction to store and discharge energy. A lead acid battery uses the

reversible reaction shown in equation 1.1



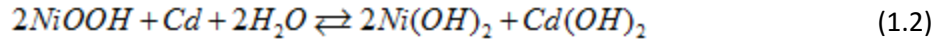
for energy storage and discharge. In a lead acid battery discharge, the elemental lead (Pb) reduces the lead oxide (PbO<sub>2</sub>) so both form as lead sulfate (PbSO<sub>4</sub>) as both have been contained in the sulfuric acid (H<sub>2</sub>SO<sub>4</sub>) electrolyte. Typical battery structure will be discussed in a later section. The lead and the sulfuric acid in the battery have been known to cause environment problems if they have not disposed properly.<sup>22</sup> The high molecular weight of lead sulfate and lead oxide also has made for a low energy density in the battery. Other considerations, for packaging for heat dispersion and chemical contents has increase the size of the battery, as well.<sup>2</sup> It has proven as an effective secondary or rechargeable battery, but the technology has been matured so there have been limited improvements to make. However, its reliability and cost-effectiveness has still made it popular for many energy storage technologies.<sup>23</sup>

#### 1.1.7 Nickel Cadmium and Nickel Metal Hydride Batteries

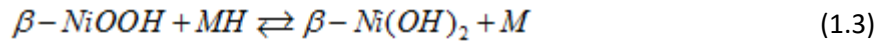
The most notable nickel based batteries have been the nickel cadmium and nickel metal hydride battery designs. Nickel cadmium batteries were greatly popular for consumer electronics applications before the 1990's, when the nickel metal hydride and lithium-ion batteries were introduced. The nickel metal hydride battery has reported to have a better energy density comparably,<sup>9,24</sup> and cadmium has shown to be toxic and carcinogenic.<sup>25</sup> Although, nickel metal hydride batteries can deliver less power and have been more susceptible to overcharge reactions that release O<sub>2</sub> and H<sub>2</sub> gases.<sup>24</sup> Because of the lack of toxicity, nickel metal hydride batteries have taken over the market for nickel cadmium batteries.<sup>26</sup> The added metal used in nickel metal hydride batteries have not typically been constructed from a single elemental metal but an alloy of many including cobalt, aluminum, manganese, and lanthanum.<sup>21</sup>

The exact chemistry of both batteries has worked similarly with the nickel cadmium reaction

shown equation 1.2



where the cadmium (Cd) reduces the cathode nickel oxide hydroxide (NiOOH) during a battery discharge. An electrolyte solution of potassium hydroxide and lithium hydroxide has been typically used in nickel cadmium batteries. For the nickel metal hydride battery reaction, the overall reaction has been described by equation 1.3



with the metal hydride reducing NiOOH with a mediation solution of potassium hydroxide. Nickel metal hydride batteries just utilize a potassium hydroxide solution.<sup>24</sup> In nickel cadmium batteries, the cadmium can react with water from the electrolyte solution so the concentration can adjust during charge and discharge.<sup>27</sup>

While nickel based batteries have reported a lower working voltage and a higher self discharge rate compared to lead acid batteries; nickel batteries have a higher energy density, cycle life, and discharge rate.<sup>28</sup> Some of the applications for nickel based batteries besides consumer electronics have been in hybrid and pure electric vehicles, power grid storage (UPS and load leveling), aircraft systems, telecommunication systems, satellites, solar power stations, and medical devices.<sup>24</sup>

#### 1.1.8 Lithium-ion, Sodium-ion, and Magnesium-ion batteries

Lithium-ion batteries have also been used for power grid applications, electric vehicles, and consumer electronics.<sup>3,29,30</sup> Lithium-ion batteries have been better than more matured battery technologies in terms of energy density, power density, discharge rate, cycle life, voltage, and self discharge.<sup>28</sup> However, lead-acid and nickel batteries have one major advantage of cost over lithium-ion batteries. The limited availability of lithium and cobalt,<sup>31</sup> which has been the redox active metal typically used in the battery, has driven the cost up considerably, even though the energy density of lithium-ion batteries are several fold higher than previous battery technologies.<sup>9</sup> Lithium-ion batteries have been



the only battery technology that has the energy density for a consumer electric vehicle to drive a comparable distance on a single charge to that driven by a gasoline based automobile on single tank of gas.<sup>32</sup>

To expand on existing lithium-ion technologies, modifications based on sodium and magnesium have been explored. Sodium and magnesium have more mass compared to lithium, but have been reported to be more abundant. Sodium battery compounds based on lithium-ion materials have reported voltages that are about 0.3 V less than their counter parts. While the lower voltage and increased weight would decrease the energy density of the material, it would have only small effect when it comes to overall battery energy density. Due to the radius of sodium it has been difficult to find a compound that can effectively cycle sodium ions unencumbered.<sup>33–35</sup> Magnesium is bivalent and is about the same size as lithium, but the charge per volume in a magnesium ion has also been a double edge sword.<sup>36</sup> The higher charge per volume has made it more difficult conduct through battery materials can be inhibited severely by localized negatively charged ions. Magnesium based batteries have also shown side reactions with electrolytes similar to that in sodium and lithium batteries due to it bivalency.<sup>37–39</sup> Lithium, sodium, and magnesium-ion batteries will be discussed and compared more thoroughly later in the chapter.

#### **1.1.10 Flow and Molten-Salt Batteries.**

Flow batteries and molten-salt batteries have been more suited toward load leveling rather than power quality devices. Flow batteries have required many moving parts like pumps and fans to circulate the redox active materials to function. Redox flow batteries have typically contained two reservoirs, one for the reducing agent and one for the oxidizing agent, separated by an ion selective membrane.<sup>2,40</sup> Due to the required usage of pumping, flow batteries have required a portion of the energy they store in order to function. This means they have been described as a less efficient battery even though the energy density can be adjusted through concentration and the power density can be controlled through

the electrode surface area.<sup>2</sup> Some of the more prominent versions of redox flow batteries have been all vanadium redox flow batteries, vanadium bromide batteries, iron-chromium batteries, and zinc-bromine batteries, polysulfide batteries.<sup>3</sup>

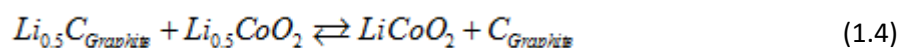
Molten-salt batteries have similarities to redox batteries in the aspect that a portion of the energy produced by the battery needs to be used for battery function. The use of the molten sodium salt, NaAlCl<sub>4</sub>, has been the most widely used electrolyte with the ceramic alumina ( $\beta$ -Al<sub>2</sub>O<sub>3</sub>) separator between the oxidizing and reducing agent. A temperature of 300°C has been needed for the salt to remain molten and for the  $\beta$ -aluminate to properly conduct the sodium ions. At room temperature, the battery will not function.<sup>2</sup> The main battery designs have been the sodium sulfur (Na-S) and the ZEBRA battery. In the sodium sulfur battery, the redox reaction has typically been between molten sodium and molten sulfur. A ZEBRA battery, named for Zero-Emission Battery Research Activities, typically has used a reaction between molten sodium and a solid transition metal chloride to produce sodium chloride and a reduced transition metal on discharge.<sup>35</sup> The metal electrodes have typically been made porous to allow for quick interaction with the molten sodium ions. Nickel chloride has typically been the metal chloride used, but iron chloride has been the second most used cathode. ZEBRA batteries have also been used electric vehicles, but it had a limited release.<sup>41</sup> Sodium-sulfur batteries also have issues with corrosion, and have less overcharge protection in comparison with ZEBRA batteries so they have not been used in automotive applications.<sup>3,42</sup> Molten salt and redox flow batteries can require expensive maintenance,<sup>2,43</sup> but they have been best suited for grid storage.

## **1.2 Battery Technologies with Emphasis on Lithium-ion Technologies**

The main focus of this dissertation will be on alkali and alkaline earth battery materials. Batteries have been typically manufactured with a multitude of components, but in spite of that they have been utilized in a many portable electronics due to their size and lack movable parts. The fundamental design of a battery has been to store energy as a single redox reaction. All batteries can be

primary or secondary in nature. Primary batteries are non-rechargeable batteries; they would be used once and discarded. The zinc-carbon AA batteries, typically sold by Duracell or Energizer, are examples of primary battery.<sup>42</sup> A secondary battery has been one that can be charged and discharge many times for multiple uses. Many lithium-ion batteries have been secondary batteries, although there have been primary lithium based batteries.<sup>42</sup>

In every battery, there are three major parts, a cathode, an anode, and an electrolyte. The purpose of these three parts has been to control the flow of electrons from the redox reaction through a voltage load as the electrons move from the anode (reducing agent) to the cathode (oxidizing agent).<sup>44</sup> Because of the safety issues of using pure lithium metal, the anode for a lithium ion battery has typically been lithium graphite.<sup>45</sup> The cathode of a lithium ion battery has mainly been lithium cobalt oxide (LiCoO<sub>2</sub>) or some doped variation of the compound.<sup>46</sup> The reaction displayed in Equation 1.4 shows the battery discharged when moving from right to left, where the lithium graphite has reduced the lithium cobalt oxide. When moving from left to right, the battery will be charged as the lithium cobalt oxide will be oxidized by lithium graphite. Lithium cobalt oxide can only cycle half lithium per formula unit stably.



A full diagram depicting how a lithium ion battery can be designed and function has been shown in Figure 1.1. The electrolyte would be used to separate the anode and cathode to prevent electronic discharge between the two directly. In many lithium-ion batteries the electrolyte solution of LiPF<sub>6</sub> dissolved in an ethylene carbonate based solvent has been typically used.<sup>10</sup> A discharged a battery powers an electronic component by moving the electrons from the anode to the cathode through an external wire. As this happens, positively charged lithium will move from the anode through the electrolyte and separator into the cathode. This balances the charge after the cathode has been reduced during discharge. When a battery has been charged, the cathode would be oxidized and the electrons would move through the wire back into the anode. The positively charged lithium anion will at the same

time move back through the electrolyte and separator into the anode, putting the battery back in a charged state.<sup>10,11,46</sup> A battery that has been charged and discharged once has been described as going through one cycle.

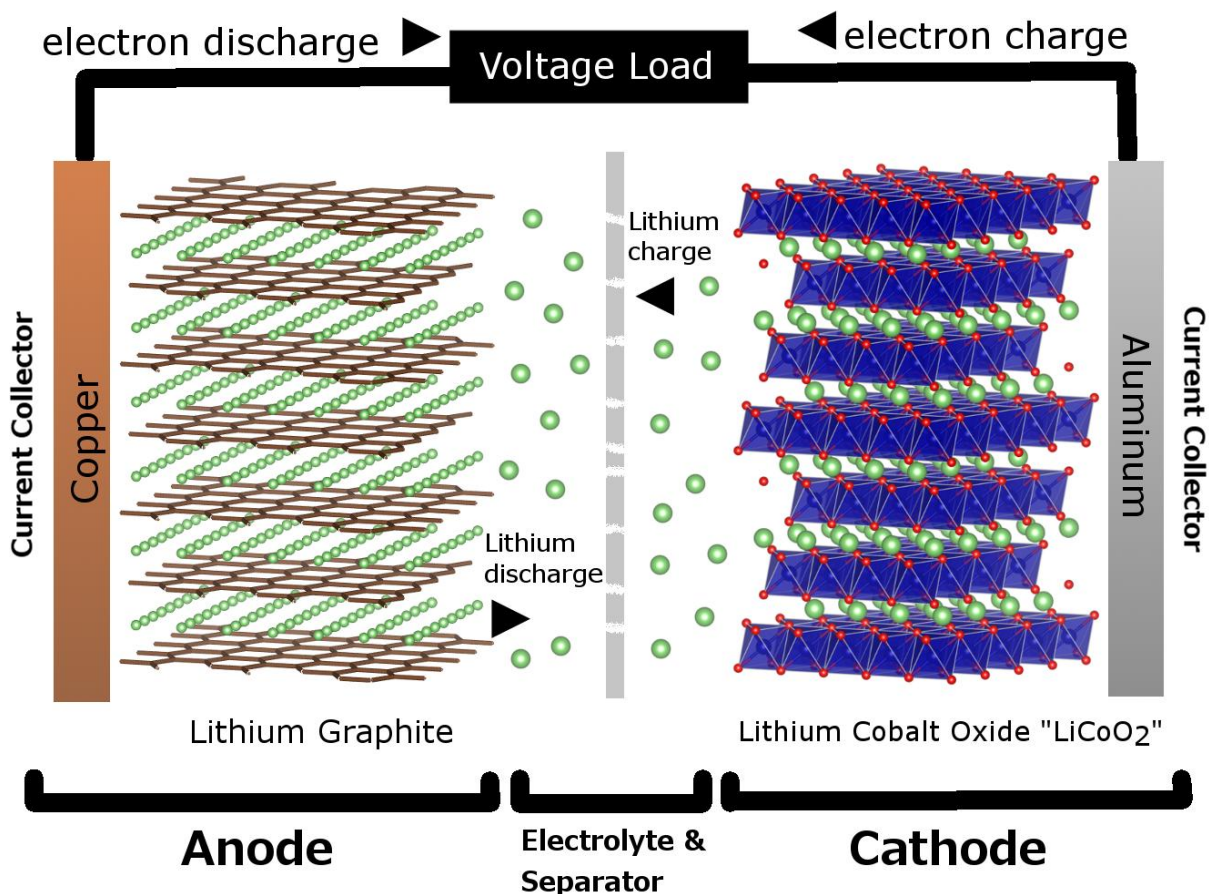


**Figure 1.1: Diagram of a typical Lithium-ion battery**

Other secondary parts of the lithium-ion battery include charge collectors and the separator. A separator of porous Teflon has typically been used to prevent the battery from shorting-circuiting if pure lithium begins to plate in the electrolyte.<sup>9,47</sup> If the battery has shorted between the two electrodes with no voltage load, the battery can overheat and catch fire.<sup>48,49</sup> While lithium graphite and  $\text{LiCoO}_2$  are moderately electronically conductive, the charge collector for each electrode enables the delivery of electrons to and from the voltage load quickly and reliably. Different electrodes use different charge collectors depending on their electrochemical stability.<sup>47,50</sup>

### 1.2.1 Energy Density and Other Considerations

The three major factors that govern how well a battery functions have been power density, energy density, and stability. Power density has been defined as the rate of energy delivery per mass, and energy density has been defined as the amount of energy stored per mass or volume. When the energy density has been stated as per mass, the nomenclature has been defined as specific energy; when defined per volume the nomenclature has been stated as the volumetric energy density. Good stability includes low degradation of the electrolyte, the electrodes, and current collectors during each complete cycle. Any undesirable side reactions between the electrolyte, electrodes, or current collectors can decrease the energy density and power density of the battery over time.<sup>46</sup> Each of the aspects has been shown to be important, but depending on application, the importance of each item may change. Lead-acid batteries typically have low energy density, but can be engineered for a quick discharge rate needed for a starter motor in an automobile.<sup>28</sup> Cell phones do not require a lot of power, but require a large amount of energy to last all day. For that application, lithium-ion batteries have been required.<sup>12</sup> Specifically, power density has dependence on ionic conductivity and electronic conductivity. High ionic and electronic conductivity have been important for fast discharge and quick energy delivery.<sup>44,46</sup> Another aspect for good power density has been the type of redox state accessed during the battery cycle. An accessible state like a transition metal d-state at the Fermi level allows for easy and quick charge/discharge compared to an oxygen p-state.<sup>9,51</sup>

Energy density has been described as a product of the capacity and working voltage as shown in equation 1.5. The equation is

$$E = CV \quad (1.5)$$

where E is the energy density, C is the charge capacity, and V is the working voltage. An increased capacity would lead to an increased energy due to the increase of available stored charge.<sup>9</sup> To calculate the theoretical capacity of a specific compound for an anode or cathode equation 1.6 is used.

$$C = \frac{nF}{M} \quad (1.6)$$

Equation 1.6 states  $n$  as the number of electrons that charge/discharge from the compound,  $F$  as Faraday's constant, and  $M$  as the molar mass of the electrode compound. The theoretical capacity,  $C$  has typically been reported in milliamp hours per gram. The theoretical capacity for normal lithium-ion cathode materials,  $\text{LiCoO}_2$ ,  $\text{LiFePO}_4$ , and  $\text{LiMn}_2\text{O}_4$  were calculated to be 140, 170, and 150 mAh/g.<sup>31</sup> The potential voltage can be theorized as well, but the theory has been extensively more involved for solid state materials. The potential of a specific material can be calculated through Equation 1.7 which relates potential to free energy.

$$E = -\frac{\Delta G}{nF} \quad (1.7)$$

The value of  $E$  have been defined as the potential of the reaction; the values  $n$  and  $F$  have been defined as the number of electrons charged/discharged and Faraday's constant respectively.<sup>31</sup> The value of  $\Delta G$  is the calculated Gibb's free energy of the redox reaction explicitly used in the battery. The free energy can be calculated from an assortment of quantum chemistry codes, including plane-wave density function theory packages like VASP, Abinit, and Quantum Espresso. The expression  $\Delta G$ , Gibb's free energy, contains information about enthalpy and entropy. However, because of the Hohenberg-Kohn theorems that define density functional theory as the absolute ground state method, a calculation using DFT would assume the lowest energetic configuration at a temperature of zero Kelvin. With this assumption  $\Delta G$  is made synonymous with  $\Delta E$ , the internal energy. Even with this assumption, many have calculated theoretical voltages with decent accuracy.<sup>52–58</sup>

### 1.2.2 The Solid Electrolyte Interface Layer

In certain cases, where the working electrolyte voltage has not been stable against the working voltages of the electrodes a solid electrolyte interface, or SEI, layer can form between the electrolyte and the electrode. It has been found to be a side reaction between the anode and the electrolyte.<sup>9,44</sup> For

lithium ion batteries, the SEI layer acts as an insulating layer that allows for the pacification of lithium ions. In sodium batteries, the SEI layer would be dissolved by the electrolyte when a pure sodium anode has been used which leads to instabilities.<sup>34</sup> In a pure magnesium anode, the SEI layer allows for less pacification compared to lithium-ion batteries and has not shown to be ionically conductive.<sup>37,39</sup>

### **1.3 Cathode Materials**

In a lithium-ion battery, the cathode has been one of the more important parts when it comes to capacity and voltage. Some cathode materials have started to reach the theoretical maximum voltage for lithium-ion batteries imposed by the lithium-fluoride reaction.<sup>59</sup> High voltage cathodes have been desirable, but expanding cathodes to materials with higher capacity could also lead to higher energy density as well. In general, an anode should have a low reduction potential with respect to lithium while cathode materials should have a high reduction potential. The reduction potential difference between anode and cathode should be maximized for the best battery voltage. There has been some research in anode materials for lithium-ion batteries, but lithium-graphite has such high gravimetric density and stability that cathode materials have received a higher interest.<sup>10,31,44,60–64</sup>

Additional aspects that make for a good cathode material have been high electronic and ionic conductivity. High electronic conductivity enables good electronic flow between redox active centers. The material should be able to be charged and discharged at a functional rate. Ionic conductivity allows for the lithium ion to move in and out the cathode material to maintain charge balance at a manageable rate.<sup>46,65</sup> The material should be structurally stable as it is cycled, as well. A lithium-ion cathode can have one of two types of responses when the material has been cycled. The material can be an intercalation type cathode or a conversion type cathode. An intercalation cathode maintains the same scaffold and overall structure as it has been cycled. The cycling interaction has been described as topotactic in nature.<sup>66</sup> A conversion type material will undergo lithium intercalation and deintercalation as a fully reversible process, but the dilithiated material will have a different crystal structure compared to the

fully lithiated material.<sup>67,68</sup>

Both types of materials have their positives and negatives, conversion materials have typically been able to maintain a constant voltage over the battery discharge while intercalation materials slightly change in voltage as the cell discharges. Conversion materials would have less cycling stability than intercalation materials due to how the charge/discharge cycle affects the stress and strain of the conversion material.<sup>69</sup>

### 1.3.1 The Electrochemical Active Lithium Titanium Sulfide Structure

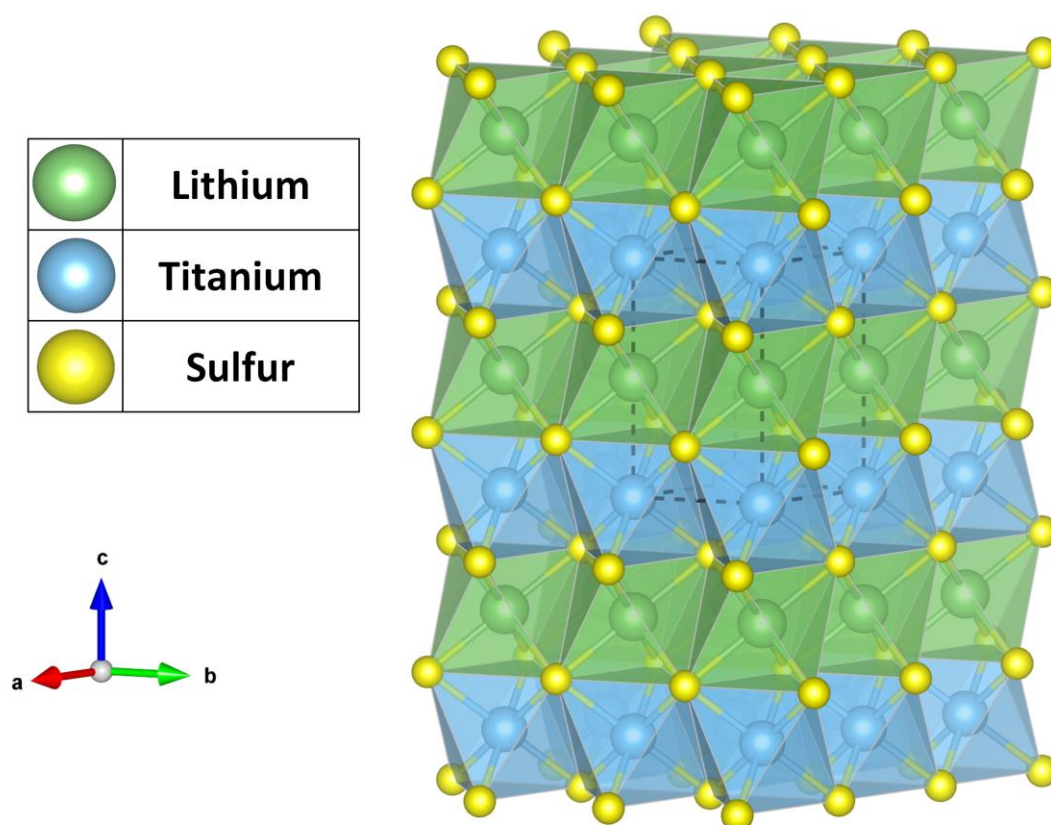


**Figure 1.2: Crystal structure of lithium titanium sulfide (LiTiS<sub>2</sub>). Black dotted line denotes unit cell.**

When looking at historically relevant lithium-ion battery materials, one of the first suggested was by Whittingham in the 1970's. The material was made by intercalating lithium into titanium sulfide, TiS<sub>2</sub>, with butyl-lithium. The lithium titanium sulfide compound, shown in Figure 1.2, was a layered intercalation compound that has a minimum ionic conductivity of  $5 \times 10^{-3}$  S/cm and a electrical



conductivity of about 500 S/cm.<sup>60,70,71</sup> However, the material had a low working voltage of 1.9V, high molar mass of 118.9280 g/mol,<sup>31</sup> and an experimental specific capacity of 210 mAh/g.<sup>72</sup> Subsequently, the energy density has been described as low compared to many compounds that have been recently discovered with an energy density of 399 Wh/kg of cathode. When the compound has been discharged, the lithium intercalation would cause the material expand by 10 percent. The feed stock material, titanium sulfide, was also expensive at the time of manufacturing and hygroscopic to the point it would release the foul smelling hydrogen sulfide.<sup>73</sup> The biggest downfall for the lithium titanium sulfide battery was the danger posed with the use of a pure lithium anode. The lithium anode was shown to have some dendritic tendencies which could lead to a short circuit of the battery, thermal runaway, and the ignition of the organic electrolyte.<sup>46,73</sup> While it was commercialized by Exxon with a LiAl anode, the material was eventually abandoned.<sup>73</sup> The comparable sodium and magnesium compounds were also explored, but the sodium based material had low cyclability and voltage compared to the LiTiS<sub>2</sub>.<sup>74,75</sup> The compound Mg<sub>x</sub>TiS<sub>2</sub> showed similar voltage to the lithium based material, but also had extremely slow ion-mobility.<sup>76</sup>

### 1.3.2 The Layered Lithium Cobalt Oxide Structure and Related Materials

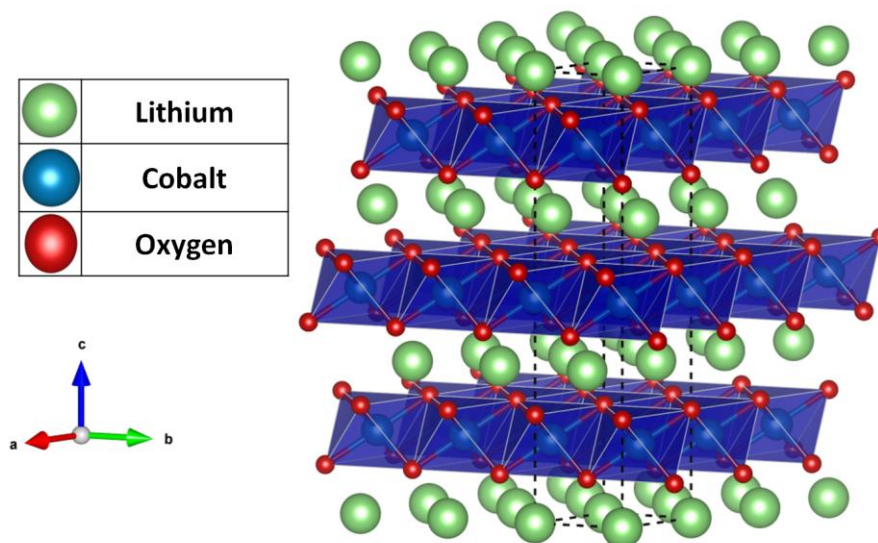


**Figure 1.3: Crystal structure of lithium cobalt oxide (LiCoO<sub>2</sub>). Black dotted line denotes unit cell**

Lithium cobalt oxide has been the battery materials most used in today's rechargeable batteries. It was discovered by John Bannister Goodenough in the 1980's<sup>77</sup> and first commercialized by Sony in the early 1990's.<sup>29,78,79</sup> While it had a similar layered structure as LiTiS<sub>2</sub>, it had a much higher working voltage of 3.8V and low molar mass of 97.8740 g/mol, leading to a much higher energy density of 551 Wh/kg.<sup>31,80</sup> The structure for lithium cobalt oxide has been shown in Figure 1.3. The lithium cobalt oxide compound has a high energy density even though it cycles a half equivalence of lithium where as lithium titanium sulfide cycles full lithium equivalence.<sup>46</sup> While electrical conductivity of the material has not been as high as LiTiS<sub>2</sub>, it has been improved upon by carbon coating the material.<sup>31,70,81</sup> Carbon coating has been used with many battery materials as a decent supplement to many poor electronic conductors.<sup>82-88</sup> While carbon coating has detracted from the weight of lithium cobalt oxide that can be used in commercial batteries, it has not affected the energy density enough to make LiTiS<sub>2</sub> a better option. Another concept that made lithium cobalt oxide a better option compared to lithium titanium sulfide was that lithium cobalt oxide does not require synthesis in air-free conditions. Lithium cobalt oxide also shrinks by 3% when intercalated in comparison with the 10% expanse by lithium titanium

sulfide. The oxygen anions in  $\text{LiCoO}_2$  have enough local negative charge to contract against the positive lithium ion when the molar lithium content of lithium cobalt oxide has been between 1 and 0.5.

Even though, lithium cobalt oxide has been labeled as a better option than lithium titanium sulfide, there have been downsides. Similar to lithium titanium sulfide, it cannot be used with a pure lithium anode due to stability issues.<sup>61,62,89</sup> For this, lithium graphite has been used for the anode, but again this has not dissuaded the use of lithium graphite because of mass and weight performance.<sup>46</sup> Graphite has never been used as an anode with  $\text{LiTiS}_2$  due to electrolyte solvents intercalating the graphite structure.<sup>46</sup> Even though lithium cobalt oxide has been distributed as the most widely used lithium-ion material, it has had one of the lowest thermal breakdown temperatures of 200°C.<sup>31,90</sup> Also while lithium may not be as abundant as other materials, cobalt has been the economical reasoning for the cost of lithium cobalt oxide batteries.<sup>91</sup> Partial replacement of cobalt with nickel, manganese, and aluminum has led to different production variations of the lithium cobalt oxide battery. Nickel and manganese has led to higher capacity and better cycle life.<sup>92,93</sup> Aluminum doping has been attributed to increased stability and deep cycling, as well.<sup>31,93</sup> Sodium parallels have been investigated for layered transition metal oxides, but they typically have lower voltage and capacity.<sup>94</sup> Some of the sodium layered compounds have produced cation ordering and structure changes that can lead to poor cycle life, as well.<sup>33,95,96</sup>

### 1.3.3 The Lithium Iron Phosphate Structure and Related Compounds

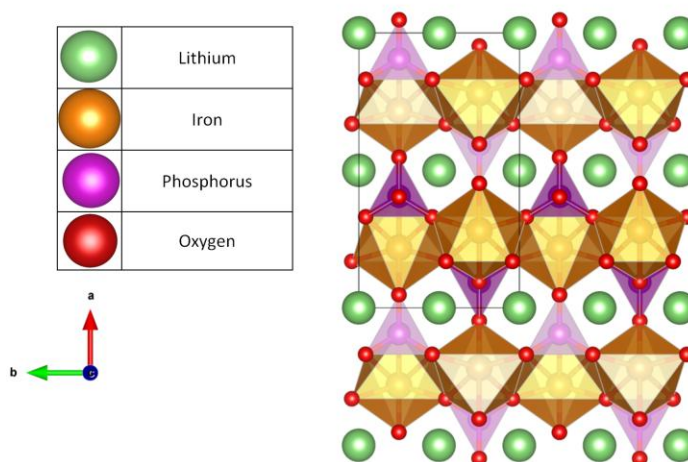


**Figure 1.4: Crystal structure of lithium iron phosphate (LiFePO<sub>4</sub>). Black box denotes unit cell.**

As a cheaper alternative to lithium cobalt oxide, the material lithium iron phosphate was postulated due to the low cost of iron and phosphorous.<sup>97</sup> The compounds lithium titanium sulfide and lithium cobalt oxide were layered to allow for two dimensional diffusivity, but LiFePO<sub>4</sub> was constructed as an olivine structure with large cavities for the lithium ion to move through. The olivine (triphylite) structure only has one dimensional diffusivity (Shown in Figure 1.4); however, the tunneled structure of the material also allows for more stability.<sup>52</sup> The phosphate anion in lithium iron phosphate has also served two purposes, the first has been to increase thermal stability and safety of the material,<sup>82,98</sup> and the second has been to increase the voltage of the material through the inductive effect.<sup>9,61</sup> The stability of the phosphorous oxygen bond has kept the oxygen anions from reacting with the electrolyte under extreme voltages, as well as pull more electron density away from the iron III cation, thus increasing the voltage of the material with respect to lithium.<sup>98</sup> The phosphate anion, however, has been a double edged sword. Because of the strength and stability of the phosphorous oxygen bond, LiFePO<sub>4</sub> has shown poor electronic conductivity in addition to poor ionic conductivity.<sup>52,82,98,99</sup> To work around the poor conductivity of lithium iron phosphate, the material has been synthesized in the form of nanoparticles for better ionic conductivity and coated with carbon for better electronic conductivity. Nanoparticles of

lithium iron phosphate shorten the necessary path for lithium ion conduction. As mentioned before, carbon increases the electrical conductivity of the material function.<sup>99,100</sup> While carbon has been used as supplement for the electronic conductivity of lithium cobalt oxide, the electronic conductivity of  $\text{LiFePO}_4$  has been found to be orders of magnitude lower than that of lithium cobalt oxide ( $\text{LiCoO}_2$ ).<sup>65</sup> The carbon coating of  $\text{LiFePO}_4$  has shown to be an absolute necessity to function appropriately in commercial batteries.<sup>99</sup> Though the use of iron and phosphorous has decreased the cost of the lithium-ion cathode, the necessary engineering methods has increased the cost.<sup>91</sup>

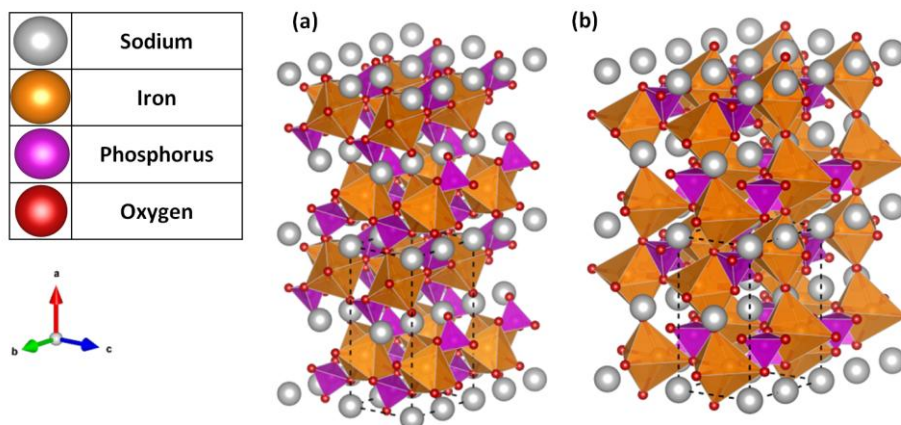


**Figure 1.5: Structures of sodium iron phosphate ( $\text{NaFePO}_4$ ); (a) Maricite (b) Triphylite. Black dotted box denotes the unit cell.**

The sodium derivative was initially said to be electrochemically inactive, but there has been a renewed interest in the compound based on the maricite polymorph. The olivine based structures have shown some electrochemical activity with room temperature liquid electrolytes, but cycle life still has yet to be improved. Both structures have been shown in Figure 1.5. Overall, the sodium versions have has reported poor cycle life, larger volume changes during cycling, and poor ionic conductivity compared to the lithium counterpart.<sup>34,35,101</sup>

### 1.3.4 The Spinel Lithium Manganate Structure

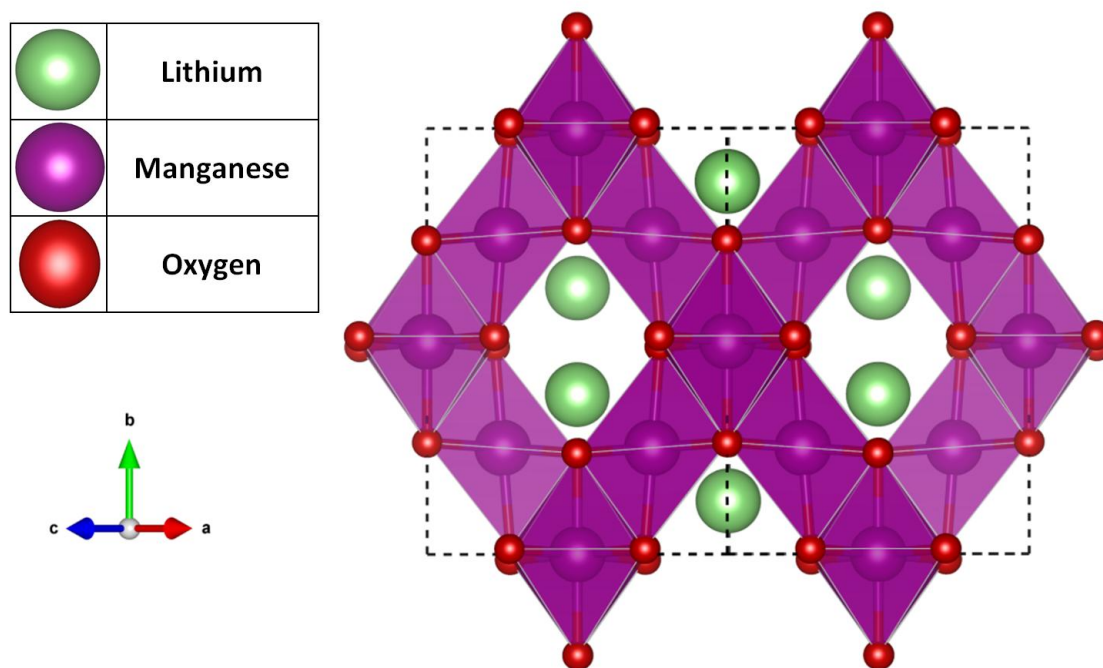


**Figure 1.6: Structure of lithium manganese oxide (LiMn<sub>2</sub>O<sub>4</sub>), showcasing tunnels for lithium-ion conduction**

Lithium manganese oxide was formulated as another alternative to lithium cobalt oxide. The structure of the compound has a spinel structure that has been shown to be related to the layered structure of lithium cobalt oxide through ionic movement. In both structures, the oxygen positions have been organized in a hexagonal pattern, but the manganese has not formed layers as it has in lithium cobalt oxide.<sup>31,102,103</sup> The manganese and lithium ions have been arranged so the manganese ions form into octahedral positions and the lithium form into tetrahedral positions. The layered manganese compound has been described as isostructural to lithium cobalt oxide, but when the compound has been cycled electrochemically, it reverts to the spinel LiMn<sub>2</sub>O<sub>4</sub> structure.<sup>104</sup> The structure for lithium manganese oxide, highlighting lithium-ion channels has been shown in Figure 1.6.

The ionic and electronic conductivity of lithium manganese oxide has been found to be between

the compounds lithium iron phosphate and lithium cobalt oxide. Lithium iron phosphate and lithium cobalt oxide have reported ionic conductivities of  $\sim 10^{-9}$  and  $\sim 10^{-4}$  S/cm respectively with similar electronic conductivities of  $\sim 10^{-9}$  and  $\sim 10^{-4}$  S/cm. While lithium manganese oxide has been measured with an electronic and ionic conductivity of  $\sim 10^{-6}$  S/cm.<sup>65</sup> The benign nature and affordability of manganese has made lithium manganese oxide an interesting prospect for lithium ion batteries, but the material has shown continuously to have a poor cyclability with exposure to the electrolyte.<sup>31</sup> During the cycling process in lithium manganese oxide, the manganese III ion that forms will disproportionate to manganese II and manganese IV. The manganese II ion will dissolve in the electrolyte. This disproportion can be exacerbated by an increased temperature as low as 60°C.<sup>105</sup>

The compound can be intercalated with butyl-lithium to molar lithium content greater than one where the extra lithium ions occupy empty octahedral sites. Because of the added lithium in the  $\text{Li}_{x+1}\text{Mn}_2\text{O}_4$  structure, there would be a manganese II/IV mixed valent system created.<sup>102</sup> When the lithium content was cycled between 2 and 1 in  $\text{Li}_x\text{Mn}_2\text{O}_4$ , the manganese II/III voltage vs. lithium was reported as 3.1V, but when the lithium content was cycled from 1 to 0 the manganese III/IV voltage raises to 4.1V. This again has to do with the inductive effect as well as the scarcity of lithium ions in the tetrahedral positions that pull electron density away from the manganese ions.<sup>9,10,106</sup> The experimental specific capacity of  $\text{LiMn}_2\text{O}_4$  has been reported be the lowest at 120 mAh/g. Comparatively, magnesium doped lithium manganese oxide has shown to have a low mobility activation barrier (0.4 eV) which has suggested a decent magnesium based battery material.<sup>37,107,108</sup>

It has been the weakest of the three main commercialized lithium-ion cathode materials due to its poor cyclability and molar mass.<sup>31,109–111</sup> The sheer cost of the compound has made it attractive for power tools, laptops, cell phones, and electrical power trains.<sup>103,110</sup>

### 1.3.5 Lithium Vanadium Oxide Structures

The lithium vanadium oxide material ( $\text{LiV}_2\text{O}_5$ ) was heavily investigated due to its ability to undergo multi-electron cycling. The  $\text{Li}_x\text{V}_2\text{O}_5$  compound can form many different phases when the compound has been cycled from one to three molar equivalences of lithium.<sup>112</sup> The five main structures reported have been designated as alpha, epsilon, delta, gamma, and omega.<sup>112,113</sup> The alpha structure of  $\text{V}_2\text{O}_5$  will convert to the epsilon and delta structure after the first equivalence of lithium has been added. It will then to the gamma structure after the second equivalence of lithium has been added. Finally, the omega structure will appear after the third and final equivalence of lithium has been added. After the compound has converted all the way to the omega structure, the compound will stay in the omega polymorph. However, lithium vanadium oxide has been ignored as a battery materials due to its large variance in cycling voltage (between 2-4V). Vanadium has been shown, in certain cases, to be hazardous to health, as well.<sup>112-115</sup>

### 1.3.6 Lithium-Sulfur Batteries

While the topic of this dissertation has primarily been on intercalation based compounds, lithium sulfide ( $\text{Li}_2\text{S}$ ) has been an attractive conversion battery alternative. The material has a large capacity which has made it a serious contender in relation to the existing intercalation batteries. The theoretical specific capacity of  $1675 \text{ mAh/g}$ <sup>116</sup> has been several fold larger than what has been available for the intercalation type lithium-ion batteries. Even with a theoretical voltage of about  $2.15\text{V}$ ,<sup>117</sup> which has been lower than many intercalation compounds, the material could have a theoretical energy density of  $2500 \text{ Wh/kg}$ . However, like many other lithium-ion conversion battery materials, the cathode has had poor interactions with electrolytes.<sup>118-120</sup> Certain electrolyte solvents like dioxolane<sup>121</sup> and propylene carbonate can dissolve some of the intermediates that form during charge and discharge of the lithium sulfur battery.<sup>117</sup> Elemental sulfur has also been a poor electronic and ionic conductor so it has to be encapsulated into carbon nanocages. The nano cages keep the particles small and increases



electronic conductivity. The carbon nanocages have been designed with space allocation for volume changes that sulfur undergoes during cycling.<sup>122</sup>

Some of the negative effects of a dissolving cathode have included: increased self discharge due charge shuttling from dissolved intermediates, poor coulombic efficiency from charge shuttling as well, and poor cyclability because necessitated reformation of sulfur and  $\text{Li}_2\text{S}$  during each cycle.<sup>117,123</sup> There have been many recent studies to counter act and lessen the negative effects of the dissolved intermediate which have included allowing the cathode and electrolyte to purposely mix into a “catholyte” while a highly selective separator has been used on the anode to only allow the conduction of the lithium ion.<sup>117,121</sup> Other methods have included tiered separators between the anode and cathode that limit the movement of the sulfur intermediates. The simplest method has included the use of room temperature liquid electrolytes which limits the solubility of the intermediates.<sup>121,124</sup> While conversion batteries are not directly relatable to many of the compounds of this study, the availability and safety of sulfur as well as potential energy density of  $\text{Li}_2\text{S}$  has made it a direct competitor to intercalation compounds. However, the battery has had serious issues with electrolyte stability that still has to be properly addressed.

#### **1.4 Anode Materials**

While the anode has been studied less, it has still been vitally important. While a good cathode has a high reduction potential verse lithium, a desirable anode will have a very low reduction potential verse lithium.<sup>9</sup> The reduction potential should not be a negative value though. If the potential for anode material has been reported as negative, lithium could plate on the surface of the anode which could lead to instabilities. Similar to a cathode, an anode should have high electronic and ionic conductivity.<sup>125,126</sup> The anode should also be relatively stable, even with intercalated lithium. The compound should be able to store a battery charge for some extended amount of time (stability), as well, and the redox state utilized in the anode should also be chemically accessible. In lithium metal, the

utilized redox state has been described as a half-filled s-band while in lithium graphite, a band with pi-bonding character has been the relevant redox state.<sup>127</sup> In both, the electronic band has only been partially filled and has been available for oxidation and reduction.

#### **1.4.1 Metal Anodes**

Metal anodes have the advantage of being low weight, malleable, and highly electronically conductive. All three would aid in the manufacturing of a lithium-ion battery.<sup>128</sup> A metals anode could decrease the weight of the overall battery because it could act as its own current collector, and the malleability would decrease the amount of processing for battery production. Unlike the cathode, it would not require production in powder form with carbon coating.<sup>129</sup>

#### **1.4.2 The Lithium Metal Anode**

In the case of lithium-ion batteries, the ideal anode would be pure lithium itself. Lithium has good electronic conductivity, a low reduction potential and a low mass for high energy density.<sup>64,129</sup> However, lithium has been reported to be highly reactive to the point of harsh battery fires in a damaged battery. A lithium anode can start to form dendrites as the battery cycles. Upon repeated charge and discharge the lithium will deposit on the anode surface and grow the dendrites. The dendrites can lead to a battery short-circuit by piercing the separator.<sup>9,10,130</sup> The short-circuit can then lead to an overheated battery and eventual fire. While lithium can form an SEI layer on the anode, overheating a battery destroys the layer and starts to thermal runaway.<sup>9,10,130</sup>

#### **1.4.3 The Lithium Aluminum Alloy**

Mixing aluminum with lithium can increase stability and decrease the formation of dendrites, but it also has been reported to decrease the capacity of the anode due to the extra aluminum content. There are two primary structures for a lithium aluminum alloy, one has been a face centered lattice with a lithium atom at the corner positions and the aluminum atomic positions on the faces to give a stoichiometric  $\text{LiAl}_3$ .<sup>131</sup> The other structure has been a NaCl or diamond-like structure. The latter

structure has been the one typically found in anodes.<sup>132</sup> The lithium titanium sulfide was stabilized with a lithium aluminum anode for commercial use, but the battery was commercially unsuccessful.<sup>46</sup> The aluminum reduces the reactivity too much.<sup>132</sup>

#### **1.4.4 Magnesium and Sodium Metal Anodes**

Because lithium has shown to be highly reactive and not an abundant metal, sodium-ion and magnesium-ion batteries have been explored, as well.<sup>31</sup> Magnesium can offer higher stability and safety to the point where the pure metal can be used as anode, but the SEI layer for magnesium inhibits ionic conductivity.<sup>37,39</sup> Sodium has also been reported to react with the electrolyte during cycling, however a proper SEI layer does not stable so the sodium will continues to react with the electrolyte.<sup>35</sup> Sodium has a body centered cubic structure like pure lithium, but magnesium has a simple hexagonal structures. For lithium-ion batteries, the SEI layer has been a convenience to prevent further electrolyte reaction, but it still has reduced battery activity. Because of the reactivity with many electrolytes, sodium based alloys have been considered for Sodium-ion anode materials.<sup>133</sup>

#### 1.4.5 The Lithium Graphite Structure and Other Carbon Anodes

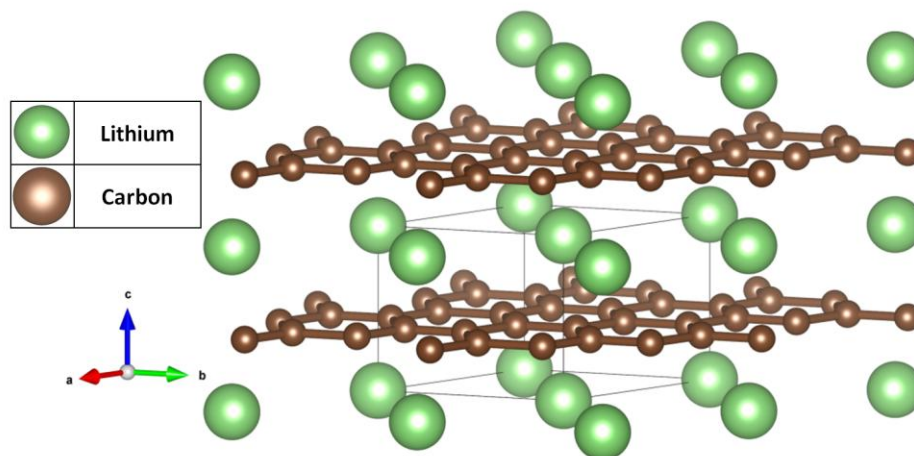


**Figure 1.7: Structure of lithium graphite ( $\text{LiC}_6$ )**

For lithium-ion batteries, lithium graphite has been the most widely used anode.<sup>31</sup> Lithium graphite has the molar ratio of  $\text{LiC}_6$  when fully lithiated (Figure 1.7). When lithium intercalates into graphite, the lithium moves in between the graphene layers to a point where the lithium has been positioned in the center of  $\text{C}_6$  ring above and below. While pure graphite has layers shifted for every other layer, the intercalation of lithium forces the layers to align.<sup>134</sup> The lithium aluminum alloy has shown to be a stable compound, but lithium graphite has a lower reduction potential than lithium aluminum. The lithium aluminum alloy is a conversion material, while Li-Graphite has worked as an intercalation compound. Also, the insertion mechanism of lithium into graphite prevents the dangerous formation of lithium dendrites. The lithium aluminum alloy also prevents dendrite formation, but intercalation compounds offer more predictability for structure change during cycling.<sup>135</sup> For sodium derivatives, it has been reported to have extremely poor absorption into graphite so the use of heat treated “hard-carbon” has been considered more for sodium based batteries.<sup>136</sup>

#### **1.4.6 Lithium Silicon Anodes**

Amorphous Silicon has also been considered due to its high capacity and low intercalation voltage. The material can hold up to 15 lithium ions per 4 Silicon atoms. However, the intercalated silicon undergoes extreme structural changes during cycling which leads to a poor cycle life. Intercalation of lithium can increase the volume of silicon by three fold.<sup>137,138</sup>

#### **1.4.7 Titanium Oxide Anodes**

The material  $\text{Li}_4\text{Ti}_5\text{O}_{12}$  has also been explored as anode material. It has been extremely thermally stable and does not form an SEI layer like lithium-graphite.<sup>31,139</sup> The working voltage of the material and high mass of the compound severely decrease the energy density of the material, but it has been suggested more for high power applications.<sup>140</sup> In comparison, the compound  $\text{Na}_2\text{Ti}_3\text{O}_7$ , has been seriously considered alternative for sodium-ion batteries. It has an extremely low voltage vs. sodium (0.3V) and has been reported to have small volume changes with intercalation and deintercalation.<sup>34,141,142</sup>

### **1.5 Electrolytes for Alkali and Alkaline Earth Metal Batteries**

The electrolyte is the medium that exists between the two electrodes that prevents direct discharge. Unlike the two electrodes, the electrolyte should be highly electrically insulating, but ionically conductive.<sup>143</sup> The purpose of the battery is to shuttle the electrical energy into voltage load and to not allow a direct discharge. A good electrolyte should have a stable working voltage window to maintain the insulating properties.<sup>9</sup> The electrolyte should not be oxidized by the cathode and it should be reduced by the anode in its charged state.<sup>9</sup>

#### **1.5.1 Organic Based Electrolytes**

In many lithium-ion batteries, solution based electrolytes have been used. The solvents need to have a low viscosity and to dissolve ions fairly readily (i.e. they are highly polar and aprotic). The solvent should also have a high boiling point but low melting point to ensure liquid mobility at a large range of

temperatures. Typically the solvent used has been ethylene carbonate mixed with another organic like propylene carbonate. Ethylene carbonate does not have a low melting point, and it has reacted with lithium graphite to form a working SEI layer. The propylene carbonate or other organic solvents have been mixed with ethylene carbonate to depress the melting point of ethylene carbonate.<sup>143,144</sup> Dioxolane based solvents have shown more reliability in lithium sulfur batteries.<sup>46,117,121</sup>

Many of the lithium salts used in the electrolyte solutions have been paired with large anions to prevent any side reactions. Small localized anions can act as Lewis bases so the delocalized charge of  $[\text{BF}_4]^-$ ,  $[\text{ClO}_4]^-$ , or  $[\text{PF}_6]^-$  inhibit most side reactions and increase solubility due to the stabilized charge.<sup>9,34,143,144</sup> The lithium hyper-chlorate salt can act as an oxidant in certain situations, however. The salt primarily used has been  $\text{LiPF}_6$  due to its overall general stability.<sup>143</sup> In terms of sodium-ion and magnesium-ion batteries, sodium ions dissolve quite readily in polar aprotic solvents due to its size;<sup>34</sup> however, magnesium tends to react to organic electrolytes because of its bivalency. So Grignard-type modifications have been designed in organic electrolytes to better shuttle the magnesium ions.<sup>38</sup>

### 1.5.2 Room Temperature Ionic Liquids

Room temperature ionic liquids have also been explored for electrolyte solvents due to their high ionic conductivity and high melting points.<sup>145</sup> Room temperature ionic liquids have employed a large cation (e.g.  $\text{R}_4\text{P}^{4+}$  where R=alkyl chain) to accompany an equally large anion (e.g. TFSI or trisfluorosulfonyl imide). Again, for anions like  $[\text{PF}_6]^-$  or  $[\text{ClO}_4]^-$  the size of the ion stabilizes the charge. Because the ions are so large, it limits the ability of the ions to form a proper lattice, but the ionic forces have help to increase the boiling point. The ions structure and symmetries have been designed to limit any localized charge.<sup>146</sup> The delocalized charge also inhibits any side redox reactions. The ionic nature of these solvents has increased the solubility and ionic conductivity of any dissolved electrolyte salts.<sup>146</sup> Magnesium based salts have shown stability for battery electrolyte application in room temperature ionic liquid solvents, as well.<sup>38</sup>

### 1.5.3 Super Ionic Conductors

Super ionic conductors have been included in the general compounds for solid state electrolytes for lithium-ion, sodium-ion, and magnesium-ion batteries. Solid state electrolytes have been desirable for their stability and safety. Solid state electrolytes would limit the formation of SEI or any other electrolyte reactions. The use of solid state electrolytes would also prevent any short circuit and thermal runaway in batteries. However, contemporary solid state electrolytes, even super ionic conductors, do not conduct ions enough to compete with the existing technology. Super ionic conductors have been labeled as NaSICON, LiSICON, and MgSICON which are abbreviations for a sodium, lithium, or magnesium Super Ionic **CON**ductor. They are constructed from sodium, lithium, or magnesium ionic compound accompanied with a redox inactive transition metal and polyoxoanion (e.g. phosphate). They have been electrically insulating, but facilitate large cavities for quick ionic conduction. One of largest ionic conductivity values reported has been a value of 0.30 S/cm at 300°C for europium doped  $\text{Na}_5\text{GdSi}_4\text{O}_{12}$ .<sup>147,148</sup>

## 1.6 Conclusion

Lithium-ion batteries and derivatives based on magnesium and sodium hold a lot of potential for low weight high density energy storage for automobiles and grid storage. Lithium-ion batteries have been an ever increasing field with many problems and research to explore to increase energy density. The purpose of the chapter was to compare lithium-ion battery materials to competing technologies and to discuss major trends in the field. Lithium-ion batteries have enough energy and power density for consumer electronics, grid storage, and electric vehicles, although the lack of lithium abundance and stability limits its use. This could be expanded on in the future with magnesium-ion batteries for increased capacity or sodium-ion batteries due to the increased elemental abundance and stability in comparison to lithium.

## ***2 A Discussion of the Experimental and Computational Methods***

A large combination of methods can be important for full and complete analysis of solid state compounds. Bench top chemistry can give investigators direct and clear results, but at times to fully understand the functionality of a material or compound, first principle calculations have been necessary.<sup>149</sup> Solid state chemistry as well as other disciplines are ever changing and it has been important to list the trivial and especially the non-trivial methods. The following is a brief synopsis of the methods used in this dissertation.

### **2.1 Synthetic Methods**

#### **2.1.1 Ceramic Sintering**

Ceramic sintering has been the most widely use synthetic method for solid state chemistry. For all intents and purposes, it has just been defined as the mixing and heating the solid materials at high temperature for extended periods of time. For effective sintering, it has been important to grind the reactants together. Grinding decreases the size of particles and increases stress and strain within the particles to allow better diffusion and reactivity between particles.<sup>150</sup> One of the most effective ways to grind reactants together has been through the use of a ball-mill. A ball mill is a device made up of a jar that has been loaded with reactants and highly durable grinding spheres to mix the reactants together. The jar would be closed and rotated for a specific amount of time to grind the reactants together. Jars and grinding spheres have been made from stainless steel or agate due to the high durability of both. Typically when a ball mill has been used the grinding and rotating would be intermittently paused and restarted to prevent overheating. Ball mills have come in two major designs, one that rotate the jar on its side and one that rotates multiple jars in a planetary fashion. Ball milling can be used for post processing of a product if a specific particle size has been desired, but if the material has been ball milled for too long or at too high of a speed, an undesirable amount of defects can form in the



product.<sup>151</sup>

Another method to increase the reactivity in ceramic sintered materials has been to press the mixed reactants at high pressures into a pellet thus increasing the interaction and surface area between the particles. After the reactant have been mixed and pressed, heating the pellet will cause the particles to react quickly due to the increased kinetic energy. While solid state reactions have been orders of magnitude slower than solution based chemistry, increased heat has been necessary to perform reactions on a reasonable time scale. Intermittent heating and grinding can effectively speed up reaction times, as well. However, as a supposed firing progresses, particle size can increase due to increased chemical reactivity and particle aggregation. Ceramic sintering can be used to synthesize meta-stable products that exist in thermodynamic local minimums, but increased time and temperature will ensure a reaction to progress to the lowest thermodynamic minimum.<sup>150,152</sup>

### **2.1.2 Soft Chemistry Methods**

Soft chemistry methods primarily has referred to low temperature (<500°C) methods used to modify composition, but preserve chemical structure.<sup>66,153</sup> This can include things like ion exchange or gentle oxidation and reduction methods. Ion-exchange involves the exchange of one ion for another, for example exchanging lithium for sodium. The target hypothetical compound (e. g.  $\text{NaFeO}_2$ ) would be mixed dry with another compound (e. g.  $\text{LiNO}_3$ ) that would contain the desired ion. The reaction would end with the desired product (e.g.  $\text{LiFeO}_2$ ) and a side product that would contain the exchanged ion (e.g.  $\text{NaNO}_3$ ). The reaction would progress at a relatively elevated temperature to increase ionic mobility and to force the side product to form. The reaction progresses forward due to the higher heat of formation of the side product compared to the heat of formation for the supplement reactant. The side product is usually washed away with solvent that will not dissolve the target compound.<sup>150</sup> Other methods involve adding oxidizing or reducing agents to modify electronic structure, or to also change the occupation of counter anions. Calcium hydride has been used to topotactically remove oxygen from transition metal

oxides.<sup>154</sup> Butyl-lithium has been used to reduce structures and add extra lithium.<sup>155,156</sup> Elements like bromine and compounds like nitrosonium tetrafluoroborate have been used to oxidize structures to remove sodium and lithium from compounds.<sup>157</sup> These reactions can be performed dry with post-reaction washings or with an added reductive or oxidizing solution. Some of these reactions have required high pressures that can be achieved in solvothermal autoclaves.<sup>158,159</sup>

### 2.1.3 X-Ray Powder Diffraction

Powder x-ray diffraction has been one of the most important methods for identification of solid state materials. Powder x-ray diffraction patterns have primarily been defined by the shape of the unit cell, symmetry of the unit cell, the atomic content positions within the unit cell, and the angle of incident x-rays with reference to the unit cell.<sup>150,160</sup> The x-rays used in this method have been made from one of two ways. The first method involves the high voltage acceleration of electrons from a metallic cathode to a metallic anode. The high impact releases x-rays from the anode; in many cases the anode used has been copper. The other way has been by synchrotron source where x-rays are released from a curved path of high speed electrons. The x-rays produced should be a well-defined wavelength, and x-ray diffraction has been found to be an elastic phenomenon so the incidental and outgoing x-ray should have the same wavelength. In conventional powder x-ray instruments, the typical detectors have been a position sensitive device (PSD), charged coupled device (CCD), and image plate device (IPD).<sup>161</sup> The intensity measured by x-ray diffraction has been described by equation 2.1:

$$I(hkl) = |S(hkl)|^2 \times M_{hkl} \times LP(\theta) \times TF(\theta) \quad (2.1)$$

In equation 2.1, the intensity  $I(hkl)$  is a function of the structure factor  $S(hkl)$ , the multiplicity of reflections  $M_{hkl}$ , a polarization factor  $LP$ , and the temperature factor  $TF$ . The values  $hkl$  have been defined as the Miller indices which will be discussed later. First off, the structure factor has been dependent on the symmetry of the cell and the atoms that exist in the cell as each element reflects x-rays with at different intensity.<sup>162,150,160</sup> In a solid periodic material, the atomic positions form a set of

lattice points, this lattice can be described minimally as a repeatable unit cell defined by its own vectors. In a lattice, there are identifiable planes of atoms that exist based on its symmetry. These planes have been what the incident x-rays refract from and produce an instrumental signal. To form a positive measurement, a large amount of refractions must occur by Bragg's law to form constructive interference in the refracted x-rays. Bragg's law has been written in Equation 2.2:

$$2d \sin \theta = n\lambda \quad (2.2)$$

In equation 2.2,  $d$  is the distance between planes of atoms,  $\theta$  is the incident x-ray angle,  $\lambda$  is the wavelength of the incident x-ray, and  $n$  is an general integer. Bragg's law essentially has defined a formal mandate that the distance between each of the planes must be a specific distance to produce constructive interference for the incoming and outgoing x-rays. The planes in the lattice can also be described as normal vectors. When these normal vectors have been scaled to the unit cell volume, the new scaled vectors would make up a reciprocal lattice which can be described by a reciprocal unit cell itself.<sup>150,163,164</sup> The reciprocal lattice vectors have units of inverse length. Each reciprocal lattice vector can be reference through another formulation called Miller indices. The miller indices,  $h$ ,  $k$ , and  $l$ , have been denoted based on where the physical lattice planes may cross through the real space unit cell.<sup>150</sup> Based on the symmetry of the cell different planes of atoms may be absent or symmetrically the same as others leading to systematic absences due to non-allowed reflections. A specific  $d$  spacing can affectively be linked to a certain reciprocal lattice vector and a Miller index. The symmetry of the unit cell plus frequency of reflection for each atom defines the structure factor. Returning equation 2.1, the value  $M_{hkl}$  has been defined as a multiplication factor to account for all of the refractions that have been symmetrically the same. The variable  $LP$  is involved with how the electric field of the x-ray photon can interact with the electric field of the atom. In many powder x-ray diffraction instruments, the angle of the x-ray source and detector are moved simultaneously making the measured angle reported in  $2\theta$ . Both the polarization factor and temperature factor are affected by the angle of the incidental x-ray.

Powder x-ray diffraction can be used to simply match a measured pattern to a known diffraction pattern or it can be used to deduce the cell and atomic positions based on the systematic absences, intensities, and peak shape.<sup>165</sup>

#### **2.1.4 Scanning Electron Microscopy (SEM)**

Scanning electron microscopy has also been used in many cases to identify particle size, phase homogeneity, and elemental content. The scanning electron microscopy method has utilized highly accelerated electrons to visualize materials at extremely small lengths. Typically a sample designed for the scanning electron microscope will be mounted on carbon paper and in some cases will be covered in a small amount of gold for image clarity. The scanning electron microscope tip will move along the sample in a raster like fashion. When the electrons have impacted the sample it produces random secondary background electrons that are read by the detector to produce high resolution images. Other information gathered from SEM has been from the back scattered electrons. The back scattered electrons interact with the compound similarly to x-ray diffraction so it highlights similar structure and composition. Lastly, the energy dispersive x-ray spectra (EDX) at various points in the image can also be taken as not all of the interactions have been elastic in nature. The energy dispersive x-ray spectra of various particles can be used to deduce phase homogeneity.<sup>166</sup>

#### **2.1.5 Inductively Coupled Plasma – Atomic Emission Spectroscopy**

Inductively coupled plasma - atomic emission spectroscopy (ICP-AES) has been a method used to quantize elemental quantities. Samples are typically dissolved in a simple solution for analysis; in most cases the simple solution has been a low concentrated solution of nitric acid. When the measurement has been taken, the solution would be nebulized and passed through a high energy argon plasma. The plasma has been produced by electromagnetic induction and electronic excitation. Electrons excited from the argon gas are then accelerated into free argon atoms to produce the plasma. When the solution has been passed through the plasma, the radiation produced from the argon excites the analyte

and emits the electronic atomic spectrum of its contents. A strong peak in the spectrum can be integrated and compared to a set of standards to quantify the elemental content. The detector allows for the simultaneous analysis of multiple elements. The ICP-AES method can be used to find the molar ratios of composing elements in a solid state chemistry compound.<sup>167</sup>

#### **2.1.6 Cyclic Voltammetry**

Electrochemical measurements like cyclic voltammetry have been important techniques for the analysis of many redox reactions; this has included biological reactions, reactions involving coordination chemistry, and even redox active materials for batteries and fuel cells.<sup>44</sup> Particularly in this dissertation, the focus will be on battery materials applications. In all cyclic voltammetry measurements, a device called a potentiostat has been typically used. A potentiostat has three major electrodes that can be attached to the cell. They have been defined as the counter, reference, and working electrode. In many cases the counter electrode and the reference electrode have been separated to make separate voltage and current measurements. The working electrode has been from where the current is measured and the potential is controlled.<sup>167</sup> The reference electrode has been self explanatory and sets the reference for the potential and lets a minute amount of current through to make voltage measurements. The counter electrode has just been used to complete the circuit for the working electrode. In the case of lithium-ion battery materials, the counter electrode and the reference electrode have been defined as the same electrode and typically tested against elemental lithium.<sup>168</sup>

Typical testing of many batteries involves the use of a coin cell or a split cell set up. To form a proper test cell, the test battery material would be mixed with binder, amorphous carbon, and an aprotic polar solvent to produce a slurry. The slurry would then be spread on a current collector (e.g. aluminum) with a doctor blade for an even coating. The coating would then be dried at an elevated temperature and a low pressure. The amorphous carbon has been used to increase electronic conductivity, and the binder has been to ensure connectivity between particles. The coated current

collector would then be placed in the cell with the reference electrode, lithium, and the electrolyte. Highly porous Teflon separators would be placed between the electrodes to prevent an electric short, as well.<sup>168</sup> The convention used when testing battery materials has designated lithium as the anode (and reference) with the cathode as the tested battery material. There has also been a slight convention difference when displaying cyclic voltammogram of a tested battery material compared to a typical cyclic voltammogram. In a normal voltammogram, the potential has been listed with the positive potential on the left and the negative potential on the right. Also, the cathodic peak shows the reduction of the tested material as a positive current while the anodic peak would be a negative current. The convention used in battery material testing places the potential on the y-axis going from negative on the left to positive on the right. The anodic peak for the charging the battery material would be shown as a positive current, and the cathodic peak for the discharge of the material would be shown as a negative current.<sup>11</sup> The convention has been shown in Figure 2.1.

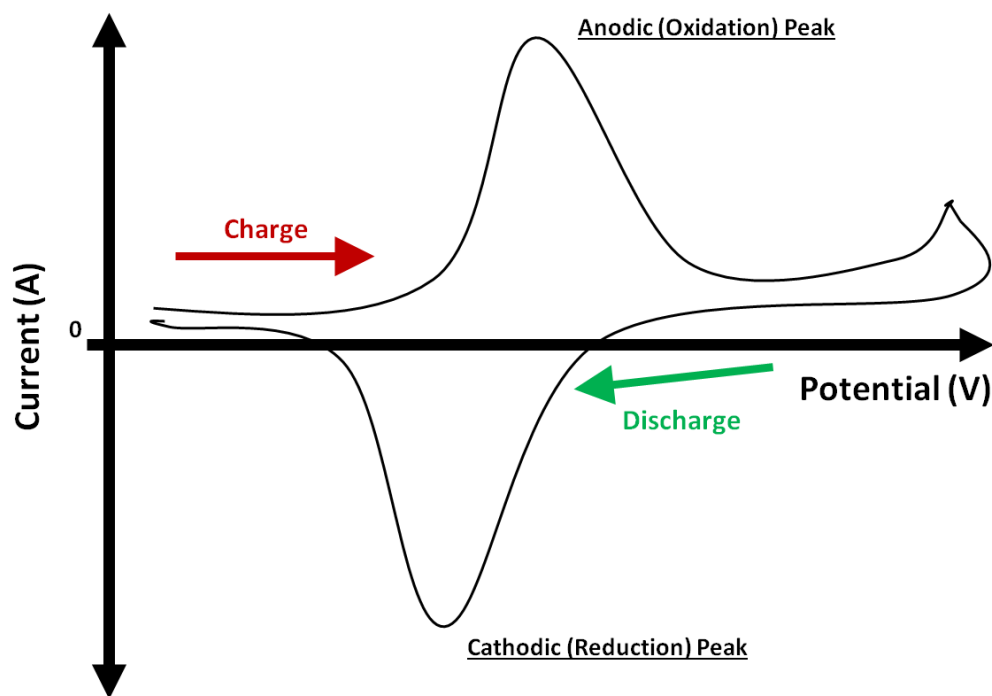


**Figure 2.1: Convention used for cyclic voltammograms of battery materials.**<sup>155,157</sup>

## **2.2 Computational Theory Methods**

### **2.2.1 General Information on Density Functional Theory**

Density functional theory (DFT) can be a very powerful tool for analyzing and exploring the properties of solid materials. It can predict and analyze many things about a compound including structural properties like cell shape and atomic positions. Understanding structural properties can lead to better understanding about ionic conduction and the dipole moment. Many electronic structures can be explored through density functional theory, as well, which allows exploration of chemical and physical properties. The energetic ordering and physical location of electronic states can help deduce what chemical reactions could be relevant. The shape and density of electronic states can predict high or low electronic conductivity. However the combination of both predicting the physical properties and the electronic states can help identify if the material can function as a cathode, a ferroelectric material, or capacitor. The general density can also be plotted to identify charge location and chemically relevant states, as well.<sup>149,169</sup>

In short, density functional theory relies on the complete density of the system, including nuclear density to produce the energy of the system. From a proper density many other properties can be predicted. The theory, by its name, uses the mathematical definition of a functional. A functional outputs a number based on an inputted function. So for density functional theory, the energy of the system would be the value produced from the real space function of the electronic density. The theory does not necessarily require the use of the Schrodinger wave-functions for a functional to work, but the concepts have been useful for understanding density functional theory. Density functional theory has relied on several fundamental theories, but the theories have not predicted how to formulate a proper functional. Theories have only predicted that a proper functional should exist, and how the functional can be used to find the ground state density.<sup>170</sup>

Two of the theories were produced by Hohenberg and Kohn. For the first one, Hohenberg and

Kohn postulated the existence of two external potentials that produce the same ground state density. They also went on to state that each external potential would be a part of its own Hamiltonian which would be attributed to its own ground state wave-function. Thus, both of the ground state wave-functions would produce the same density. However, when each of the separate wave-functions would be used as a trial functions in the Hamiltonian of the other, the eigenvalues produced would lead to an inequality for each substitution. The inequalities would then be added together to show the absurdity of equal values being unequal, even though they have both been for the ground state wave-function.<sup>170,171</sup>

The other theory by Hohenberg and Kohn has stated that with the correct functional, the correct ground state density can produce the lowest energy. This was proven through the fact that if a specific density exists, it produces an external potential, which in turn determines a specific Hamiltonian and wave-function. Because the ground state wave-function can be found through the variational principle, so should similar principles apply to the density.<sup>170,171</sup>

The final main theory was proposed by Kohn and Sham, and it suggested the use of non-interacting wave-functions in the density finding process. The suggestion of utilizing non-interacting wave-functions arose out of the difficulty of calculating kinetic energy accurately in DFT. In the Kohn-Sham orbital approach, the kinetic energy would be calculated through the use of the typical momentum operator found in a Hamiltonian. The rest of the energy of the orbital would be calculated by an effective potential defined by the partial derivative of the energy functional with respect density. The overall energy of the density has the kinetic energy taken from the Kohn-Sham orbital, the columbic repulsion that exists would be defined by the density functional, and the exchange-correlation energy of the system would be defined by the density functional, as well. The density of the system would also be defined so the Kohn Sham orbitals raised to the 2nd power return the density of the system. Typically when searching for the lowest energy density, an effective potential would be created from a starting



guess density. The potential and effective Hamiltonian is applied to the Kohn-Sham orbitals. A new density would be constructed and the potential would be recalculated. Although, there has been debates on the meaning of the Kohn-Sham orbitals they have still been used for electronic analysis. The Kohn-Sham method is also not required for density functional theory, but has been heavily used in the community.<sup>170,172</sup>

### 2.2.2 Basis Sets

In chemistry, many of the calculations have been performed with Slater or Gaussian basis-sets for their Kohn-Sham orbitals; however, many solid state applications benefit from the use of plane-wave basis sets. Plane wave basis are sinusoidal and reflect the periodic nature of solid state systems. Other consideration for solid state calculations has been the use of k-points. K-points would define a mesh in the reciprocal lattice space as fractional coordinates of the Brillouin zone. The Brillouin zone is a form of a reduced reciprocal unit-cell.<sup>164</sup> Each k-point describes a phase interaction between the calculated cell and other cells that would surround it to form energy band based on bonding and anti-bonding interactions. At a k-point coordinate of (0, 0, 0), toward the center of the Brillouin zone, the orbitals of the calculated cell would be completely in phase with each other and represent more of a bonding interaction. At a k-point coordinate of ( $\pi/(2 \cdot \text{length})$ ,  $\pi/(2 \cdot \text{length})$ ,  $\pi/(2 \cdot \text{length})$ ), toward the edge of the Brillouin zone, the orbitals of the calculated cell would be completely out of phase with each other and it would represent more of an anti-bonding interaction.<sup>149,173</sup> Many of the popular plane wave codes have been VASP, Quantum Espresso, and Wien2K.<sup>174-177</sup>

If accurate calculations would be desired, the basis set should be properly defined. While VASP has a fairly robust set of suggested wave-function cut-offs, a convergence test based on the energy cut-off plane-wave basis and the amount of k-points should be performed. The higher the energy cut-off for a plane wave basis set, the larger the basis set would be defined, and with more k-points the better description of the energy bands formed. To find an acceptable basis set, several calculations with

different energy cut-offs and k-point amount can be calculated independently of each other. The plotted the total energy of the cell as a function of the energy cut-off or number of k-points should converge with respect to a specific energy cut-off or k-point amount. If the cell parameters of a unit cell would be relaxed, the basis set would be affected as the plane waves used would be defined a multiple of the reciprocal lattice vectors constrained by a specific plane wave energy cut-off.<sup>149,178</sup> A calculation can be repeated to compare the new and old basis set due to the cell change.

### **2.2.3 Potentials Used in Many Plane Wave Calculations**

Potentials and pseudo potentials refer to how the locality of the core electrons would be applied to the plane-wave basis. Augmented plane-waves and linearized augmented plane waves have been modified as a piece-wise function. Near the core, inside a conveniently defined sphere called a muffin tin sphere, the wave-function would be defined by localized functions. Outside of the radius, the wave-function has general plane-wave sinusoidal characteristics. Orthonormality and gradient are preserved at the boundaries. These have represented the most accurate potentials, but the most computationally expensive.<sup>179</sup>

Norm-conserving potentials have been the least accurate, but the oldest plane-wave potential design. In norm-conserving potentials, the core inside a conveniently define radius would be described by a pseudo-potential function that would be defined by the charge and interaction of the core with the surrounding valance wave-functions. Inside the core the wave-function would not be accurately described due to the non-localized nature of the plane waves. Each plane-wave would be restricted to be orthonormal to each other even in the core radius.<sup>179-181</sup>

Ultrasoft pseudo-potentials would relax the normal conservation of the wave-functions to decrease the wave-function cut-off and basis set of the valance states. This however, has required an increased basis set for the functionality of the core pseudo-potentials and requires an added correction term for the calculation of the energy of the core. This correction term would be dependent on the

orbital overlap matrix. Overall, ultrasoft pseudo-potentials have been computationally less expensive and more accurate.<sup>180,182</sup>

The projector augmented plane wave method calculates the wave-functions of the core with a different plane-wave basis compared to the outside the core. Inside the core the valence wave-functions would not be accurately described, but the inaccurate core functions would be subtracted and substituted with the high quality core-functions through a transformation operator. Both the core and valence functions would be updated with respect one another. The projector augmented plane-wave method has been a decent mix between computationally accuracy and inexpensiveness.<sup>182,183</sup>

#### **2.2.4 Density Functionals Used in Many Plane Wave Calculations**

What differentiates each density functional has been how it describes the exchange and correlation energy of the system. The exchange functional represents the interactions between electrons due to them being indistinguishable fermions with spin. The correlation functional describes electron-electron interaction not described by coulombic repulsion or electron exchange.<sup>170</sup> The most generic has been that of the local density approximation. In the local density approximation, the exchange functional has been calculated according to the homogeneous electron gas approximation, and the correlation functional has been calculated from a random phase approximation calculation of the homogeneous gas. Local density approximation has been better suited for metals.<sup>170</sup> The next higher tier on the Jacob's ladder of DFT includes the general gradient approximation. The general gradient approximation builds off the localized density approximation to include information on the gradient and slope of the density. Some of the most prominent general gradient approximations used in solid state have included Perdew-Burke-Ernzerhof '96 and Perdew-Wang '91.<sup>184-186</sup> The functional widely used by chemists has included the BLYP functional which combines the Becke '88 exchange functional with the Lee-Yang-Parr correlation functional. What differentiate each has been how the gradient would be calculated or approximated to handle low gradients and density cusps.<sup>186</sup> This method has been better

suited for ionic materials.<sup>170</sup>

Then next higher up has included meta-GGA functionals which has included the use of the second derivative of the density to calculate the exchange correlation energy. The modified Becke-Johnson potential would be an example of a meta-GGA functional. The highest on Jacob's ladder would be the hybrid-GGA functionals. Hybrid functionals have involved replacing a portion of the exchange functional with a fraction of Hartree-Fock exact exchange. Some of the majorly used hybrid functionals have been HSE06, PBE0, and B3LYP.<sup>149,170,187–190</sup> Hybrid functionals have typically been the most expensive calculations, and even though it has been placed higher on the ladder it may not always describe the system better. Sometimes modifications and corrections to DFT have been needed. This includes the used of the corrective DFT+U method which involves adding a Hubbard U to the calculation. The Hubbard U represents an energy penalty to raise specific unoccupied Kohn-Sham states based on a localized orbital charge, while other occupied Kohn-Sham states have been lowered due to their occupation and localized exchange. The DFT+U method has been used for many correlated materials with localized electrons. The DFT+U method has usually shrunk the size of affected orbitals.<sup>191–194</sup>

### **2.2.5 Geometry Optimization**

Many plane-wave codes have supported the optimization of atomic positions and cell parameters. Some of the most widely used optimization methods include the conjugate gradient method and many quasi-Newtonian methods. Many DFT codes rely on the Born–Oppenheimer approximation so cell parameters and atomic positions would be updated after each DFT calculation. They would be updated according to structural forces and the position of the structure on the multidimensional potential energy surface. The multidimensional potential energy surface has been defined by all electronic and atomic positions. The conjugate gradient method updates atomic and cell position after each calculation based on the largest gradient at a specific point on the PE surface until the gradient has been extremely small or positive at the bottom of a local minimum. Quasi-Newtonian

methods have used the second derivative Hessian matrix to find the local minimum of the surface. How the Hessian has been approximated would be determined by a specific method. Both methods can be used to find thermodynamically stable or meta-stable compounds.<sup>195–201</sup>

The nudged-elastic band method has been a widely used method to find the activation energy of a transition state. This method has been particularly useful for the prediction of ionic conductivity in a system. In the method, two structures that exist in their own local minimum of the potential energy surface would be linked by a band which contains progressive images of the structure moving from one minimum to the other. Each image would experience extra force constraints perpendicular and parallel to the band and reaction pathway. The forces parallel to the band would mandate the images to be equal distances from each other on the band. The forces perpendicular to the band would be based on the forces experienced due to the PE surface. The nudged elastic band method has been typically relaxed according to conjugate gradient and quasi-Newtonian methods. The band should relax to a saddle point to find a transition state according to transition state theory.<sup>200,202,203</sup>

## **2.2.6 Density of States and Band Structures**

The density of states has been a description of the general electronic structure and the energetic order of the Kohn-Sham orbitals. It would be plotted based the integration of the amount of k-points and states at a particular energy level in a specific reciprocal volume. States can also be distinguished based on spin and element. Distinguishing the states based on the elemental character requires weights to be calculated from the partials charges of the containing elements.<sup>149,170</sup> Density of states can highlight band gaps between valance (HOMO) and conduction (LUMO) states.<sup>149,163,164,173</sup>

Band structures have been the calculation of energy levels plotted as a function of k-points along high symmetry directions. The band structure can be used to identify the periodic symmetry of a collection of electronic states in a band. It can also be used to find a direct and indirect band gap which has identified allowed and non-allowed electronic transitions. Both the density of states and band

structures could be described as more detail spin ladders for crystal materials.<sup>149,163,164,173</sup>

### **3 Charge Transfer Semiconductor $\text{SrFeO}_2\text{F}$**

#### **3.1 Introduction to Metal Oxyfluorides**

Fluorinating metal oxides have been one of the ways to modify their structure and electronic configuration. While oxygen and fluorine both have similar electronegativity, the difference in their oxidation states can lead to some interesting oxyfluoride materials. Usually in these compounds the metal center will typically bond closer to the oxygen atoms of the compound in comparison to the fluorine atoms. This would happen because the oxygen atoms typically have an oxidation state of negative two while the fluorine atoms have an oxidation state of only negative one. However, there have been special cases where better bonding between the fluorine and metal center has occurred and where the oxygen and fluorine atoms bond in an ordered fashion.<sup>204</sup> The purpose of this chapter is to analyze the potential oxygen fluorine ordering after the fluorination of  $\text{SrFeO}_2$ .<sup>205</sup>

Some notable oxyfluoride compounds have been  $\text{NaCaNb}_2\text{O}_6\text{F}$ ,  $\text{PbFeO}_2\text{F}$ ,  $\text{Sr}_2\text{NdCu}_2\text{O}_5\text{F}$ , and  $\text{Sr}_2\text{MnGa}(\text{O},\text{F})_6$ , and battery materials  $\text{LiFe}(\text{PO}_4)\text{F}$  and  $\text{LiFe}(\text{SO}_4)\text{F}$ .<sup>206–211</sup> The study of the compound  $\text{NaCaNb}_2\text{O}_6\text{F}$  and its analogous structures,  $\text{NaSrNb}_2\text{O}_6\text{F}$ ,  $\text{KCaNb}_2\text{O}_6\text{F}$ , and  $\text{KSrNb}_2\text{O}_6\text{F}$  have shown structural control between a Dion-Jacobson structure and a pyrochlore structure. This has depended on the ratio of ion size between the niobium in the compound and the elements in the A' and A position in the  $\text{A}'\text{ANb}_2\text{O}_6\text{F}$  structure.<sup>211,212</sup> The compound,  $\text{PbFeO}_2\text{F}$ , could be described as a direct structural analog to the compound of this chapter,  $\text{SrFeO}_2\text{F}$ . The  $\text{PbFeO}_2\text{F}$  compound has been discovered as a multiferroic material and was found to be antiferromagnetic below 500 K; however, above that temperature the compound would decompose. There was no reported oxygen and fluorine ordering, though<sup>210,213</sup>. The compound,  $\text{Sr}_2\text{NdCu}_2\text{O}_5\text{F}$ , was found to be similar to the  $\text{La}_2\text{SrCu}_2\text{O}_6$  structure, and the fractionally doped  $\text{Sr}_2\text{Nd}_{0.2}\text{Ca}_{0.8}\text{Cu}_2\text{O}_5\text{F}$  structure was found to be a superconductor at a temperature of 85K. Alternatively the study on  $\text{Sr}_2\text{MnGa}(\text{O},\text{F})_6$ , where varying amounts of oxygen and fluorine share

positions,<sup>206,208</sup> has shown how differing amounts of fluorine and oxygen can impose differences in structural distortions.

### 3.1.1 $[\text{CuO}_4]^{2-}$ Based Materials

In the 1980's there was an explosion of research on high temperature superconductivity after many copper oxide compounds were found to conduct electricity with no resistance at low temperatures that were higher than BCS superconductivity theory predicted.<sup>214</sup> Much of these superconductors were shown to have a planar  $[\text{CuO}_4]^{2-}$  structure to exist in the compound. The symmetry of the planar  $[\text{CuO}_4]^{2-}$  has been reported to propagate the electronic Bose-Einstein condensate, which enables the low resistivity. It is still unknown whether this has been mediated through magnons or phonons.<sup>215,216</sup> In certain cases, the formation of these  $[\text{CuO}_4]^{2-}$  layers can be controlled and synthesized through the use of fluorinating compounds like HF,  $\text{XeF}_2$ ,  $(\text{CH}_2\text{CF}_2)_n$  and other compounds. Under the right conditions fluorine can be utilized to separate the  $[\text{CuO}_4]^{2-}$  layers and has been reported to make it possible for the superconductivity to form.<sup>217-219</sup> While superconductivity has not shown up in any other transition metal oxyfluorides, fluorination can be used to control magnetism and other properties within these compounds.<sup>220</sup>

### 3.1.2 Superconductivity

Superconductivity has been defined as the state that certain materials can achieve in which all electronic resistivity vanishes. The transition from normal state to a superconducting state occurs when the temperature of a material has been lowered below a specific temperature in the presence of a low magnetic field. Type I and Type II superconductors have been described thoroughly by the theory proposed by John Bardeen, Leon Cooper, and John Robert Schrieffer to form what has been known as the BCS theory.<sup>221,222</sup>

In the theory, as the temperature of the material decreases, random thermal fluctuations begin to dissipate. The atomic positions in the lattice then become more sensitive to motions of the electron



and as an electron moves it would pull and distort the lattice to produce a phonon (i.e. quantized lattice movement) that follows the electron. The phononic movement of the lattice toward one electron localizes the positive charge and attracts another electron in its wake. The phononic mediation between the two electrons forms a quasi particle known as a Cooper pair.<sup>223,224</sup> In a Cooper pair, the electrons have been reported to have equal and opposite angular momentum in relation to each other so the Cooper pair effectively will act as a Boson instead of a fermion similar to most electrons. Because the Cooper pairs have been reported to act as bosons they can accumulate into the same quantum state and act as a collective group. Because they have been paired perfectly with each other, they do not induce electronic resistance in each other.<sup>223</sup>

As a magnetic field can be imposed on the superconductor, it can interrupt the interaction between the two electrons. A superconductor will attempt to counter-act this through the Meisner effect where the superconductor will begin to produce small circular currents that produce a magnetic field opposite to the applied field.<sup>225</sup> However, at a certain magnetic field, labeled as the critical magnetic field, the applied field becomes too much and the superconductive state can dissipate. Increased temperature increases thermal fluctuations which will remove the mediation between the electrons in a Cooper pair, and at its critical temperature, the state will completely diminish.<sup>226</sup>

Type I and II traditional superconductors have been similar to each other, and can be described meaningfully by BCS theory. The only difference has been how they would be affected by a magnetic field. Both have shown the Meisner effect below their respective critical magnetic field, but in a Type I superconductor the superconducting state immediately will dissipate above the critical magnetic field. While in a type II superconductor, the superconductive state will not immediately break down at the first critical field. Instead, at a magnetic field above this point, the superconducting state will start to diminish exponentially as the magnetic field reaches another critical magnetic field where all of the superconducting state will have vanished. Between the two critical magnetic fields, the superconductor

will begin to form vortexes with normal state material encompassed in the center. As the magnetic field increases the normal state sections will get larger until there will be no more superconducting state left.<sup>224,226</sup>

High temperature superconductors, like the copper oxide compounds, have not been described by BCS theory. They do have a critical superconducting temperature and two critical magnetic fields similar to Type II superconductors.<sup>226</sup> They have also been postulated to form Copper-pairs necessary for a superconducting state, but it has not been hypothesized to be through phonon mediation.<sup>219,227</sup> Type I and II superconductors have been reported to pure metals in their normal state, undoped high  $T_c$  superconducting compounds have been more similar to Mott insulators. In order to form a superconducting state the high  $T_c$  superconducting compound has to be doped with elements that produce electrons or holes in the compound. High  $T_c$  superconducting compounds have been a part of a larger set of materials called correlated electron materials.<sup>228</sup> In High  $T_c$  superconducting materials and correlated electron materials, the electrons are highly localized and correlate heavily toward the location of another. Electrons in correlated materials experience less of averaged repulsion from the other electrons, but their energy has a heavily dependence on the localization of other electronic states. These materials can form charge density and spin density waves which shown a periodic localization of charge or spin.<sup>217-219</sup> For High  $T_c$  superconductors it has been reported that as the electron moves through the material, the localized coulomb repulsion removes any other electron density immediately around it to produce a localized positively charged hole which attracts another electron to form a Cooper pair.<sup>219,227</sup> This theory describing Cooper pair mediation by localized spin and density fluctuations has only been described through the copper oxide layered structures. This theory has not been universally accepted as there have been a few inconclusive experimental studies, and has not described the superconductivity iron pictinide structures.

### 3.1.3 Charge Transfer Semiconductors

Charge transfer semiconductors have been defined as materials that have different elemental character between the valence band and the conduction band, and that the band gap between these two would be on the order of a typical semiconductor. The range of a proper band gap has been somewhat subjective, but has usually been less than 5 eV. The electron interactions that occur in these types of compounds can be similar to those found in Mott insulators. Both can involve the localization of charge to split the electronic band. However, unlike charge transfer semiconductors, Mott insulators have valence and conduction bands of the same elemental character, and typically have a larger band gap. In many cases, a charge transfer semiconductor would have been a Mott insulator if another set of bands from a different element had not crossed Mott insulator band gap.<sup>192,229</sup>

### 3.1.4 The FeOF Compound

Iron oxyfluoride materials have been shown have an interesting assortment of properties. The iron oxyfluoride structure, FeOF, has shown to exist in a structure similar to the rutile structure associated with  $\text{TiO}_2$ , but has shown to order the arrangement of oxygen and fluorine. The ordering was emphasized by a slight elongation of the fluorine iron bond compared to the oxygen iron bond shown by electron diffraction. While the compound  $\text{FeF}_2$  has a pure rutile structure, FeOF decreases in the c-direction of the unit cell compared to  $\text{FeF}_2$ . The ordering of the structure has been postulated to be from difference in oxidation states and electronegativity. The iron oxygen bond has been shorter due to the overlap between iron and oxygen orbitals compared to that of fluorine and iron orbitals. Because the fluorine atoms have been slightly more electronegative compared to the oxygen, fluorine has contracted orbitals to increase the difficulty to bond with iron. However, at the same time oxygen typically has an oxidation state of negative two compared to an oxidation state of negative one for fluorine so oxygen bonds have been closer due to electrostatics, as well.

The  $\text{FeO}_{2-x}\text{F}_x$  structure was initially suggested as an alternative lithium ion battery

material.<sup>56,230,231</sup> Both Kim et al.<sup>231</sup> and Pereira et al.<sup>230</sup> experimented on the compound and found while the material could cycle, it would break down into a Li-Fe-O-F rock salt phase as it was cycled. Both investigators showed that the compound had an open cell voltage of 2.0V, but Kim et al. has shown the compound forms a core-shell type of particle with stoichiometrically more oxygen in the outer shell compared to the inner shell. While there has been a drastic structure change on cycling, it has shown that  $\text{FeO}_{2-x}\text{F}_x$  can work as a battery material once the compound stabilizes structurally. However, less structure change during electrochemical cycling has lead to better battery durability.

Chevier et al. also has given reasons as to why FeOF would be a desirable compound for battery materials.<sup>56</sup> The material,  $\text{FeF}_2$  has been reported to be a pure rutile structure compound, but it has all iron II ions in the structure which has made it unusable as a lithium-ion battery material. When changing from the  $\text{FeF}_2$  structure to the FeOF structure the oxidation state of iron goes from II to III. As the material FeOF contains all iron III ions, it has been made electrochemically accessible as a battery material if it would be reduced with lithium to form  $\text{LiFeOF}$ . Chevier has also shown the compound FeOF has a valance band with primarily oxygen character while the compound  $\text{FeF}_2$  has a valance band with primarily iron character due to the iron II ions. Based on the difference between FeOF and  $\text{FeF}_2$ , it has been suggested that the FeOF structure could be lithiated to access the iron II/III redox couple, and the lithiated state,  $\text{LiFeOF}$ , would have electrochemically accessible iron states at the Fermi level based on the  $\text{FeF}_2$  electronic structure. However, as Pereira et al.<sup>230</sup> And Kim et al.<sup>231</sup> have shown the structure has not maintained the rutile type structure to become electrochemically available. Nevertheless, the structure FeOF has been prime example of how a controlled modification of an iron oxyfluoride compound could be used to manipulate the electronic structure of the material.

### 3.1.5 Fluorinated Cathode Materials

Besides  $\text{Li}_x\text{FeOF}$ , there have been many who have also explored fluorinated batteries as an alternative. Both sodium based batteries<sup>61,101,141,232–234</sup> and lithium based batteries have been

explored.<sup>63,235–239</sup> Fluorination can also be used to increase lithium ion diffusivity on surfaces.<sup>235</sup> The compound  $\text{Na}_2\text{FePO}_4\text{F}$  and its lithium alternative have been explored as an alternative to  $\text{LiFePO}_4/\text{NaFePO}_4$  based batteries.<sup>238</sup> The compound  $\text{NaFePO}_4$  has two different structures, and the thermodynamic structure has been electrochemically active but has degraded as it has been used.<sup>240–242</sup> The material,  $\text{LiFePO}_4$ , has been widely popular due to its high voltage, abundant materials, and high specific energy; however, due to the poor electronic conductivity of the material, it has been engineered into carbon coated nano-sized particles. This has been an expensive process and almost has almost negated the advantages of its high specific energy and abundant materials. The triphylite structure for which  $\text{LiFePO}_4$  exists, has only one dimensional ionic conductivity while  $\text{Li}_2\text{FePO}_4\text{F}$  (and  $\text{Na}_2\text{FePO}_4\text{F}$ ) have two-dimensional conductivity.<sup>101,233,238</sup> While carbon coating have been needed for electrochemical activity of  $\text{Na}_2\text{FePO}_4\text{F}$  and  $\text{Li}_2\text{FePO}_4\text{F}$ , both have reversible voltages of 3.0 and 3.5 V. Both compounds would undergo phase changes during cycling, but the volume change upon cycling was to be found half of that for  $\text{LiFePO}_4$ .<sup>238</sup> The related compound of  $\text{LiFeSO}_4\text{F}$  has also been explored for battery applications, and even though the compound can exist in two structures both have been electrochemically active with high voltages. The tavorite structure has a voltage of 3.6 V while the triplite structure has a voltage 3.9 V. The triplite structure has a much smaller volume change of 0.6% compared to that of tavorite structure, but both have been similar to each other energetically.<sup>63,236,237</sup> Because of the polyoxoanions in the structure, the electron localization of the compounds increases, but the use of fluorination has made it possible to isolate a high energy redox couple. However, the large mass and the poor electronic conductivity of each oxyfluoride material have decreased their appeal. Continuing research has been ongoing.<sup>87,234,237,243,244</sup>

### 3.1.6 The $\text{SrFeO}_2\text{F}$ compound

While  $\text{FeOF}$  has shown the possibility to produce an ordered structure involving iron, oxygen, and fluorine. It has been postulated that oxygen and fluorine ordering could be applied to other types of

structures to form a layered structure similar to many fluorinated copper oxides superconductors,<sup>245</sup> but with iron instead. While d-symmetry superconductivity has been limited to only square planar copper oxide structures, the  $\text{SrFeO}_2\text{F}$  compound would still have a correlated electronic structure with merit to study. Some suggested applications could include heterogeneous catalysts, solar cells and other general electronics.<sup>228,246–250</sup>

The compound  $\text{SrFeO}_2\text{F}$  could be postulated as the iron analogue of the fluorinated copper oxide superconductors. A supposed ordered structure of  $\text{SrFeO}_2\text{F}$  has been shown in Figure 3.1. The structure would contain a plane of the repeated  $[\text{FeO}_2]$  structure separated by a plane of fluorine atoms. The forced symmetry of a correlated planar iron-oxide system could lead to some interesting phenomena and a better understanding of a planar correlated system.

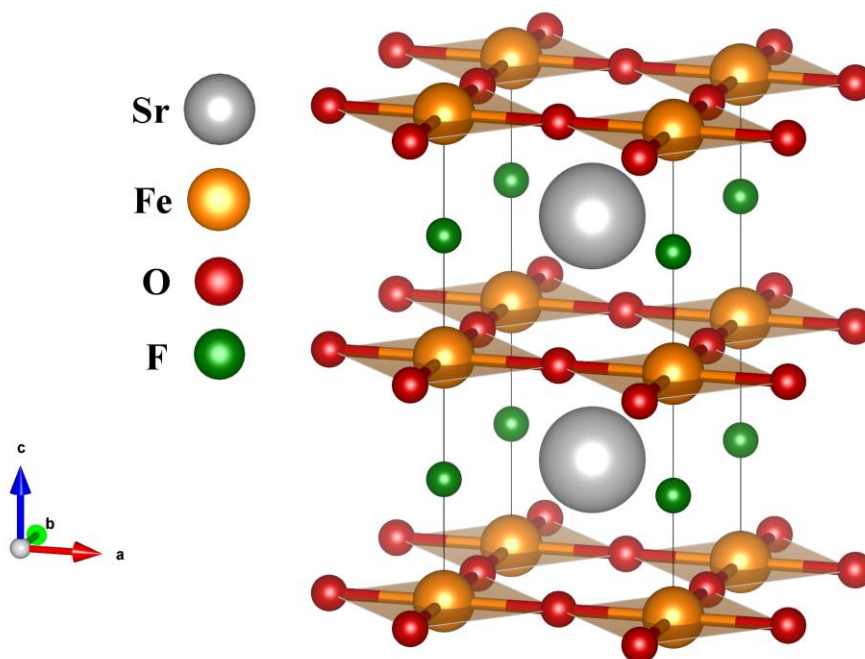


**Figure 3.1: Idealized structure of ordered  $\text{SrFeO}_2\text{F}$** <sup>251</sup>

To synthesize  $\text{SrFeO}_2\text{F}$ , Berry et al. has fluorinated  $\text{SrFeO}_{3.6}$  with poly(vinylidene fluoride) to attempt to produce ordered  $\text{SrFeO}_2\text{F}$ .<sup>206</sup> The fluorination was successful, but there was no reported oxygen fluorine ordering. Berry et al. had first synthesized  $\text{SrFeO}_{3.6}$  by reacting  $\text{SrCO}_3$  and  $\text{Fe}_2\text{O}_3$  in air at  $1250^\circ\text{C}$  for 24 hours. The compound,  $\text{SrFeO}_{3.6}$ , was then reacted with  $(\text{CH}_2\text{CF}_2)_n$  at  $400^\circ\text{C}$  in  $\text{N}_2$  for 24

hours to produce disordered  $\text{SrFeO}_2\text{F}$ . What was reported through  $^{57}\text{Fe}$  Mossbauer and variational magnetic analysis was that the compound coalesced into an antiferromagnetic state below 685K. The compound would stay antiferromagnetic until 300K when random spin fluxuations began to form. While an overall antiferromagnetic ordering of the crystal has begun to dissipate, localized competing magnetic interactions could be still present at low temperature. This has been supported by the ZFC and FC of  $\text{SrFeO}_2\text{F}$  between 0K to 400K having shown differing magnetic responses. From their analysis of the quadruple splitting in the Mössbauer studies, the ratio of cis to trans arrangement of fluorine on iron center was found to be 4 to 1. Berry et al. had produced primarily cis- $\text{SrFeO}_2\text{F}$ .<sup>207</sup>

The synthesis of  $\text{SrFeO}_2\text{F}$  was not single step process going from  $\text{SrFeO}_{3.5}$  to  $\text{SrFeO}_2\text{F}$ , but involved two steps. In the first step  $\text{SrFeO}_{3.5}$  has been reduced to  $\text{SrFeO}_2$  an infinite layered compound<sup>252,253</sup> with a metal hydride similar to  $\text{CaH}_2$ . The infinite layered compound would then be fluorinated by  $\text{XeF}_2$  to produce the desired ordered  $\text{SrFeO}_2\text{F}$  compound. The infinite layered compound would make good starting point as an analog of the square planar  $[\text{CuO}_4]^{2-}$  structure. The compound,  $\text{XeF}_2$ , was used for fluorination instead of HF and other methods due to oxidative ability of  $\text{XeF}_2$  and the safety compared to other fluorination methods.<sup>158,159</sup> The general synthetic route has been outlined for this chapter in comparison to the route performed by Berry et al. has been shown in Figure 3.2

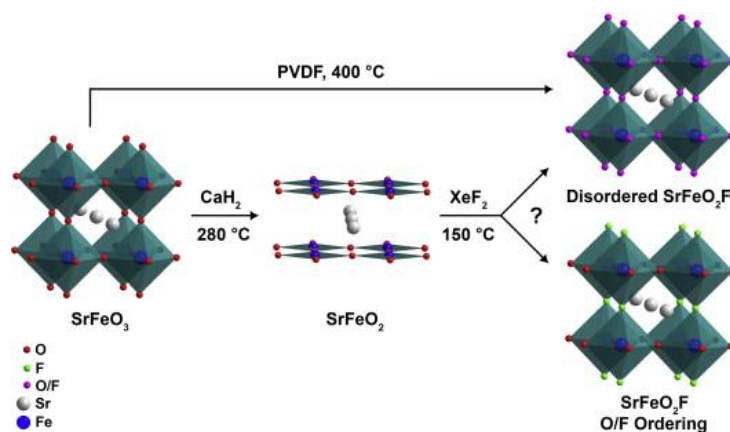


**Figure 3.2 Synthetic Routes for  $\text{SrFeO}_2\text{F}$**

## **3.2 Experimental Details**

### **3.2.1 Synthesis of the $\text{SrFeO}_{3-\delta}$ Compound**

Molar amounts of  $\text{SrCO}_3$  (99.9%) and  $\text{Fe}_2\text{O}_3$  (99.99%) to produce 5 g of  $\text{SrFeO}_{3-\delta}$  were mixed and ball milled at 350 rpm for 30 minutes and pressed into 3/4 inch pellets at 5 pounds of pressure. The pellets were then reacted at 1000°C in air for 48 hours. The pellets were then quenched in air to maintain the perovskite structure and to prevent any alternative structures due to oxygen deficiency.

### **3.2.2 Synthesis of the $\text{SrFeO}_2$ Infinite Layered Compound**

The synthesized  $\text{SrFeO}_{3-\delta}$  was reduced to produce  $\text{SrFeO}_2$ . It was prepared via a modified literature method<sup>252</sup> where large quantities of sample were produced to avoid batch inconsistencies. The amount of 4.75 g (25 mmol) of the previously synthesized  $\text{SrFeO}_{3-\delta}$  was ground with 4.20 g (100 mmol) of  $\text{CaH}_2$  in a nitrogen filled glovebox. The  $\text{CaH}_2$  was initially washed with anhydrous pentane under nitrogen to remove the mineral oil, resulting in a fine white powder. The precursor mixture was then loaded into an ampoule, connected to a silicon oil bubbler, taken out from the glovebox, and lowered through the top of a muffle furnace. The material was fired at 280°C for 48 hours with no intermittent grindings. The ampoule was connected to a silicon oil bubbler for hydrogen pressure release. After completion of the reaction, the product was washed with four 100 ml aliquots of a saturated  $\text{NH}_4\text{Cl}$  in methanol solution to remove any remaining  $\text{CaH}_2$  as well as the  $\text{CaO}$  reduction byproduct.

### **3.2.3 Strontium Iron Oxyfluoride Synthesis**

The compound  $\text{SrFeO}_2\text{F}$  was then oxidized from the synthesized  $\text{SrFeO}_2$ . The reaction was prepared in a nitrogen glove box in purge mode where 0.289 g of  $\text{XeF}_2$  was weighed out in a nickel crucible due to the high reactivity of  $\text{XeF}_2$ . Subsequently, the  $\text{XeF}_2$  and 0.5 g of  $\text{SrFeO}_2$  were loaded into a 50 ml Teflon lined autoclave and heat at 150°C for 48 hours. While  $\text{XeF}_2$  has been one of the safer methods for fluorination, proper safety and ventilation should be maintained. Xenon difluoride can form



hazardous HF from exposure to moisture.

### **3.2.4 X-Ray Powder Diffraction Measurements**

Powder X-ray diffraction was performed on a Bruker D2 Phaser with a copper source with a  $K\alpha_1$  wavelength of 1.5418 Å. A dome-shaped air-free sample holder was used to measure the diffraction pattern of the moisture sensitive oxyfluoride. The synchrotron powder X-ray diffraction (SPXD) pattern was collected on the Argonne National Lab Synchrotron BM-11 beam line using a 0.8 mm kapton capillary. The synchrotron source wavelength was 0.373822 Å. Rietveld refinement was performed on each synthesized structure. Each parameter was optimized separately initially with final refinement of all parameters

### **3.2.5 Mössbauer Measurements**

The  $^{57}\text{Fe}$  Mössbauer spectroscopy of the oxyfluoride was carried out utilizing a  $^{57}\text{Fe}$  co-source in a rhodium matrix at room temperature on polycrystalline powders pressed between two sheets of Mylar film due to the extreme air-sensitivity of the oxyfluoride. This sample preparation procedure can lead to variations in the relative intensities of the 2nd and 5th peaks of the sextets. This can also affect the intensities of doublet lines in presented in the Mössbauer spectrum due to preferred orientation. The measured spectrum was evaluated using Fit;o)—a Mössbauer spectrum fitting program

### **3.2.6 Measurement of Magnetic Properties**

Magnetic measurements were taking with a Quantum Design SQUID and Quantum Design PPMS. The temperature dependence of DC magnetic susceptibility was measured on powder samples with a Quantum Design SQUID magnetometer at  $H = 1000$  Oe in the temperature range 4–400K. Samples were loaded into gelatin capsules under  $\text{N}_2$ , placed into a plastic sample holder, and cooled to 4K under zero magnetic field. All measurements were performed by warming the samples under the applied magnetic field after cooling to 4 K in zero magnetic field (ZFC, zero field cooling) and by cooling the samples in the applied magnetic field (FC, field cooling). The field dependence of DC magnetic

susceptibility, AC magnetization, and specific heat measurements were performed on a powder sample with a Quantum Design PPMS. The AC magnetic susceptibility data was collected between 4 and 310 K by varying the frequency from 50 to 10,000 Hz.

### 3.2.7 Stoichiometry Characterization

The average iron oxidation state was determined by iodometric titration. The iodometric titration procedure has been described previously.<sup>254</sup> Care was taken to avoid exposure to oxygen by blowing nitrogen over the flask of the dissolved sample. Fluorine content was investigated by the ion selective electrode (ISE) technique. The ISE measurements were performed using a Hanna Instruments HI 4110 fluoride combination ISE electrode with an ion- activity buffer (TISAB II) by the calibration curve method. Careful attention was paid to both the temperature of the material and the electrode equilibration time before recording the voltage response. Inductively coupled plasma (ICP) spectroscopy was performed on Vista-MPX CCD Simultaneous ICP–OES instrument (Varian Inc.). A sample of 10 mg of  $\text{SrFeO}_2\text{F}$  was weighed out in the glovebox and dissolved in an appropriate amount of nitric acid then diluted for ICP analysis.

### 3.2.8 Optimization of the A-C Parameter in Ordered $\text{SrFeO}_2\text{F}$

With the full potential Wien2K 11.1 code based on the linearized augmented plane waves method, an comparison of the iron oxygen bond length and the iron fluorine bond length was considered in an ordered cell of  $\text{SrFeO}_2\text{F}$ .<sup>174</sup> The initial cell has been listed in Table 3.1. As the  $\text{SrFeO}_2\text{F}$  structure would essentially be a modification of the  $\text{SrFeO}_{3-6}$  perovskite structure, an initial cell of  $\text{SrFeO}_{3-6}$  was modified with the iron fluorine bonds propagated in the [001] direction. The initial lattice parameters for the ordered  $\text{SrFeO}_2\text{F}$  were taken from the parameter calculated from the powder XRD pattern of disordered  $\text{SrFeO}_2\text{F}$ .<sup>206,207</sup> The values for  $R_{\text{K}_{\text{max}}}$ ,  $G_{\text{max}}$ , k-points and muffin tin radius were specified at each optimization instance.

**Table 3.1: Starting cell of SrFeO<sub>2</sub>F for optimization (listed atomic positions assume the lowest symmetry and no equivalent positions)**

a (Å)	b (Å)	c (Å)	$\alpha$ (°)	$\beta$ (°)	$\gamma$ (°)
3.956	3.956	3.956	90	90	90

Element	x/a	y/b	z/c
Sr	0.5	0.5	0.5
Fe	0.0	0.0	0.0
O	0.5	0.0	0.0
O	0.0	0.5	0.0
F	0.0	0.0	0.5

### 3.2.9 Spin-Polarized SCF Calculations for Ordered and Disorder SrFeO<sub>2</sub>F Magnetic Structures

With Wien2K 14.2, a super cell was constructed from the optimized structure found in Figure 3.8. In the cell, the c parameter was double and the a and b parameter were rotated by  $\pi/4$  radians around the c-axis and multiplied by a factor of  $\sqrt{2}$ .<sup>174</sup> The super cell was specified to have 4 inequivalent iron positions and to maintain a D<sub>4h</sub> point group symmetry. The ordered structures were calculated with an assumed symmetry of P4/mmm with 2000 k-points in the Brillion zone, an RK<sub>max</sub> of 9.0 and G<sub>max</sub> of 18. The muffin tin radii were defined as 2.00, 1.88, 1.66, 1.82 a.u. for Sr, Fe, O, F respectively. From the relaxed VASP structure, the fluorine disordered electronic structure was calculated with a new symmetry and cell mandated by Wien2K 14.2, and with an RK<sub>max</sub> of 9.0, a G<sub>max</sub> of 18, and 4330 k-points with muffin tin radii of 2.10, 1.88, 1.66, 1.82 a.u. for Sr, Fe, O, and F respectively. All structures were also calculated with and without a Hubbard U<sub>eff</sub> value of 4.0 eV with the method specified by Anisimov in 1993.<sup>255</sup> The spin-polarized functional used was the Perdew-Burke-Ernzerhof '96 functional.<sup>256</sup>

### 3.2.10 Relaxations of the Ordered and Disordered SrFeO<sub>2</sub>F Structure

The relaxation of ordered and disordered SrFeO<sub>2</sub>F was performed in VASP 5.2.12<sup>176,177,257,258</sup> with the conjugate gradient method for ionic and cell relaxation.<sup>195</sup> The Perdew-Wang '91 functional<sup>259</sup> and the projector augmented wave method<sup>182,183</sup> were used with a plane wave cut-off of 500 eV and a 1000 k-point mesh in the Brillion zone.

### 3.2.11 Plotting of the Total and Spin Densities of the Ordered and Disordered SrFeO<sub>2</sub>F Structures

The total and spin densities produced by Wien2K 14.2<sup>174</sup> were plotted in VESTA 3.3.5.<sup>251</sup> The total densities in the ordered SrFeO<sub>2</sub>F structures were plotted as a blue isosurface with a value of 0.3 e/Å<sup>3</sup>. At the edge of the cell, inside the isosurface, the density has been described by a heat map with blue-yellow-red mapping constrained from 0 to 8 e/Å<sup>3</sup>. For the spin densities plotted for the ordered SrFeO<sub>2</sub>F structures, the isosurface was constrained with a value of  $\pm 0.035$  e/Å<sup>3</sup> with blue representing positive spin density and red representing negative spin density. At the edge of the cell inside the isosurface, the density has been described by a heat map with red-yellow-blue mapping constrained from -0.5 to 0.5 e/Å<sup>3</sup>. Strontium has been removed for clarity in the plots. For the total spin densities plotted for the disordered SrFeO<sub>2</sub>F structure, a blue isosurface was constrained with a value of 0.3 e/Å<sup>3</sup>. At the edge of the cell, inside the isosurface, the density has been described by a heat map with blue-yellow-red mapping constrained from 0 to 5 e/Å<sup>3</sup>. The spin densities of the disordered SrFeO<sub>2</sub>F structures were plotted according to the same values used for the spin densities of the ordered SrFeO<sub>2</sub>F structures.

### 3.3 Results and Discussion

#### 3.3.1 The Powder X-ray Diffraction Pattern of the Experimental $\text{SrFeO}_3$ Structure

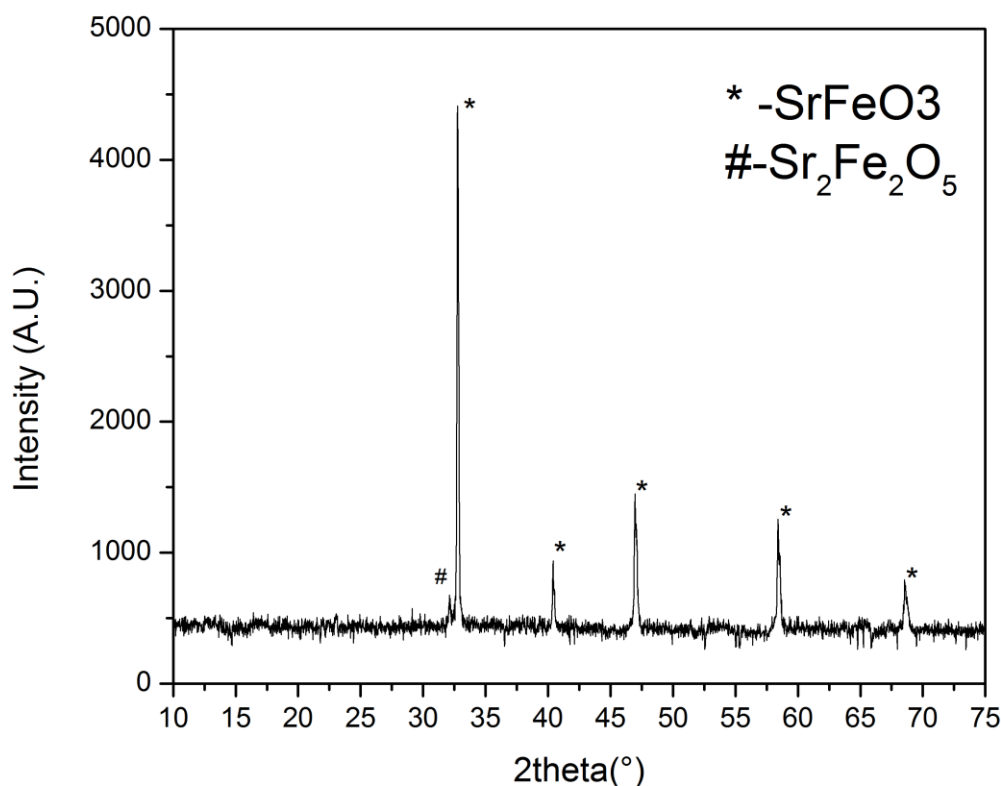


**Figure 3.3: The powder XRD pattern of  $\text{SrFeO}_{3-\delta}$  (WL = 1.5418 Å)**

The powder XRD pattern for the  $\text{SrFeO}_{3-\delta}$  structure, shown in Figure 3.3, was a highly symmetric perovskite and was pure enough for the next step. The impurity in the x-ray was  $\text{Sr}_2\text{Fe}_2\text{O}_5$  or otherwise known as  $\text{SrFeO}_{2.5}$ , a brownmillerite modification of  $\text{SrFeO}_{3-x}$  compound. The preparation of  $\text{SrFeO}_2$  from  $\text{SrFeO}_{3-\delta}$  was inconsequential to oxygen vacancies so the impurity was not detrimental to the synthesis of  $\text{SrFeO}_2$ . The exact oxygen content of  $\text{SrFeO}_{3-\delta}$  can be difficult to identify due to a dependence of oxygen partial pressure and temperature.<sup>260</sup> Oxygen deficiencies in  $\text{SrFeO}_{3-\delta}$  have been a consequence of the instability and non-spherical symmetry of the iron IV ion.

### 3.3.2 The Powder X-ray Diffraction of the Experimental $\text{SrFeO}_2\text{F}$ Structure

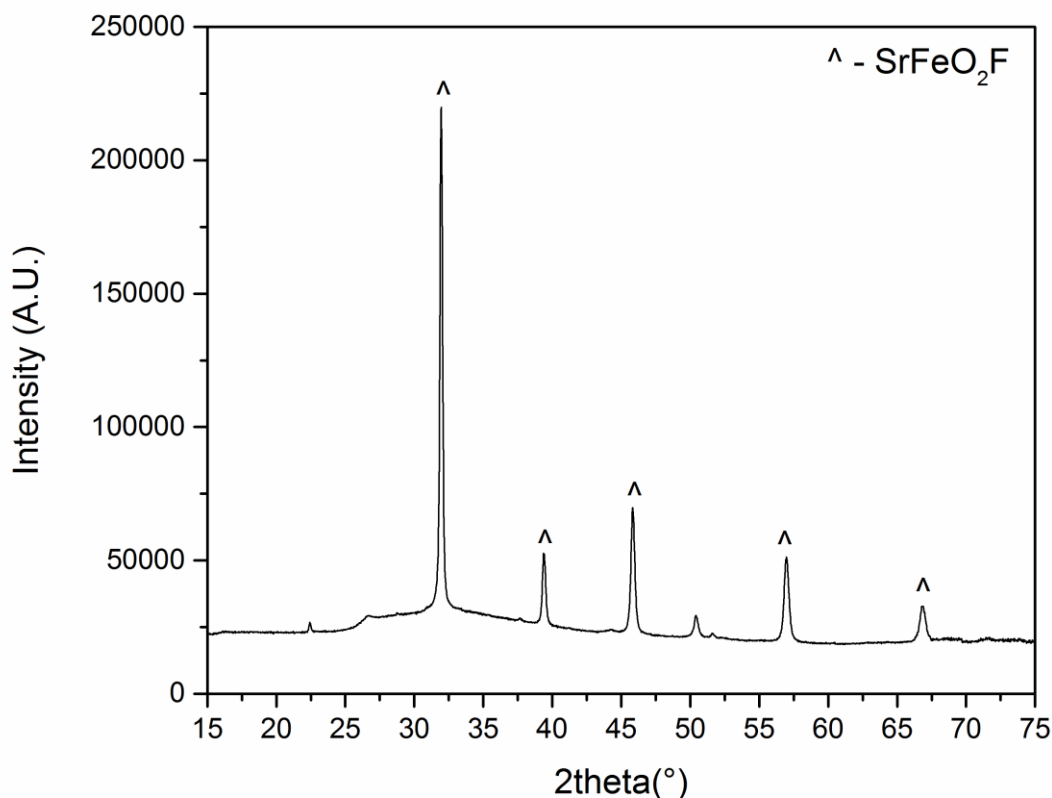


**Figure 3.4: The powder XRD pattern of  $\text{SrFeO}_2\text{F}$  (WL = 1.5418 Å)**

The powder XRD pattern shown in Figure 3.4 for the compound  $\text{SrFeO}_2\text{F}$  was pure with exception of a defect from the dome protection. This has been unavoidable as  $\text{SrFeO}_2\text{F}$  was highly air sensitive. The temperature for the synthesis of  $\text{SrFeO}_2\text{F}$  was limited to  $150^\circ\text{C}$  due to the formation of  $\text{SrF}_2$  at  $250^\circ\text{C}$ . The reaction temperature was lower compared to the previous reaction temperature of  $400^\circ\text{C}$ , but previous attempts at synthesizing ordered  $\text{SrFeO}_2\text{F}$  have shown the disordered structure.<sup>206,207</sup> From the iodometric titration and ICP analysis, an oxidation state of 2.99+ for iron was found and the stoichiometry of the compound was found to be  $\text{Sr}_{1.00(1)}\text{Fe}_{1.00(1)}\text{O}_{2.01(1)}\text{F}_{0.99(1)}$ .

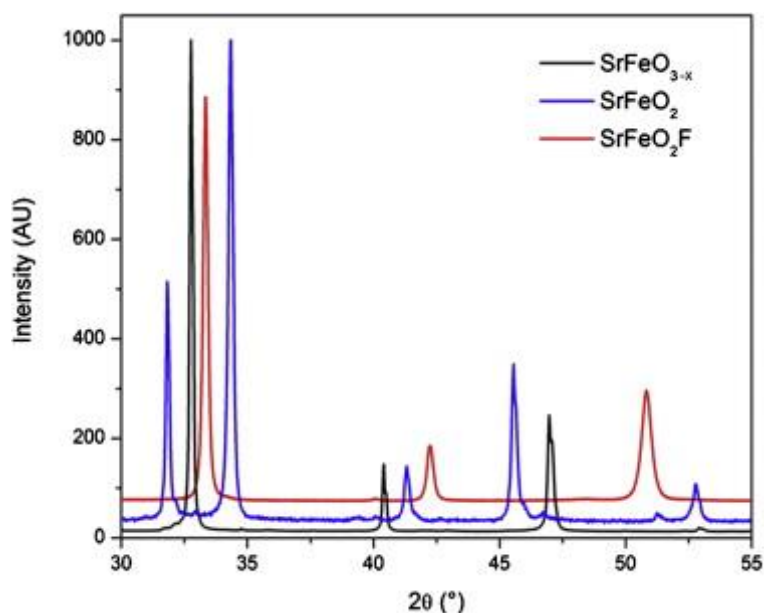


**Figure 3.5: PXD comparison of the patterns for  $\text{SrFeO}_{3-\delta}$ ,  $\text{SrFeO}_2$ , and  $\text{SrFeO}_2\text{F}$**

The XRD pattern shown in Figure 3.3, 3.4, and 3.5 has shown the same reflections for the perovskite space group  $\text{Pm}\bar{3}\text{m}$  for  $\text{SrFeO}_{3-\delta}$  and  $\text{SrFeO}_2\text{F}$ . In the case of oxygen and fluorine ordering, it could still be considered unclear from the XRD pattern above. As oxygen and fluorine atoms scatter electrons with similar power, it can be difficult to see the difference between the two. Figure 3.4 has shown the powder XRD pattern of all three compounds,  $\text{SrFeO}_{3-\delta}$ ,  $\text{SrFeO}_2$  and  $\text{SrFeO}_2\text{F}$  where the main peak of  $\text{SrFeO}_2$  has split due to its symmetry. If fluorine ordered  $\text{SrFeO}_2\text{F}$  should have had a noticeable difference in length between iron oxygen and iron fluorine bonds then it should have produced an XRD pattern similar to that of  $\text{SrFeO}_2$ . The lattice parameters in each structure and the refined structure data have been shown in Table 3.2 and 3.3. Previous literature shows unit cell parameter to be  $a = 3.956 \text{ \AA}$ .<sup>206,207</sup> To explore the bond distances in an ordered  $\text{SrFeO}_2\text{F}$  structure, plane wave density functional theory was used to optimize an ordered structure of  $\text{SrFeO}_2\text{F}$ .

**Table 3.2: Unit cell parameters for  $\text{SrFeO}_{3-\delta}$ ,  $\text{SrFeO}_2$ , and  $\text{SrFeO}_2\text{F}$**

Compound	Space group	Unit cell parameters ( $\text{\AA}$ )	Volume ( $\text{\AA}^3$ )
$\text{SrFeO}_{3-\delta}$	$\text{Pm}\bar{3}\text{m}$	$a = 3.851$	55.11
$\text{SrFeO}_2$	$\text{P}4 / \text{mmm}$	$a = 3.991$ $c = 3.478$	55.35
$\text{SrFeO}_2\text{F}$	$\text{Pm}\bar{3}\text{m}$	$a = 3.955(1)$	61.86(4)

**Table 3.3: Refined structural data for the SrFeO<sub>2</sub>F structure**

Atom	Wyckoff position	x	y	z	Occupancy	U <sub>iso</sub> (Å <sup>2</sup> )
Sr	1b	0.5	0.5	0.5	1	0.03(2)
Fe	1a	0	0	0	1	0.13(4)
O/F	3d	0	0	0.5	0.66/0.33	0.96(2)

### 3.3.3 Optimizations of Ordered SrFeO<sub>2</sub>F

Starting from the experimental lattice parameters of SrFeO<sub>3-δ</sub>, a set of single point calculations for SrFeO<sub>2</sub>F were made with the a and c parameters modified from 3.876 to 3.995 Å over 4 equal spaced values each, for a total mesh of 16 structures that were calculated. In the optimizations of ordered SrFeO<sub>2</sub>F, it has been assumed that a = b due to the symmetry of the cell. In comparing the a and c lattice parameters, the iron oxygen and iron fluorine bond would be compared directly. Each calculation was performed with the Perdew-Burke-Ernzerhof functional,<sup>185,256</sup> an RK<sub>max</sub> of 7.0, a G<sub>max</sub> of 12.0, and 5000 k-points in the Brillion zone with the muffin tin radii set to 2.50, 1.85, 1.64, and 1.64 a.u. for Sr, Fe, O, and F respectively. The convergence was set to 0.0001 Ry. The energy was calculated with respect to the a and c parameter was plotted in Figure 3.6.



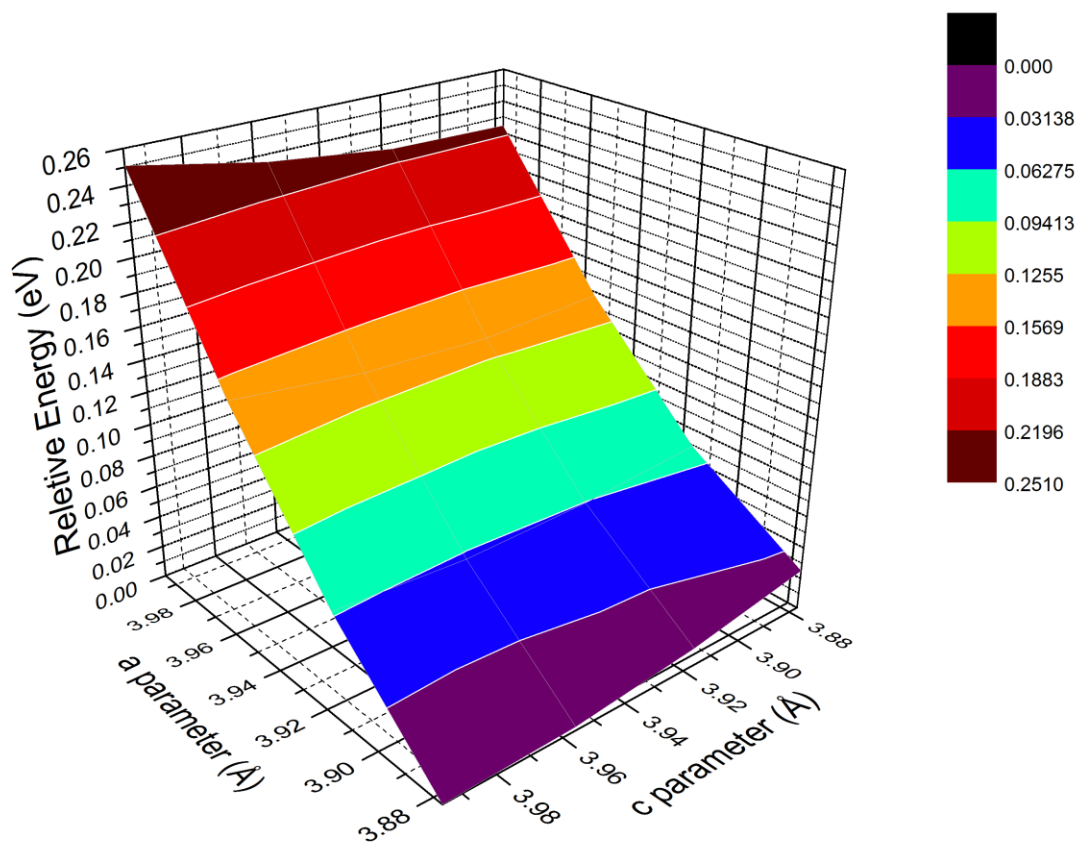


**Figure 3.6: Optimization of SrFeO<sub>2</sub>F as a function of lattice parameter a and c from 3.876 to 3.995 Å. The colors highlight the energy levels in electron volts.**

While Figure 3.6 does not highlight any local minimum for ordered SrFeO<sub>2</sub>F, it has been clearly shown that the iron fluorine bond distance would be different compared to the iron to oxygen bond distance according to the listed lattice parameters.

A new set of calculations were performed to have a better resolution of the potential energy surface. For the single point calculations, the a and c parameters were each varied from 3.758 to 4.114 Å over 10 equal spaced increments, for a total mesh of 100 structures that were calculated for Figure 3.6. Again, it has been assumed that a = b in each calculation. Each calculation was performed with the Perdew-Burke-Ernzerhof functional, an RK<sub>max</sub> of 8.0, a G<sub>max</sub> of 12.0, and 5000 k-points in the Brillion zone with the muffin tin radii set to 2.50, 1.85, 1.64, and 1.64 a.u. for Sr, Fe, O, and F respectively. The convergence was set to 0.0001 Ry, again.

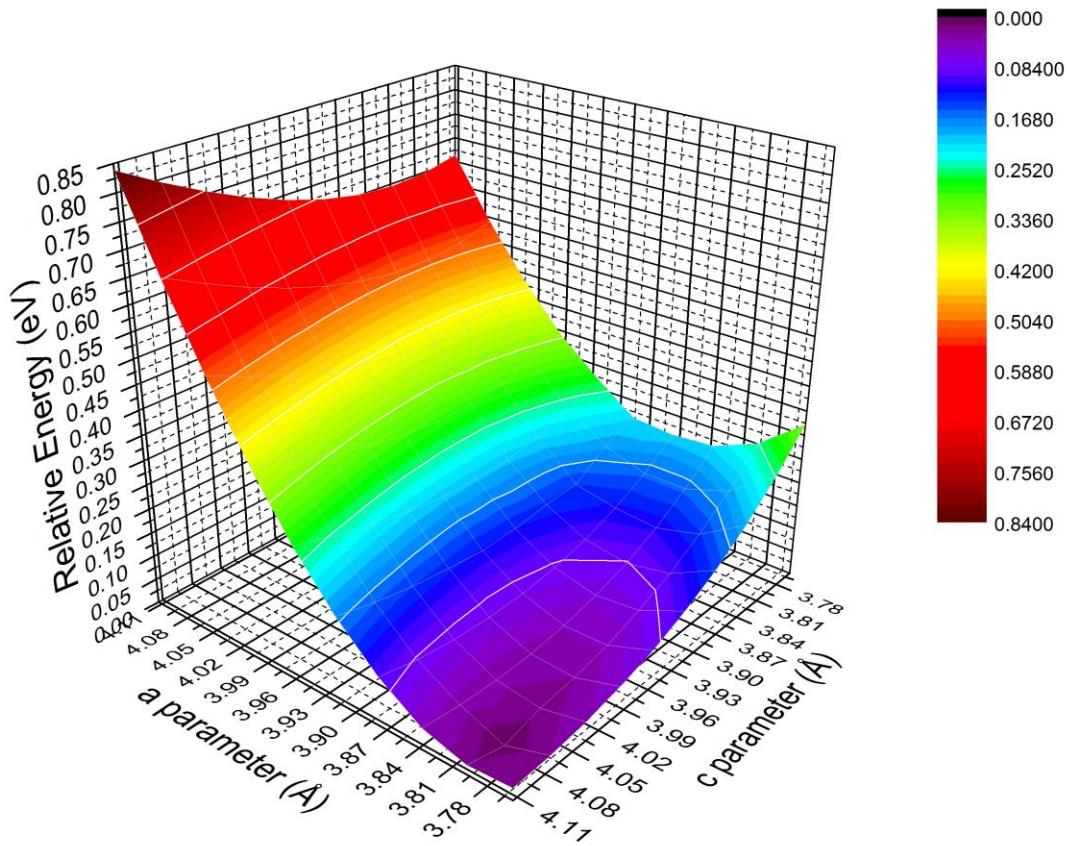


**Figure 3.7: Optimization of SrFeO<sub>2</sub>F as a function of lattice parameter a and c from 3.758 to 4.114 Å. The colors highlight the energy levels in electron volts.**

Figure 3.7 has shown a clear minimum at 3.80 Å for parameter a and 4.08 Å for parameter c. However, the depth of the well has not been fully characterized and resolved as a minimum close to the edge of the potential energy surface. Two final calculations centered close to the minimum were performed to fully resolve the potential well.

An alternative set of calculations have been shown in Figure 3.8, centered on the lattice parameter for SrFeO<sub>3-δ</sub> (3.85Å), was explored for SrFeO<sub>2</sub>F with LDA instead of GGA to attempt to reduce computational cost. It was centered on SrFeO<sub>3-δ</sub> lattice length to better probe the iron oxygen bond length. The a and c parameter were modified each from 3.542 to 4.1195 Å with 16 equal spaced increments for a total mesh of 256 structures. Each calculation was performed with pure LDA, an RK<sub>max</sub> of 8.0, a Gmax of 14.0, and 1000 k-points in the Brillion zone, and a 0.0001 Ry convergence with the

muffin tin radii set to 2.16, 1.62, 1.43, and 1.43 a.u. for Sr, Fe, O, and F respectively.

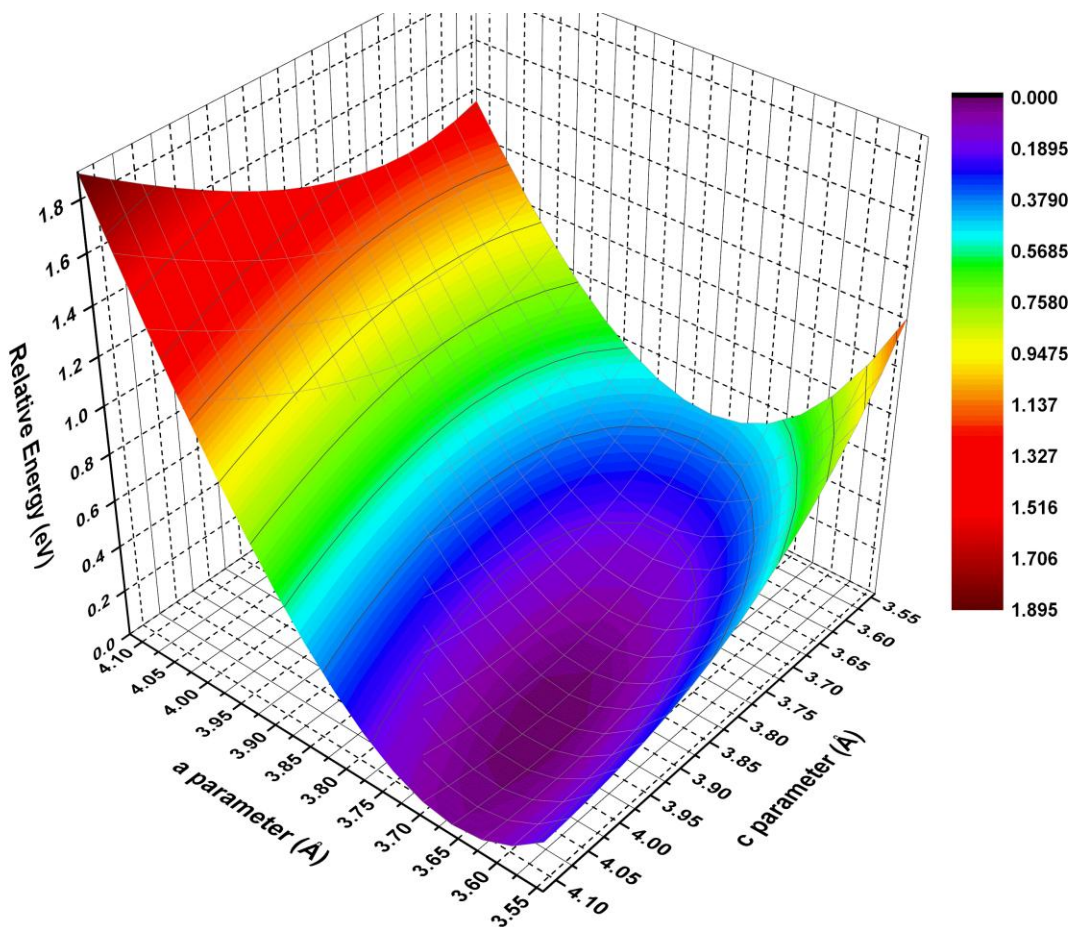


**Figure 3.8: Optimization of SrFeO<sub>2</sub>F as a function of lattice parameter  $a$  and  $c$  from 3.542 to 4.1195 Å with LDA. The colors highlight the energy levels in electron volts.**

A minimum at this LDA optimization was also performed to analyze how LDA may compare to the optimization with a GGA functional like PBE96. The minimum was found to be at 3.696 Å for the  $a$  parameter and 3.927 Å for the  $c$  parameter.

The last set of calculations was performed for the best calculation of lattice parameters without sacrificing accuracy and shown in Figure 3.9. The set of calculations were centered on a structure with an  $a$  parameter of 3.696 Å and a  $c$  parameter of 3.85 Å. For each structure the  $a$  parameter was modified from 3.326401 to 4.02864 Å with 20 equal spaced increments and the  $c$  parameter was modified each from 3.465003 to 4.196501 Å with 20 equal spaced increments for a total mesh of 400 structures. Each calculation was performed with PBE96, an  $RK_{\text{max}}$  of 8.0, a  $G_{\text{max}}$  of 15.0, a convergence of 0.0001 Ry and

5000 k-points in the Brillion zone with the muffin tin radii set to 2.21, 1.66, 1.47, and 1.53 a.u. for Sr, Fe, O, and F respectively.

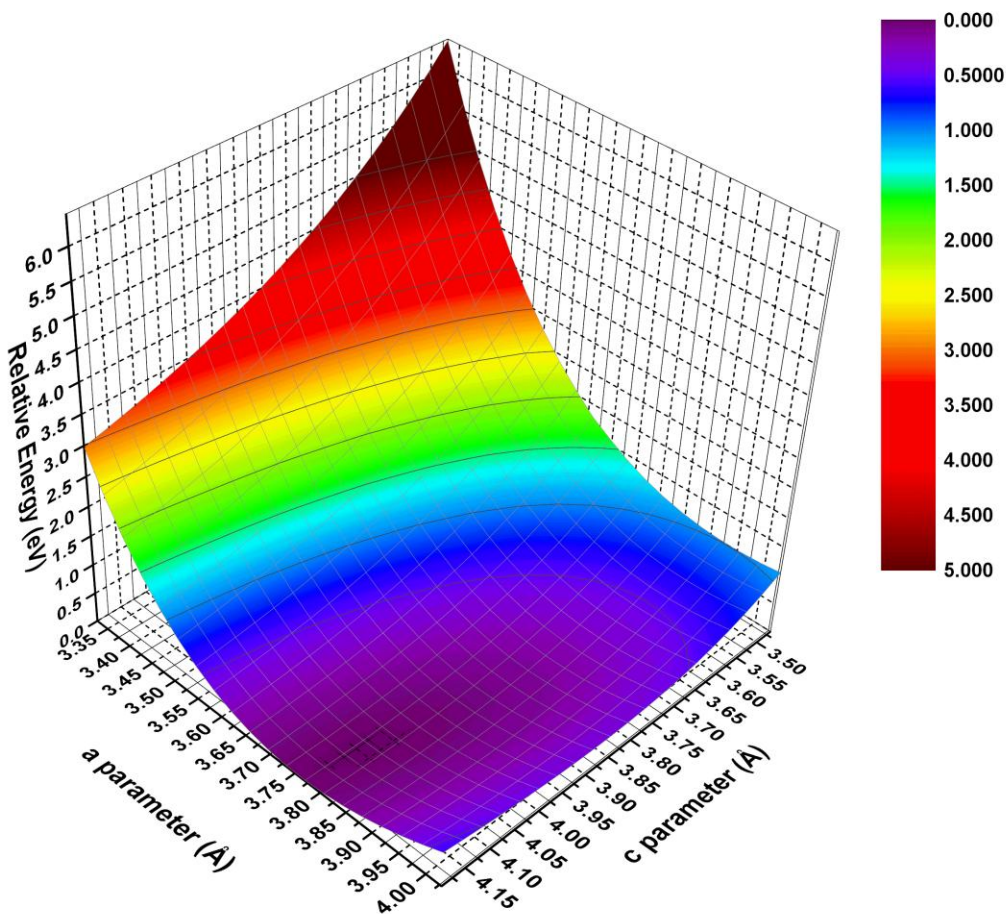


**Figure 3.9: Optimization of SrFeO<sub>2</sub>F from 3.35 to 4.00 Å for the a parameter, and 3.50 to 4.15 Å for the c parameter**

The last optimization had a minimum at an a parameter of 3.76992 Å and a c parameter of 4.1195 Å. As this surface has the best surface resolution with the best basis set option, it has been marked as the accepted value for further calculations. However, the other calculation have shown a strong difference between the a parameter (the iron oxygen bond) and the c parameter (the iron fluorine bond). The synthesis of the SrFeO<sub>2</sub>F stated here has most likely not produced an ordered SrFeO<sub>2</sub>F structure based on these results.



### 3.3.4 Magnetization Data of SrFeO<sub>2</sub>F

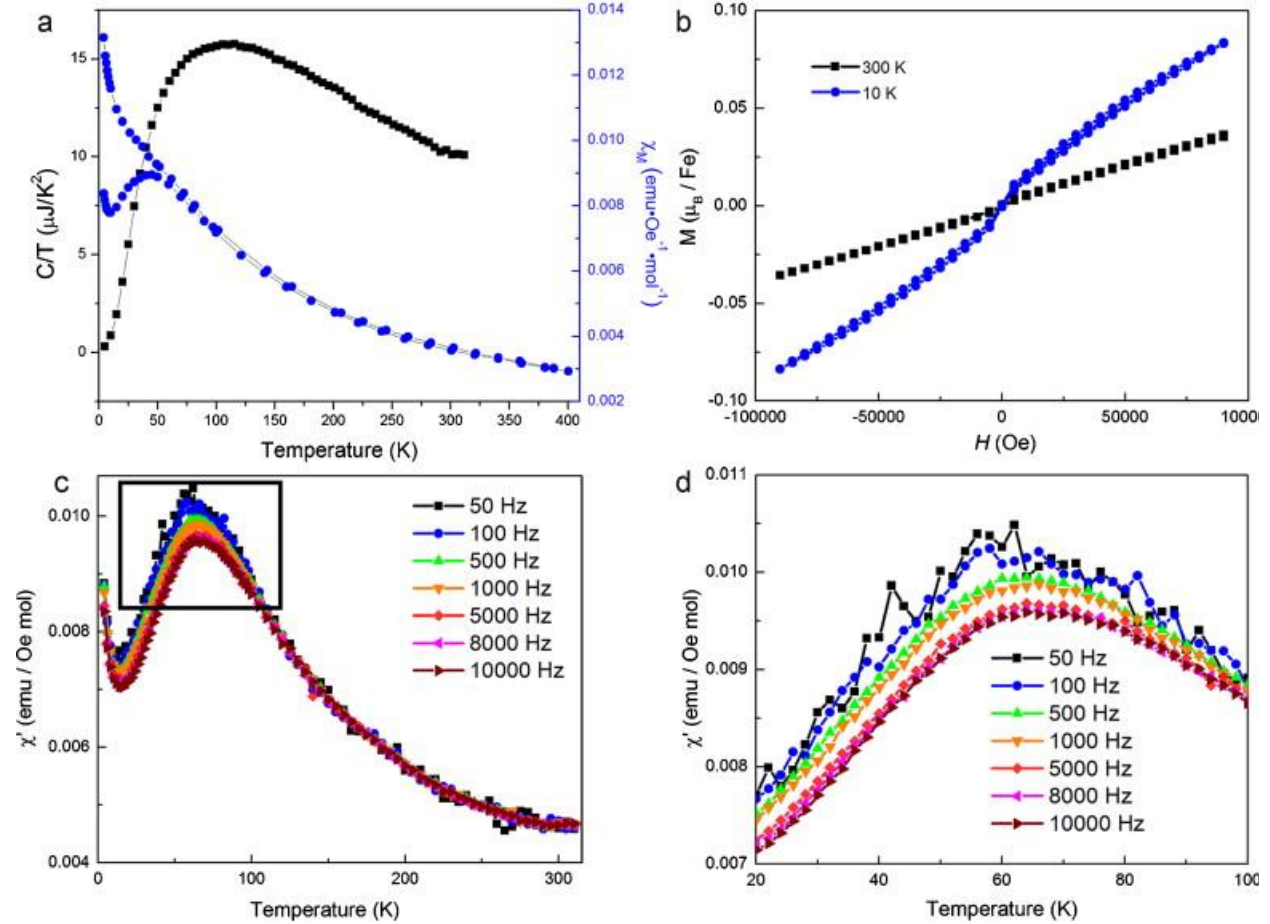


**Figure 3.10: Magnetic data of SrFeO<sub>2</sub>F (a) DC Magnetization at H=1000 Oe (b) Hysteresis at 10K and 300K from  $\pm 10000$  Oe (c) AC susceptibility highlighted in (d)**

While both this work and the work from Berry et al. show fairly non-existent magnetic hysteresis, the work of Berry et al. has shown a weaker magnetic response.<sup>206,261,262</sup> Their work also has also shown a magnetic transition below 300K due to a divergence between the FC and ZFC directions compared to this work where the divergence has occurred below 60K as shown in Figure 3.10. Although Berry et al. did not report AC susceptibility; this work reports the occurrence of a spin-glass system below 60K due to the frequency variation in section c and d of Figure 3.10.

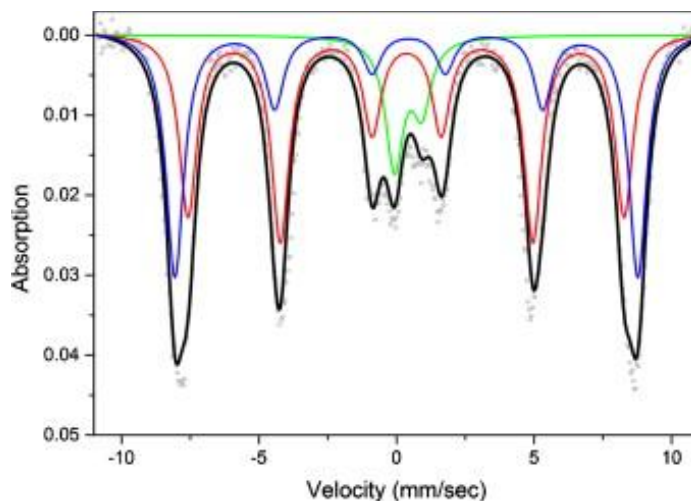


**Figure 3.11: Mössbauer spectrum of SrFeO<sub>2</sub>F at room temperature. It is fitted with three iron centers: Fe1 (blue line), Fe2 (red line), and Fe3 (green line).**

When examining the Mössbauer in SrFeO<sub>2</sub>F, the data shows a local hyperfine field giving evidence of a local magnetic moment near room temperature. Berry et al. has shown that there has been a magnetic transition around 700 K. Due to the waning magnetization shown in Figure 3.10 and 3.11 it has been supported to be antiferromagnetic. The Mössbauer spectrum has been shown in Figure 3.11 and Table 3.4. Compared to Berry et al. it has been shown that there has been significantly more cis-fluorination bonding in this work compare to their work through an equation relating bond angle and quadrupole splitting as used by Berry et al.<sup>206,207</sup>

**Table 3.4: SrFeO<sub>2</sub>F Mössbauer spectrum fitting parameters.**

Site	Isomer shift ±0.02 (mm/s)	Quadrupole splitting ±0.02 (mm/s)	Hyperfine magnetic field ±0.08 (T)	Line width ±0.02 (mm/s)	Area ±2 (%)
Fe1	0.42	0.11	51.43	0.79	41
Fe2	0.33	0.04	49.29	0.8	46
Fe3	0.42	1.04	—	0.81	13

### 3.3.5 Energetic Comparison of the Magnetic Structures of Order SrFeO<sub>2</sub>F

With the assumption to utilize the lowest energy a-c ratio from Figure 3.8, a large super-cell of ordered SrFeO<sub>2</sub>F was constructed according to the details mentioned in the methods section. A super cell was used to compare different types of magnetic arrangements that could exist in the ordered SrFeO<sub>2</sub>F structure as many correlated electron materials have been magnetic. While it has been

discussed that the synthesized  $\text{SrFeO}_2\text{F}$  has not been reported to be ordered, comparing different magnetic structures would be useful in identifying an idealized magnetic structure. Table A.11 lists the atomic positions utilized in the super cell. While Table A.11 assumes P1 symmetry with no equivalent positions, the structure was calculated with a P4/mmm symmetry. The structure was also calculated with and without a  $U_{\text{eff}}$  value of 4 eV. A Hubbard  $U_{\text{eff}}$  value of 4 eV was used as that has been the typical value used in many iron oxide compounds with an iron III charge.<sup>263</sup> For future notice, the mention of the Hubbard  $U_{\text{eff}}$  value has assumed the double counting value,  $J$ , has been accounted for.

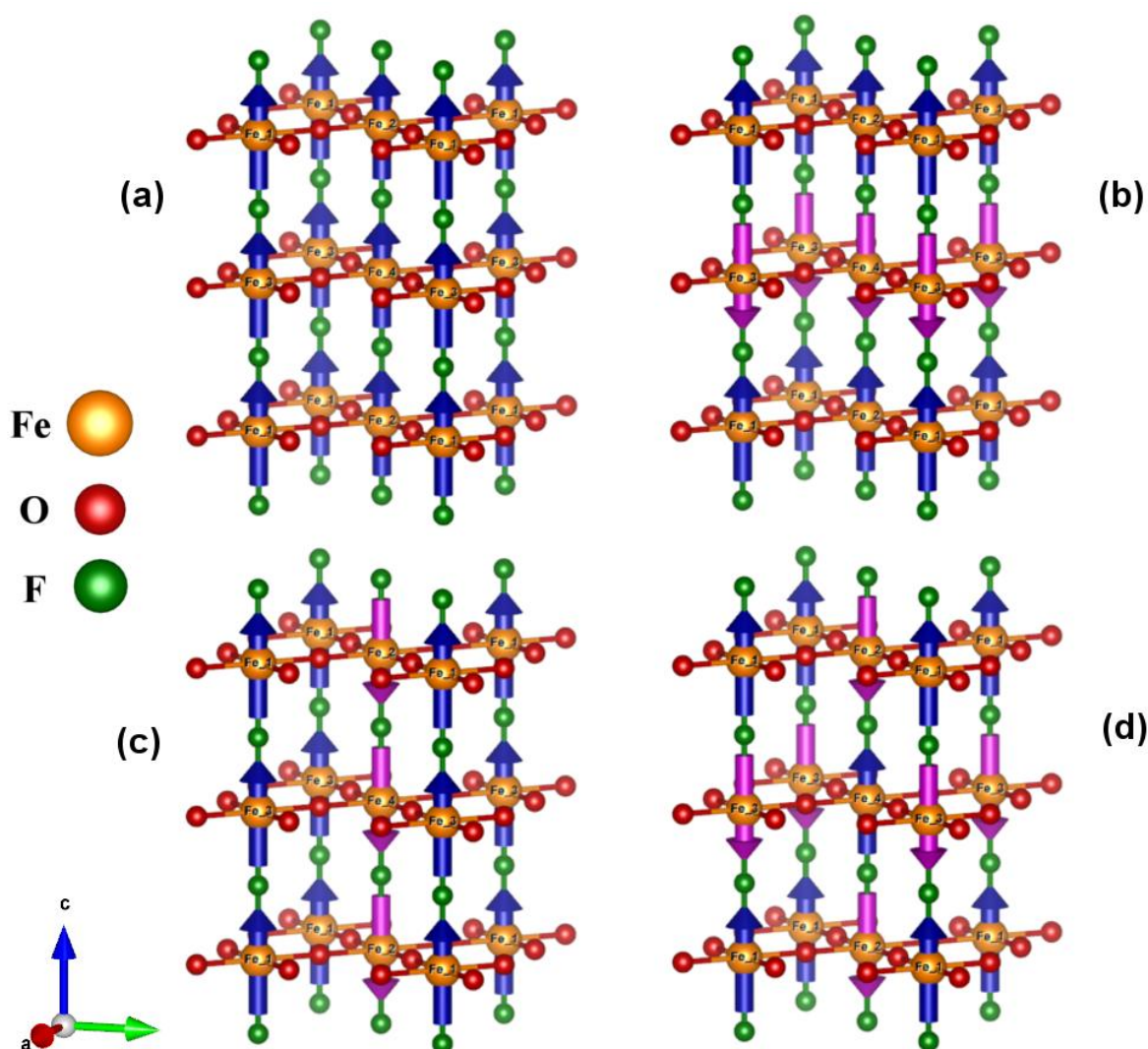


Figure 3.12: Analyzed magnetic structures for the super cell  $\text{SrFeO}_2\text{F}$ . Labeled structures match labels in Table 3.5. Strontium has been removed for clarity.

The different magnetic structures calculated have been shown in Figure 3.11 with the data expressed in Table 3.5. The first structure, labeled (a) in Figure 3.12, would be the completely ferromagnetic structure where all iron atoms were spin up. The ferromagnetic structure has been used for a control structure. The oxidation state of iron in  $\text{SrFeO}_2\text{F}$  should be iron III, and it should have a d5 configuration with a high spin configuration based on the coordinating anions surrounding each iron atom. Based on the electronic environment and the tetragonal symmetry of the cell, it would not be hypothesized to be energetically favorable for a ferromagnetic cell. Structure (b) has a ferromagnetic interaction between the iron-oxygen-iron bonds while antiferromagnetic interactions between the iron-fluorine-iron bonds effectively making antiferromagnetic  $\text{FeO}_2$  sheets. Structure (c) would be the opposite of (b) with antiferromagnetic iron fluorine columns where a ferromagnetic interaction in the iron-fluorine-iron bonds would occur and an antiferromagnetic interaction would occur in the iron-oxygen-iron bonds. In structure (d), the entire cell was antiferromagnetic between the iron-oxygen-iron and iron-fluorine-iron bonds.

**Table 3.5: Energetic analysis of the magnetic structures for  $\text{SrFeO}_2\text{F}$**

With No added $U_{\text{eff}}$									
Structure	Absolute Energy (Ry)	Absolute Energy (eV)	Relative Energy (eV)	Total Magnetic Moment ( $\mu\text{B}/\text{cell}$ )	Moment per Iron 1 ( $\mu\text{B}$ )	Moment per Iron 2 ( $\mu\text{B}$ )	Moment per Iron 3 ( $\mu\text{B}$ )	Moment per Iron 4 ( $\mu\text{B}$ )	Moment per Iron Average ( $\mu\text{B}$ )
Ferromagnetic (a)	-37626.01321	-511928.175	0.2783558	13.9687	2.92448	2.92448	2.92448	2.92448	2.92448
Sheet AFM (b)	-37626.03367	-511928.454	0.0000000	0.00000	2.88904	2.889	-2.88905	-2.88899	2.88902
Column AFM (c)	-37625.93727	-511927.142	1.3116079	0.00005	3.31725	-3.31724	3.31722	-3.3172	3.3172275
Total AFM (d)	-37625.95889	-511927.436	1.0173918	-0.00005	3.26149	-3.2615	-3.26149	3.26147	3.2614875
With $U_{\text{eff}}$ of 4.0 eV									
Structure	Absolute Energy (Ry)	Absolute Energy (eV)	Relative Energy (eV)	Total Magnetic Moment ( $\mu\text{B}/\text{cell}$ )	Moment per Iron 1 ( $\mu\text{B}$ )	Moment per Iron 2 ( $\mu\text{B}$ )	Moment per Iron 3 ( $\mu\text{B}$ )	Moment per Iron 4 ( $\mu\text{B}$ )	Moment per Iron Average ( $\mu\text{B}$ )
Ferromagnetic (a)	-37625.27285	-511918.102	0.9345863	18.31835	3.90127	3.90126	3.90138	3.90144	3.9013375
Sheet AFM (b)	-37625.28039	-511918.205	0.8319593	0.00004	3.9083	3.90829	-3.90829	-3.90828	3.90829
Column AFM (c)	-37625.32964	-511918.875	0.1618912	0.00000	3.99939	-3.99939	3.99939	-3.99939	3.99939
Total AFM (d)	-37625.34154	-511919.037	0.0000000	0.00000	3.98248	-3.98248	-3.98248	3.98248	3.98248



As the magnetic structures were calculated with and without a Hubbard  $U_{\text{eff}}$  value, the reported energetic ordering of both sets of calculations has been shown in Table 3.5. The structure labels used in Figure 3.12 and Table 3.5 will be used for future comparisons and discussions. An attempt to perform a paramagnetic spin polarized calculation was performed with and without a Hubbard  $U_{\text{eff}}$  value; however, the calculations were difficult to properly convergence, thus highlighting importance of high spin iron for this material. Without a paramagnetic calculation, the ferromagnetic arrangement would have the simplest magnetic arrangement for a control. From Table 3.5, it can be shown that with and without a  $U_{\text{eff}}$  value that the total antiferromagnetic structure (d) has been grouped energetically with the antiferromagnetic column structure (c) while the ferromagnetic structure (a) has been grouped with the antiferromagnetic sheet structure (b). The energetic groups have maintained an energetic order within their respective groups, with and without a Hubbard  $U_{\text{eff}}$  value. However, when calculated without a Hubbard  $U_{\text{eff}}$  value, the ferromagnetic structure (a) and the antiferromagnetic sheet structure (b) were lower in energies. With a Hubbard  $U_{\text{eff}}$  value the complete antiferromagnetic structure (d) and antiferromagnetic column structure (c) were the lowest in energy. Another major difference between structures with and without a Hubbard  $U_{\text{eff}}$  value was the magnitude of magnetic moment for all of them. Wien2K has been a plane wave code that explicitly uses the LAPW and the APW methods which require a muffin tin sphere to separate the charge around the nucleus with the extra charge in the interstitial region. The muffin tin sphere has been an arbitrary radius for calculation efficiency in both of these methods. The muffin tin radius has been defined as the same values for calculations with and without the Hubbard  $U_{\text{eff}}$  value. So when defining the magnetic moment shown in Table 3.5, only the portion of the magnetic moment inside the muffin tin sphere has been reported. A lower magnetic value would support less electronic localization and large diffusivity. Without a Hubbard  $U_{\text{eff}}$  value the magnetic moments were small and irregular between each of the individual magnetic states. The states were mostly likely diffuse and not highly localized as the calculations with a Hubbard  $U_{\text{eff}}$  value were,

This has also been supported by the occupation Tables A.1 to A.10 in Appendix A. Without a Hubbard  $U_{\text{eff}}$  value, the ferromagnetic structure (a) and antiferromagnetic sheet structure (b) have lower magnetic moments of about 2.9  $\mu\text{B}$  which would be significantly lower than expected for a d5 iron. The magnetic calculations with a Hubbard  $U_{\text{eff}}$  value each have consistent atomic magnetic moments of about 3.9  $\mu\text{B}$ . The magnetic moments of the Hubbard  $U_{\text{eff}}$  values were slightly lower than expected, but again the moment was only calculated inside the muffin tin sphere. The values were more agreeable to what would be expected for a high spin iron oxyfluoride.

### 3.3.6 Density and Spin-Density of the Ordered $\text{SrFeO}_2\text{F}$ Magnetic Structures

To further look at how the structures differ in relation to a Hubbard  $U_{\text{eff}}$  value and a magnetic arrangement, the total density and the spin density for each of the magnetic structures were plotted for the PBE96+U and PBE96 functionals. The plotted total densities have been shown with an isosurface with a value  $0.3 \text{ e}/\text{\AA}^3$  including 2-D density highlights on the edges of the unit cell. For posterity, only the total density for the Total AFM structure has been shown in Figure 3.13 and 3.14. There was absolutely no noticeable difference between each of the magnetic structures. In fact, there was not a noticeable difference for the total density with or without a Hubbard  $U_{\text{eff}}$  value as shown in Figure 3.13 and 3.14. The only real difference in Figures 3.13 and 3.14 was that of the density between the iron and fluorine atoms and the iron and oxygen atoms. Between the iron and oxygen atoms, there was slightly more density shared in comparison to the density between the iron and fluorine atoms. This has suggested more of a covalent nature between iron and oxygen compared to the bonding between the iron and fluorine atoms.

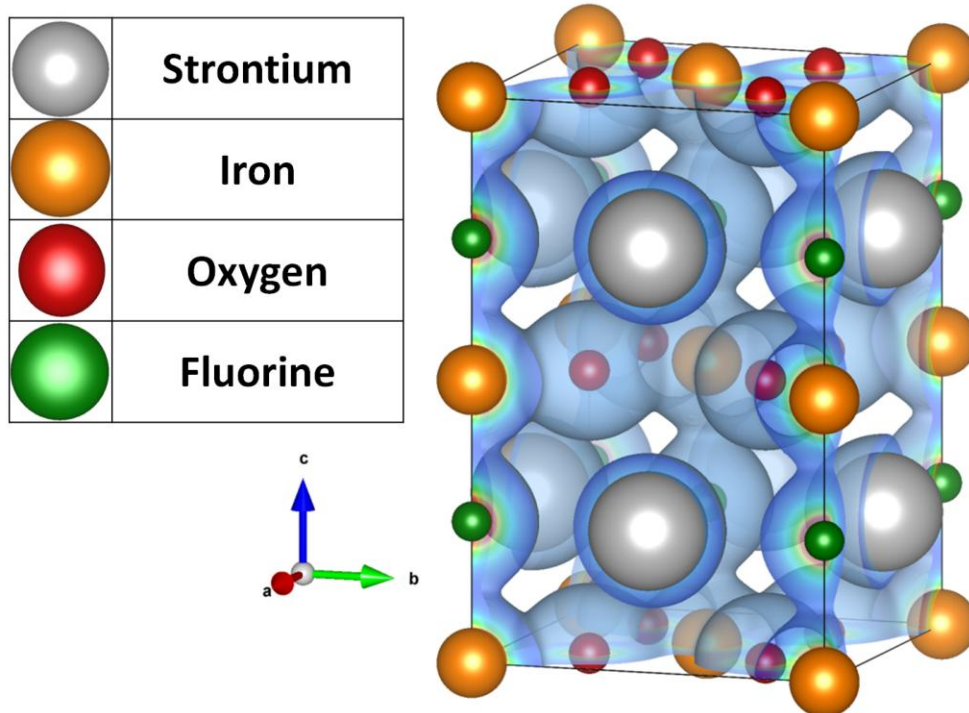


Figure 3.13: Total density calculated from the total AFM structure (d) calculated with PBE96.

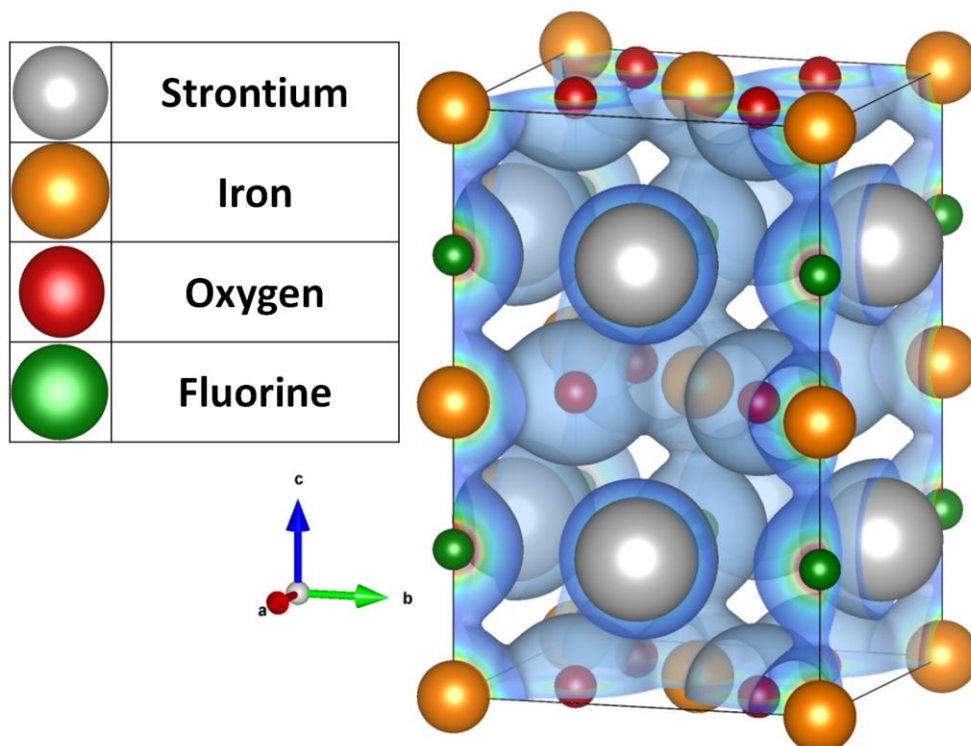


Figure 3.14: Total density calculated from the total AFM structure (d) calculated with PBE96+U.

The plotted spin densities were plotted from the PBE96 magnetic structures and shown in Figures 3.15, 3.16, 3.17, 3.19, and the spin densities for the PBE96+U magnetic structures were shown in Figures 3.18, 3.20, 3.21, 3.22. The plotted spin densities have given a much better understanding as to why the energies were so different for each of the values reported in Table 3.5. In each of the plotted spin densities the blue surface highlights the positive spin densities, and the red highlights the negative spin densities. The ferromagnetic structure (a) has shown in Figures 3.15 and 3.20 a primarily spin up (positive) densities for both the PBE and PBE+U structure which was expected. The spin densities for the antiferromagnetic sheet structure (b) has shown alternating positive and negative 2-D layers of spin density in Figures 3.16 and 3.21, while both of the spin densities for the antiferromagnetic column structure (c) has shown alternating positive and negative 1-D stripes of spin density in Figure 3.17 and 3.18. The spin density for the total antiferromagnetic structure (d) has shown a phase change between each iron center in Figures 3.19 and 3.22.

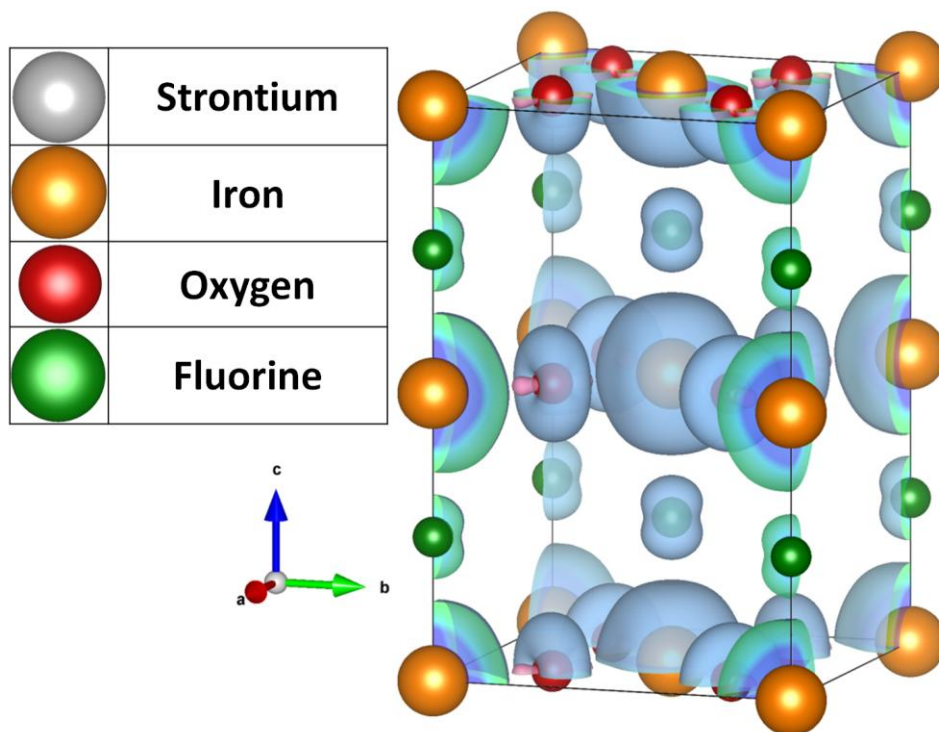
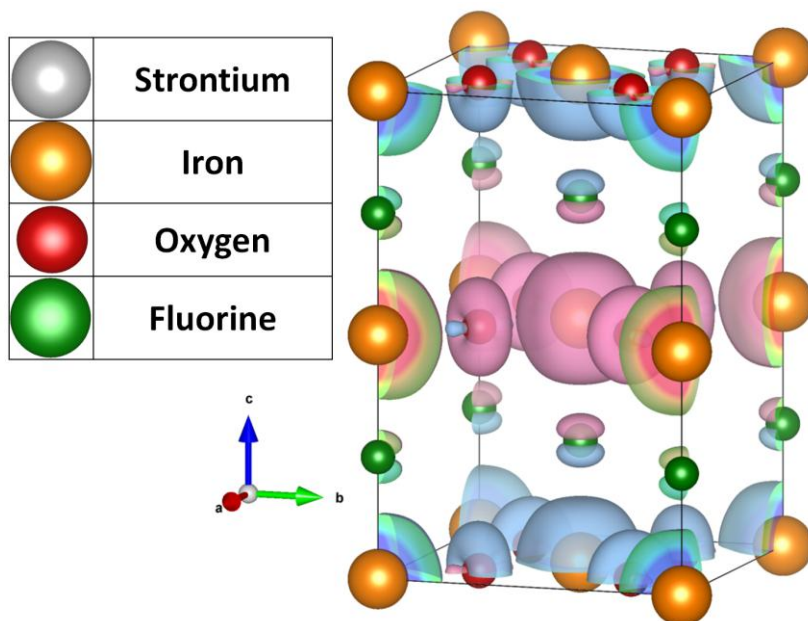


Figure 3.15: Spin density from the FM structure (a) calculated by PBE96.



**Figure 3.16: Spin density from the AFM sheet structure (b) calculated by PBE96.**

There have been some slight deviations from the expected behavior for the calculated spin densities, especially for the surfaces calculated from PBE96. From the PBE96 calculated spin densities of the ferromagnetic structure (a) and the antiferromagnetic sheet structure (b), a donut shaped spin density has formed on the oxygen atoms in both structures as shown in Figures 3.15 and 3.16. The antiferromagnetic sheet structure (b) and the ferromagnetic structure (a) were close energetically as labeled in Table 3.5, as well. This type of spin density has not been expected for the oxygen atoms in the structure. The occupation Tables A.1 and A.2 for the compound  $\text{SrFeO}_2\text{F}$  have shown disproportional spin between each of the p-orbitals in each of the oxygen and fluorine atoms for the ferromagnetic structure (a), while the spin occupations of the fluorine atoms were equal in the antiferromagnetic sheet structure (b). Similar to many transition metal oxides, the magnetic arrangement can be communicated through the anion so a portion of the magnetic moment would exist on the directly bonded anion. However, further analysis about the unconventional donut shaped spin density could be explained by the diffusivity of PBE96 calculations.<sup>264</sup> The diffusive nature of the density for the ferromagnetic (a) and the antiferromagnetic sheet structure (b) allow for the opposite spin density to form at points were

there would be low density or where nodes should supposedly form. Even though, there has been some bonding between the oxygen atoms and the iron atoms, the structure has been expected to behave primarily as an ionic structure with low density between the atoms.

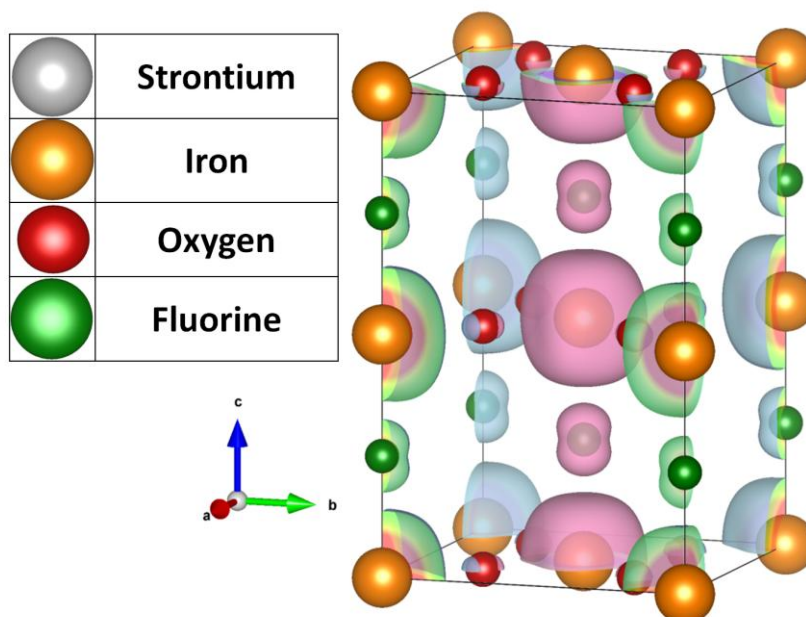


Figure 3.17: Spin density from the AFM column structure (c) calculated by PBE96.

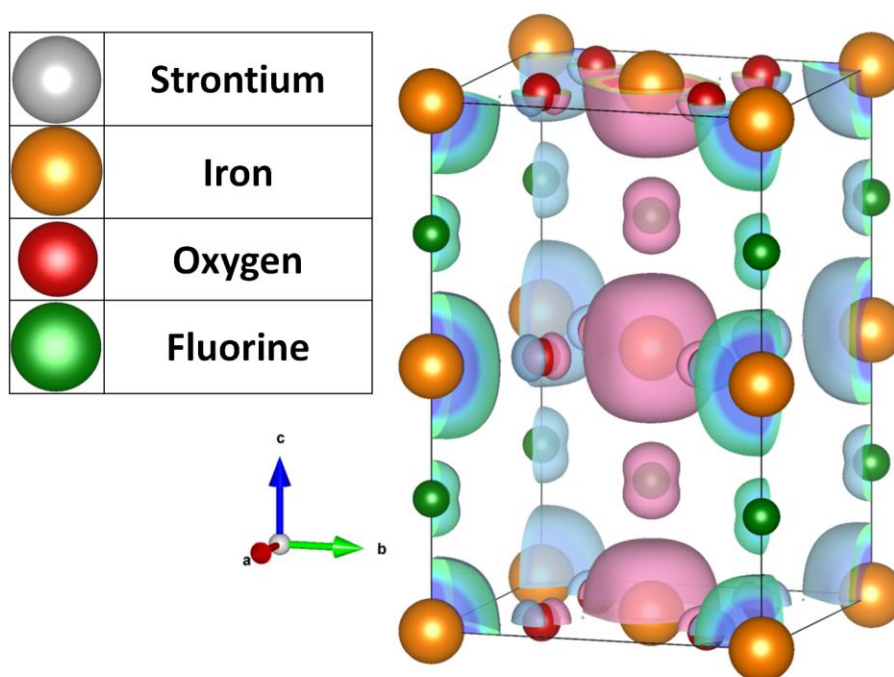
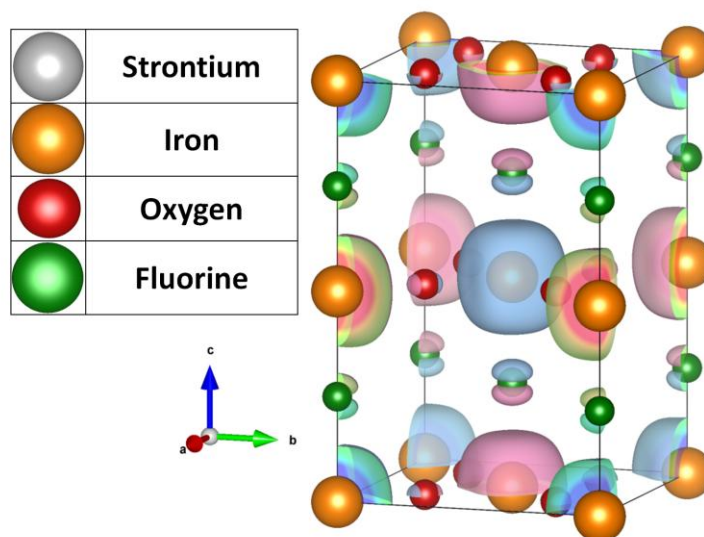


Figure 3.18: Spin density from the AFM column structure (c) calculated by PBE96+U.



The spin densities for the antiferromagnetic column structure (c) calculated for PBE96 and PBE96+U, as shown in Figures 3.17 and 3.18, have produced the alternating positive and negative columns of spin density, but the spin density structure calculated by PBE96 has shown significantly less spin density on the oxygen atoms compared to the density calculated by PBE96+U. The diffusivity of PBE96 has not imposed a disproportionate occupation effect like it has for the ferromagnetic structure (a) and the antiferromagnetic sheet structure (b). The spin boundaries for the antiferromagnetic column structure (c) has been less noticeable at the spin boundaries of the PBE96 spin density compared to the PBE96+U spin density because of the diffusivity of the PBE96 density.<sup>265</sup> The non locality of PBE density has allowed the oxygen atom to better maintain a paramagnetic behavior while the localization of boundary in the PBE96+U density has imposed the hard spin boundary. This effect was also shown in the oxygen atoms on the PBE96 and PBE96+U structure of the total antiferromagnetic structure (d); both the antiferromagnetic column structure (c) and complete antiferromagnetic structure (d) were reported to be close energetically in Table 3.5. The spin densities for the antiferromagnetic column structure (c) have also shown disproportional spin on the fluorine atoms that propagate the ferromagnetic interaction through the iron-fluorine-iron bond.



**Figure 3.19: Spin density for the total AFM structure (d) calculated by PBE96.**

The diffusivity of the PBE96 functional can have different effects based on the magnetic environment used for calculation. The effect it had on the ferromagnetic structure (a) and the antiferromagnetic sheet structure (b) had caused portions of the opposite spin density to sneak out in otherwise consistent spin arrangement fields. While for the antiferromagnetic column structure (c) and total antiferromagnetic structure (d), the PBE96 density had relaxed any spin boundaries on the connecting anions. There has also been a huge difference on how the diffusivity has affected oxygen and fluorine atoms which could be explained by a difference in effective Z which also would dictate the bond length to the iron III center. The oxygen was predicted to have a shorter bond to iron, and the iron fluorine bonds were calculated to be longer. The two dimensional nature of the  $\text{FeO}_2$  planes has lessened the effect of spin boundaries through rotational symmetry for the antiferromagnetic column structure (c) in Figure 3.17 and the total antiferromagnetic structure (d) in Figure 3.18, but it has restricted the spin more for the ferromagnetic structure (a) in Figure 3.15 and antiferromagnetic sheet structure (b) in Figure 3.16. A proper way to fully analyze and confirm the effects of diffusivity on the spin densities could be through calculating the differing magnetic structures with varying Hubbard  $U_{\text{eff}}$  parameters.

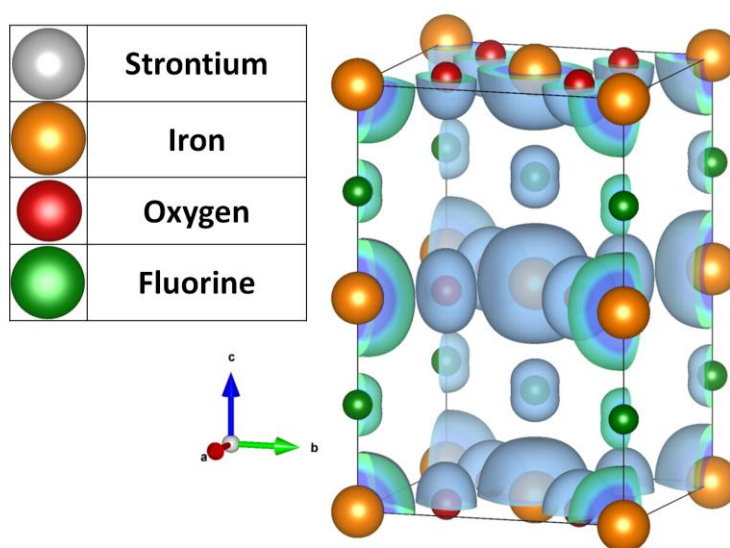


**Figure 3.20: Spin density from the FM structure (a) calculated by PBE96+U.**



All of the spin densities for the PBE96+U structures were more consistent, especially when comparing the iron fluorine and iron oxygen bonds. The spin boundaries were clearly on the oxygen or fluorine atoms. The PBE96+U structures have more localized d-orbitals as shown by the high magnetic moments for each iron center in Table 3.5. The spin-densities of the PBE96+U have more expected spin-densities with no irregularities.

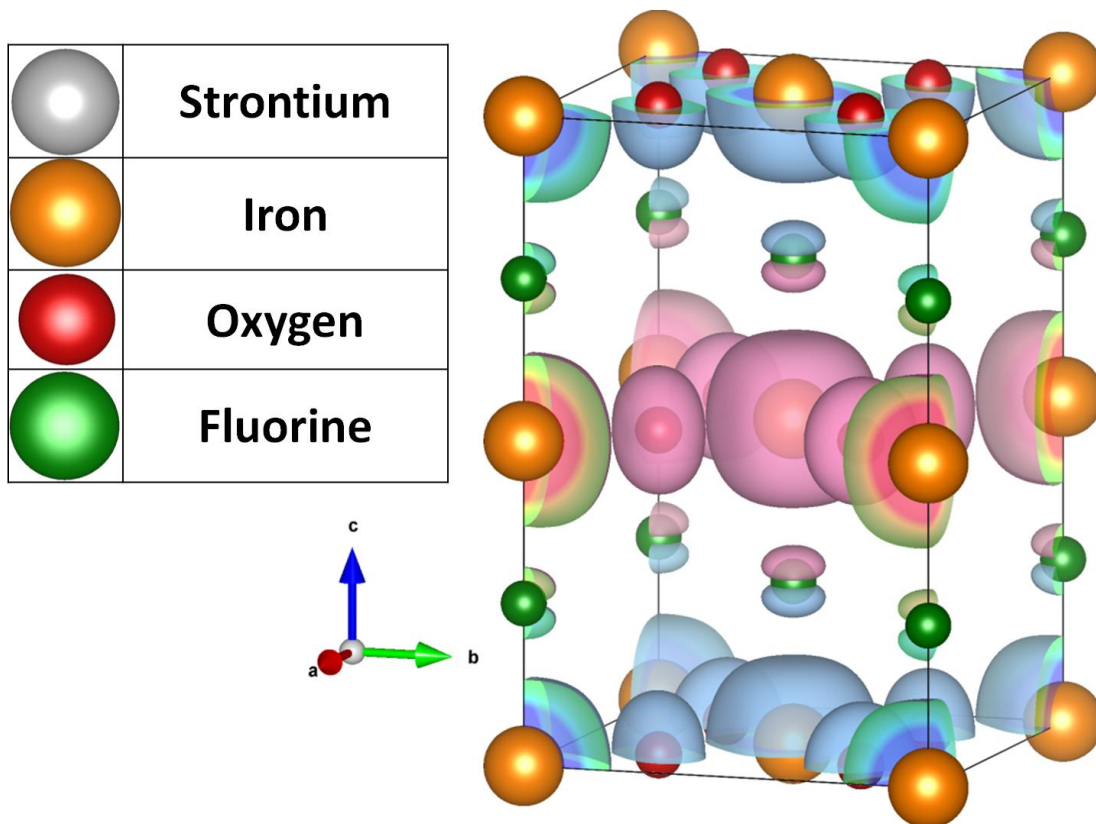


**Figure 3.21: Spin density from the AFM Sheet structure (b) calculated by PBE96+U.**

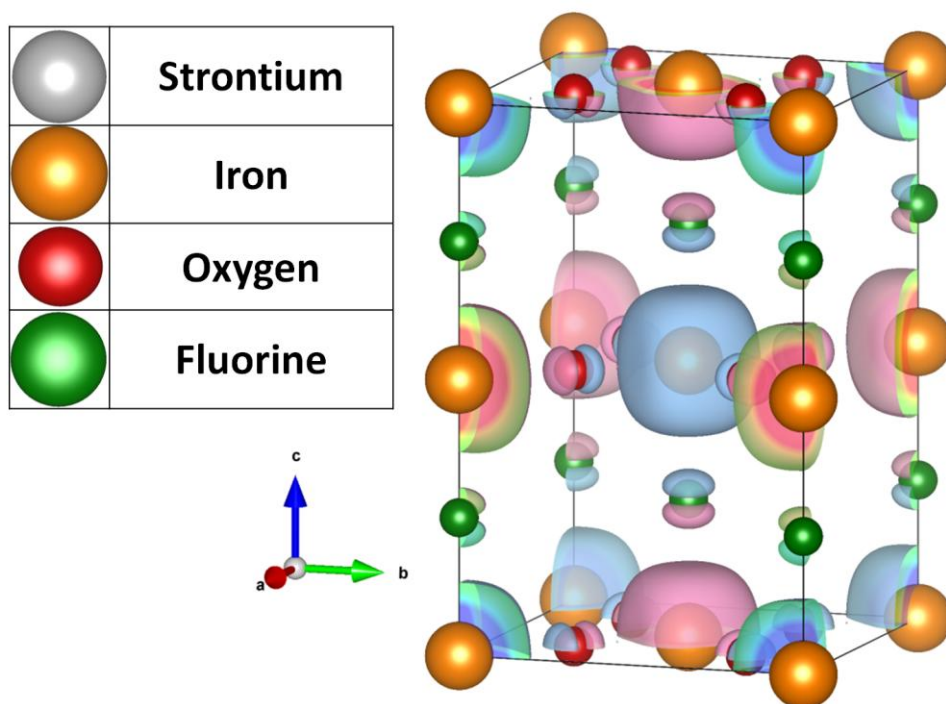


**Figure 3.22: Spin density from the total AFM structure (d) calculated by PBE96+U.**

### 3.3.10 Density and Spin-Density of the Disordered $\text{SrFeO}_2\text{F}$ structure

A disordered  $\text{SrFeO}_2\text{F}$  cell was first optimized in VASP with the conjugate gradient method with the PAW method. The super cell used in the ordered magnetic calculations was modified by interchanging a single oxygen and fluorine atom. The initial and optimized disordered structures have been shown in Tables A.12 and A.13 of the Appendix. The ordered structure was calculated with energy of -131.768 eV and the disordered structure was calculated with energy of -133.088 eV. The disordered structure was lowered in energy because it would break the symmetry to allow the positively charged iron ions to move closer to the bivalent oxygen ions in comparison to the monovalent fluorine ions. The total densities of the disordered structure were plotted for PBE96 and PBE96+U functional which have shown minimal difference similar to the ordered  $\text{SrFeO}_2\text{F}$  structures. The total densities were plotted in Figure 3.23 and 3.24. A large difference was shown in the bonding between iron oxygen bonds and the iron fluorine bonds. The iron oxygen bond showed more density sharing between the ions compared to

the bonding between iron and fluorine ions. However, similar to the ordered structures, the spin density has shown a difference between the PBE96 and PBE96+U calculated structures in Figures 3.25 and 3.26. The differences were not as large as they were in the ordered  $\text{SrFeO}_2\text{F}$  spin density structures. The PBE96 spin density has shown a larger spin density surface compared to the PBE96+U density which has shown to be more contracted. For much of the spin density plotted for the disordered  $\text{SrFeO}_2\text{F}$  structure the spin boundary has been located on the anions. While the local distortion of the disordered structure has not matched the experimental PXD pattern it would be important to keep in mind that the PXD pattern would be the averaged structure over thousands of unit cells. It would not represent the local structure which has been illustrated by the differing Mössbauer spectra in this and previous work.<sup>161</sup>

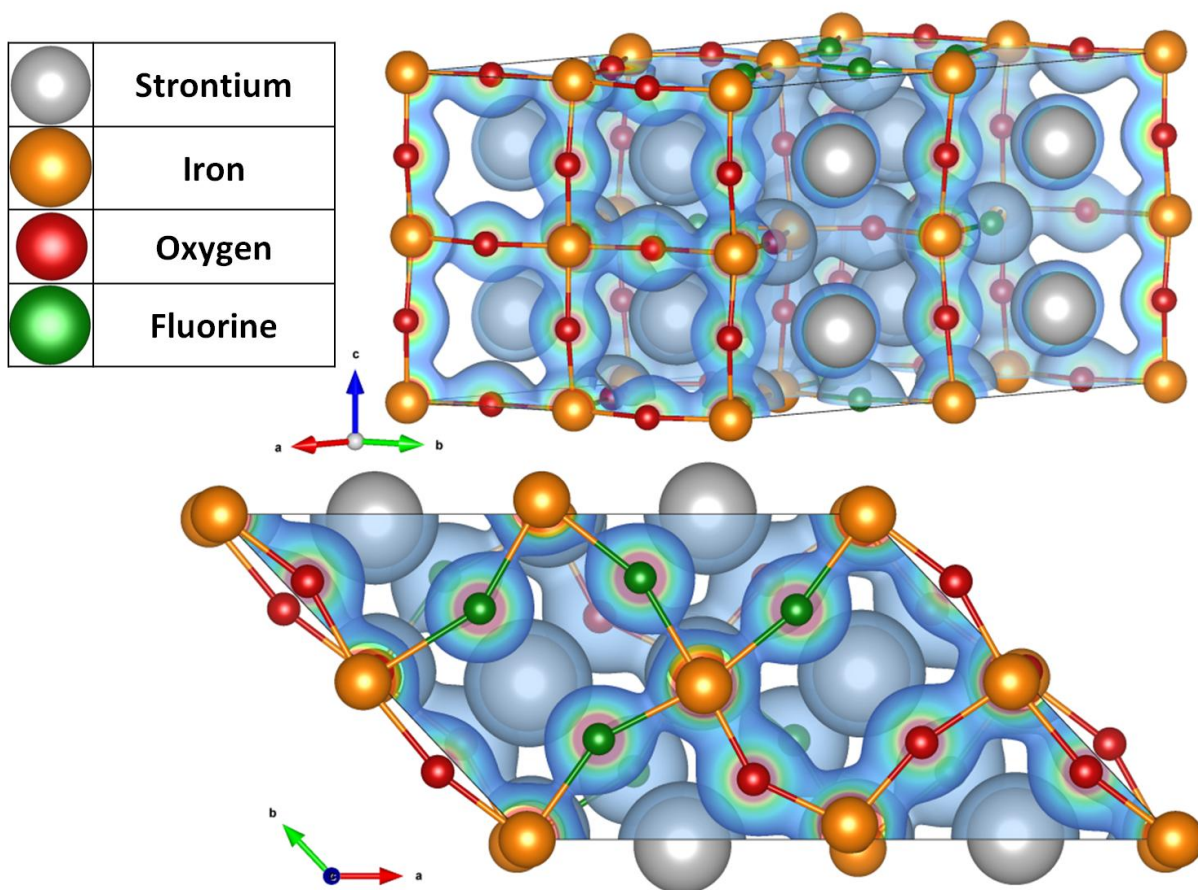


**Figure 3.23: Total density from the disordered  $\text{SrFeO}_2\text{F}$  structure calculated by PBE96.**

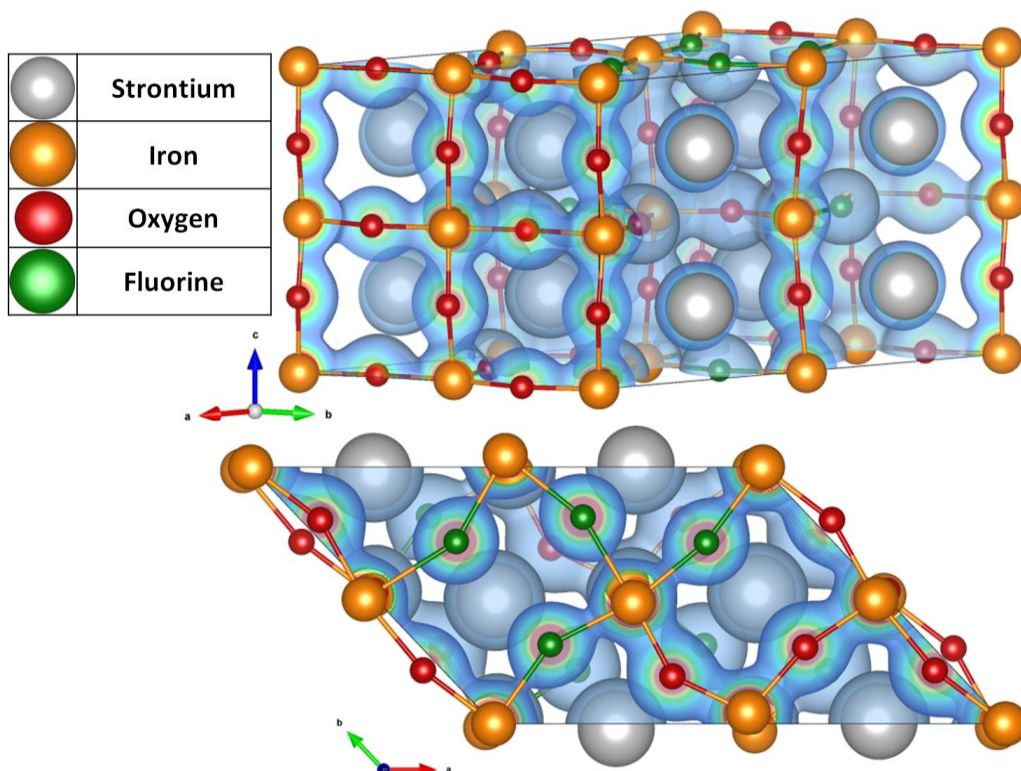


Figure 3.24: Total density from the disordered  $\text{SrFeO}_2\text{F}$  calculated by PBE96+U.

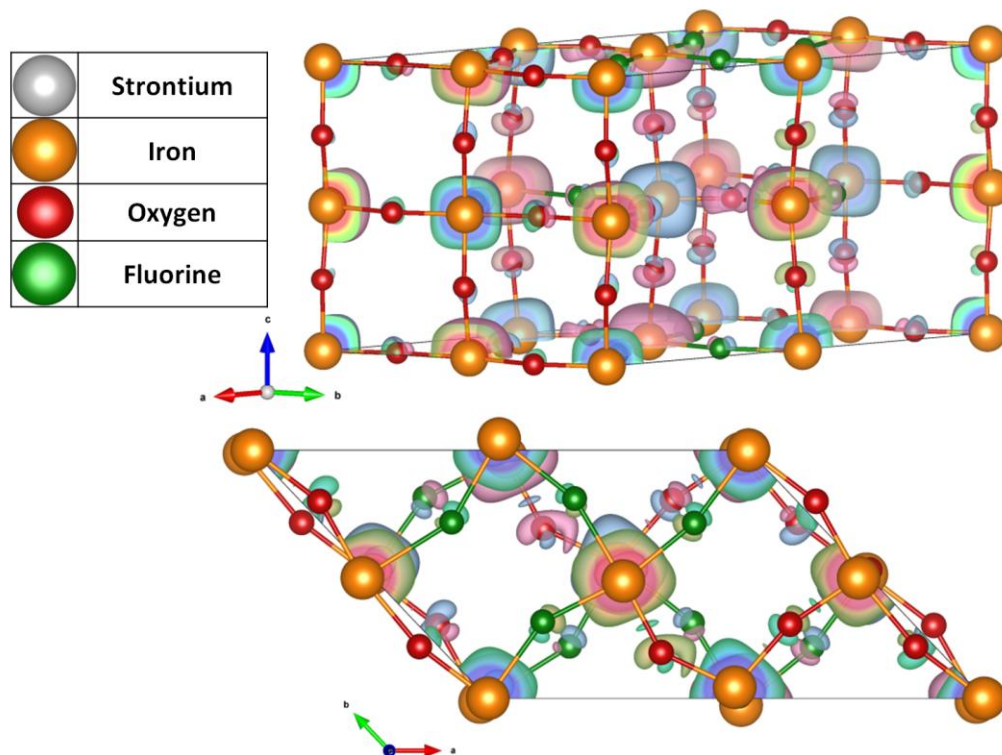
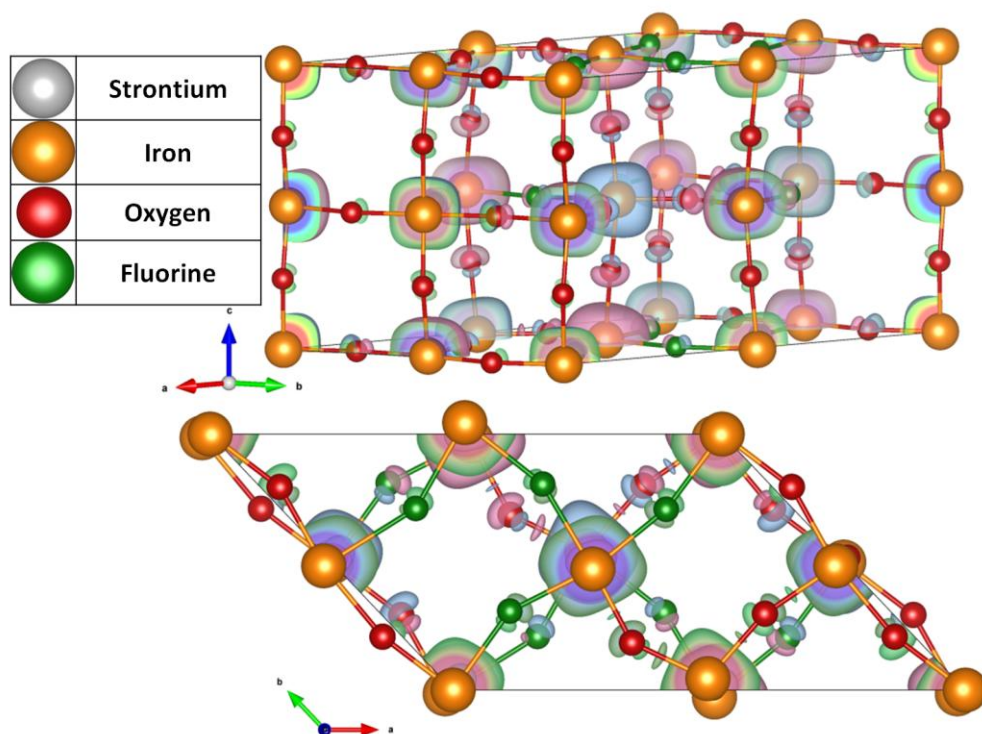


Figure 3.25: Spin density from the disordered  $\text{SrFeO}_2\text{F}$  calculated by PBE96.





**Figure 3.26: Spin density from the disordered  $\text{SrFeO}_2\text{F}$  structure calculated by PBE96+U.**

### 3.3.7 The Density of States for Ordered and Disordered $\text{SrFeO}_2\text{F}$ Structure

The density of states was plotted for the total antiferromagnetic structure for the PBE96 and PBE96+U functional and shown in Figures 3.24 and Figure 3.25. The density of states for the disordered structure was plotted for the PBE96 and PBE96+U functional, as well. They were shown in Figures 3.26 and 3.27. The PBE96 functional has erroneously produced a metallic zero band gap structure. The experimental  $\text{SrFeO}_2\text{F}$  has a yellow color so it has been expected to be a gapped compound. The PBE96 functionals have shown the fluorine states to be the lowest in energy, the oxygen states to be the next highest in energy, with the iron states at the Fermi level. For the PBE96+U functional, the iron states have been split due to the band occupancy, which would be expected for the Hubbard  $U_{\text{eff}}$  method. For the PBE96+U functional the oxygen states have shown significant less mixing with the iron state than the fluorine states due to the energetic ordering. The ordered  $\text{SrFeO}_2\text{F}$  structures for the PBE96+U and PBE functionals have obviously shown better symmetry between the each spins compared to the

disordered structure. The disordered PBE96+U functional has also produced a larger band gap compared the PBE96+U functional for the ordered structure from symmetry breaking. The ordered and disordered PBE96+U functional for the  $\text{SrFeO}_2\text{F}$  structures have also shown the formation of a charge transfer semi-conductor with valance oxygen states and conduction iron states.

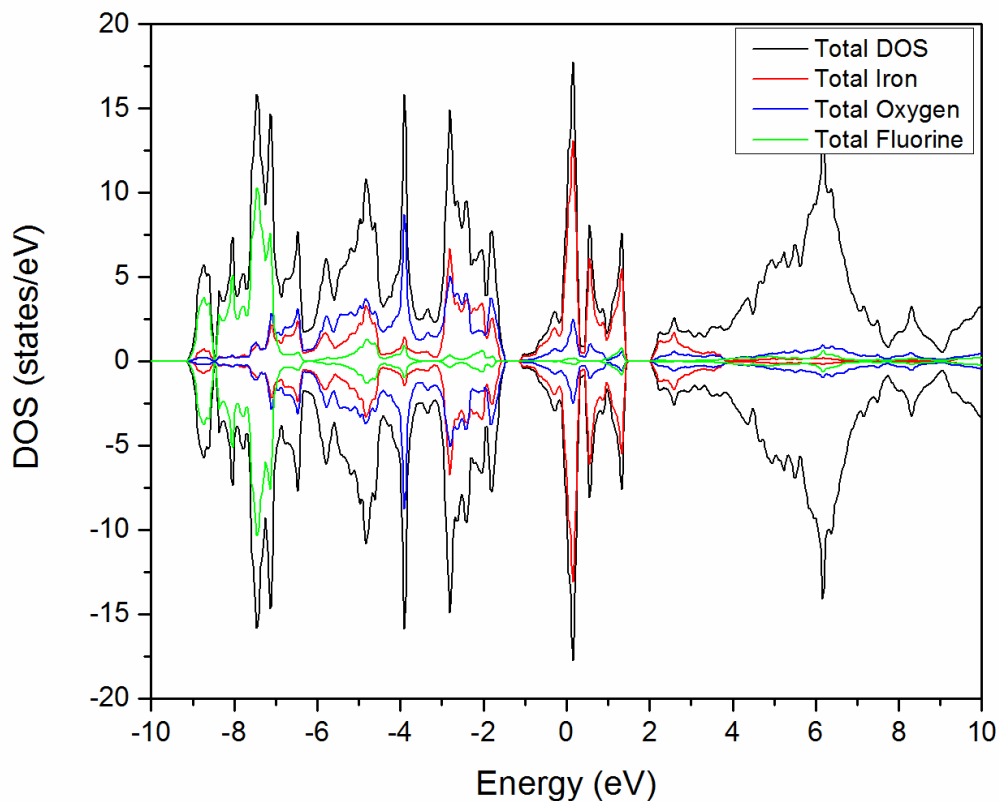


**Figure 3.28: Density of states for the total antiferromagnetic structure (d) calculated by PBE96.**

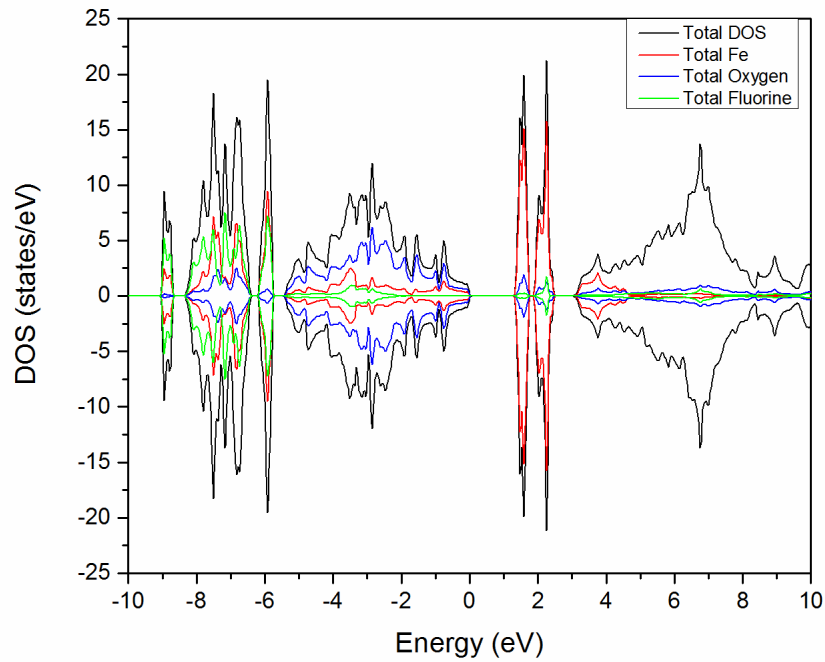


Figure 3.29: Density of states for the total antiferromagnetic structure (d) calculated by PBE96+U.

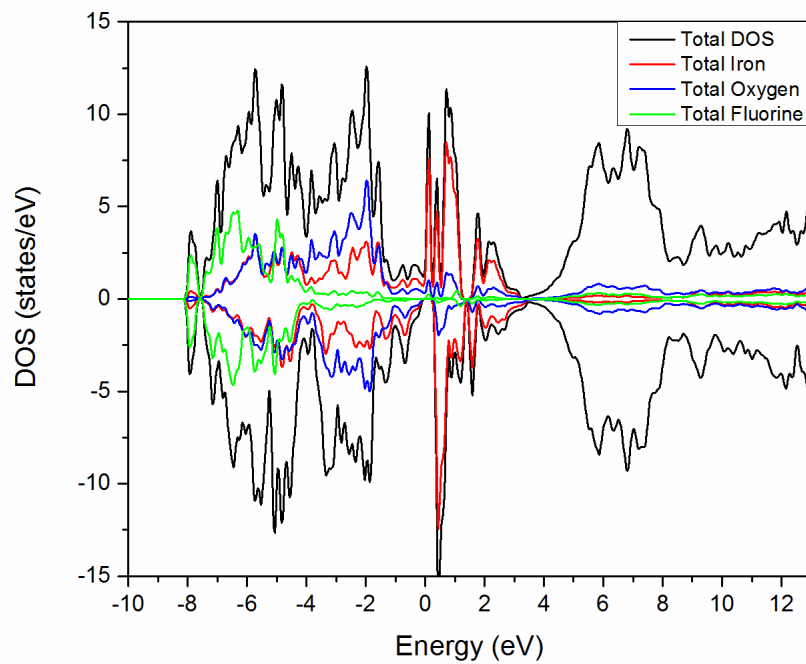
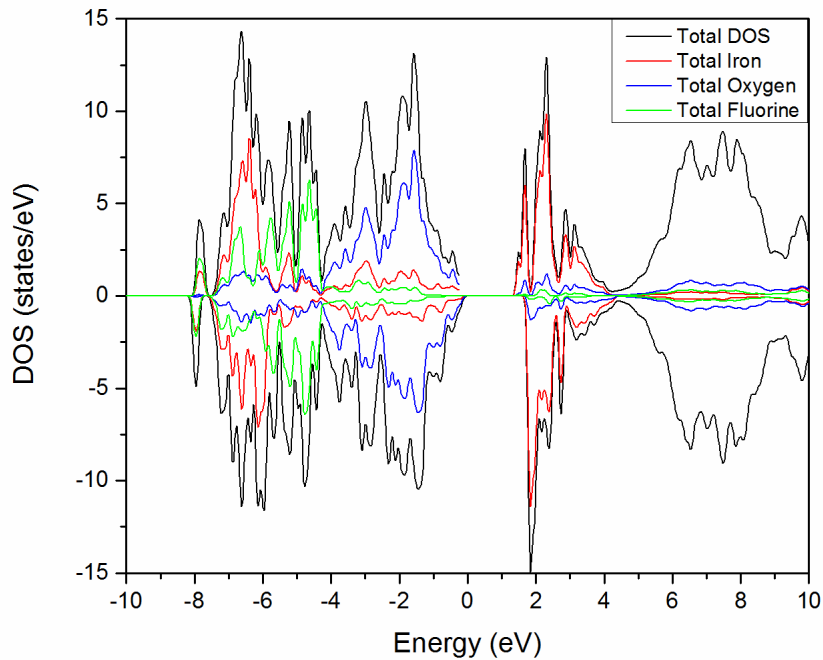


Figure 3.30: Density of states for the total antiferromagnetic structure (d) calculated by PBE96.



**Figure 3.31: Density of states for the disordered  $\text{SrFeO}_2\text{F}$  structure calculated by PBE96+U.**

Finally the density of states for the ordered  $\text{SrFeO}_2\text{F}$  structure with the total antiferromagnetic magnetic structure (d) was calculated with the modified Beck-Johnson potential from the PBE96 density. This was done for better accuracy, and was shown in Figure 3.28. The band gap from the mBJ potential has shown a gap better suited for the color of the compound. It has also shown the iron states to be energetically in between the oxygen and fluorine state unlike what was shown in the density of states in for the PBE96+U functional.



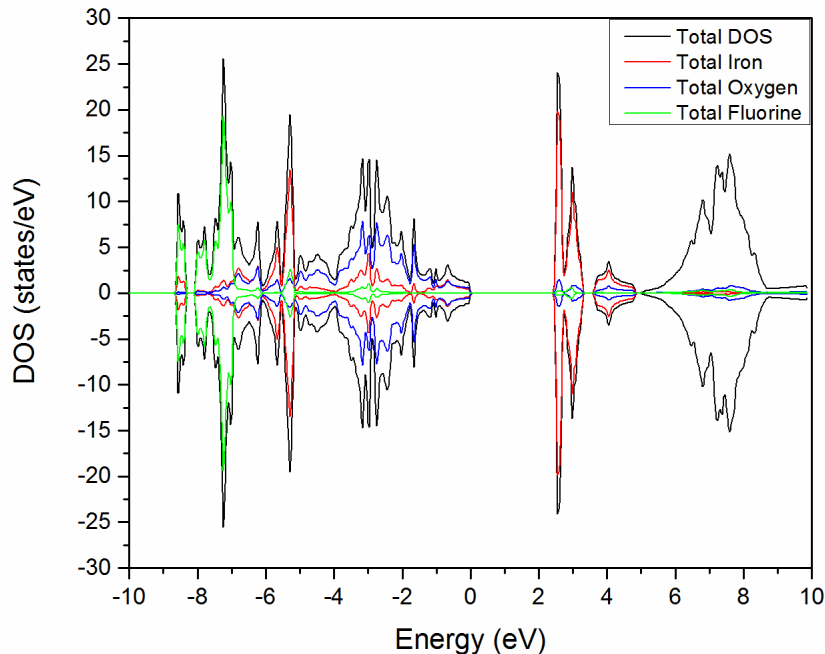


**Figure 3.32: Density of states for the total antiferromagnetic structure (d) PBE96 with mBJ ordered structure**

### 3.3.8 Mössbauer Parameter Calculations

Mossbauer parameters for different electronic structures were calculated and reported in Table 3.6 for varying temperature smearing, Hubbard  $U_{\text{eff}}$  value's, oxygen fluorine disordering, and potentials like modified Beck-Johnson<sup>174,266–268</sup>. All were based on the initial ordered PBE96 calculations. Unfortunately they have not produced values that match the experimental values. Even though many of core hyperfine values have matched experiment, and the values for isomer shifts have shown better predictions by the PBE96 functional.<sup>269</sup> The quadrupole splitting has been more challenging to properly predict as it has relied on the shape of the nucleus besides the electron density. The PBE96 values have been too low for the disordered structure, but have also been defined as too high for the values calculated for structures calculated with a Hubbard  $U_{\text{eff}}$  value. The modified Becke-Johnson potential has shown values between the values calculated for PBE96 and PBE96+U functional, but it has still been too high. Modified Becke-Johnson was used because it shown produce accurate quadrupole splitting values

based on calculations in the past<sup>268</sup>. Perhaps using the modified Beck-Johnson on the disordered  $\text{SrFeO}_2\text{F}$  structure with the PBE96 functional could lead to better quadrupole values. Another trend that could be postulated has been for the amount overlap between the fluorine and iron states in the density of states could lead to higher quadrupole splitting. The compound  $\text{FeF}_2$  has a high electron field gradient which has lead to the high quadrupole splitting.<sup>269,270</sup> So better overlap with fluorine could mean a higher quadrupole splitting. The quadrupole values that were calculated by the disordered  $\text{SrFeO}_2\text{F}$  structure with the PBE96 functional have more of a cis fluorine arraignment and better match the experimental values; however, further analysis should be performed to find a proper potential to better predict Mössbauer parameters for the iron oxyfluoride,  $\text{SrFeO}_2\text{F}$ .

**Table 3.6: Calculated Mossbauer Parameters**

	Density at nucleus(1/au <sup>3</sup> )	Isomer Shift [mm/s]	EFG [10 <sup>21</sup> V/m <sup>2</sup> ]	Quadrupole Splitting [mm/s] <sup>271</sup>	Asymmetry Parameter <sup>169-273</sup>	Adjusted Quadrupole Splitting	Hyperfine (kGuass) (Valance)	Hyperfine (kGuass) (Total)	Hyperfine (kGuass) (Core)
Fe-BBC	15309.81612	0						-321.746	
Antiferromagnetic ordered SrFeO <sub>2</sub> F calculated with PBE									
Fe1	15308.29252	0.443368764	8.7083	1.451383333	0	1.451383333	215.298	-204.415	-419.713
Fe2	15308.29251	0.443372256	8.70782	1.451303333	0	1.451303333	-215.294	204.416	419.71
Fe3	15308.29251	0.443369928	8.70845	1.451408333	0	1.451408333	-215.3	204.416	419.716
Fe4	15308.29248	0.443378658	8.70805	1.451341667	0	1.451341667	215.294	-204.413	-419.707
Antiferromagnetic ordered SrFeO <sub>2</sub> F calculated with PBE+U, U=4.0 eV									
Fe1	15308.61509	0.349501185	17.62697	2.937828333	0	2.937828333	221.844	-299.948	-521.792
Fe2	15308.61508	0.349502349	17.62697	2.937828333	0	2.937828333	-221.843	299.949	521.792
Fe3	15308.61512	0.349492164	17.62696	2.937826667	0	2.937826667	-221.845	299.947	521.792
Fe4	15308.61505	0.349511079	17.62698	2.93783	0	2.93783	221.842	-299.95	-521.792
Antiferromagnetic ordered SrFeO <sub>2</sub> F calculated with PBE+U, U=6.0 eV									
Fe1	15308.75111	0.309919074	17.94583	2.990971667	0	2.990971667	219.901	-319.937	-539.838
Fe2	15308.75111	0.309919074	17.94583	2.990971667	0	2.990971667	-219.901	319.937	539.838
Fe3	15308.75111	0.309919074	17.94583	2.990971667	0	2.990971667	-219.901	319.937	539.838
Fe4	15308.75111	0.309919074	17.94583	2.990971667	0	2.990971667	219.901	-319.937	-539.838
Antiferromagnetic ordered SrFeO <sub>2</sub> F calculated with PBE+U, U=4.0 eV. States Smeared to reflect a temperature of 298K.									
Fe1	15308.61503	0.349516608	17.62602	2.93767	0	2.93767	221.846	-299.949	-521.795
Fe2	15308.61503	0.349516608	17.62602	2.93767	0	2.93767	-221.846	299.949	521.795
Fe3	15308.61504	0.349514571	17.62602	2.93767	0	2.93767	-221.846	299.949	521.795
Fe4	15308.61503	0.349518645	17.62602	2.93767	0	2.93767	221.846	-299.949	-521.795
Antiferromagnetic ordered SrFeO <sub>2</sub> F calculated with the modified Becke-Johnson potential from PBE									
Fe1	15442.91009	-38.73034323	13.44782	2.241303333	0	2.241303333	48.067	-660.92	-708.987
Fe2	15442.91009	-38.73034352	13.44782	2.241303333	0	2.241303333	-48.067	660.92	708.987
Fe3	15442.91009	-38.73034352	13.44782	2.241303333	0	2.241303333	-48.067	660.92	708.987
Fe4	15442.91009	-38.73034352	13.44782	2.241303333	0	2.241303333	48.067	-660.92	-708.987
Antiferromagnetic disordered SrFeO <sub>2</sub> F calculated with PBE									
Fe1	15308.02708	0.520611513	11.43257	1.905428333	0.11267	1.909455497	216.61	-249.434	-466.044
Fe2	15308.09311	0.501397365	-3.72929	-0.621548333	0.86073	-0.694064421	-87.098	371.544	458.642
Fe3	15307.95469	0.541676421	9.6594	1.6099	0.92819	1.826494442	-208.668	261.245	469.913
Fe4	15308.04412	0.515651709	4.84119	0.806865	0.5039	0.840317418	101.653	-364.731	-466.384
Antiferromagnetic disordered SrFeO <sub>2</sub> F calculated with PBE+U, U=4.0 eV									
Fe1	15308.36712	0.421659582	15.21474	2.53579	0.06368	2.537503253	226.928	-302.043	-528.971
Fe2	15308.39607	0.413235132	5.45203	0.908671667	0.84398	1.010806493	-114.715	410.992	525.707
Fe3	15308.32622	0.433560318	12.41709	2.069515	0.89073	2.327138694	-221.568	305.215	526.783
Fe4	15308.33357	0.431423214	6.14477	1.024128333	0.58991	1.0818974	121.502	-405.103	-526.605

### 3.4 Conclusion

From the experimental data and the magnetic data calculated with PBE96+U, it has been shown that SrFeO<sub>2</sub>F should be a G antiferromagnet.<sup>274</sup> The localization of the d-orbitals has split the occupied and unoccupied orbitals in a Mott-like fashion; however, due to the energetic location of oxygen p-states, the compound has formed a charge transfer semi-conductor similar to many oxyfluoride compounds.<sup>56</sup> The valance states for SrFeO<sub>2</sub>F have an oxygen character while the conduction states have an iron character. The experimental Mössbauer have reported values that have been hard to replicate with theory. Predicting Mössbauer parameters has required accurate modeling of the core, which can be difficult to do with a plane wave basis, even with an LAPW/APW method which has a full potential.<sup>183</sup>

Due to the location of the iron electronic states and the 2+ charge for the strontium atom, the compound could be explored as a magnesium or lithium-ion cathode material. Replacing strontium in

$\text{SrFeO}_2\text{F}$  with magnesium could produce an analog structure as a battery material. As the perovskite compound  $\text{SrFeO}_{3-\delta}$  has shown to exist, so does the perovskite compound  $\text{MgFeO}_3$  even though magnesium has a significantly smaller ionic radius.<sup>36</sup> However, because the ionic radii would be so small in such a large cavity, a half molar equivalence of magnesium or a whole equivalence of lithium could be intercalated into the compound to attempt to probe the iron II/III redox couple. It could also be proposed that a reduction of the unoccupied iron states could pin them to the top of the oxygen band. While two-dimension ordering has not happened as projected, the oxygen and fluorine disorder combined with the local bond distortion could lead to large channels for ionic conduction. The disordering aspect negates on application for a 2-D spin density wave while aiding in another application for batteries. Also while the iron II/III redox couple has typically been low, the fluorine in the compound could artificially increase it with the induction effect.<sup>9</sup>

One of the caveats of replacing magnesium with strontium would be the distortion, as well. While the perovskite  $\text{MgFeO}_3$  has been shown to exist, it has been unknown if  $\text{MgFeO}_2\text{F}$  would be stable. Magnesium has also been labeled as bivalent, and while it could mean more charge exchange per battery cycle, magnesium has been a small ion with a lot of charge per volume. The small bivalent ion has typically formed strong bonds with oxygen,<sup>150</sup> and it may still could inhibit another cation in the large strontium cavity.

Other future work could include nudge elastic band studies on different mechanisms of fluorination of the  $\text{SrFeO}_2$  structure to compare the direct fluorination with fluorination aided by an oxygen hopping mechanism.<sup>202</sup> Also further studies analyzing spin density distribution of the different magnetic structure as a function of the Hubbard  $U_{\text{eff}}$  value could be performed.

## ***4 Analysis of the Iron II/III and the Iron III/IV Redox Couples in Iron-based Metal Oxides***

### **4.1 Introduction**

The search for new battery materials with a higher energy density has been an important venture. While the most widely used battery materials of  $\text{LiCoO}_2$  and  $\text{LiFePO}_4$  have been adequate, there remains room for improvement. An alternative cathode material that has been explored has been  $\text{T-LiFeO}_2$  due to the high abundance of iron and the large voltage associated with the iron III/IV redox couple.<sup>275,276</sup> There have been large assortments of polymorphs for the  $\text{LiFeO}_2$  structure. Many of the polymorphs have been similar to that of layered- $\text{LiCoO}_2$ , but each structure has not been ordered into the defined layers like  $\text{LiCoO}_2$ . In each structure, the oxygen positions have been the same, but according to how the lithium and iron positions have been ordered, the polymorph would be the alpha, beta, or gamma polymorph.<sup>275,277,278</sup> Other structures not related to the alpha beta, and gamma structures have been the corrugated-layer, the geothite-type, and the Hollandite-type structures.<sup>275,277</sup> All have had limited electrochemical functionality, due to poor electronic conductivity and electrolyte degradation from the overall instability of the iron IV ion. Many of the previous structures have shown some form of electrochemical degradation that lowers the cycled voltage to about 2-3V vs. lithium.<sup>277,279-286</sup> This has suggested a reaction of iron IV ion with the electrolyte to degrade the structure so compound most likely cycles the iron II/III redox couple.<sup>287-289</sup> One of the least studied polymorphs has been the  $\text{T-LiFeO}_2$  structure.<sup>157,277</sup> The  $\text{T-LiFeO}_2$  structure has been isostructural to the  $\beta\text{-NaFeO}_2$  polymorph. Consequentially, the  $\text{T-LiFeO}_2$  structure has been only synthesized through ion exchange of the  $\beta\text{-NaFeO}_2$  structure.<sup>290,291</sup> It has also been reported to break down to a  $\text{LiFe}_5\text{O}_8$  structure when the cycling of iron III/IV redox couple was attempted.<sup>277</sup> The material degraded due to same reasons listed above.

It was recently suggested that the T-LiFeO<sub>2</sub> structure could potentially access both the iron II/III redox couple and the iron III/IV redox couple due to the large cavities of the parent  $\beta$ -NaFeO<sub>2</sub> structure. Both the delithiated T-Li<sub>0.42</sub>FeO<sub>2</sub> structure and the lithiated T-Li<sub>1.57</sub>FeO<sub>2</sub> have been synthesized through soft-chemistry methods. Moderated to high voltages (3-5 V) was postulated to be used to cycle between T-Li<sub>1-x</sub>FeO<sub>2</sub> and T-LiFeO<sub>2</sub> to access the iron III/IV redox couple while lower voltages (1-3 V) could be used to cycle between T-LiFeO<sub>2</sub> to T-Li<sub>1+x</sub>FeO<sub>2</sub> to access the iron II/III couple. The iron III/IV redox couples have been reported to be high, while iron II/III redox couples have been reported to be lower. Coupled with a theoretical capacity of 526 mAh/g (assuming a full two-electron transfer) the energy density of this material could significantly outperform the previous materials, LiCoO<sub>2</sub> and LiFePO<sub>4</sub>.<sup>157</sup>

The T-Li<sub>x</sub>FeO<sub>2</sub> has experimentally shown to allow cobalt doping up to 10%. Through doping, access one of the two potential redox couples, the iron II/III redox couple, was shown to cycle for at least three cycles. The cathodic peak for the iron II/III redox couple was experimentally observed at 1.8 V verse lithium; however, for the iron III/IV redox couple only the anodic peak was observed at 4.4 V. The iron III/IV redox couple was not able to be effectively cycled in this case.<sup>157</sup> Unfortunately, this could have been from T-Li<sub>1-x</sub>FeO<sub>2</sub> (iron IV) reacting with organic electrolytes and decomposing similar to other polymorphs. In this chapter, cobalt doped T-LiFeO<sub>2</sub> will be revisited with a different electrolyte to ascertain if the iron III/IV redox couple would be electrochemically available in the correct environment. The use of room temperature ionic liquids have been used instead of the typically used LiPF<sub>6</sub> salt dissolved in organic carbonate solvents. Room temperature liquid electrolytes have been reported to have large stable voltage window for lithium battery materials.<sup>292,293</sup> Exploration of alternative dopants chromium, nickel, and vanadium have made, as well. Cobalt has limited abundance, therefore alternative dopants could potentially make the doped T-LiFeO<sub>2</sub> material more economically favorable due to the use of higher abundant elemental materials.<sup>31</sup>

Other theoretical explorations of the T-LiFeO<sub>2</sub> structure have been performed in relation to the

experimental results. Surfaces for the bond valance sum analysis and the bond valance mismatch analysis have been plotted for T-LiFeO<sub>2</sub>,  $\beta$ -NaFeO<sub>2</sub>, CF-LiFeTiO<sub>4</sub>, and CF-Li<sub>2</sub>FeTiO<sub>4</sub>.<sup>294,295</sup> In this chapter, the surfaces for the bond valance sum analysis and bond valance mismatch analysis were used to speculate and compare the ionic conductivity of the T-LiFeO<sub>2</sub> structure to that of the  $\beta$ -NaFeO<sub>2</sub> structure, and that of the highly ion conductive CF-LiFeTiO<sub>4</sub>, and CF-Li<sub>2</sub>FeTiO<sub>4</sub> structures.<sup>296</sup>

Lastly, different arrangements of lithium atoms in the T-Li<sub>0.5</sub>FeO<sub>2</sub>, T-LiFeO<sub>2</sub> and T-Li<sub>1.5</sub>FeO<sub>2</sub> structures were relaxed with plane wave density functional theory (DFT) methods to attempt to find comparable structures to the experimental T-Li<sub>0.42</sub>FeO<sub>2</sub>, T-LiFeO<sub>2</sub>, and T-Li<sub>1.57</sub>FeO<sub>2</sub> structures. From the computationally generated structures, the iron II/III and III/IV redox potentials with respect to lithium would be calculated with Hubbard U<sub>eff</sub> corrected DFT and hybrid functionals. The DFT+U methods and hybrid functionals have been typically used for transition metal oxides due to the highly localized d-orbital in many transition metal oxides.<sup>193,297</sup> Finally, the density of states for the relaxed structures were calculated for DFT+U and hybrid functionals. The density of states would show the chemically relevant states and give insight into how the material may function as a battery material.<sup>51</sup>

## **4.2 Methods**

### **4.2.1 Synthesis of 10% Doped $\beta$ -NaFeO<sub>2</sub>**

Molar amounts of CoC<sub>2</sub>O<sub>4</sub>•2H<sub>2</sub>O and FeC<sub>2</sub>O<sub>4</sub>•2H<sub>2</sub>O were mixed with a 5% molar excess of Na<sub>2</sub>CO<sub>3</sub>(99.7%), the mixture was ball milled for 45 min at 500 rpm in a planetary ball-mill. The mixture was then pressed into 3/4 inch ~0.5 g pellets at 8 metric tons. The pellets were then fired at 150°C for 2 hours, 230°C for 2 hours, heated to 850°C over 8 hours, and held for 6 hours at 850°C. The pellets were then reground, pressed, and raised to 1000°C over eight hours which were then held at 1000°C for 12 hours. The pellets were reacted under a constant flow of oxygen in an alumina boat.

### **4.2.2 Lithium Exchange of 10% Cobalt Doped $\beta$ -NaFeO<sub>2</sub>**

Two molar equivalences of LiNO<sub>3</sub> (99%) were mixed with one molar equivalence of the

previously made 10% cobalt doped  $\beta$ -NaFeO<sub>2</sub>. The mixture was then ball-milled for 30 min at 400 rpm in a planetary ball mill. The mixture was heated at 225°C for 48 hours under a constant flow of oxygen. The resulting mixture was then washed with dry methanol in a nitrogen purged soxhlet extractor to remove the excess nitrate byproducts.

#### **4.2.3 Synthesis of Chromium, Nickel, and Vanadium Doped $\beta$ -NaFeO<sub>2</sub>**

The compound  $\beta$ -NaFeO<sub>2</sub> was doped with 2.5%, 5.0%, 10.%, 15% and 25% molar equivalences of chromium, nickel, and vanadium. There were slight variations to the synthetic methods for the doped  $\beta$ -NaFeO<sub>2</sub> compounds, but the initial steps were mainly the same. To synthesize, molar amounts of Na<sub>2</sub>CO<sub>3</sub> (99.7%) and Fe<sub>2</sub>O<sub>3</sub> (99.5%) were mixed with molar amounts of Cr<sub>2</sub>O<sub>3</sub> (99.6%), NiO (99.8%), or V<sub>2</sub>O<sub>3</sub> depending on the desired dopant. A molar excess of 5% was used for Na<sub>2</sub>CO<sub>3</sub> to account for sodium volatility.<sup>157</sup> The mixtures were then ball-milled for 30 minutes at 500 rpm in a planetary ball-mill. The mixtures were then pressed into 3/4 inch ~0.5 g pellets at 5 tones. The majority of the pellets were then heated to 850°C over six hours in alumina boat and then held at that temperature for 12 hours. Subsequently, the pellets were heated over two hours to a final temperature of 1000°C and held for a specified amount of time shown in Table 4.1. For pellets heated to only 850°C, the temperature was heated over 6 hours and held for a time specified in Table 4.1. Reactions at 700°C were heated over 2 hours and held for a time specified in Table 4.1. Reactions at 700°C showed a lack of reaction by visible analysis only.



**Table 4.1: Final reaction temperatures for chromium, nickel, and vanadium dopings of  $\beta$ -NaFeO<sub>2</sub>**

Metal dopant	Max temperature (°C)	Time at max temperature (hours)
Chromium	1000	48
Chromium	1000	24
Chromium	850	48
Chromium	850	50 (with intermittent grinding at 48 hours)
Chromium	700	48
Nickel	1000	72
Nickel	1000	48
Nickel	1000	120 (with intermittent grinding at 72 hours)
Nickel	850	48
Vanadium	1000	48
Vanadium	1000	24
Vanadium	850	48
Vanadium	850	72 (with intermittent grinding at 72 hours)
Nickel	1000	7 days

#### 4.2.4 Powder X-Ray Diffraction Measurement and Scanning Electronic Microscopy

Powder x-ray diffraction measurements of final products were performed with a Bruker D2-Phaser containing a copper source with a  $K\alpha_1$  wavelength of 1.5418 Å. Samples containing lithium were measured under nitrogen in a purge box. All scanning electronic microscopy measurements, including back-scattering methods and EDX, were performed on the JEOL JSM 6610LV with samples mounted on carbon paper. An accelerated voltage of 20kV was used for all images.

#### 4.2.5 Cyclic Voltammetry

All cyclic voltammetry measurements were prepared and performed under argon with a two electrode cell with a lithium disk as the counter and reference electrode. Electrochemical testing was initially performed with a MTI stainless steel split-cell. The active material was made from a combination of 74% by weight of 10% cobalt doped T-LiFeO<sub>2</sub>, 15% Super C carbon, 8% Poly(vinylidene fluoride), and 3% carbon tubes (50 nm multi-walled from cheaptubes.com) for added electronic conductivity. The mixture was then ball-milled at 200 rpm for 10 minutes and 450 rpm for 20 minutes. The dry mixture was then mixed with 3 ml of N-methyl-2-pyrrolidone over 12 hours to produce mixed slurry. The formed slurry was then spread on the working electrode of aluminum, platinum, or carbon paper (MTI Corp.)

with a doctor blade set to a thickness of 50 microns (unless otherwise noted). The slurry was dried at a temperature of 130°C at 20 mmHg of argon over 12 hours. The 19 mm disk was then cut from the coated electrode and pressed at about 2000lb/sq in. The pressed working electrode was then placed in the cell with a lithium anode, several Teflon separators, and with 1.0 milliliter (unless otherwise noted) of a solution of either 1 molar equivalence of LiTFSI dissolved in 9 molar equivalences of Pyr<sub>13</sub>FSI or 1 molar equivalence of LiTFSI dissolved in 9 molar equivalences of Pyr<sub>13</sub>TFSI. The equipment used to measure the cyclic voltammetry was a Gamery Reference 600 potentiostat. The LiTFSI was from Solvay, and the solvents Pyr<sub>13</sub>TFSI and Pyr<sub>13</sub>FSI were from Solvionic.

#### 4.2.6 Surfaces of Bond Valance Analysis

The bond valance surfaces were made using “BVS\_mapping” produced by Matthew Dyer.<sup>298</sup> In accordance to bond valance sum theory, the surface was plotted with a B value of 0.37 and  $r_0$  value of 1.466 Å for lithium oxygen bonds and a  $r_0$  value of 1.803 Å for sodium oxygen bonds.<sup>294,295</sup> The surfaces were plotted with a data point spacing of 0.2 Å. For the mismatch plots, an assumed valance of 1.0 was used. The cut-off radius to calculate each point was a radius of 3 Å for the lithium containing compounds, and a cut-off of 2 Å for the sodium containing compounds.

#### 4.2.7 Structure Relaxation of the T-Li<sub>x</sub>FeO<sub>2</sub> Structures

All unit cells were constructed from the initial unit cell found by Armstrong et al.<sup>277</sup> The full unit cell used consists of four lithium atom, four iron atoms, and eight oxygen atoms for the base T-LiFeO<sub>2</sub> structure. Lithium atoms were added or removed in order to construct the cells for the T-Li<sub>1.5</sub>FeO<sub>2</sub> and T-Li<sub>0.5</sub>FeO<sub>2</sub> structures. All cells were initially calculated and relaxed with VASP 5.2.12<sup>177,182,258,299</sup> with an energy cut-off of 500 eV, ~200 k-points in the IBZ, and the PBE96 functional<sup>185,256</sup> using the PAW method.<sup>182,183</sup> The cell parameters and the ion positions were relaxed and adjusted according to the conjugate gradient method<sup>195</sup> with a convergence of 10<sup>-3</sup> eV. Subsequent relaxations were performed with the same parameters except the PBE96 functional was corrected with a Hubbard  $U_{\text{eff}}$  of 4.0 eV or

6.0 eV applied through the rotationally invariant method.<sup>300</sup> Any mention of a Hubbard  $U_{\text{eff}}$  in the chapter assumes a  $U_{\text{eff}}$  with double counting  $J$  already accounted for. Energetic values used for open-cell voltage calculations and density of states were calculated from single point calculations of the different structures with an energy cut-off of 500 eV,  $\sim 550$  k-points in the IBZ, the PBE96 functional, and a Hubbard  $U_{\text{eff}}$  when appropriate. All single point calculations were spin polarized and performed with a convergence of  $10^{-4}$  eV. The antiferromagnetic  $\text{T-Li}_x\text{FeO}_2$  structures were relaxed with a C-type magnetic ordering where the magnetic coupling between the atomic planes would be ferromagnetic, but the coupling would be antiferromagnetic within the atomic planes.<sup>301</sup> For the OCV calculations, a single unit cell of lithium was relaxed with an energy cut-off of 175 eV and 8000 k-points.

#### 4.2.8 Magnetic Cell Relaxations of the $\text{T-LiFeO}_2$ and $\beta\text{-NaFeO}_2$ Structures

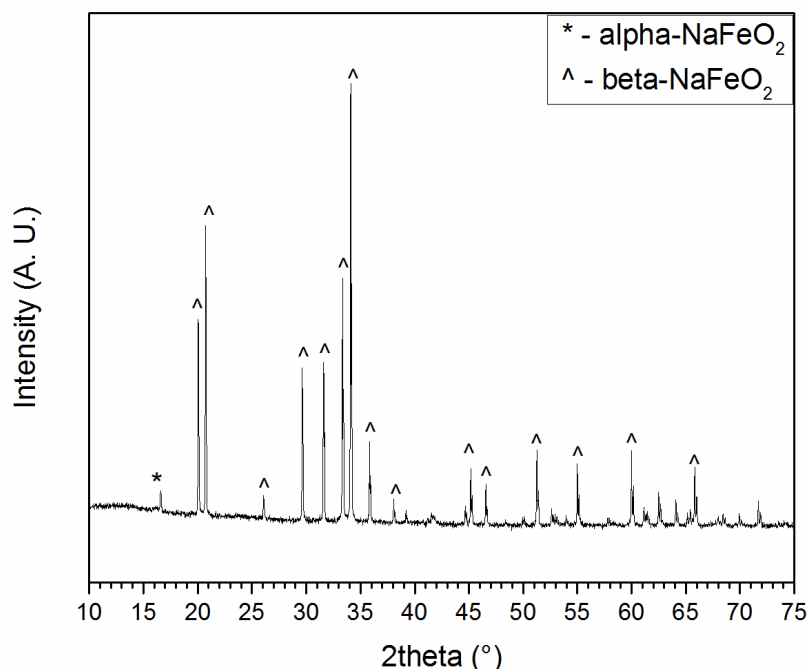
The initial unit cell for  $\text{LiFeO}_2$  was taken from Armstrong et al.<sup>277</sup> with Quantum Espresso 5.1,<sup>175,302</sup> the cell was relaxed with spin polarization, 60 k-points, a 130 Ry wave-function cut-off, a 1040 Ry core density cut-off, the PAW method,<sup>182,183</sup> the PBE96 functional,<sup>185,256</sup> an energetic convergence of  $10^{-5}$  Ry, and a force convergence of  $10^{-4}$  Ry/bohr. The cell was relaxed with the angles kept at  $90^\circ$  to preserve the orthorhombic symmetry and the iron and cell parameters were relaxed with the quasi-Newton method of the Broyden–Fletcher–Goldfarb–Shanno algorithm.<sup>196–199,201,202</sup> Each relaxation was done with respect to a different magnetic arrangement.

The initial unit cell for  $\beta\text{-NaFeO}_2$  was taken from a previous structure.<sup>290</sup> The magnetic cell relaxations were done similarly to the of the  $\text{T-LiFeO}_2$  except that 120 k-points, a 140 Ry wave-function cut-off, a 1120 Ry core density cut-off were used. The magnetic arrangement of one iron atom was kept at a positive spin for the sake of reducing unnecessary calculations.

## 4.3 Electrochemical Investigation of the T-Li<sub>x</sub>FeO<sub>2</sub> System in Room Temperature

### Ionic Liquids

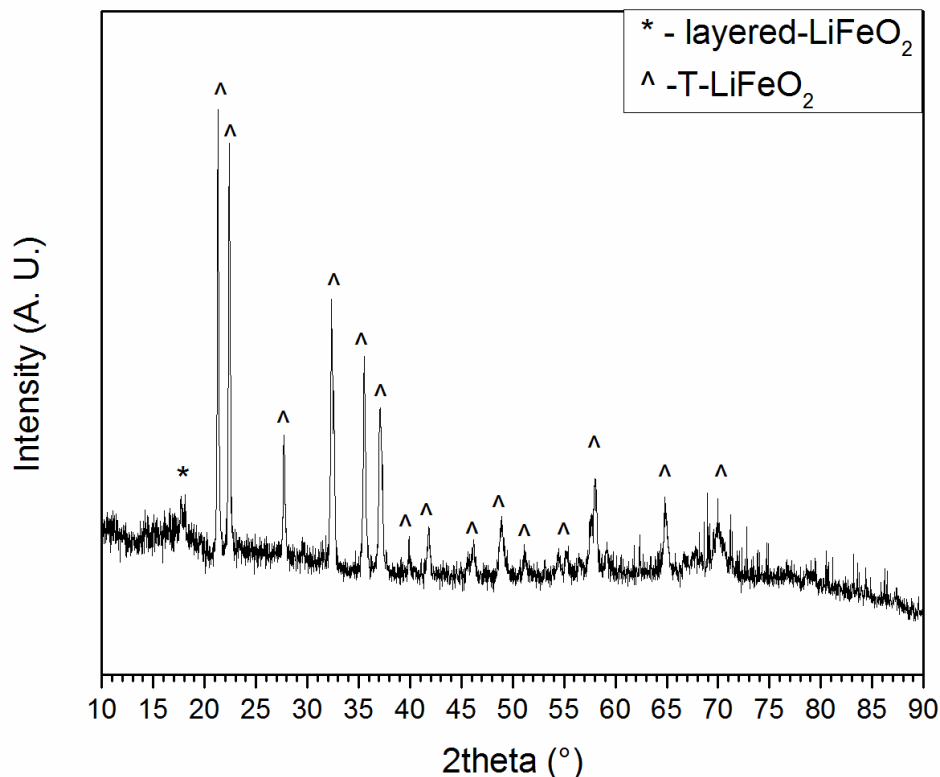
#### 4.3.1 Powder X-ray Diffraction Pattern of 10% Cobalt Doped $\beta$ -NaFeO<sub>2</sub>



**Figure 4.1: Powder x-ray diffraction of 10% cobalt doped  $\beta$ -NaFeO<sub>2</sub>. (WL=1.5418 Å)**

Figure 4.1 has shown the reported PXD of  $\beta$ -NaFe<sub>0.9</sub>Co<sub>0.1</sub>O<sub>2</sub>. It was synthesized from molar amounts of Na<sub>2</sub>CO<sub>3</sub>, Fe<sub>2</sub>O<sub>3</sub>, and Co<sub>3</sub>O<sub>4</sub>. The cobalt doping of  $\beta$ -NaFeO<sub>2</sub> was performed to inject a slight excess of electrons in the structure for added electronic conductivity.<sup>303</sup> Previous work has shown that the  $\beta$ -NaFeO<sub>2</sub> structure can be doped with cobalt up to 15%.<sup>157</sup> The x-ray diffraction pattern has been shown pure with the exception of small percentage (<3%) of  $\alpha$ -NaFeO<sub>2</sub>. With 10% of cobalt doped into the compound, the side product would not be detrimental to the electrochemical functionality of the compound. The indexing of the PXD pattern of  $\beta$ -NaFe<sub>0.9</sub>Co<sub>0.1</sub>O<sub>2</sub> produced the set of lattice parameters ( $a = 5.6732(3)$  Å,  $b = 7.1311(7)$  Å, and  $c = 5.3810(4)$  Å ) that were in line with values similar to pure  $\beta$ -NaFeO<sub>2</sub>.<sup>304</sup>

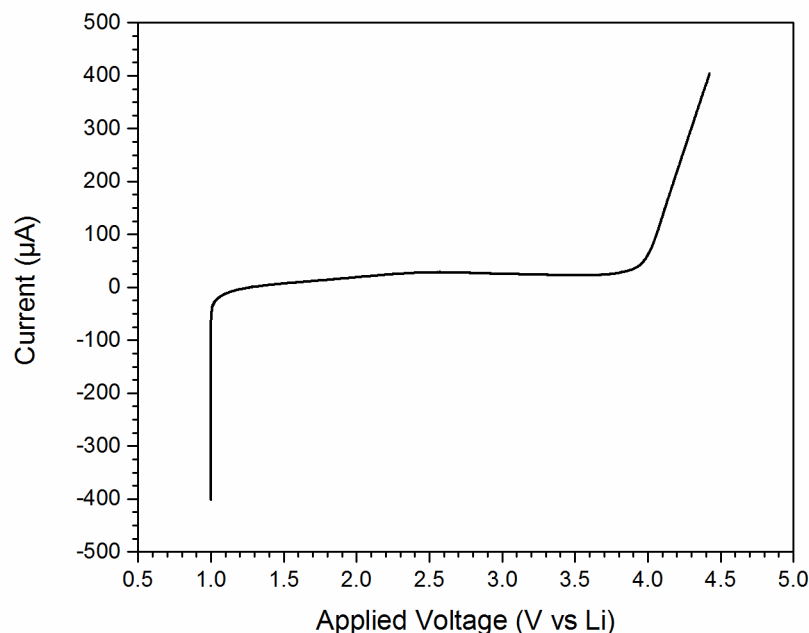
#### 4.3.2 Powder X-ray Diffraction Pattern of the Lithium Exchange of 10% Cobalt Doped $\beta$ -NaFeO<sub>2</sub>



**Figure 4.2: Powder x-ray diffraction pattern of 10% cobalt doped T-LiFeO<sub>2</sub>. (WL=1.5418 Å)**

The 10% cobalt doped  $\beta$ -NaFeO<sub>2</sub> was ground with two molar equivalences of LiNO<sub>3</sub> and sintered. The resulting product was washed for 5 days with dry methanol in a soxhlet extractor to remove the nitrate byproducts. The PXD pattern of the post washed compound, 10% cobalt doped T-LiFeO<sub>2</sub>, has been plotted in Figure 4.2. The resulting PXD pattern again has shown a minimal intensity from the layered phase, but all other peaks match the expected phase. The indexed PXD pattern produced the lattice parameters of  $a = 5.4921(9)$  Å,  $b = 6.3970(15)$  Å, and  $c = 5.0520(13)$  Å which were in line with previous T-LiFeO<sub>2</sub> structures.<sup>304,277</sup>

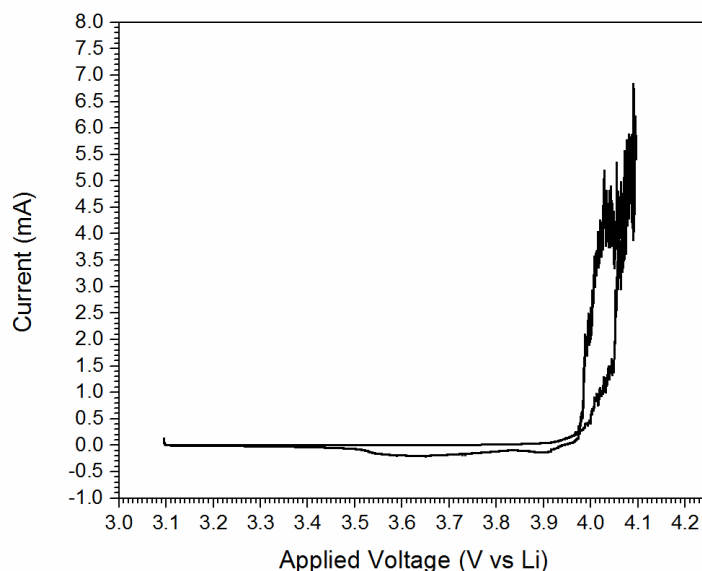
#### 4.3.3 Cyclic Voltammetry of the T-LiFe<sub>0.9</sub>Co<sub>0.1</sub>O<sub>2</sub> Compound



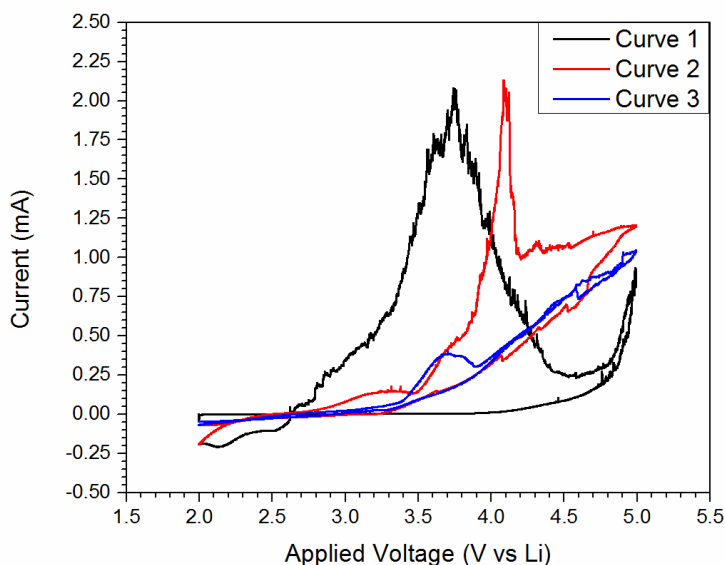
**Figure 4.3: Linear voltammetry with a pure aluminum cathode, a 1:9 electrolyte solution of LiTFSI:Pyr<sub>13</sub>FSI, and an anode of pure lithium. After a 10 second delay, the electrochemical split-cell was swept from 1 to 5 V at a rate of 1 mV/s.**

Figure 4.3 has shown the reaction of aluminum with the electrolyte, LiTFSI<sub>0.1</sub>Pyr<sub>13</sub>FSI<sub>0.9</sub>; a solution made with room temperature ionic liquids. A desirable voltammetry spectrum would have shown a flat spectrum. Aluminum has been the typical current collector used to analyze most lithium-ion battery materials; however, it has been reported that aluminum can react with LiTFSI.<sup>305</sup> The previous report was unclear, whether the interaction was from undesirable water content within the LiTFSI solution. High concentrations of the RTIL can counter act corrosion effects.<sup>305</sup> The solvents were purchased with promise of extremely low water content and extreme care was taken to prevent water contamination. Unfortunately, the current increase at 4.0 V has shown a reaction with the aluminum current collector and the electrolyte, thus an alternative current collector for the cathode material would have to be used. A test reaction using lithium cobalt oxide on a carbon paper current collector was performed and has been shown in Figures 4.4 and 4.5. Electrochemical cycling has shown an

undesirable side reaction at 3.95 V.



**Figure 4.4:** Cyclic voltammetry with a lithium cobalt oxide (50 micron layer) cathode on a carbon paper current collector, a 1:9 electrolyte solution of LiTFSI:Pyr<sub>13</sub>FSI, and a lithium anode. After a 10 second delay, the electrochemical split-cell was swept from 3.1 to 4.1 V at a rate of 0.028 mV/s.



**Figure 4.5:** Cyclic voltammetry with a carbon paper cathode, a 1:9 electrolyte solution of LiTFSI:Pyr<sub>13</sub>FSI, and a lithium anode. The electrochemical split-cell was swept from 2 to 5 V at a rate of 0.083333 mV/s for three cycles/curves.

Because of the undesirable side reaction, several additional tests similar to the one shown in Figure 4.5 were performed. Similar to the previous tests, only the current collector was used in place as the cathode. However, cycling has shown electrochemical decomposition with the carbon paper and electrolyte. It was also hypothesized to have been a reaction with the steel split-cell, as well. To deduce all side reactions, several electrochemical tests in a 10 ml beaker were performed. The test of a platinum current collector with a lithium anode has been shown in Figure 4.6.

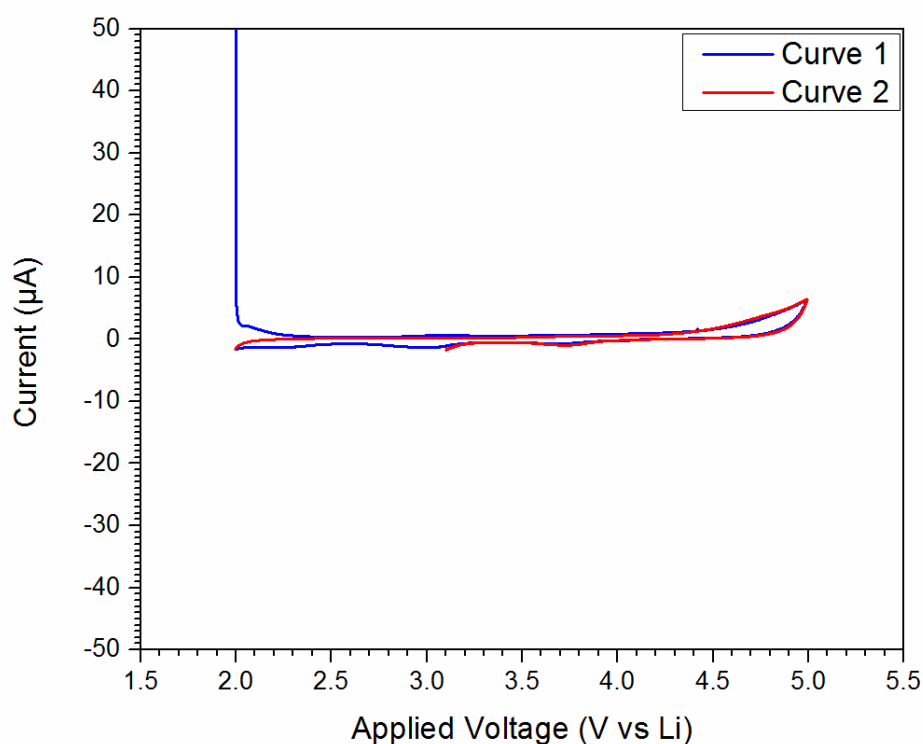


**Figure 4.6: Cyclic voltammetry with a platinum cathode, a 1:9 electrolyte solution of LiTFSI: Pyr<sub>13</sub>FSI of 3 ml, and a lithium anode. The electrochemical beaker cell was swept from 2 to 5 V at a rate of 0.177778 mV/s for two cycles/curves.**

Not surprisingly, the noble platinum metal has shown to be stable with minimal side reactions which would be desirable for a current collector. There has been not oxidation or reduction in Figure 4.6. An electrochemical test of the carbon paper was also performed in the 10 ml beaker cell. The carbon paper current collector tested against the lithium anode in the 10 ml beaker cell was reported in



Figure 4.7. Unfortunately, it has been shown that the carbon paper undeniably reacts with the electrolyte as shown by Figure 4.7. Platinum would ultimately have to be used as the current collector.

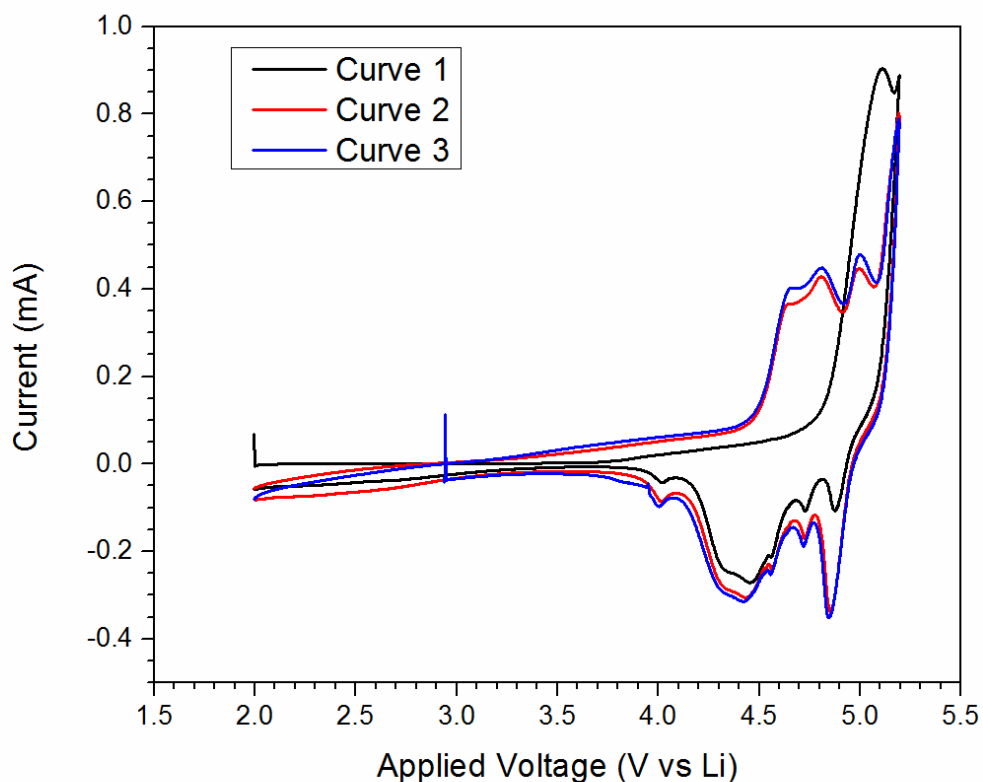
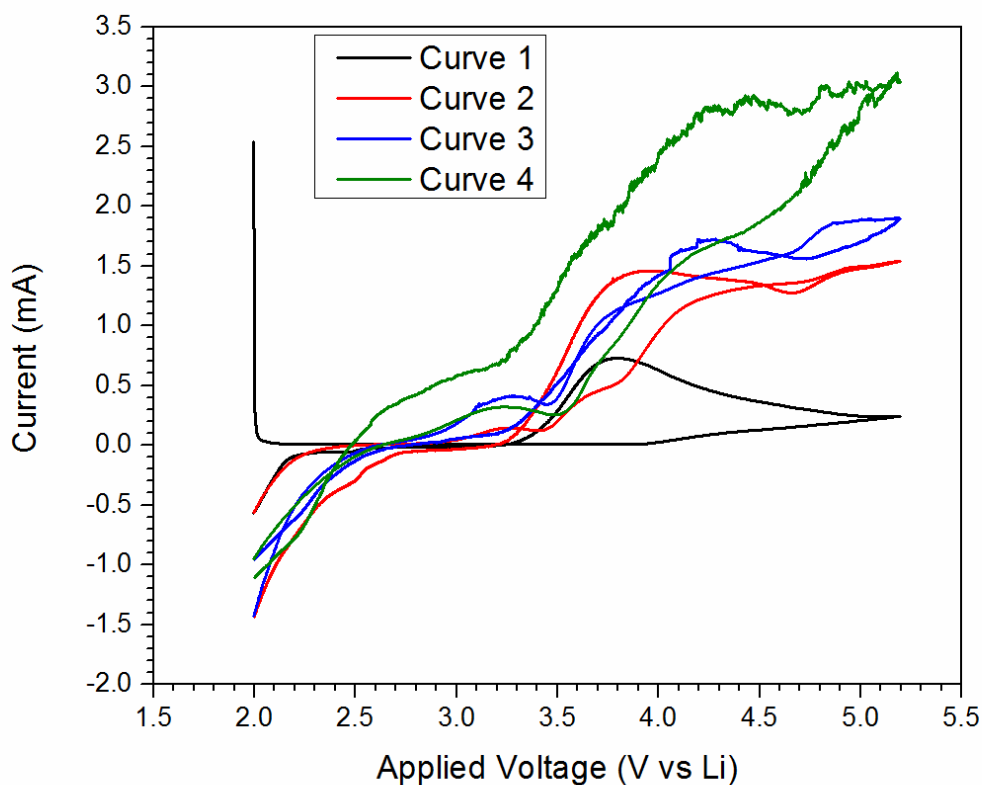
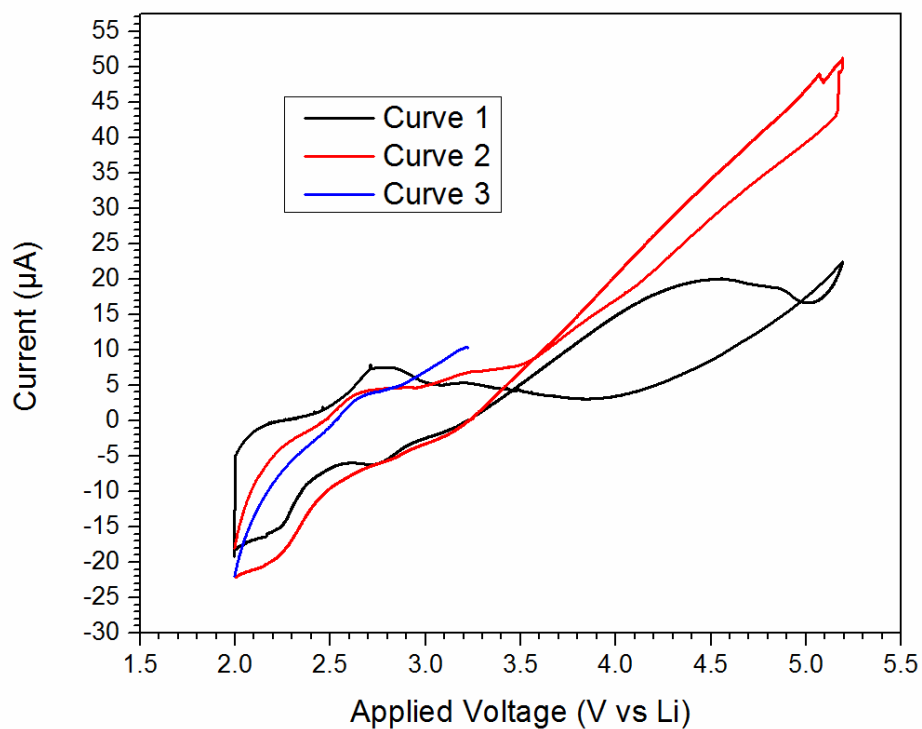


Figure 4.7: Cyclic voltammetry with a carbon paper cathode, a 1:9 electrolyte solution of LiTFSI: Pyr<sub>13</sub>FSI of 3 ml, and a lithium anode. The cell was swept from 2 to 5.2 V at a rate of 0.177778 mV/s for three cycles/curves.



**Figure 4.8: Cyclic voltammetry with a platinum cathode, a 1:9 electrolyte solution of LiTFSI:Pyr13FSI, and a lithium anode. The cell was swept from 2 to 5.2 V at a rate of 0.177778 mV/s for four cycles/curves.**

However, a side reaction has been shown in a steel split-cell containing a platinum current collector and a lithium anode. Figure 4.8 has shown the non-cyclable nature of the electrochemical split-cell. Ultimately, a final test was performed with only the platinum current collector used as the cathode as the steel split-cell used as the anode. Figure 4.9 has confirmed the reaction of the RTIL electrolyte with the steel split-cell due to the irregular cyclic voltammogram. Figure 4.10 has shown the split-cell after the cycling performed in Figures 4.5 and 4.8.



**Figure 4.9:** Cyclic voltammetry with a platinum cathode, a 1:9 electrolyte solution of LiTFSI:Pyr13FSI, and an empty anode in a steel cell. After a 60 minute delay, the cell was swept from 2 to 5.2 V at a rate of 0.177778 mV/s for three cycles/curves. The measurement was stopped midway through the third cycle.



**Figure 4.10:** Pictures of the electrochemical cell after cyclic voltammetry with a lithium anode and a 1:9 electrolyte solution of LiTFSI:Pyr<sub>13</sub>FSI for a carbon paper cathode (left) or a platinum cathode (right)

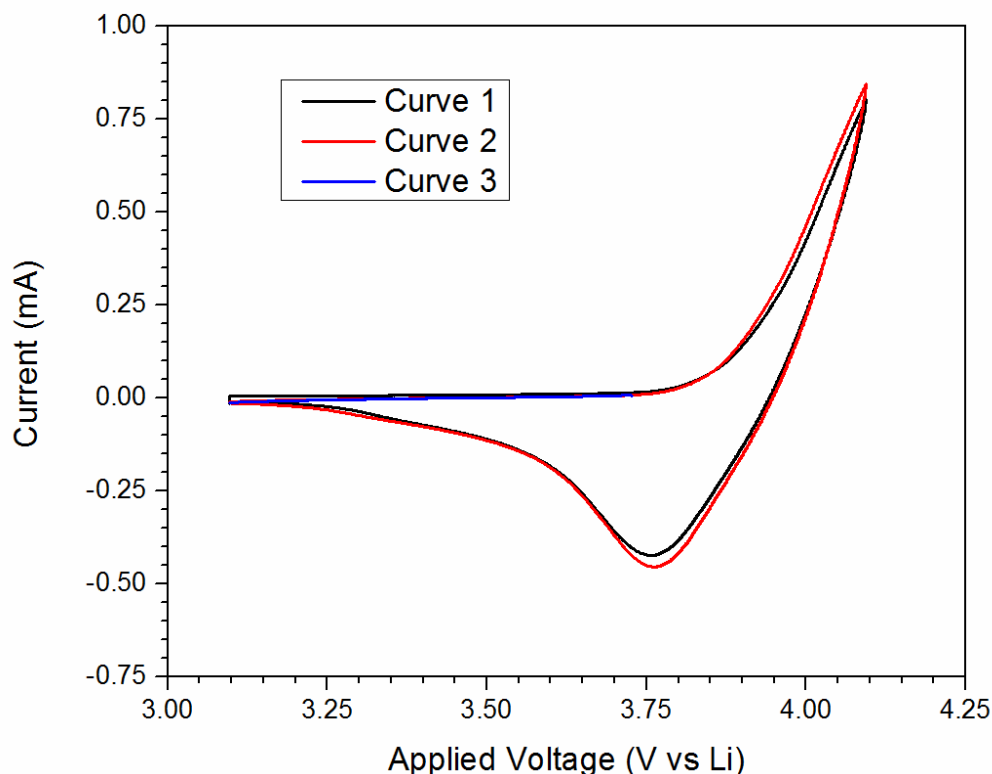


**Figure 4.11: Cyclic voltammetry with a lithium cobalt oxide on a platinum cathode, a 1:9 electrolyte solution of LiTFSI:Pyr13FSI of 3 ml, and a lithium anode. After a 60 minute delay, the electrochemical beaker cell was swept from 3.1 to 4.1 V at a rate of 0.05556 mV/s for three cycles/curves. The test was stopped midway through the third cycle.**

A test of the cathode material,  $\text{LiCoO}_2$ , on platinum was performed in the 10 ml beaker cell. The cyclic voltammogram, shown in Figure 4.11 has given a consistent and reversible cycle, even though it was not optimized. An attempt to line the bottom of the split-cell with a Teflon sheet was made. In the attempt, the platinum current collector covered a 10 by 10 mm hole in the Teflon sheet that allowed the platinum to make contact with the split-cell. This was done in order to complete the electrochemical circuit. The platinum current collector was sealed to the Teflon sheet with Teflon grease to prevent the split-cell from interacting with the electrolyte, but the attempts to limit side reactions with this method had proved unhelpful. The electrolyte was still able to flow around the seal so the electrolyte could still react with the steel split-cell. This method has been only the first attempt to circumnavigate the side

reactions with the electrolyte.

Shown in Figure 4.12 was the primary cell design that allowed for proper cycling of the  $\text{T-LiFe}_{0.9}\text{Co}_{0.1}\text{O}_2$  compound. Typically the split-cell design has the counter electrode attached to the top portion of the cell; however, in the case of the modified split-cell, shown in Figure 4.12, the counter electrode has been attached to the bottom with the pure platinum working attached to the top. For clarity, the lithium anode was placed on the bottom on the bottom, followed by three to five Teflon separators, and finally the lithium-ion cathode material deposited on the platinum current collector at the top. The platinum current collector was forced down with a folded Teflon disk to maintain a reasonable ionic connection between the electrodes and separators. Subsequent generations of the modified split-cell utilized a weighted 5 ml glass vile to hold the electrodes and separators down. Reversible cyclability of the modified split-cell has been shown in Figure 4.13. Newer generations of the modified split-cell were used with a weighted glass vile were used for more even pressure. If the pressure had been uneven, a short circuit of the modified split-cell could form. An example of effervescence that forms from a short circuit has been shown in Figure 4.14. A short circuit would lead to a rapid reaction with the electrolyte.



**Figure 4.12:** Picture of the working modified split-cell design. All subsequent tests on  $\text{T-LiFe}_{0.9}\text{Co}_{0.1}\text{O}_2$  were performed with on a modified split-cell set up pressed with a weight glass vile.

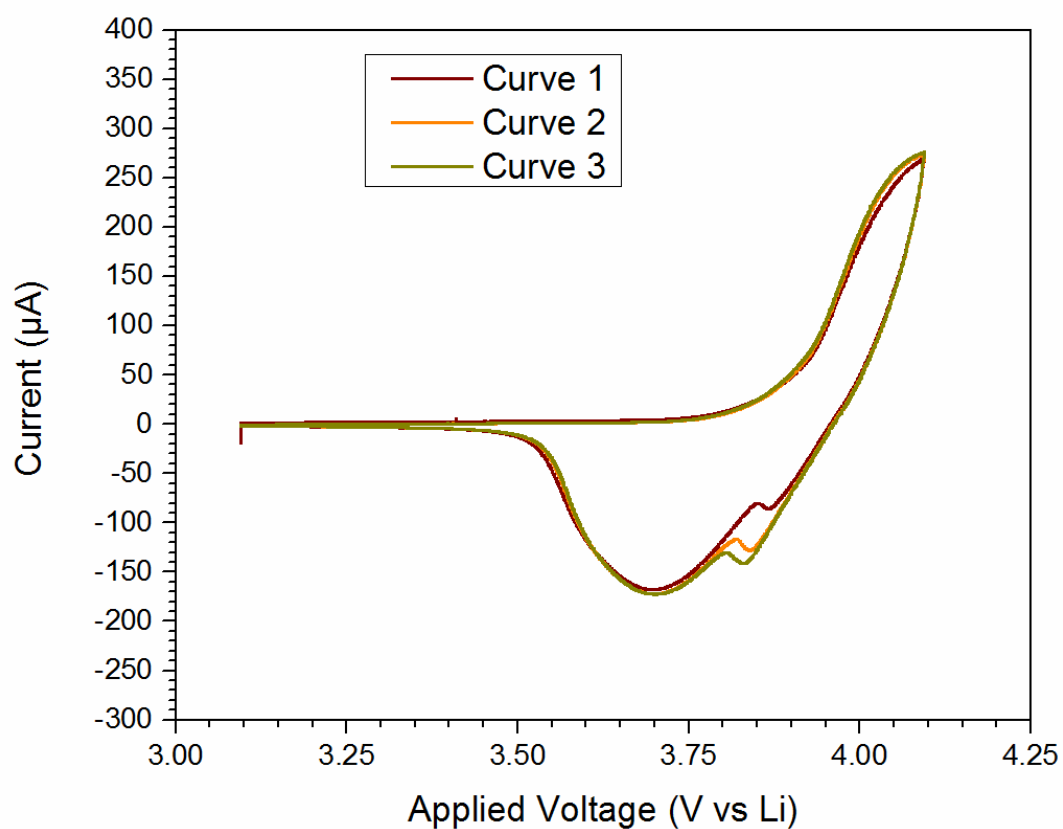


**Figure 4.13: Cyclic voltammetry with a lithium cobalt oxide on platinum cathode, a 1:9 electrolyte solution of LiTFSI:Pyr13FSI, and a lithium anode. After a 300 second delay, the modified split-cell was swept from 3.1 to 4.1V at a rate of 0.0925924 mV/s for three cycles/curves.**

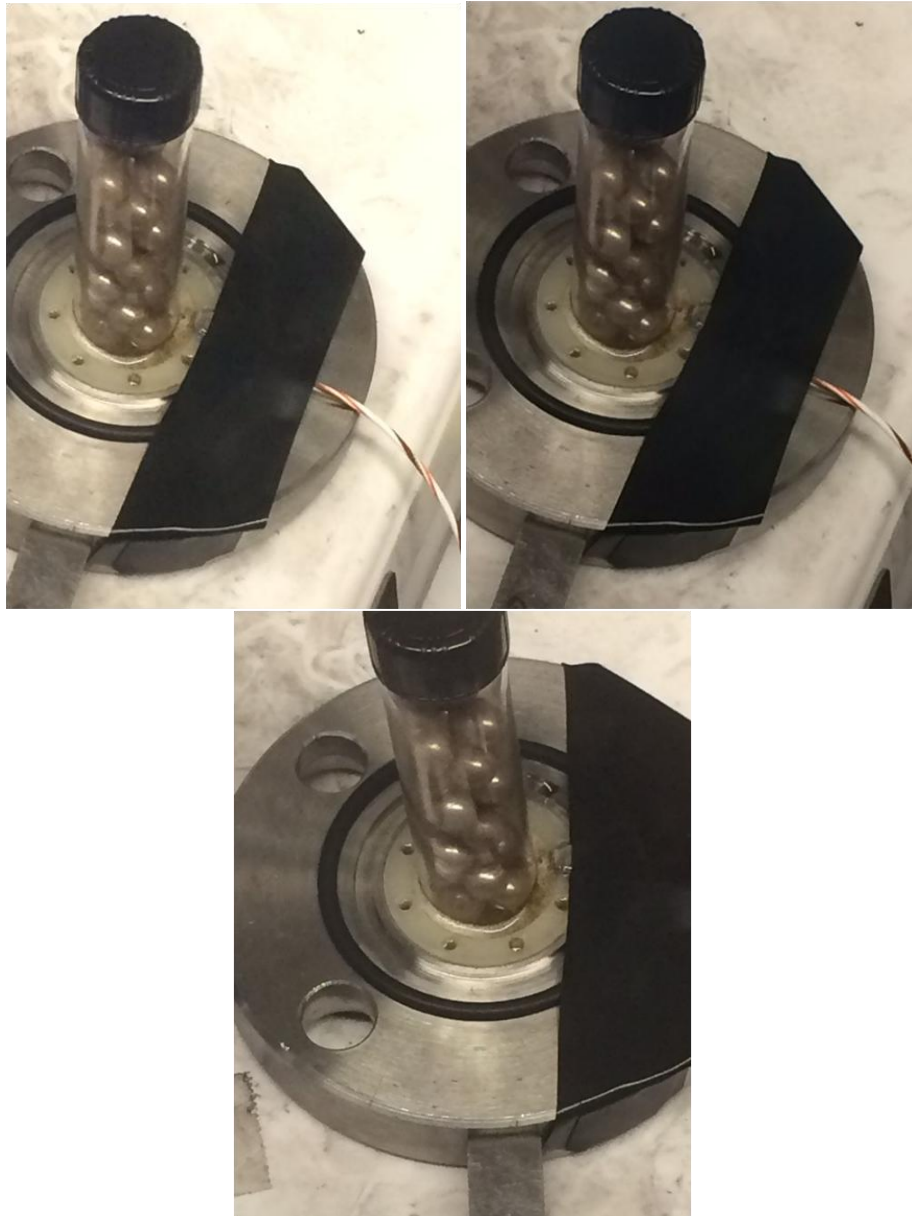


**Figure 4.14: Example of short circuit. Effervescence is shown to form**

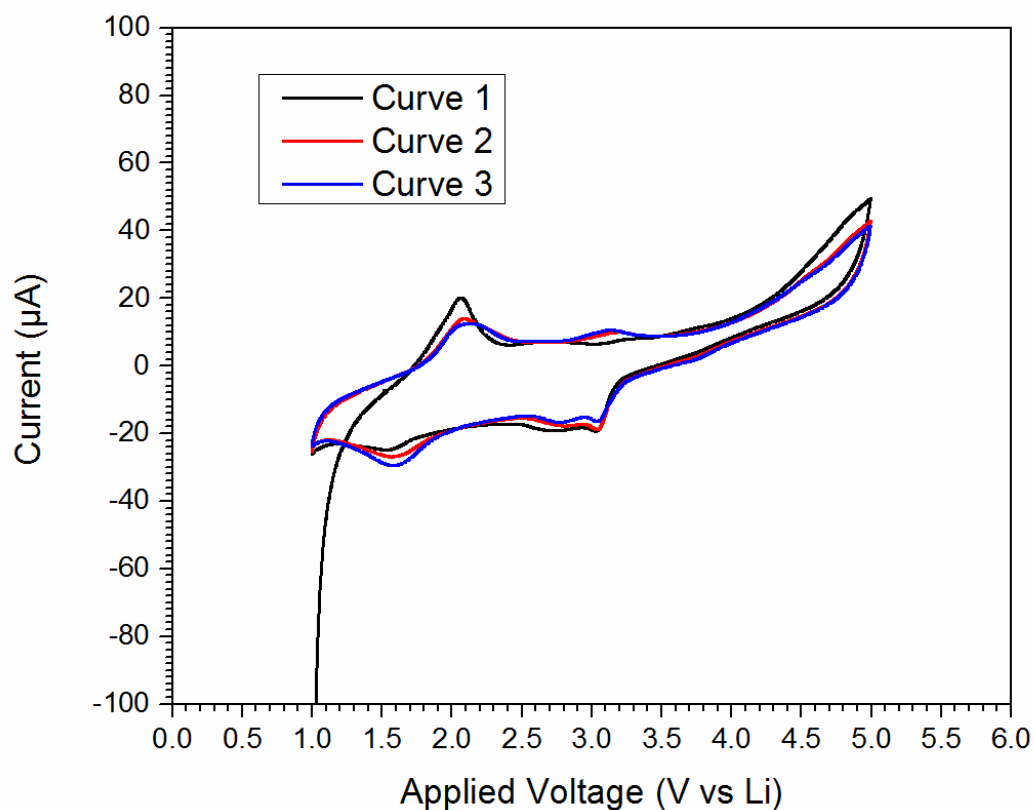


**Figure 4.15: Cyclic voltammetry with a 10% cobalt doped T-LiFeO<sub>2</sub> on platinum cathode, a 1:9 electrolyte solution of LiTFSI:Pyr<sub>13</sub>TFSI of 800 microliters, and a lithium anode. After a 30 second delay, the modified split-cell was swept from 1 to 5 V at a rate of 0.37037 mV/s for three cycles/curves.**

With the functioning modified split-cell, the first electrochemical cycling of 10% cobalt doped T-LiFeO<sub>2</sub> was performed and plotted in Figure 4.15. Although, the cyclic voltammetry has shown minimum current, the anodic peak at 2.0 V and the cathodic peak at 1.6 V have suggested the electrochemical availability of the iron II/III redox couple. The small peaks that have formed at 3.1 and 3.0 V could be indicative of the layered LiFeO<sub>2</sub> structure,<sup>275</sup> or it could be a break-down of the cathode material. A change of solvents from Pyr<sub>13</sub>FSI to Pyr<sub>13</sub>TFSI solvent was made due to the dwindling source of highly expensive Pry<sub>13</sub>FSI for future electrochemical tests.



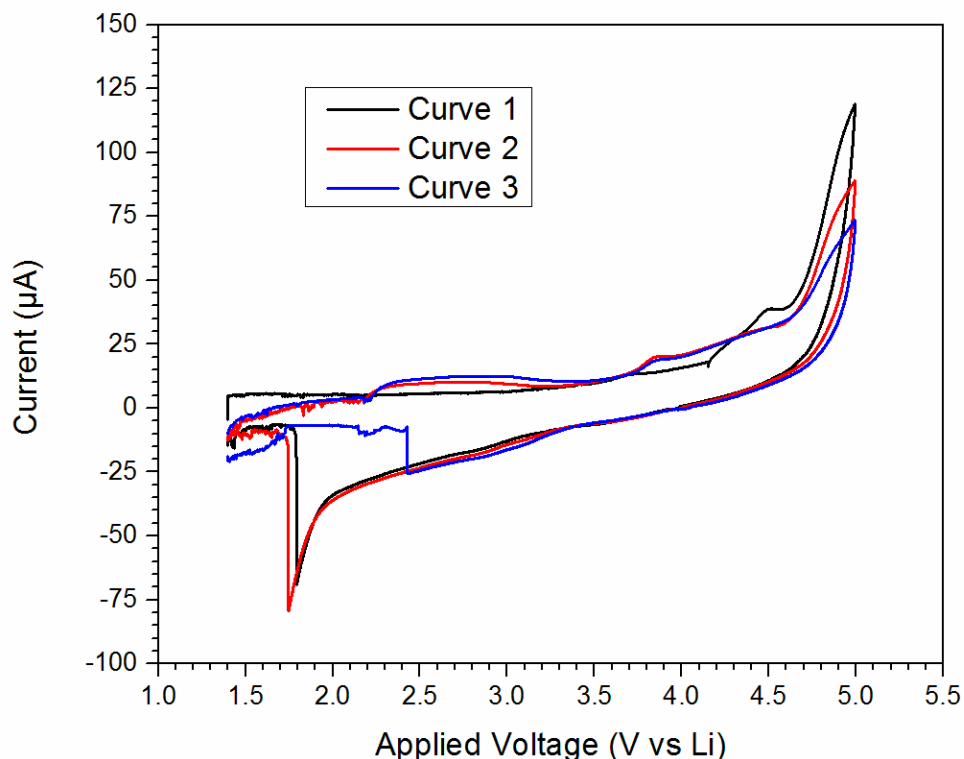


**Figure 4.16:** Cyclic voltammetry with a 10% cobalt doped T-LiFeO<sub>2</sub> on platinum cathode, a 1:9 electrolyte solution of LiTFSI:Pyr<sub>13</sub>TFSI of 800 microliters, and a lithium anode. After a 60 minute delay, the modified split-cell was swept from 1.4 to 5 V at a rate of 0.1 mV/s for three cycles/curves.

A slower cycling of the modified split-cell was performed in Figure 4.16. The figure has suggested a proposed deintercalation of the T-LiFe<sub>0.9</sub>Co<sub>0.1</sub>O<sub>2</sub> compound at 4.5 V for the iron III/IV redox couple. However, there has been no visible hint of an intercalation peak for the iron III/IV cathodic peak. There has been some kind of cell degradation due to irregular cycling. The reason for the irregular cycling could also from a short circuit or electrolyte decomposition.<sup>51</sup>

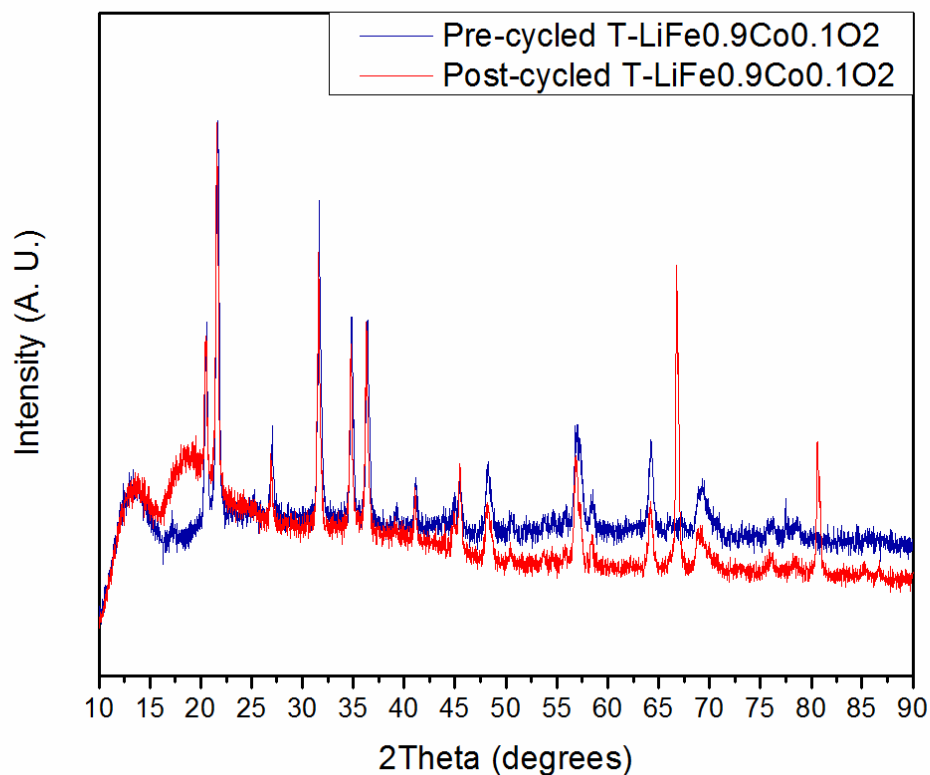


**Figure 4.17: Comparison of T-LiFe<sub>0.9</sub>Co<sub>0.1</sub>O<sub>2</sub> before and after the compound was cycled from 1.7 V to 4.6 V at a scan rate of 0.1 mV/s for six cycles/curves.**

An analysis of T-LiFe<sub>0.9</sub>Co<sub>0.1</sub>O<sub>2</sub> stability under electrochemical cycling was performed and reported in Figure 4.17. The powder x-ray diffraction pattern of the dried T-LiFe<sub>0.9</sub>Co<sub>0.1</sub>O<sub>2</sub> slurry was taken before and after electrochemical cycling. The background has been found to be high and irregular due to the amount of carbon used in the slurry, but the structure has maintained mostly with exception to the high angle reflection peaks at 63 and 82 degrees. These peaks have not been identified and have not been matched to existing phases. They could be indicative of ion ordering.

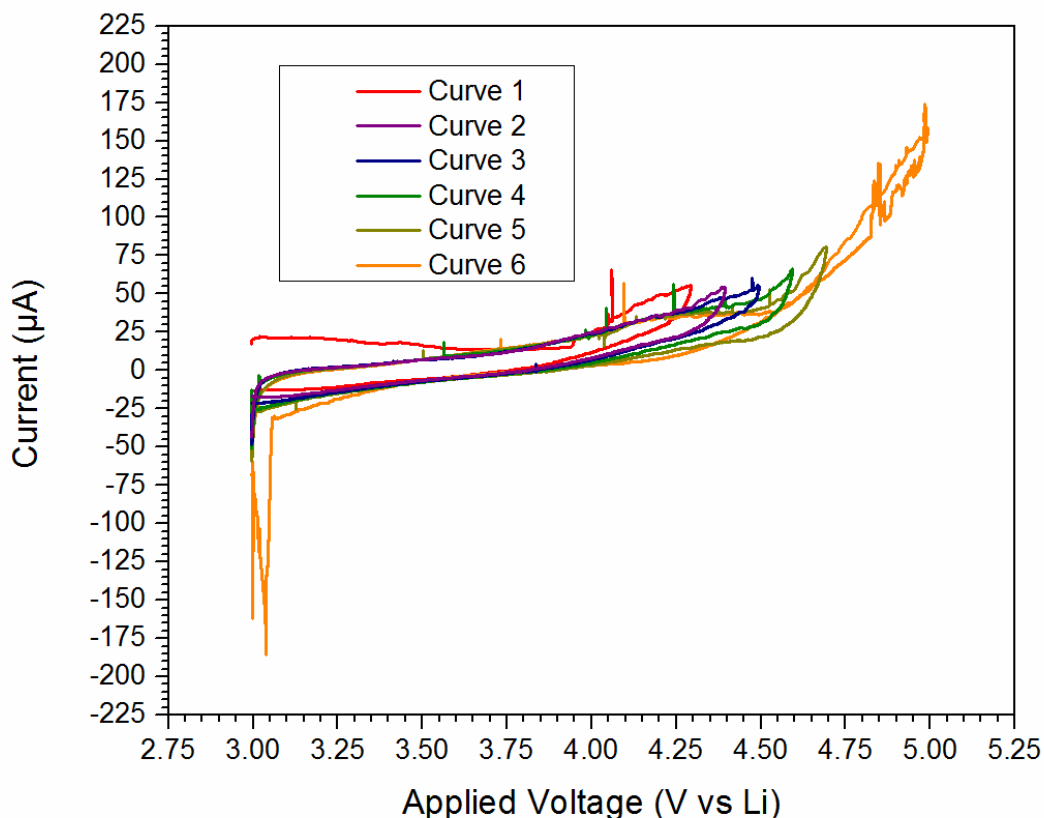


**Figure 4.18: Cyclic voltammetry with a 75 micron layer of 10% cobalt doped T-LiFeO<sub>2</sub> on platinum cathode, a 1:9 electrolyte solution of LiTFSI:Pyr<sub>13</sub>TFSI of 800 micro liters, and a lithium anode. After a 60 minute delay, the modified split-cell was swept from 3.0 to 4.3, 4.4, 4.5, 4.6 4.7, and 5.0 V at a rate of 0.0416669 mV/s for six cycles/curves. Curves 5 and 6 were performed at 50°C**

The cycling of another prepared modified split-cell for the T-LiFe<sub>0.9</sub>Co<sub>0.1</sub>O<sub>2</sub> active materials was performed with respect to increasing voltage has been reported in Figure 4.18. Even though Figure 4.16 hinted at the deintercalation of lithium in T-LiFe<sub>0.9</sub>Co<sub>0.1</sub>O<sub>2</sub>, Figure 4.18 has shown no deintercalation peak even for cycles 5 and 6 which were cycled at temperature of 50°C. A temperature of 50°C was previously reported as being close to the thermal decomposition temperature of T-LiFeO<sub>2</sub>.<sup>157</sup> Also the large increase in current at 5 V has been mostly likely indicative of electrolyte decomposition.

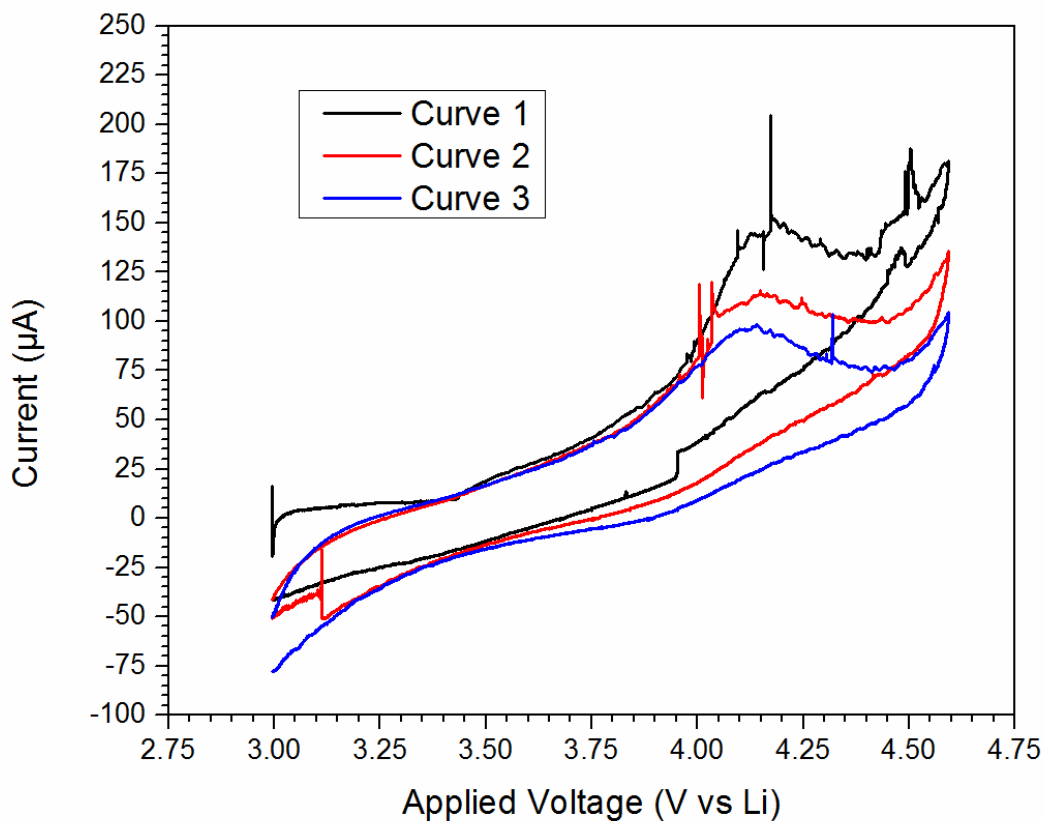


**Figure 4.19: Cyclic voltammetry with a 75 micron layer of 10% cobalt doped T-LiFeO<sub>2</sub> on platinum cathode, a 1:9 electrolyte solution of LiTFSI:Pyr<sub>13</sub>TFSI of 800 microliters, and a lithium anode. After a 60 seconds delay, the modified split-cell was swept from 3.0 to 4.6 V at a rate of 0.0416669 mV/s for three cycles/curves at a temperature of 75°C.**

Another three cycles for the modified split-cell used in Figure 4.18 were ran between 3.0 and 4.6 V and reported in Figure 4.19. In Figure 4.19, the modified split-cell was cycled at a temperature of 75°C. The anodic peak at 4.2 V could have been the deintercalation of lithium, but it was probably degradation of the electrode due to the high temperature and non-reversible cyclability.

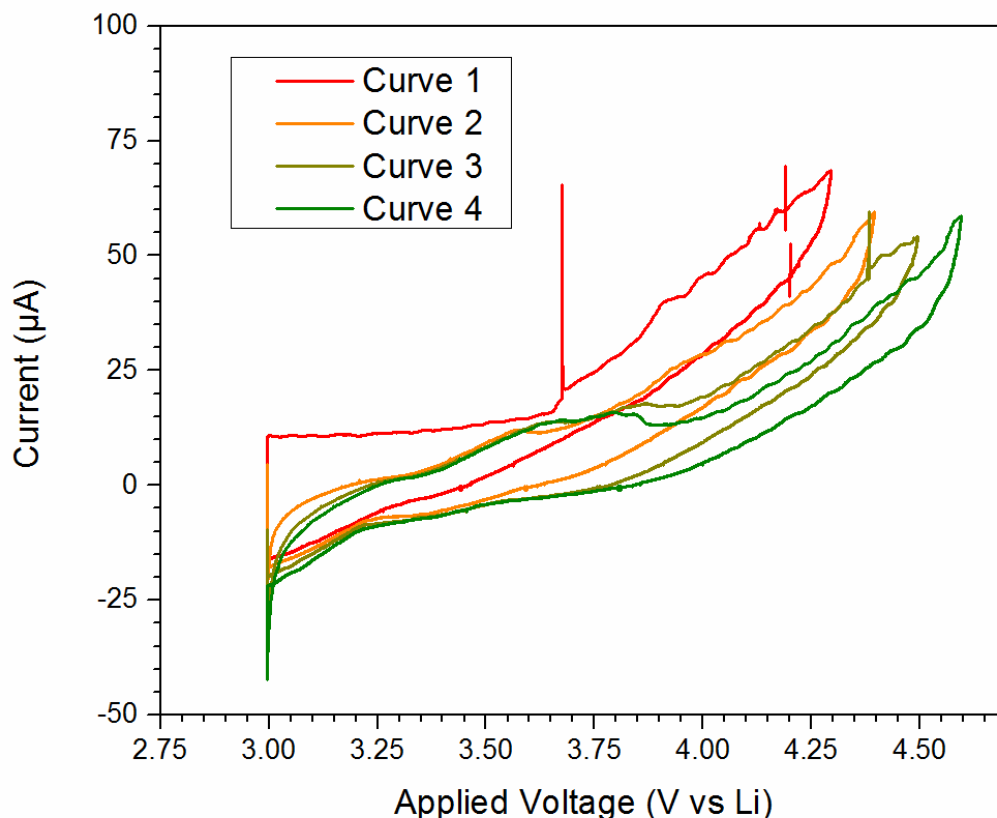


**Figure 4.20: Cyclic voltammetry with a 75 micron layer of 10% cobalt doped T-LiFeO<sub>2</sub> on platinum cathode, a 1:9 electrolyte solution of LiTFSI:Pyr<sub>13</sub>TFSI of 800 microliters, and a lithium anode. After a 60 minute delay, the modified split-cell was swept from 3.0 to 4.3, 4.4, 4.5, and 4.6 V at a rate of 0.0416669 mV/s for four cycles/curves at a temperature of 40°C**

A new modified split-cell was cycled from a voltage of 3.0 V to an increasing varied voltage of 4.3, 4.4, 4.5, and 4.6 V at a constant temperature of 40°C as shown in Figure 4.20. Repeatedly, the cycling of T-LiFe<sub>0.9</sub>Co<sub>0.1</sub>O<sub>2</sub> has shown no deintercalation, though there has been less decomposition of the electrolyte shown. Figure 4.21 has shown the modified split-cell from Figure 4.20 after it has been cycled again, between 3.0 V and 4.6 V over three cycles at 40°C at a slower scan speed of 0.0178 mV/s, but the cycles have shown irregularity and non-reversibility. The iron III/IV redox couple has still not been electrochemically accessed.

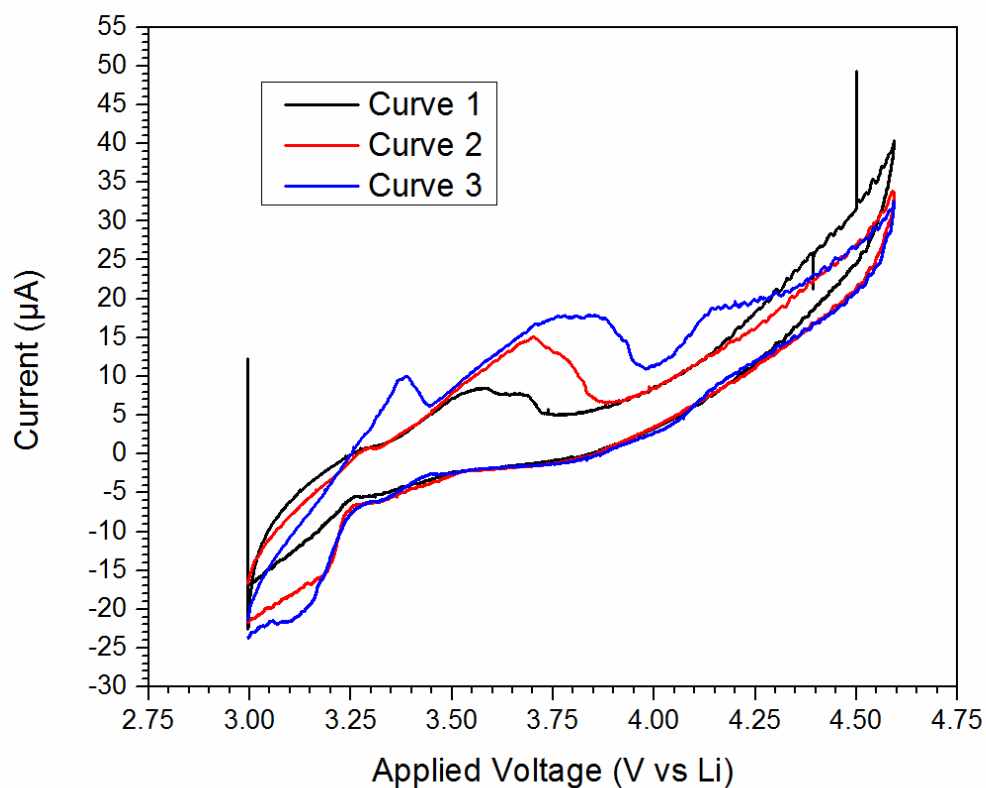


**Figure 4.21:** Cyclic voltammetry with a 75 micron layer of 10% cobalt doped  $\text{T-LiFeO}_2$  on platinum cathode, a 1:9 electrolyte solution of  $\text{LiTFSI}:\text{Pyr}_{13}\text{TFSI}$  of 800 microliters, and a lithium anode. After a 60 seconds delay, the modified split-cell was swept from 3.0 to 4.6 V at a rate of 0.0177778 mV/s for three cycles/curves at a temperature of 40°C.

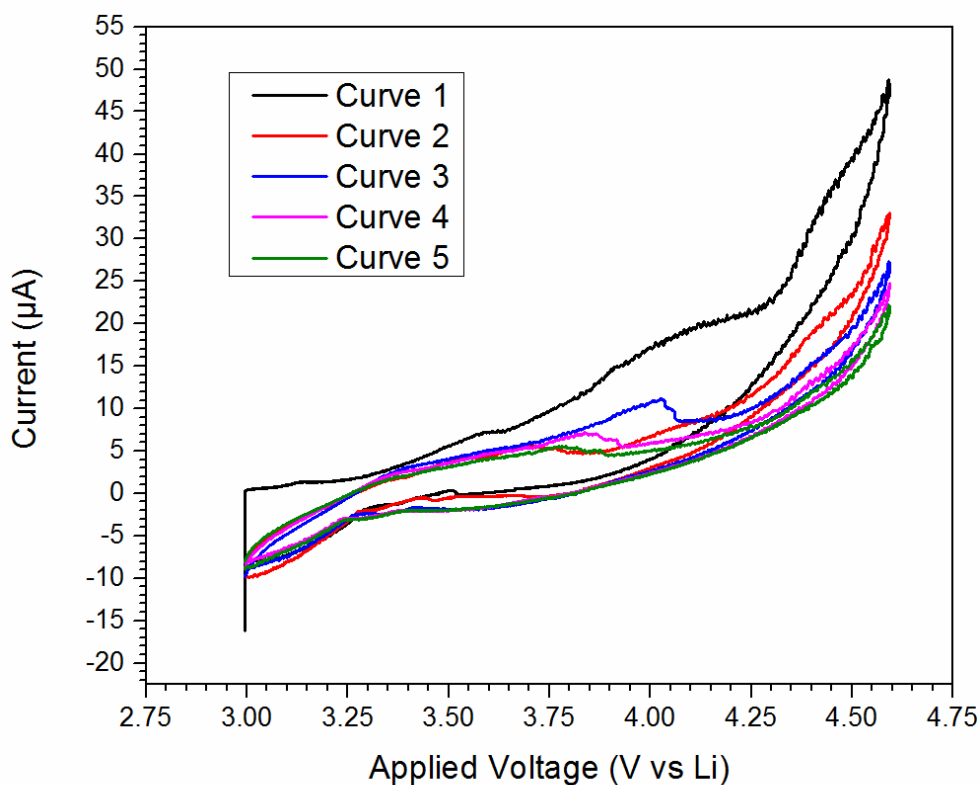


**Figure 4.22: Cyclic voltammetry with a 75 micron layer of 10% cobalt doped T-LiFeO<sub>2</sub> on platinum cathode, a 1:9 electrolyte solution of LiTFSI:Pyr<sub>13</sub>TFSI of 800 microliters, and a lithium anode. After a 12 hour delay the cell was swept from 3.0 to 4.6 V at a rate of 0.008889 mV/s for five cycles/curves at a temperature of 40°C.**

The final test of electrochemical accessibility of the iron III/IV redox couple has been reported in Figure 4.22. The modified split-cell was allowed to equilibrate at 40°C for 12 hours and then cycled at a rate of 1/50 C. The modified split-cell was equilibrated to allow for an even electrolyte solution. A temperature of 40°C was used to increase ionic mobility without decomposing the active material. The scan speed was performed at a slow rate to account for low ionic conductivity from large particle size irregularities. The top voltage was limited to 4.6V to prevent any type of electrolyte decomposition. Even with all considerations, a fully identifiable deintercalation and intercalation peak for the iron III/IV redox couple has not been identified. The iron III/IV redox couple of T-LiFe<sub>0.9</sub>Co<sub>0.1</sub>O<sub>2</sub> has shown to be not electrochemically accessible, at all.

#### 4.4 Investigation of Chromium, Nickel, and Vanadium Doped $\beta$ -NaFeO<sub>2</sub>

Nickel, chromium, and vanadium doping of the pre-requisite  $\beta$ -NaFeO<sub>2</sub> structure was attempted. The use of nickel as a dopant was used to inject extra electrons into the compound while the use of vanadium and chromium was used for dope holes into the compound.<sup>125</sup> Doping of cobalt has shown to work in the past, but the abundance of cobalt has been lacking compared to other transition metals.<sup>31</sup> Introducing holes and extra electrons would promote increased conductivity.<sup>63,125</sup> For an initial test of the stability of a vanadium, nickel, or chromium ion coordinated to an oxygen ion in a tetrahedral environment, the ratios of the ionic radii for vanadium, chromium, nickel, and iron coordinated to oxygen were calculated from the reported Shannon radii and reported in Table 4.2.<sup>36,306</sup> The radius ratio can be used to predict the stability and coordination preference

**Table 4.2: Radius ratio for various oxidation states of transition metals coordinated to oxygen (CN = coordination number) Red highlighted cells have octahedral preference while green highlighted cell have tetrahedral preference. Blue are the Shannon Radii.**

		Oxygen 2- CN = 4	Oxygen 2- CN = 6
		1.38	1.4
Vanadium 3+ CN=6	0.64	0.463768116	0.457142857
Nickel 3+ CN=6 High Spin	0.6	0.434782609	0.428571429
Nickel 3+ CN=6 Low Spin	0.56	0.405797101	0.400000000
Nickel 2+ CN=4	0.55	0.398550725	0.392857143
Nickel 2+ CN=SqPI	0.49	0.355072464	0.350000000
Nickel 2+ CN=6	0.69	0.500000000	0.492857143
Chromium 3+ CN=6	0.615	0.445652174	0.439285714
Cobalt 3+ CN=6 High Spin	0.61	0.442028986	0.435714286
Cobalt 3+ CN=6 Low Spin	0.545	0.394927536	0.389285714
Iron 3+ CN=4 High Spin	0.49	0.355072464	0.350000000
Iron 3+ CN=6 High Spin	0.645	0.467391304	0.460714286
Iron 3+ CN=6 Low Spin	0.55	0.398550725	0.392857143

A value of 0.414 for the radius ratio has been the reported threshold between an octahedral and tetrahedral coordination preference. For a value higher than 0.414, the preferred coordination would be octahedral while a value lower than 0.414 would have preferred a tetrahedral coordination. A value of 0.732 or higher for the radius ratio would prefer a cubic coordination and radius ratios below 0.2247



prefer triangular coordination.<sup>307</sup> From first glance, it would seem that chromium and vanadium would not prefer a tetrahedral coordination; however, the values were fairly close to the threshold where the rule can relax.<sup>308</sup> Nickel, cobalt, and iron centers would support a tetrahedral coordination under the right spin conditions. The coordination structures that have been suggested by the radius ratio have only been general guidelines and not explicit rules, but the guideline would be more likely to relax near the thresholds. The thresholds made by the theory have assumed hard spheres for the ionic radii. There would still be a possibility that chromium, nickel, and vanadium ions could be doped into a tetrahedral coordination such as in the  $\beta$ -NaFeO<sub>2</sub> structure.<sup>308</sup> For convenience, only the side products have been labeled in the powder x-ray diffraction analysis of chromium, nickel, and vanadium doped  $\beta$ -NaFeO<sub>2</sub>.

#### 4.4.1 Chromium Doping of $\beta$ -NaFeO<sub>2</sub>

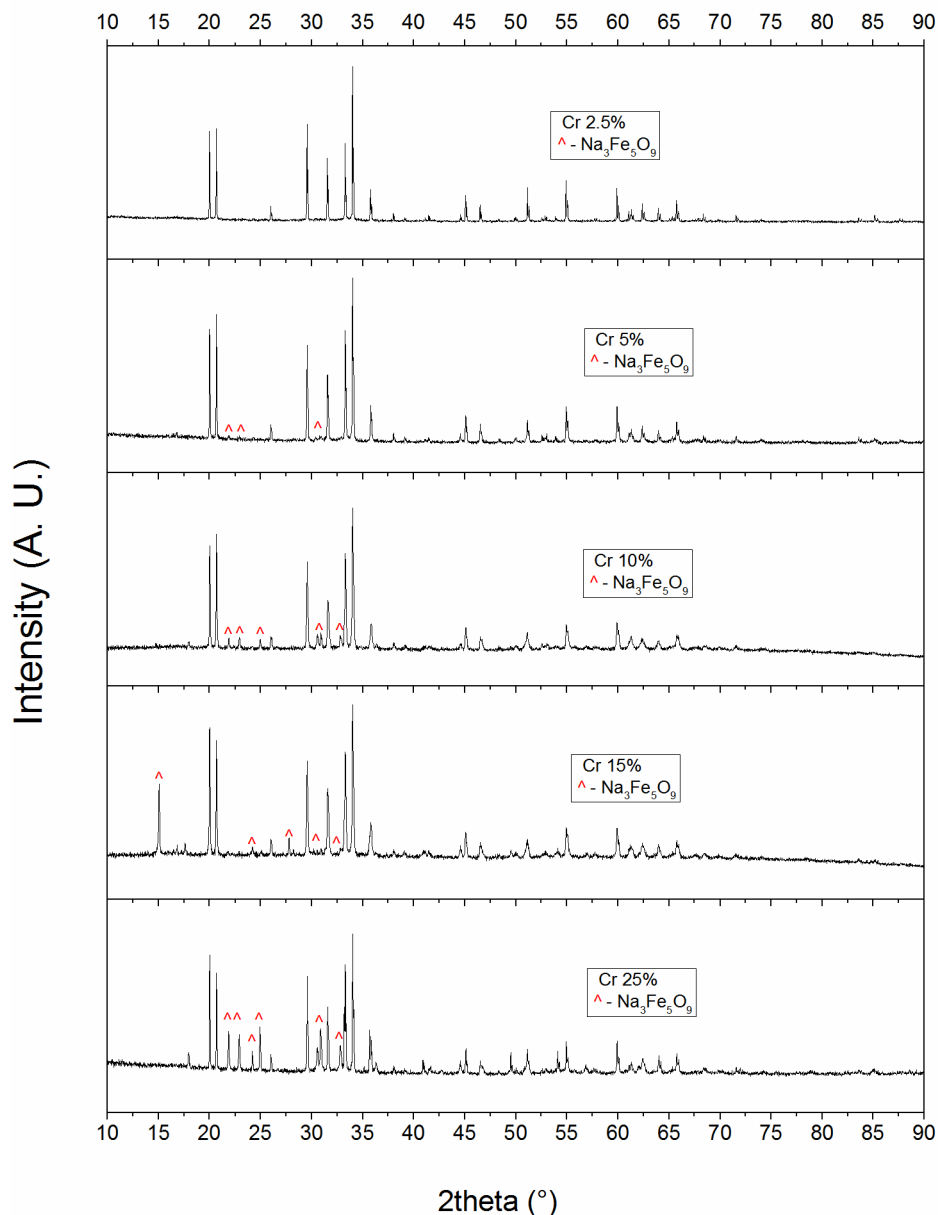


**Figure 4.23: Powder x-ray diffraction patterns of  $\beta$ -NaFeO<sub>2</sub> doped with different molar amounts of chromium (2.5, 5, 10, 15, and 25%). Mixtures were heated to a maximum value of 850°C for 48 hours. (WL = 1.5418 Å)**

In experiment, doping  $\beta$ -NaFeO<sub>2</sub> with chromium has shown to be difficult. From Figure 4.23, it would seem that the doping of chromium has been limited between a doping of 2.5% and 5%. Any attempt to dope higher than that amount, has forced the Na<sub>3</sub>Fe<sub>5</sub>O<sub>9</sub> phase to become more prominent in the powder x-ray diffraction pattern.<sup>309</sup> The Na<sub>3</sub>Fe<sub>5</sub>O<sub>9</sub> phase contains tetrahedral and octahedral

coordination position for each transition metal center. The chromium ions in this structure would have most likely moved into the octahedral coordination positions. The chromium III ion would not have spherical shape such as the as the iron III ion has due to the unequal d-orbital occupations.

From the varying temperatures at which the  $\text{Na}_2\text{CO}_3$ ,  $\text{Fe}_2\text{O}_3$ , and  $\text{Cr}_2\text{O}_3$  mixture has been heated, the best temperature used to attempt to synthesize chromium doped  $\beta\text{-NaFeO}_2$  has been a profile of  $850^\circ\text{C}$  for 48 hours. At lower temperatures such as,  $700^\circ\text{C}$ , the reactants remain unchanged. As shown in Figures 4.24 and 4.25, higher and longer temperatures have increased the prominence of the  $\text{Na}_3\text{Fe}_5\text{O}_9$  phase in the powder x-ray diffraction pattern. This has lead to the initial conclusion that chromium doped  $\beta\text{-NaFeO}_2$  would only be a meta-stable compound compared to  $\text{Na}_3\text{Fe}_5\text{O}_9$  as the more stable compound.

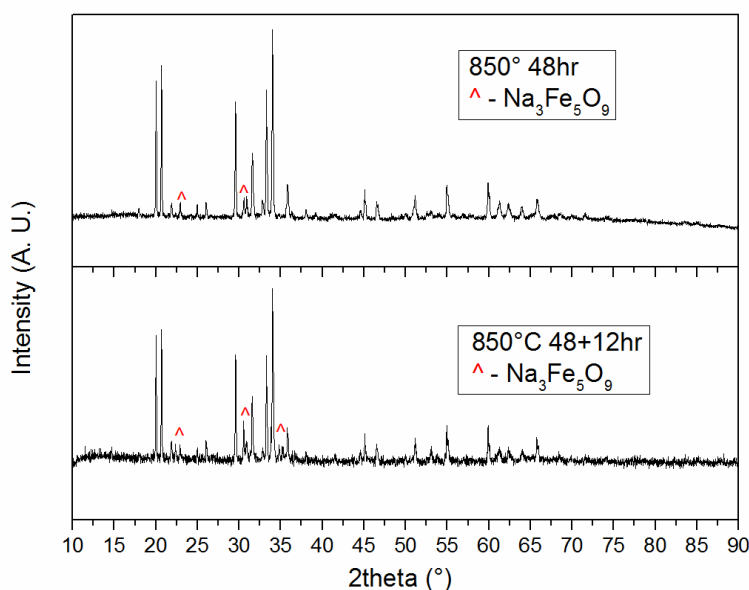


**Figure 4.24: Powder x-ray diffraction patterns of 10% molar chromium doped  $\beta\text{-NaFeO}_2$  fired at several temperature profiles. The bottom PXD pattern was heated for a total of 50 hours with an intermittent grinding at 48 hours. In comparison to Figure 4.25, the pattern was scanned for one hour. (WL =  $1.5418 \text{ \AA}$ )**

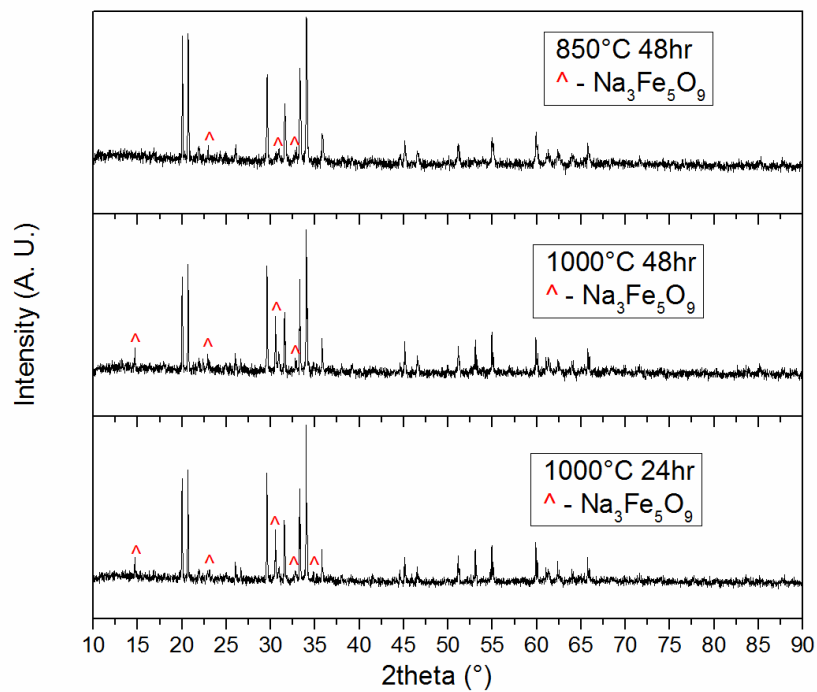


**Figure 4.25: Powder x-ray diffraction patterns of 10% molar chromium doped  $\beta$ -NaFeO<sub>2</sub> fired at several temperature profiles. In comparison of Figure 4.24, the pattern was scanned for two hours. (WL = 1.5418 Å)**

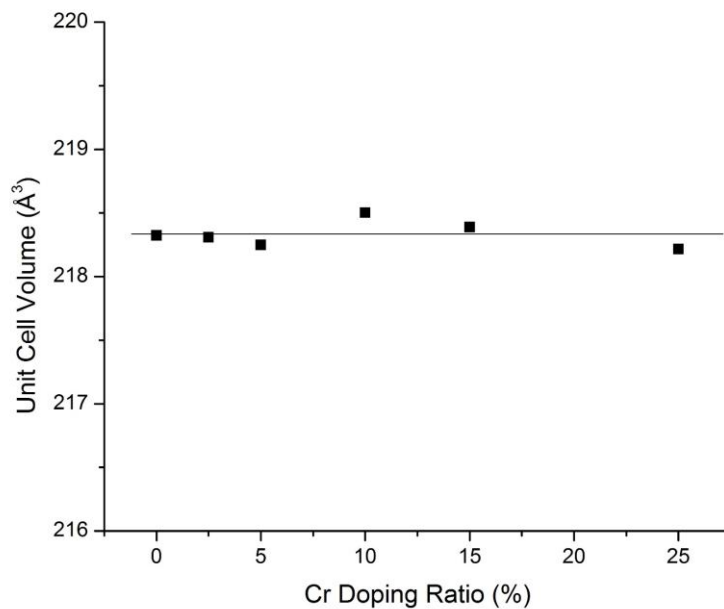


**Figure 4.26: Le Bail analysis of chromium doped  $\beta$ -NaFeO<sub>2</sub>. (Reacted at 850°C for 48 hours)**

While Figure 4.23 has suggested that a small amount of chromium can be doped into the

$\beta$ -NaFeO<sub>2</sub> structure by the lack of other x-ray phases, proper PXD indexing must be performed to analyze the effectiveness of the doping. From the PXD patterns, the unit cell volumes of the indexed patterns from Figure 4.23 have been reported in Figure 4.26.<sup>310</sup> If there had been proper doping of the  $\beta$ -NaFeO<sub>2</sub> compound, there would have been a linear trend of the cell volume in relation to the dopant amount.<sup>161</sup> There has been, however, no linear relation. In order to further analyze the doping of  $\beta$ -NaFeO<sub>2</sub>, a sample of the 2.5% chromium doped  $\beta$ -NaFeO<sub>2</sub> which has been heated at 850°C for 48 hours, has been analyzed by scanning electron microscope. A SEM picture of 2.5% chromium doped  $\beta$ -NaFeO<sub>2</sub> has been reported in Figure 4.27 with a particle size around 2  $\mu$ m.

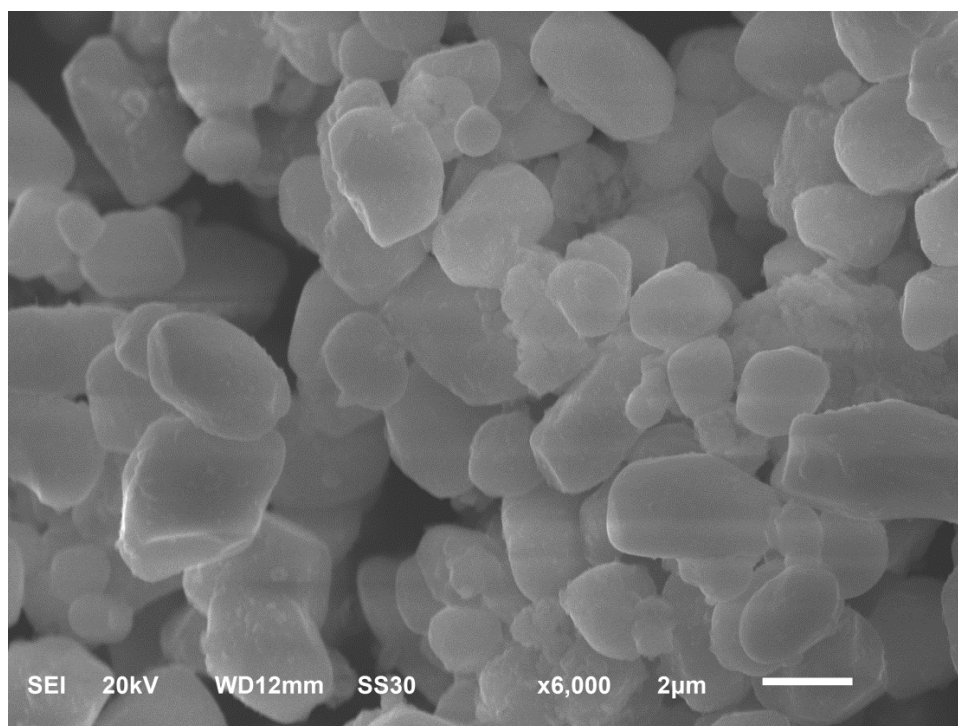


**Figure 4.27: SEM image of 2.5% chromium doped  $\beta$ -NaFeO<sub>2</sub>**

Back scatter analysis had also been done on the sample which has been shown in Figure 4.28. A back scattering typically would show how homogenous a mixture or a compound was synthesized by the lack of contrast in the image. The most of the particles have shown to be homogeneous, but when the energy dispersive x-ray (EDX) spectrum was taken at two different points in the image, it was clear that the mixture was not homogeneous. Figure 4.29 and Table 4.3 have shown the measured EDX

spectrum from the first position (labeled spectrum 6 in Figure 4.28) while Figure 4.30 and Table 4.4 has reported the measured EDX spectrum for the second position (labeled spectrum 7 in Figure 4.28). When comparing the two spectra, it can be shown that both positions have differing amounts of chromium which suggests a lack of homogeneity and that the doping of  $\beta$ -NaFeO<sub>2</sub> with chromium has not occurred.

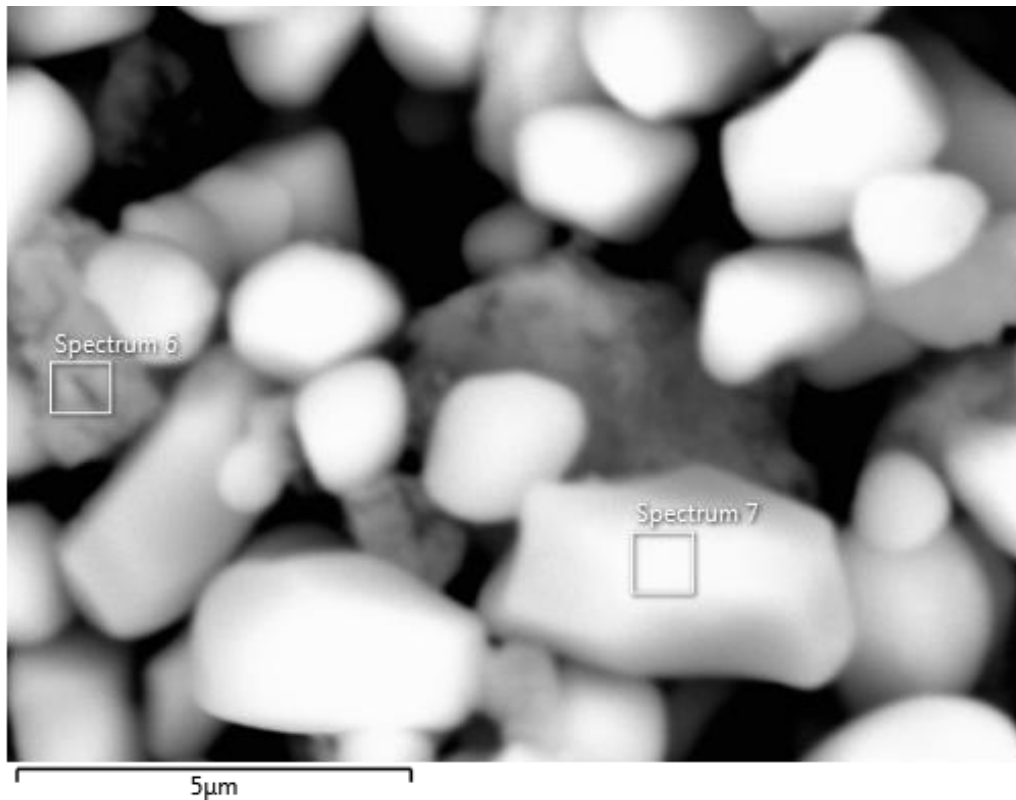


**Figure 4.28: Back scatter SEM image of 2.5% chromium doped  $\beta$ -NaFeO<sub>2</sub> with the measured EDX spectra at the designated selections.**

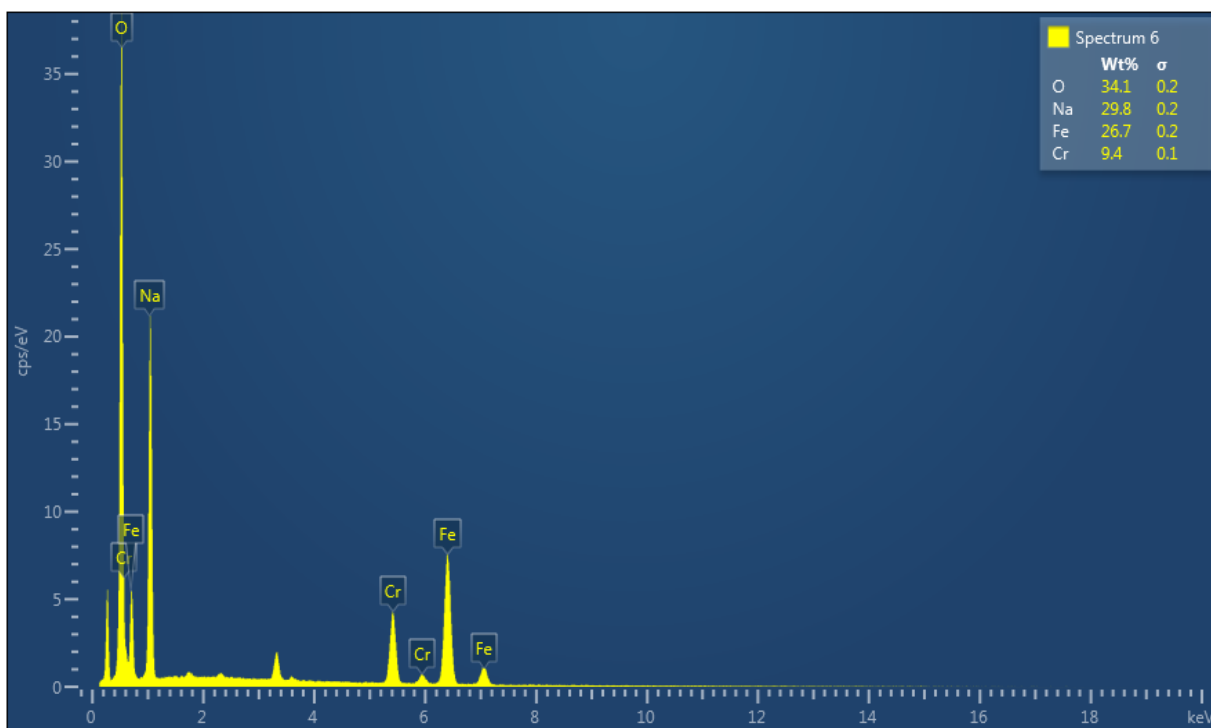


Figure 4.29: EDX spectrum from labeled spectrum 6 in Figure 4.28

Table 4.3: Counted weights and ratio from Figure 4.29

Element	Apparent concentration	Weight percent
O	80.02	34.07
Na	24.38	29.82
Cr	11.47	9.36
Fe	29.83	26.74
Total:		100.00

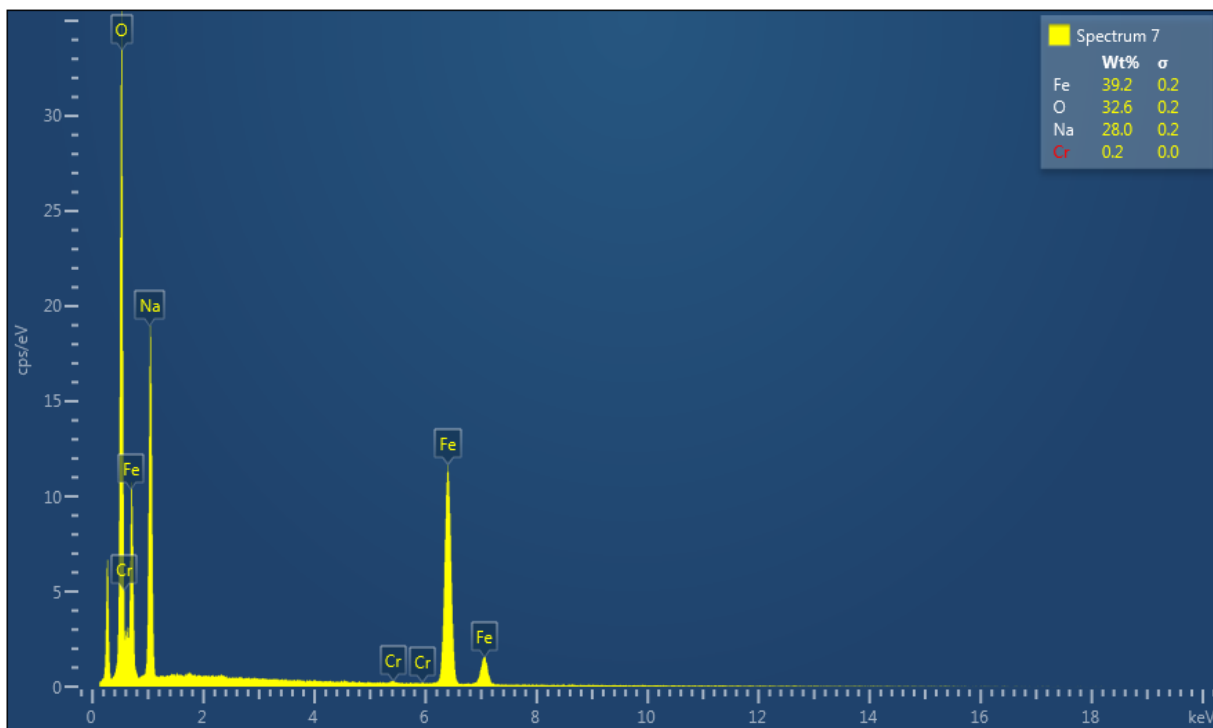


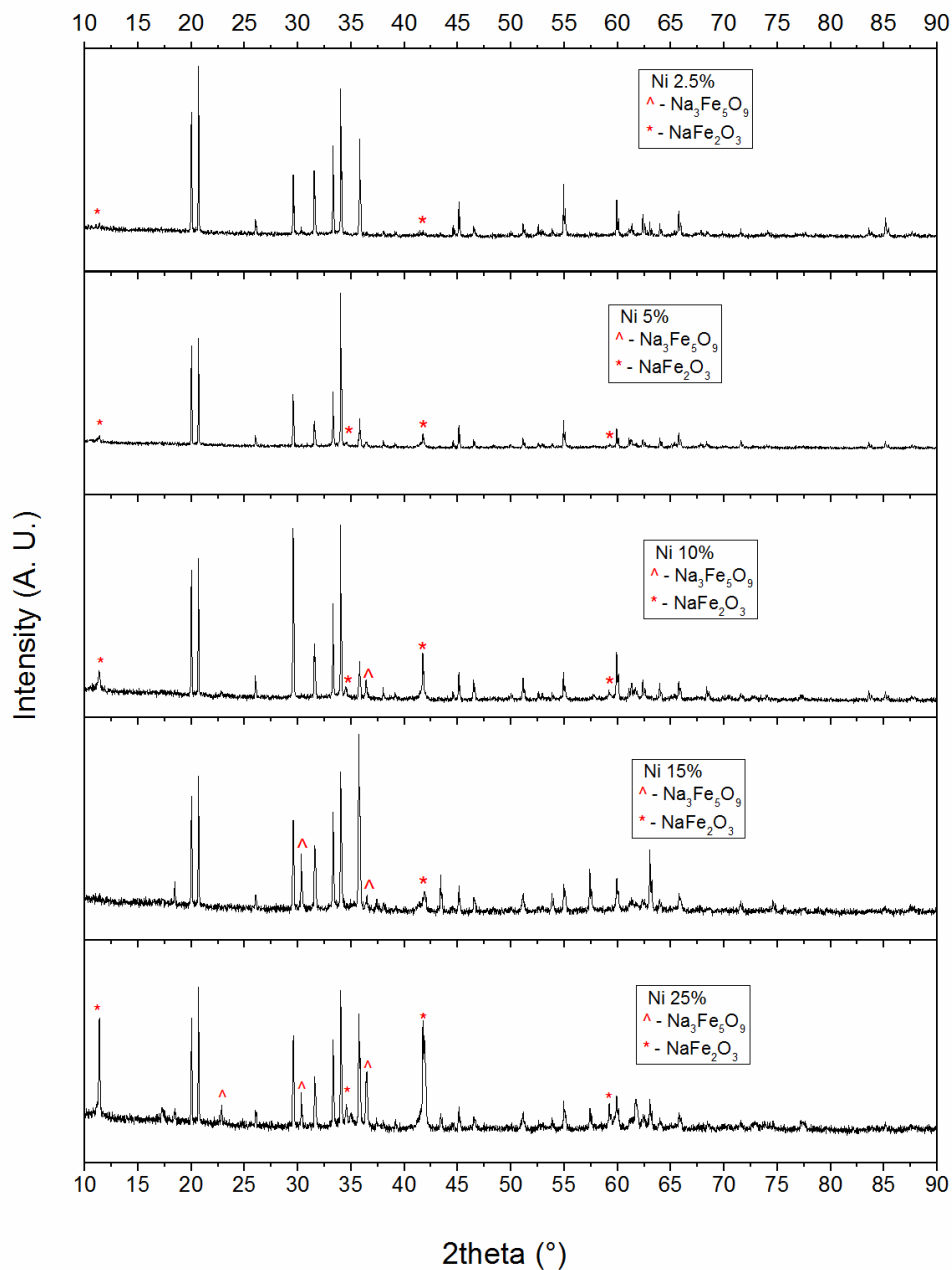
Figure 4.30: EDX spectrum from labeled spectrum 7 in Figure 4.28

Table 4.4: Counted weights and ratio from Figure 4.30

Element	Apparent concentration	Weight percent
O	77.35	32.55
Na	22.25	28.05
Cr	0.27	0.20
Fe	46.62	39.20
Total:		100.00



#### 4.4.2 Nickel Doping of $\beta$ -NaFeO<sub>2</sub>



**Figure 4.31: Powder x-ray diffraction patterns of  $\beta$ -NaFeO<sub>2</sub> doped with different molar amounts of nickel (2.5, 5, 10, 15, and 25%) Mixtures were heated to a maximum value of 1000°C for 72 hours (WL = 1.5418 Å)**

A maximum doping of 25% nickel attempted for the  $\beta$ -NaFeO<sub>2</sub> compound, as well, but there was also a dopant limit of about 2.5% and 5% as illustrated in Figure 4.31. However, unlike the attempted chromium doping of  $\beta$ -NaFeO<sub>2</sub>, the increased temperature and time has aided the formation of the

$\beta$ -NaFeO<sub>2</sub> phase, but only to a point. At low temperatures, the NaFe<sub>2</sub>O<sub>3</sub> phase has appeared in the PXD patterns. The NaFe<sub>2</sub>O<sub>3</sub> phase has all octahedral coordination position for transition metal ion centers, but ion centers would not be isovalent.<sup>311</sup> The NaFe<sub>2</sub>O<sub>3</sub> structure has two iron III positions and one iron II positions. The formation of the NaFe<sub>2</sub>O<sub>3</sub> phase would be expected, as the attempted doping of nickel in the  $\beta$ -NaFeO<sub>2</sub> compound has required the nickel II oxide compound. The nickel II ions would have ideally taken the iron II positions in the formation of NaFe<sub>2</sub>O<sub>3</sub> phase. As the nickel doped  $\beta$ -NaFeO<sub>2</sub> material was heated for longer times, the NaFe<sub>2</sub>O<sub>3</sub> phase would dissipate and the Na<sub>3</sub>Fe<sub>5</sub>O<sub>9</sub> phase would become more pronounced.<sup>309</sup> This has been reported in Figures 4.32 and 4.33.

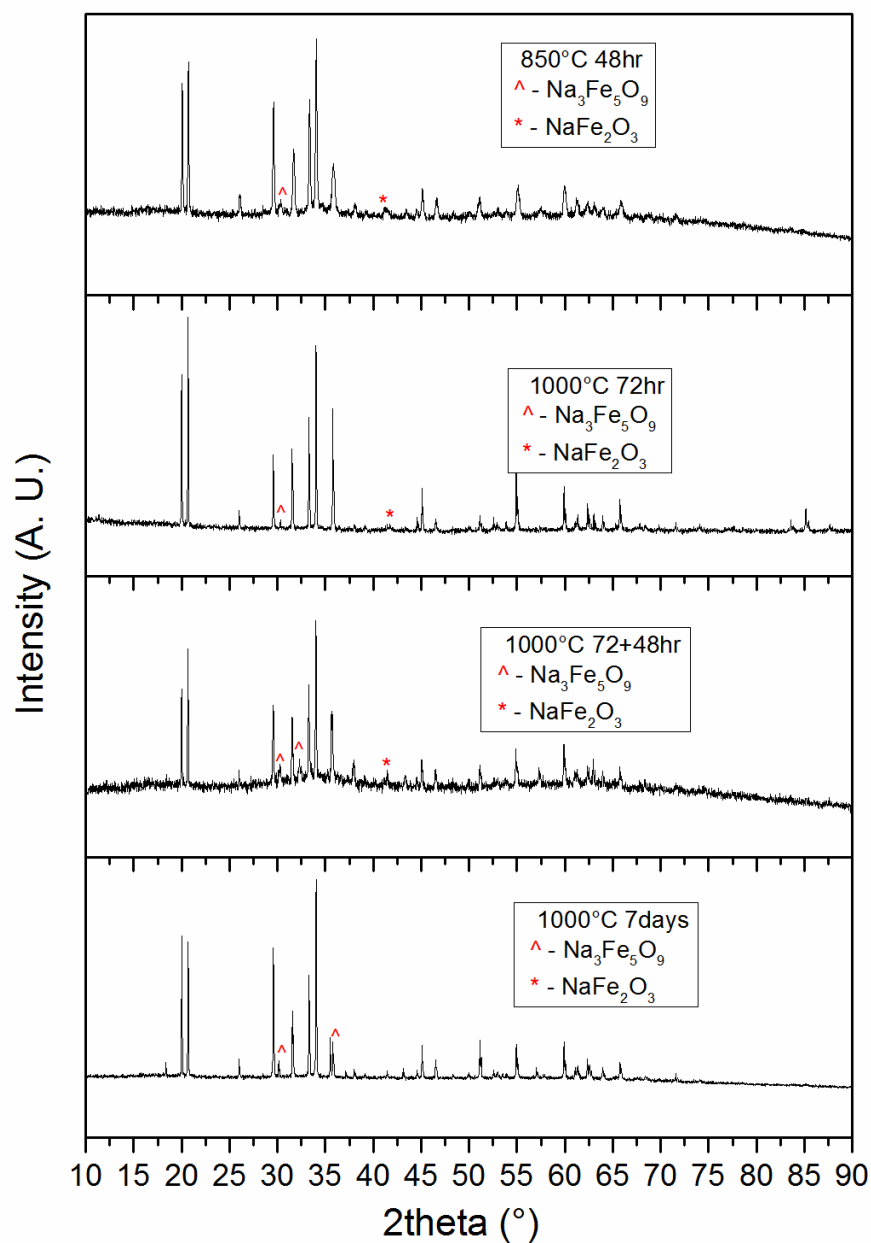


Figure 4.32: Powder x-ray diffraction patterns of 2.5% molar nickel doped  $\beta$ - $\text{NaFeO}_2$  fired at several temperature profiles. The PXD pattern, second from the bottom, was heated for a maximum of 120 hours with an intermittent grinding at 72 hours. (WL = 1.5418 Å)

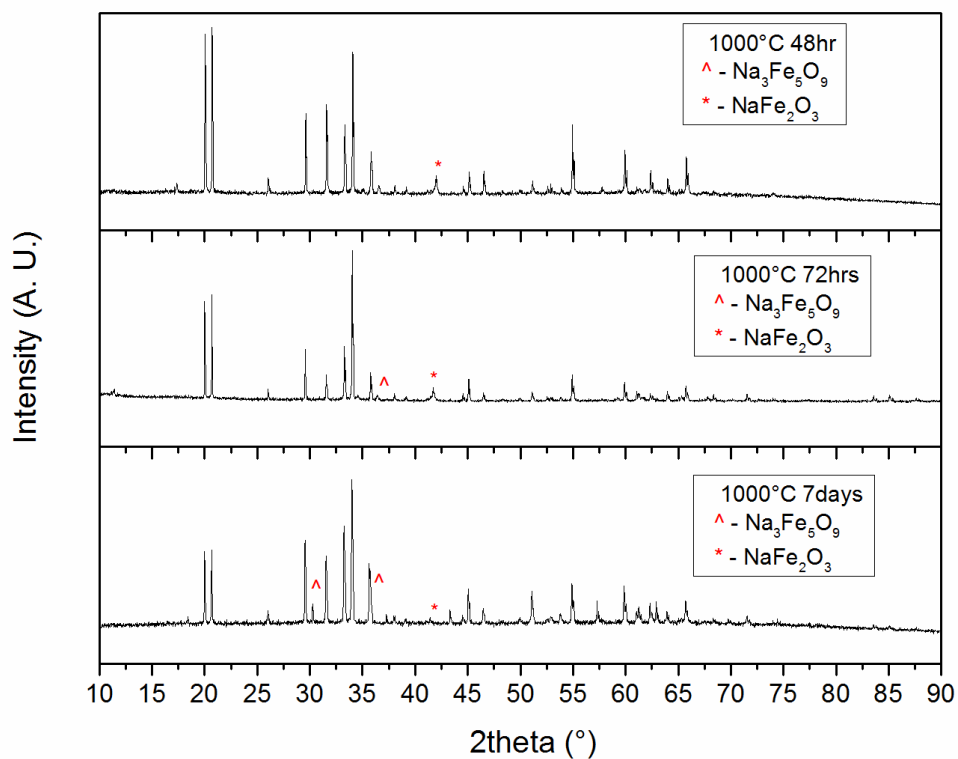


Figure 4.33: Powder x-ray diffraction pattern of 5% molar nickel doped  $\beta$ - $\text{NaFeO}_2$  fired at several temperature profiles. (WL = 1.5418 Å)

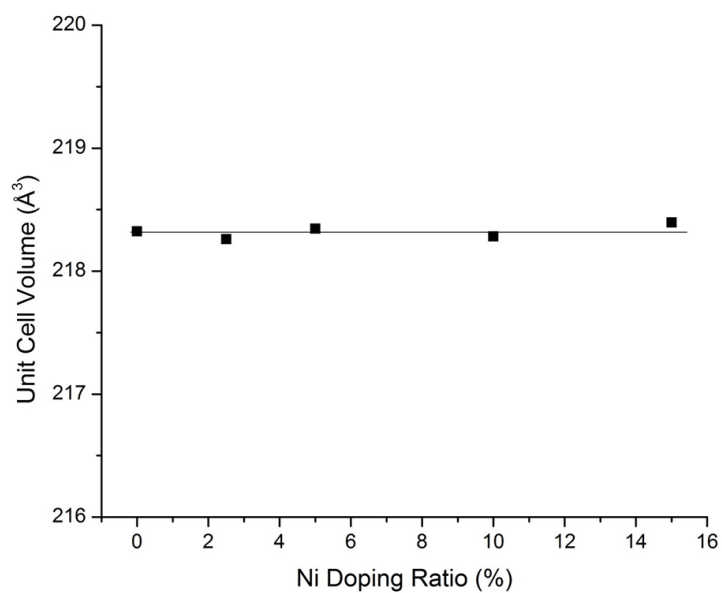
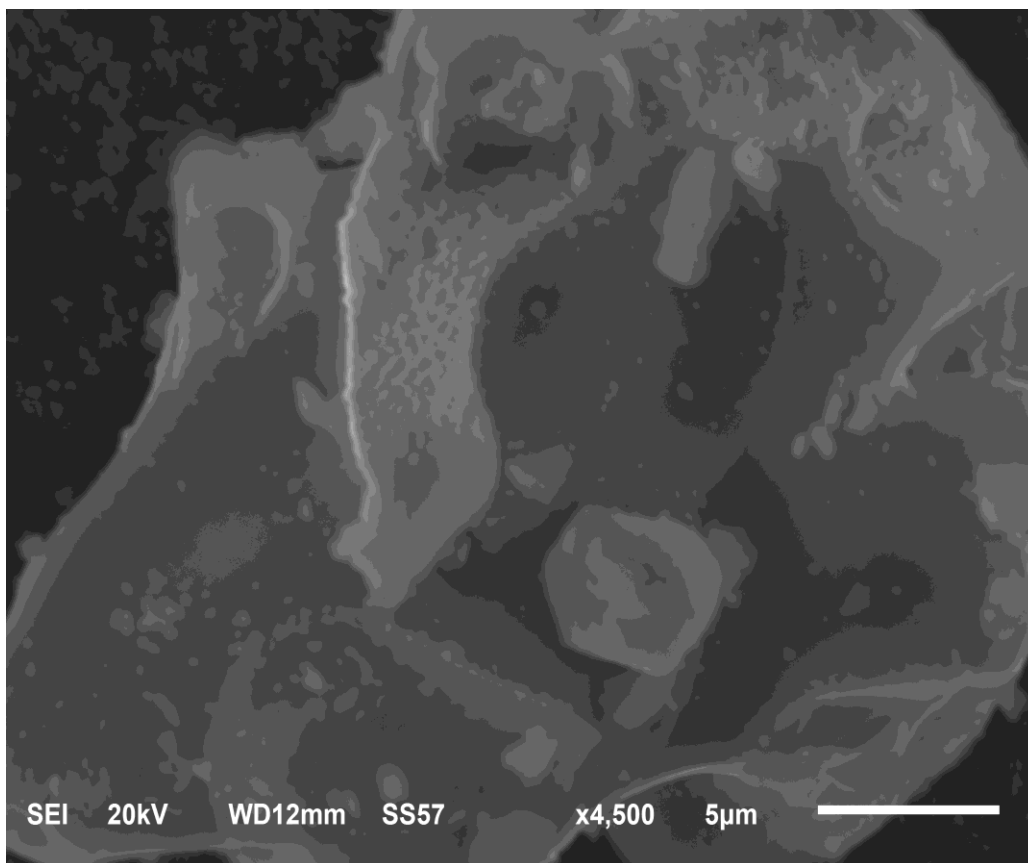


Figure 4.34: Le Bail analysis of nickel doped  $\beta$ - $\text{NaFeO}_2$ . (Reacted at 1000°C for 72 hours)

Indexing of the powder x-ray diffraction patterns from Figure 4.31 was also performed to identify any instance of nickel doping; however, Figure 4.34 has shown no linear dependence between the cell volume and the dopant amounts of nickel.<sup>310</sup> The SEM image of 2.5% doped nickel has been shown in Figure 4.35 with the reported particle sizes as large as tens of microns. The back scattered SEM image has been reported in Figure 4.36, and while it has shown some homogeneity, the two measured EDX spectra have shown different nickel contents. The two EDX measurements for labeled spectra 11 and 12 in Figure 4.36 have been reported in Figures 4.37 and 4.38 and Tables 4.5 and 4.6. They have both shown inconsistent amounts of nickel in the two samples. The second spectrum has shown no nickel content at all.



**Figure 4.35: SEM image of 2.5% nickel doped  $\beta$ -NaFeO<sub>2</sub>**

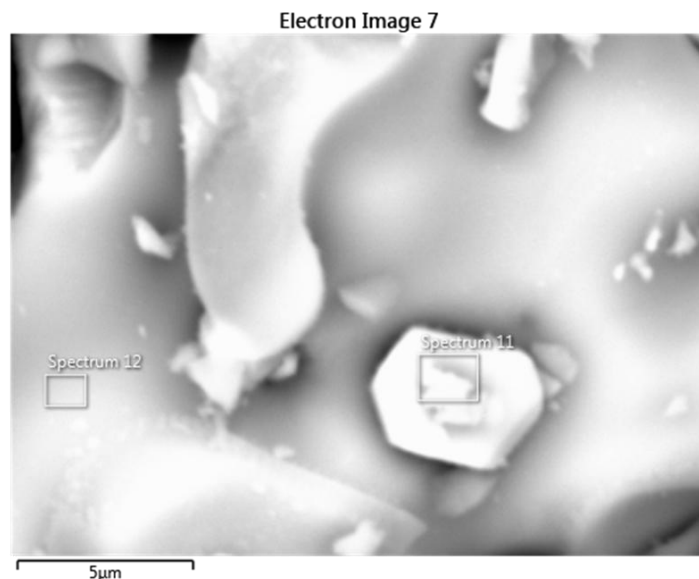


Figure 4.36: Back scatter SEM image of 2.5% nickel doped  $\beta$ -NaFeO<sub>2</sub> with EDX spectra at the designated selections.

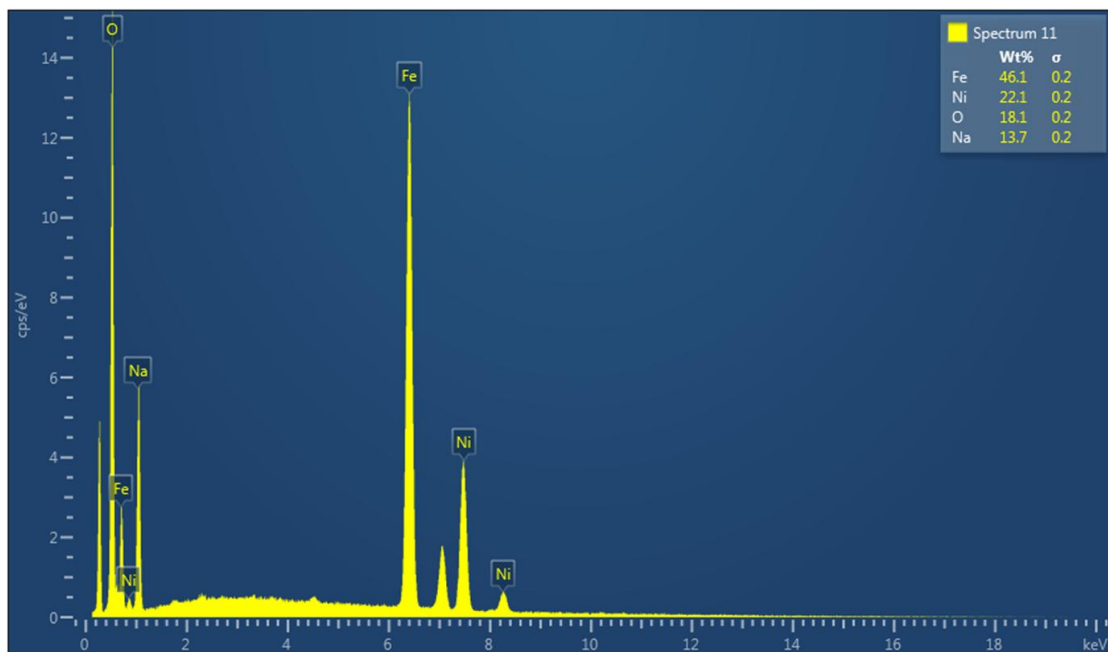


Figure 4.37: EDX spectrum from labeled spectrum 11 in Figure 4.36

Table 4.5: Counted weights and ratio from Figure 4.37

Element	Apparent Concentration	Weight percent
O	40.18	18.06
Na	8.30	13.69
Fe	63.92	46.13
Ni	27.92	22.12
Total:		100.00

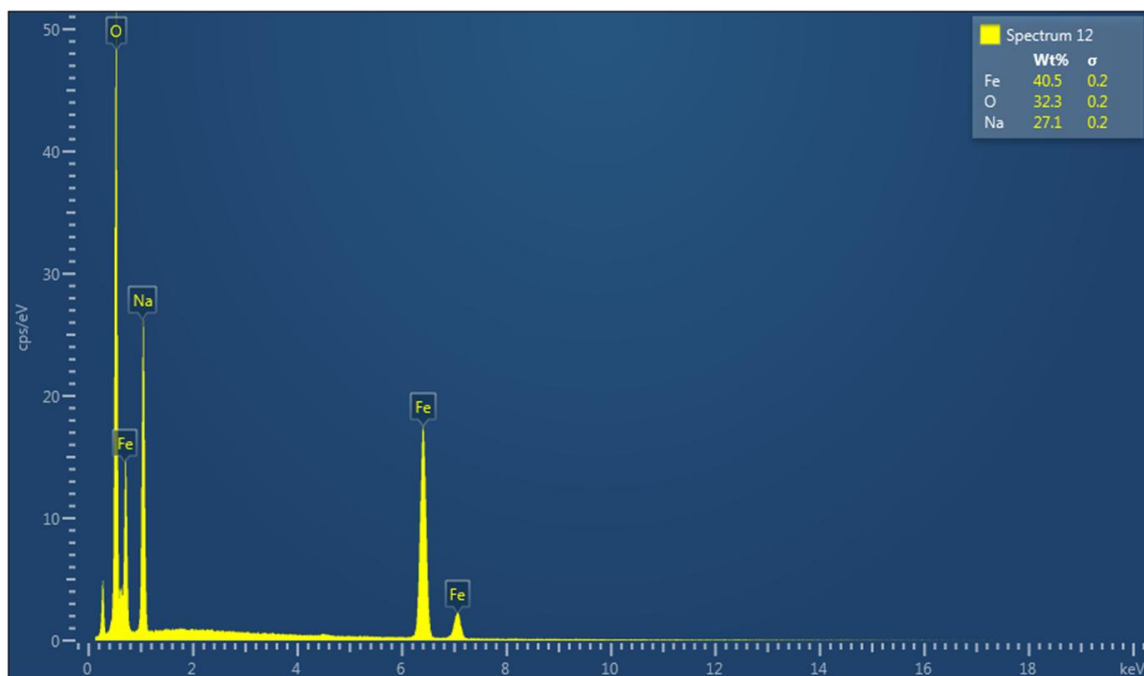
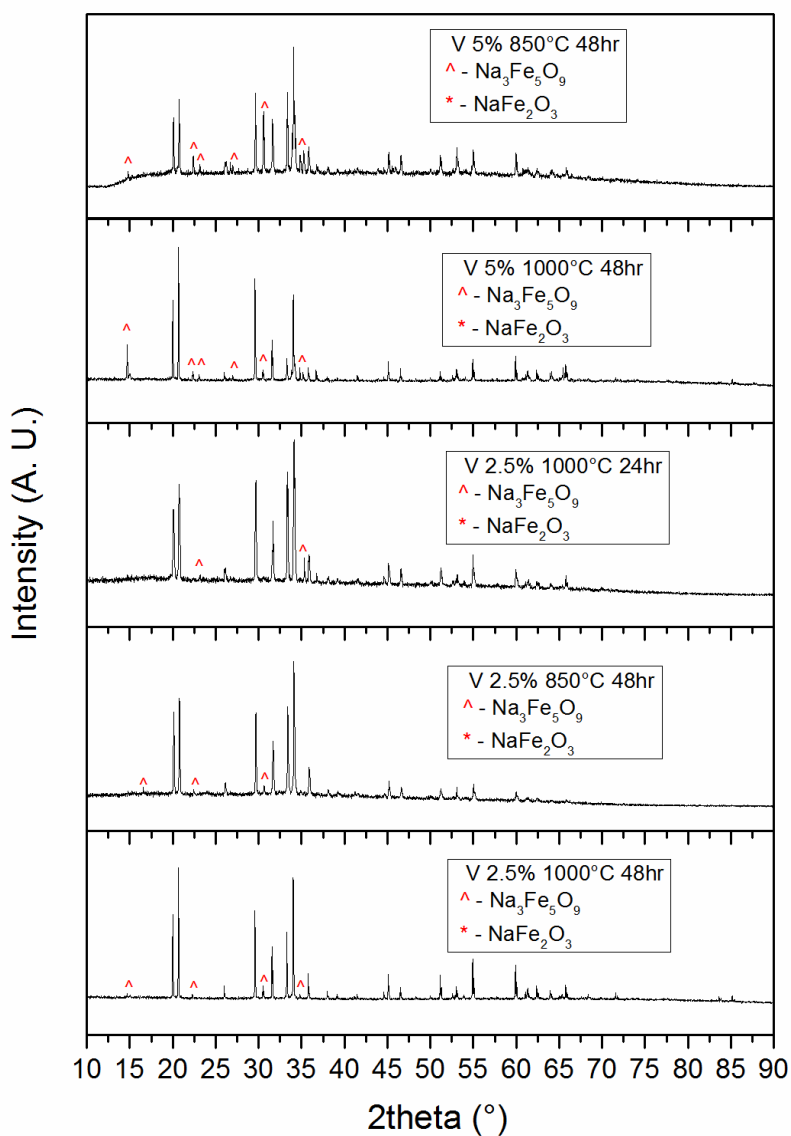


Figure 4.38: EDX spectrum from labeled spectrum 12 in Figure 4.36

Table 4.6: Counted weights and ratio from Figure 4.38

Element	Apparent concentration	Weight percent
O	78.49	32.33
Na	21.66	27.12
Fe	49.41	40.54
Total:		100.00

#### 4.4.3 Vanadium Doping



**Figure 4.39: Powder x-ray diffraction patterns of  $\beta\text{-NaFeO}_2$  doped with a variety of different vanadium compositions at a variety of different temperature profiles. (WL = 1.5418 Å)**

Vanadium was the final element attempted for the doping of  $\beta\text{-NaFeO}_2$  due to the ability of vanadium to access multiple redox couples and the spherical symmetry of the vanadium III ion, but it has not assimilated into the  $\beta\text{-NaFeO}_2$  structure similar to previous dopings.<sup>112</sup> The measured powder x-ray diffraction patterns have been plotted in Figure 4.39. In contrast to the other attempted dopants, vanadium doping has shown substantial side products at vanadium contents as low as 2.5%. From the



shown evidence in this section, the doping of the  $\beta$ -NaFeO<sub>2</sub> compound with chromium, nickel, and vanadium has been unsuccessful which has been most likely due to the size and shape of each transition metal ion. The ionic radii of each ion must have been too large for tetrahedral coordination and the non spherical shape of the nickel II ion would hinder tetrahedral coordination, as well.<sup>308</sup>

## **4.5 Bond Valance Analysis of $\beta$ -NaFeO<sub>2</sub>, T-LiFeO<sub>2</sub>, CF-LiTiFeO<sub>4</sub>, and CF-Li<sub>2</sub>TiFeO<sub>4</sub>**

### **4.5.1 Plotted Surfaces for the Bond Valance Analysis of $\beta$ -NaFeO<sub>2</sub>**

Bond valance sum has been a theory used to analyze coordination stability, but it has also been used to compare and analyze ionic conductivity in solid state materials.<sup>294,295,298,312</sup> In Figure 4.40, the surface of the sodium to oxygen bond valance sum for the  $\beta$ -NaFeO<sub>2</sub> structure has been calculated. The surface has shown minimal connection between the sodium coordination sites, thus the structure should have limited ionic conductivity in order to maintain a proper bond valance sum. The surface for the bond valance sum plotted in Figure 4.40 was expanded to a bond valance sum value of 1.1 instead of the ideal value of 1.0 for sodium. The surface for the bond valance mismatch analysis was also calculated and plotted in Figure 4.41. The mismatch surface has been plotted as the difference between the calculated bond valance sum and the ideal bond valance value of 1.0.<sup>295</sup> The ideal bond valance sum would represent the ideal valance charge for a specific element based on the equilibrium coordination sphere. Distorting the ideal bond length distorts the bond valance sum from the ideal value. Different elements have different thresholds depending on how much their bond valance sum can change and remain stable. The mismatch surface has been plotted to represent how much an ion can distort within a bond valance sum threshold. The value plotted in Figure 4.41 was plotted with a mismatch threshold of  $\pm 0.15$  which has shown where the sodium ion can move within a bond valance sum of  $1.0 \pm 0.15$ .<sup>294,295,312</sup>

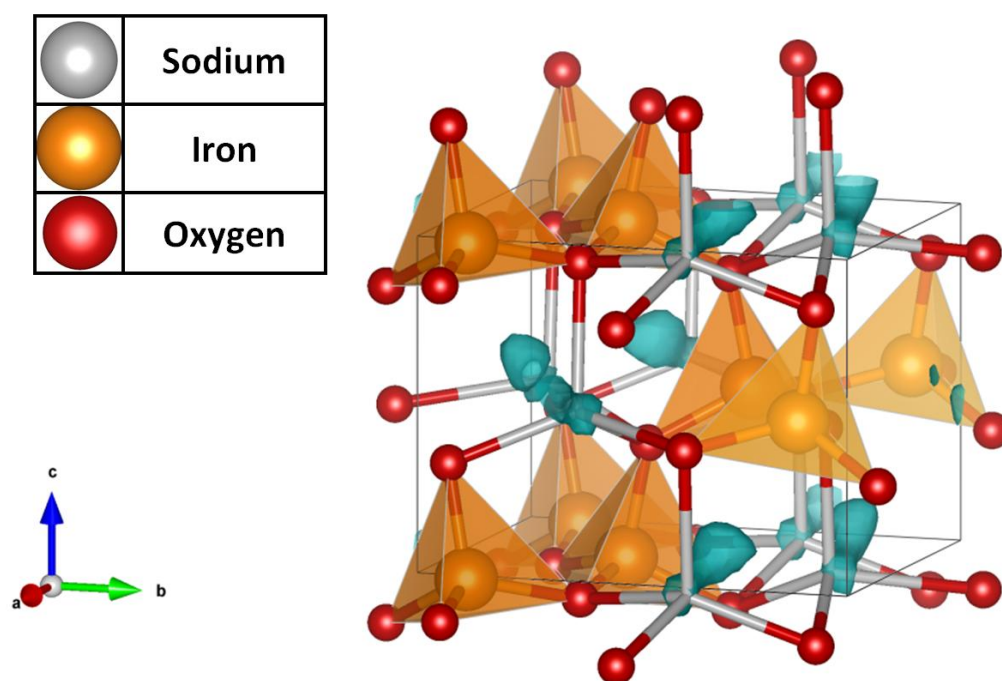


Figure 4.40: Surface of the bond valence sum analysis for sodium-oxygen bonds in  $\beta$ -NaFeO<sub>2</sub>. The surface is plotted for a bond valence sum value of 1.1.

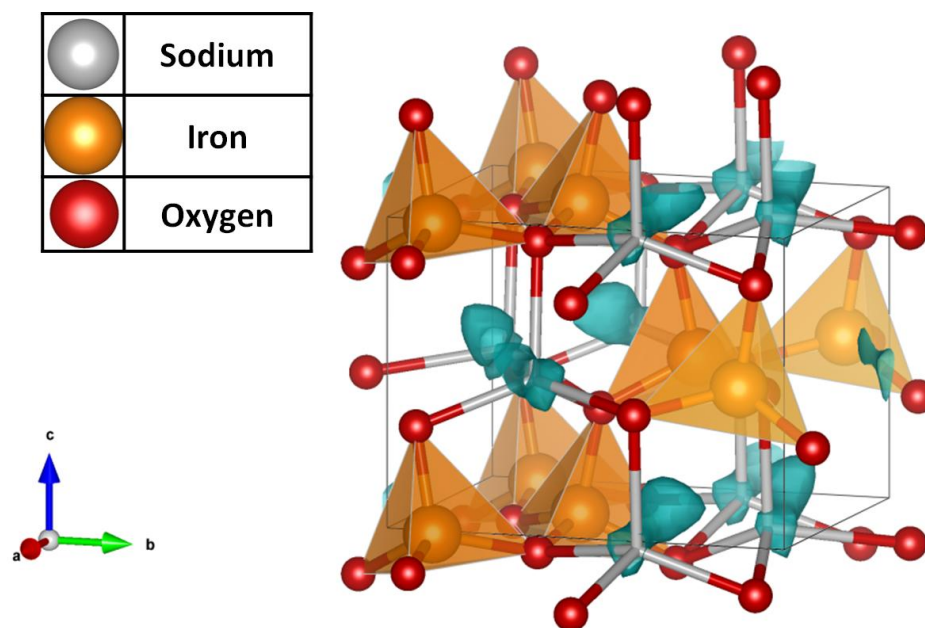
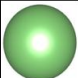
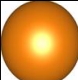
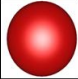


Figure 4.41: Surface of the bond valence mismatch analysis for sodium-oxygen bonds in  $\beta$ -NaFeO<sub>2</sub>. The surface is plotted for a bond valence surface mismatch threshold of  $\pm 0.15$ .

#### 4.5.2 Plotted Surfaces for the Bond Valance Analysis of T-LiFeO<sub>2</sub>

In comparing the surfaces of the bond valance sum analysis of T-LiFeO<sub>2</sub> and  $\beta$ -NaFeO<sub>2</sub>, the surface for the bond valance sum of T-LiFeO<sub>2</sub> has shown significantly more connectivity compared to the surface of  $\beta$ -NaFeO<sub>2</sub>. The surface bond valance sum of T-LiFeO<sub>2</sub> has been plotted in Figure 4.42 for a bond valance sum value of 1.1. The high connectivity of the surface of the bond valance sum should mean the T-LiFeO<sub>2</sub> structure should have a better ionic conductivity in comparison to the  $\beta$ -NaFeO<sub>2</sub> structure. Decent ionic conductivity of T-LiFeO<sub>2</sub> would rely on the distortion of the bond valance sum to a value of 1.1 to be chemically stable. The surface of the bond valance mismatch analysis for T-LiFeO<sub>2</sub> has been plotted in Figure 4.43 with a mismatch threshold of  $\pm 0.15$ . The bond valance mismatch surface of the T-LiFeO<sub>2</sub> structure has shown high connectivity which would suggest high ionic conductivity, as well. Distortions of the bond valance sum to values of 1.1 or 1.15 can be unstable for many elements, but for the case of lithium, it has shown to be stable at higher values of the bond valance sum compared to other elements.<sup>295</sup> The T-LiFeO<sub>2</sub> compound should have decent ionic conductivity. The electrochemical cyclability of T-LiFeO<sub>2</sub> has shown to be reversible for the iron II/III redox couple but not the iron III/IV redox couple. Theoretical analysis of the ionic conductivity of T-LiFeO<sub>2</sub> has suggested dependent of the electronic states for the electrochemical instability of the iron III/IV redox couple.

	Lithium
	Iron
	Oxygen

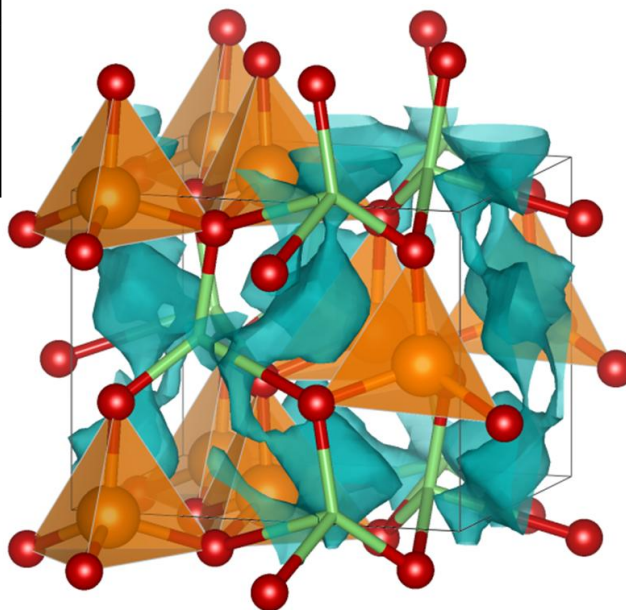
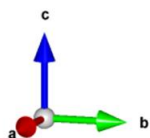
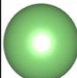
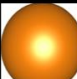
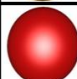


Figure 4.42: Surface of the bond valence sum analysis for lithium-oxygen bonds in T-LiFeO<sub>2</sub>. The surface was plotted for a bond valence sum value of 1.1.

	Lithium
	Iron
	Oxygen

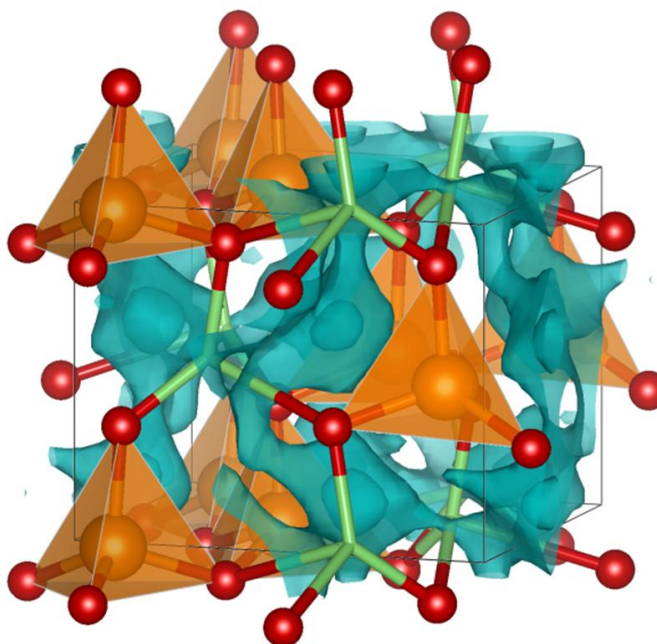
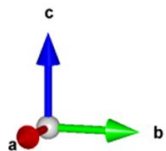


Figure 4.43: Surface of the bond valence mismatch analysis for lithium-oxygen bonds in T-LiFeO<sub>2</sub>. The surface is plotted for a bond valence mismatch threshold of  $\pm 0.15$ .

#### 4.5.3 Plotted Surfaces for the Bond Valance Analysis of CF-LiFeTiO<sub>4</sub>

The compounds of Li<sub>2</sub>FeTiO<sub>4</sub> and LiFeTiO<sub>4</sub> have shown comparable electrochemical functionality in comparison to T-LiFeO<sub>2</sub>. The two materials, CF-Li<sub>2</sub>FeTiO<sub>4</sub> and CF-LiFeTiO<sub>4</sub>, have cycled efficiently well between the CF-Li<sub>2</sub>FeTiO<sub>4</sub> structure containing iron II and the CF-LiFeTiO<sub>4</sub> structure containing iron III. The iron II/III redox couple for this set of compounds has cycled at a voltage of about 2.0 V for 20 cycles at a high charge/discharge rate.<sup>296</sup> However, when the electrochemical oxidation of the CF-LiFeTiO<sub>4</sub> compound has been attempted in order to access the iron IV state, the materials has cycled poorly between the supposed FeTiO<sub>4</sub> structure and the CF-LiFeTiO<sub>4</sub> structure. Attempting to probe the iron III/IV redox couple would not be electrochemically impossible, but it has typically been difficult to do in many iron oxide type materials. In many cases the iron II states have been available at the Fermi energy just above the oxygen p-states. In the case of the iron III/IV redox couple, the increases positive charge of the iron ion with less electron shielding has lowered the iron IV and III states below oxygen p-states. Thus, attempted electrochemical cycling of the iron III/IV redox couple would be inaccessible and the material would be inherently unsafe due to the formation of peroxides.<sup>9,51,313,314</sup> However, the electronic valance states for the CF-Li<sub>2</sub>FeTiO<sub>4</sub> and CF-LiFeTiO<sub>4</sub> structures have yet to be properly analyzed yet.

The surface of the bond valance sum of CF-LiFeTiO<sub>4</sub> with the optimized value of 1.0 has been shown to have high connectivity between each unit cell in Figure 4.44. The surface of the bond valance mismatch analysis of CF-LiFeTiO<sub>4</sub> was plotted with a mismatch threshold of  $\pm 0.05$  in Figure 4.45. The bond valance mismatch surface has shown high surface connectivity, as well. Due to the small mismatch threshold required to connect the bond valance mismatch surface, the material should have extremely high ionic conduction. Experimentally, this has been supported by the facile electrochemical cycling between the CF-Li<sub>2</sub>FeTiO<sub>4</sub> and CF-LiFeTiO<sub>4</sub> compounds.<sup>296</sup> Even with the low voltage available between the CF-Li<sub>2</sub>FeTiO<sub>4</sub> and CF-LiFeTiO<sub>4</sub> structure, ionic conductivity and cyclability has made it a high contender for load leveling grid storage technology.<sup>2</sup>

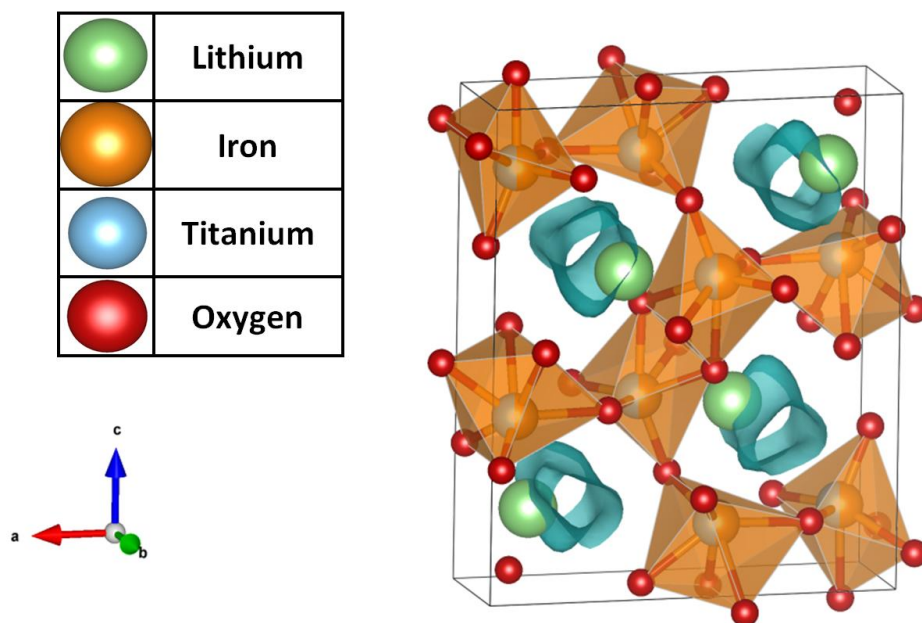


Figure 4.44: Surface of the bond valence sum analysis of lithium-oxygen bonds in CF-LiFeTiO<sub>4</sub>. The surface is plotted for a bond valence sum value of 1.0.

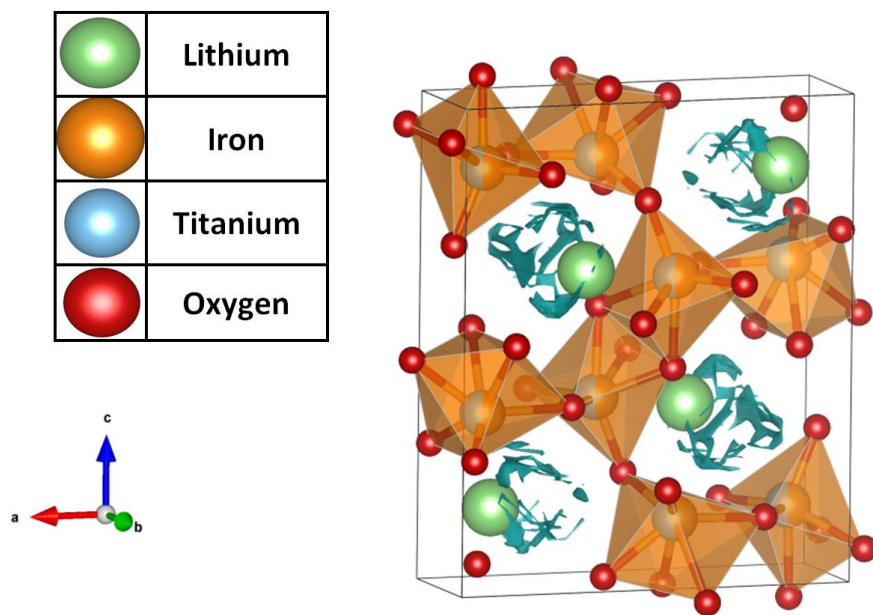
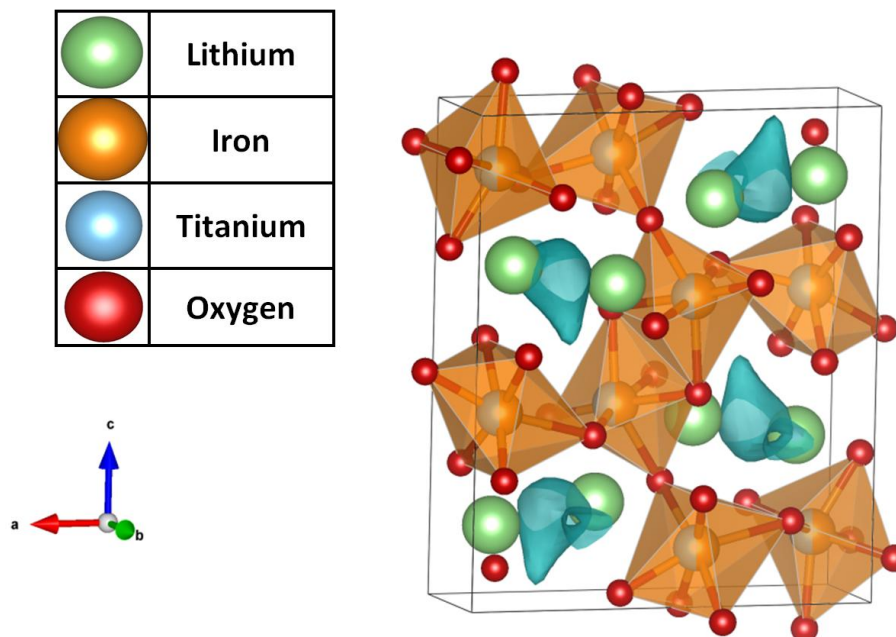


Figure 4.45: Surface of the bond valence mismatch analysis for lithium-oxygen bonds in CF-LiFeTiO<sub>4</sub>. The surface is plotted for mismatch threshold of  $\pm 0.05$ .

#### 4.5.4 Plotted Surfaces of the Bond Valence Analysis of CF-Li<sub>2</sub>FeTiO<sub>4</sub>



**Figure 4.46: Surface of the bond valence sum analysis for lithium-oxygen bonds in CF-Li<sub>2</sub>FeTiO<sub>4</sub>. The surface was plotted for a bond valence sum value of 1.0.**

The Figure 4.46 shows the bond valence sum of the CF-Li<sub>2</sub>FeTiO<sub>4</sub> structure with the preferred value of 1.0, and the Figure 4.47 shows the bond valence mismatch with a bond valence mismatch value of  $\pm 0.05$ . Both support the high ionic conductivity as it has been with the CF-LiFeTiO<sub>4</sub> structure. The surfaces connect between each unit cell even with such a small mismatch threshold. The structure only has one dimensional diffusivity, but the channels have been highly conductive. Much of the conclusions about CF-LiFeTiO<sub>4</sub> can be made about CF-Li<sub>2</sub>FeTiO<sub>4</sub>.



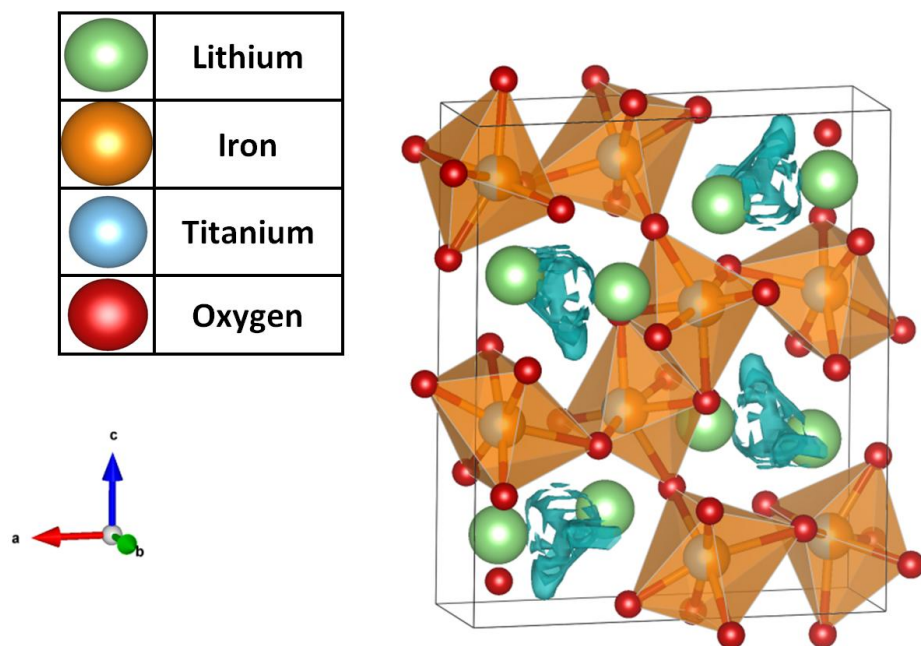


**Figure 4.47:** Surface of the bond valance mismatch analysis for lithium-oxygen bonds in  $\text{CF-Li}_2\text{FeTiO}_4$ . The surface was plotted for a mismatch threshold of  $\pm 0.05$ .



## 4.6 Computational Investigation of the T-Li<sub>x</sub>FeO<sub>2</sub> System as a Multi-Redox Lithium-ion Battery

### 4.6.1 Dependence of Lithium Ion Position in the T-Li<sub>x</sub>FeO<sub>2</sub> Structures.

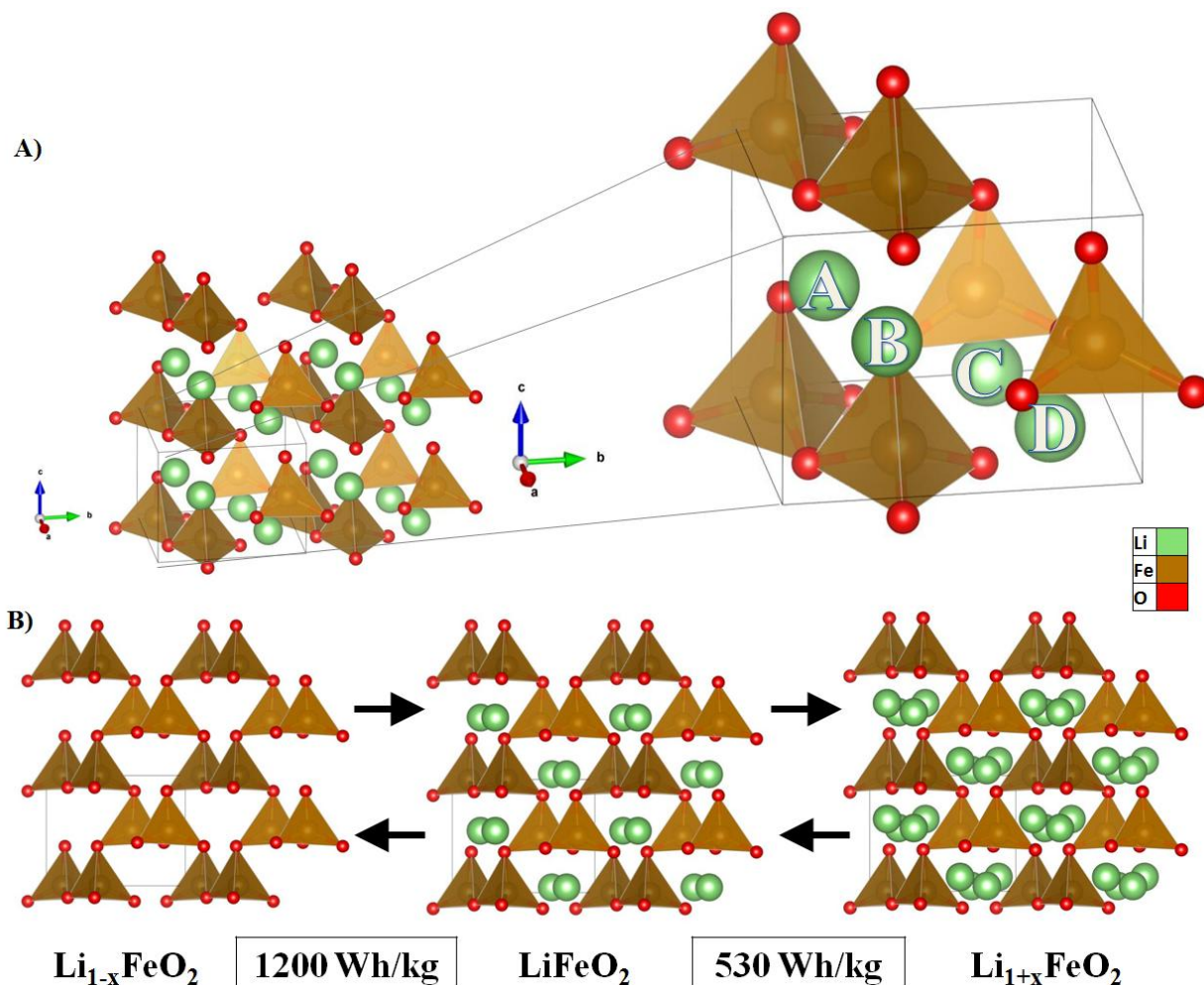


**Figure 4.48: General crystal structures of T-Li<sub>x</sub>FeO<sub>2</sub>. A) Denotes the lithium ion arrangement of the T-Li<sub>0.5</sub>FeO<sub>2</sub> structures calculated in Table 4.7 and the size of the cells used in the calculations B) General scheme of T-Li<sub>x</sub>FeO<sub>2</sub> electrochemical cycling.**

Because of the lack of electrochemical access of the iron III/IV redox couple, it has become important to explore the electronic structures of the T-Li<sub>0.5<x<1.5</sub>FeO<sub>2</sub> crystal structures with density functional theory. The density functional analysis would begin with exploring how lithium ion vacancies and added lithium ions would affect the energy and atomic structure of the experimental T-LiFeO<sub>2</sub> structure. The T-Li<sub>0.5</sub>FeO<sub>2</sub>, T-LiFeO<sub>2</sub>, and T-Li<sub>1.5</sub>FeO<sub>2</sub> structures were relaxed with the relative energies

shown Table 4.7. Figure 4.48 part A relates to lithium ion positions that have been used in the computation unit cell for the T-  $\text{Li}_{0.5}\text{FeO}_2$  structures with the energies reported in Table 4.7. For example, the values associated with the T- $\text{Li}_{0.5}\text{FeO}_2$  (BD, AC) label have been associated with the relaxation energies for lithium ion locations at position B and D or A and C by visible symmetry. Section B of Figure 4.48 has highlighted the large channels in the T- $\text{Li}_{0<x<2}\text{FeO}_2$  structures and the full amount of energy density that could potentially be realized. In each T- $\text{LiFeO}_2$  unit cell, it has 4 lithium atoms, 4 iron atoms, and 8 oxygen atoms. It also has two channels with 2 lithium atoms per channel in each unit cell. One channel has been located in the top left portion of the cell, while the other channel has been located on the bottom right. It has been shown in Table 4.7 for the T- $\text{Li}_{0.5}\text{FeO}_2$  structure that lithium ion positions placed in different channels but not staggered was the lowest calculated energy structure. The T- $\text{Li}_{0.5}\text{FeO}_2$  structure with the lithium ions in the same channel had a higher energy. Lithium ion positions that had been placed in different channels and were staggered between channels caused the spin state of the iron centers to become low spin. This configuration had raised the energy significantly due to iron centers being in an unexpected high spin state.

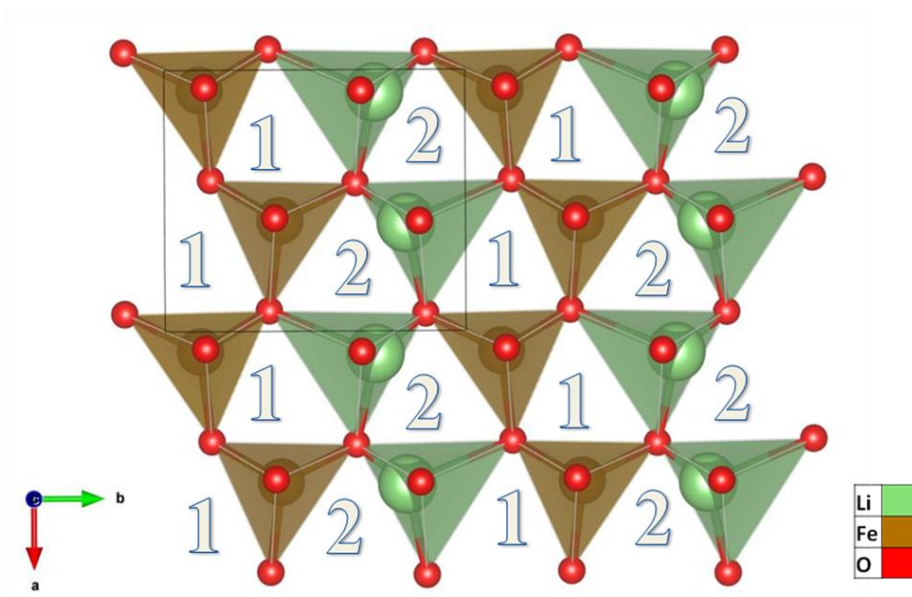


**Figure 4.49: Different arrangements of the added lithium-ions in the T- $\text{Li}_2\text{FeO}_2$  structures reported in Table 4.7. The unit cell is highlighted with the black outline**

Figure 4.49 has shown the location of the added lithium ions in each layer in the T-Li<sub>1.5</sub>FeO<sub>2</sub> (and T-Li<sub>2</sub>FeO<sub>2</sub>) structures before relaxation, with the calculated relaxation energies reported in Table 4.7. Placement of the added lithium ions has been located in the octahedral positions adjacent to the normal tetrahedral positions. Position 1 has been attributed to the lithium ions that have been primarily adjacent to tetrahedral iron positions and position 2 has been attributed to lithium ions that have been primarily adjacent to tetrahedral lithium positions. A comparison of these two general position was performed with a pair of relaxations for each of the T-Li<sub>2</sub>FeO<sub>2</sub> structures. Not surprisingly, The added lithium ions adjacent to tetrahedral iron positions were reported to be higher in energy by 167 meV per unit cell. From the relaxations comparing the added lithium ions in the T-Li<sub>2</sub>FeO<sub>2</sub> structures, different T-Li<sub>1.5</sub>FeO<sub>2</sub> structures were constructed with the added lithium ions adjacent to the tetrahedral lithium positions. The lithium ion positions in T-Li<sub>1.5</sub>FeO<sub>2</sub> were relaxed under the assumption that the added lithium ions should be in different lithium ion channels, thus there should be three lithium ions in each channel of the unit cell. A comparison of the relaxation energies of the added lithium ions in the T-Li<sub>2</sub>FeO<sub>2</sub> and T-Li<sub>1.5</sub>FeO<sub>2</sub> structures have been reported in Table 4.7. The two T-Li<sub>1.5</sub>FeO<sub>2</sub> structures were similar in energy. The structure with the added lithium ions adjacent within each channel has shown to be the lowest in energy.

**Table 4.7: PBE96 Calculated energies and magnetic moment of T-Li<sub>x</sub>FeO<sub>2</sub> type structures calculated with PBE. Structures are described by Figure 4.48 and Figure 4.49. Li<sub>1.5</sub>FeO<sub>2</sub> structures were based on structure 2 of Li<sub>2</sub>FeO<sub>2</sub>. Bolded structures were chosen for further analysis.**

Structure	Relative Energy (eV)	Iron 1 ( $\mu_B$ )	Iron 2 ( $\mu_B$ )	Iron 3 ( $\mu_B$ )	Iron 4 ( $\mu_B$ )
T-Li <sub>0.5</sub> FeO <sub>2</sub> (AB,CD)	21.861411	2.924	-3.288	2.927	-3.289
<b>T-Li<sub>0.5</sub>FeO<sub>2</sub>(BD,AC)</b>	21.845285	2.889	2.906	-3.298	-3.304
T-Li <sub>0.5</sub> FeO <sub>2</sub> (BC,AD)	22.804690	-0.047	-0.039	0.048	0.035
<b>T-LiFeO<sub>2</sub></b>	12.305286	3.948	3.948	3.948	3.948
<b>T-Li<sub>1.5</sub>FeO<sub>2</sub>(adjacent, 2)</b>	6.135727	3.749	3.749	3.703	3.703
T-Li <sub>1.5</sub> FeO <sub>2</sub> (staggered, 2)	6.136176	3.699	3.698	3.753	3.752
T-Li <sub>2</sub> FeO <sub>2</sub> (2)	0.000000	3.438	3.446	3.443	3.450
T-Li <sub>2</sub> FeO <sub>2</sub> (1)	0.167105	3.448	3.444	3.445	3.449

Much of the lowest energy structures were expected as they separated the cation charges apart from each other with few exceptions. These structures have been used for further calculations including open cell voltage (OCV) and the density of states. The structures used from Table 4.7 were The  $\text{T-Li}_{0.5}\text{FeO}_2$ (BD,AC),  $\text{T-LiFeO}_2$ ,  $\text{T-Li}_{1.5}\text{FeO}_2$ (adjacent,2) structures. For posterity, they have been referred to as  $\text{T-Li}_{0.5}\text{FeO}_2$ ,  $\text{T-LiFeO}_2$ , and  $\text{T-Li}_{1.5}\text{FeO}_2$  in further sections.

#### 4.6.2 Calculated Electrochemical Potentials

**Table 4.8: Absolute unit cell energies for the  $\text{T-Li}_{0.5}\text{FeO}_2$ ,  $\text{T-LiFeO}_2$ ,  $\text{T-Li}_{1.5}\text{FeO}_2$  structures for the PBE96+U and HSE06 functionals**

	Ferromagnetic structures					C-type antiferromagnetic structures	
	Relaxed with PBE96		Relaxed with PBE96+U		Relaxed with PBE96	Relaxed with PBE96+U	
Structure	Energy (eV) calculated with PBE96+U for a $U_{\text{eff}}$ of 4.0 eV	Energy (eV) calculated with PBE96+U for a $U_{\text{eff}}$ of 6.0 eV	Energy (eV) calculated with PBE96+U for a $U_{\text{eff}}$ of 4.0 eV	Energy (eV) calculated with PBE96+U for a $U_{\text{eff}}$ of 6.0 eV	Energy (eV) calculated with HSE06	Energy (eV) calculated with PBE96+U for a $U_{\text{eff}}$ of 4.0 eV	Energy (eV) calculated with PBE96+U for a $U_{\text{eff}}$ of 6.0 eV
$\text{T-Li}_{0.5}\text{FeO}_2$	-86.1182	-82.7516	-86.2863	-83.0213	-139.305	-86.2862	-83.0200
$\text{T-LiFeO}_2$	-98.5348	-95.9916	-98.5374	-96.0089	-153.346	-99.1249	-96.4161
$\text{T-Li}_{1.5}\text{FeO}_2$	-104.314	-101.623	-105.068	-102.575	-158.910	-105.2420	-102.9950

The single point energies of the  $\text{T-Li}_{0.5}\text{FeO}_2$ ,  $\text{T-LiFeO}_2$ ,  $\text{T-Li}_{1.5}\text{FeO}_2$  structures were calculated with the PBE96+U functional with a corrective Hubbard  $U_{\text{eff}}$  value of 4.0 eV or 6.0 eV and with the HSE06 functional.<sup>187–189</sup> The single point energies were calculated after being relaxed with the PBE96 and PBE96+U functional with their respective  $U_{\text{eff}}$  value. Other C-type antiferromagnetic  $\text{T-Li}_{0.5}\text{FeO}_2$ ,  $\text{T-LiFeO}_2$ ,  $\text{T-Li}_{1.5}\text{FeO}_2$  structures were relaxed with the PBE96 functional and then the PBE96+U functional with a Hubbard  $U_{\text{eff}}$  value of 4.0 eV or 6.0 eV. The energies have been reported in Table 4.8. The calculated open cell potentials have been listed in Table 4.9. It is important to mention that the  $\text{T-Li}_{0.5}\text{FeO}_2$  structures would relax to a C-type antiferromagnetic structure regardless of the starting magnetic arrangement. The C-type antiferromagnetic structures have shown to be the more stable arrangement in comparison of the ferromagnetic structures. The differences in energies between ferromagnetic and C-type antiferromagnetic structures have been displayed to be as high as 600 meV for the  $\text{T-LiFeO}_2$  structure. Because the  $\text{T-Li}_{0.5}\text{FeO}_2$  structures have relaxed to a C-type antiferromagnetic state regardless of starting magnetic structure, they have under predicted the open cell voltages calculated for the iron

III/IV redox couple for the ferromagnetic based structures. Many of the values calculated for the iron III/IV open cell potentials have been calculated higher than the measured oxidation value of 4.4 V. The reduction potential for the iron III/IV redox couple has not been experimentally measured. The open cell potentials for the iron III/IV redox couple were reported high, but the open cell potentials calculated by the HSE06 functional have been calculated too high for the iron III/IV redox couple and too low for the iron II/III redox couple in comparison to the experimental value of 1.8 V.<sup>157</sup> Although the HSE06 functional has been higher on the “Jacob’s ladder” of DFT, it has performed worse than PBE96+U in this case.<sup>149</sup> The open cell potentials calculated with the PBE96+U functional for the iron II/III redox couple have been lower than the experimental values, but they were better than the values calculated by the HSE06 functional. The open cell potential calculated from the C-type antiferromagnetic structures with the PBE96+U functional for a  $U_{\text{eff}}$  value of 4.0 eV for the iron III/IV redox couple has shown the most promise. It has not been artificially lowered due to  $\text{T-Li}_{0.5}\text{FeO}_2$  having an antiferromagnetic structure and  $\text{T-LiFeO}_2$  having a ferromagnetic structure. Alternatively, the open cell potential calculated from the C-type antiferromagnetic structure with the PBE96+U functional for a  $U_{\text{eff}}$  of 6.0 eV for the iron II/III redox couple has shown the best agreement with experiment. It could have been artificially increased because of the higher  $U_{\text{eff}}$  value. Typically a  $U_{\text{eff}}$  value of 4.0 eV has been attributed to the iron III and iron II states while a  $U_{\text{eff}}$  value of 6.0 eV has been attributed to calculations performed for the iron IV states.<sup>56,315,316</sup> Discussion of the different effective Hubbard  $U_{\text{eff}}$  values for the  $\text{T-Li}_x\text{FeO}_2$  have been discussed in a later section.

**Table 4.9: Calculated open cell voltages with respect to lithium for the PBE96+U and HSE06 functionals**

PBE96 Relaxed Structures			Calculated Potential (V)	PBE96+U Relaxed Structures			Calculated Potential (V)
Ferromagnetic structure with a $U_{\text{eff}} = 4 \text{ eV}$				Ferromagnetic structure with a $U_{\text{eff}} = 4.0 \text{ eV}$			
T-Li <sub>0.5</sub> FeO <sub>2</sub>	→	T-LiFeO <sub>2</sub>	4.315979	T-Li <sub>0.5</sub> FeO <sub>2</sub>	→	T-LiFeO <sub>2</sub>	4.23324
T-LiFeO <sub>2</sub>	→	T-Li <sub>1.5</sub> FeO <sub>2</sub>	0.997476	T-LiFeO <sub>2</sub>	→	T-Li <sub>1.5</sub> FeO <sub>2</sub>	1.37308
Ferromagnetic structure with $U_{\text{eff}} = 6 \text{ eV}$				Ferromagnetic structure with $U_{\text{eff}} = 6.0 \text{ eV}$			
T-Li <sub>0.5</sub> FeO <sub>2</sub>	→	T-LiFeO <sub>2</sub>	4.727684	T-Li <sub>0.5</sub> FeO <sub>2</sub>	→	T-LiFeO <sub>2</sub>	4.60148
T-LiFeO <sub>2</sub>	→	T-Li <sub>1.5</sub> FeO <sub>2</sub>	0.923191	T-LiFeO <sub>2</sub>	→	T-Li <sub>1.5</sub> FeO <sub>2</sub>	1.39093
Ferromagnetic structure with a Hybrid Functional (HSE06)				Antiferromagnetic structure with a $U_{\text{eff}} = 4.0 \text{ eV}$			
T-Li <sub>0.5</sub> FeO <sub>2</sub>	→	T-LiFeO <sub>2</sub>	5.128294	T-Li <sub>0.5</sub> FeO <sub>2</sub>	→	T-LiFeO <sub>2</sub>	4.52707
T-LiFeO <sub>2</sub>	→	T-Li <sub>1.5</sub> FeO <sub>2</sub>	0.889582	T-LiFeO <sub>2</sub>	→	T-Li <sub>1.5</sub> FeO <sub>2</sub>	1.16640
Experimental values				Antiferromagnetic structure with a $U_{\text{eff}} = 6.0 \text{ eV}$			
T-Li <sub>0.5</sub> FeO <sub>2</sub>	→	T-LiFeO <sub>2</sub>	4.4	T-Li <sub>0.5</sub> FeO <sub>2</sub>	→	T-LiFeO <sub>2</sub>	4.80573
T-LiFeO <sub>2</sub>	→	T-Li <sub>1.5</sub> FeO <sub>2</sub>	1.8	T-LiFeO <sub>2</sub>	→	T-Li <sub>1.5</sub> FeO <sub>2</sub>	1.39736

#### 4.6.3 Calculated Structural Parameters

**Table 4.10: Calculated cell parameters and volumes for the T-Li<sub>x</sub>FeO<sub>2</sub> structures calculated at various levels of theory. (FM = Ferromagnetic, AFM = antiferromagnetic)**

		a (Å)	b (Å)	c (Å)	alpha (°)	beta (°)	gamma (°)	Volume (Å <sup>3</sup> )
PBE FM	T-Li <sub>0.5</sub> FeO <sub>2</sub>	5.45333	6.5859	5.25485	90.0131	89.9678	90.5817	188.718500
	T-LiFeO <sub>2</sub>	5.56425	6.49495	5.09297	90.0000	90.0000	89.9745	184.057400
	T-Li <sub>1.5</sub> FeO <sub>2</sub>	5.47775	6.61646	5.14677	89.9993	89.9980	87.9277	186.414100
	T-Li <sub>0.5</sub> FeO <sub>2</sub> (low spin)	5.35386	6.41809	5.01066	89.8615	90.0015	90.0003	172.173300
PBE96+U, $U_{\text{eff}} = 4.0 \text{ eV}$ FM	T-Li <sub>0.5</sub> FeO <sub>2</sub>	5.59713	6.60935	5.22946	90.0084	89.9837	90.4850	193.448441
	T-LiFeO <sub>2</sub>	5.55930	6.48552	5.08267	90.0000	90.0000	90.0026	183.255673
	T-Li <sub>1.5</sub> FeO <sub>2</sub>	5.62398	6.28846	5.61542	90.0084	89.9982	91.0504	198.562712
PBE96+U $U_{\text{eff}} = 6.0 \text{ eV}$ FM	T-Li <sub>0.5</sub> FeO <sub>2</sub>	5.63986	6.59462	5.24058	90.0001	89.9960	90.5443	194.902277
	T-LiFeO <sub>2</sub>	5.57854	6.48628	5.06862	90.0000	90.0000	89.9826	183.402859
	T-Li <sub>1.5</sub> FeO <sub>2</sub>	5.64019	6.4072	5.47131	90.0090	90.0006	92.6401	197.511382
PBE96 AFM	T-Li <sub>0.5</sub> FeO <sub>2</sub>	5.46598	6.57757	5.26798	90.0042	90.0058	90.5890	189.388686
	T-LiFeO <sub>2</sub>	5.48485	6.44229	5.11634	90.0034	89.9959	89.9974	180.785920
	T-Li <sub>1.5</sub> FeO <sub>2</sub>	5.68499	6.42914	5.12885	89.8893	90.0379	89.0868	187.433208
PBE96+U, $U_{\text{eff}} = 4.0 \text{ eV}$ AFM	T-Li <sub>0.5</sub> FeO <sub>2</sub>	5.59419	6.61172	5.24732	89.9996	90.0001	90.3809	194.079792
	T-LiFeO <sub>2</sub>	5.54500	6.47434	5.08088	90.0002	89.9999	90.0013	182.404657
	T-Li <sub>1.5</sub> FeO <sub>2</sub>	5.70296	6.21856	5.56481	91.2789	90.5804	91.5672	197.217060
PBE96+U, $U_{\text{eff}} = 6.0 \text{ eV}$ AFM	T-Li <sub>0.5</sub> FeO <sub>2</sub>	5.64443	6.60314	5.24622	89.9991	90.0031	90.3282	195.528623
	T-LiFeO <sub>2</sub>	5.54902	6.47285	5.08223	90.0003	89.9995	89.9988	182.543405
	T-Li <sub>1.5</sub> FeO <sub>2</sub>	5.71693	6.22533	5.57168	88.6314	89.4712	91.5360	198.157065
Experiment <sup>157</sup>	T-Li <sub>1.57</sub> FeO <sub>2</sub>	5.52	6.39	5.11	90	90	90	180.5
	T-LiFeO <sub>2</sub>	5.49	6.42	5.06	90	90	90	178.11
	T-Li <sub>0.88</sub> FeO <sub>2</sub>	5.48	6.38	5.04	90	90	90	175.88
	T-Li <sub>0.42</sub> FeO <sub>2</sub>	5.46	6.39	5.02	90	90	90	175.16

The cell parameter and volumes of the  $\text{T-Li}_{0.5}\text{FeO}_2$ ,  $\text{T-LiFeO}_2$ , and  $\text{T-Li}_{1.5}\text{FeO}_2$  structures relaxed at various levels of DFT have been reported in Table 4.10. Cell parameters for experimentally relevant compounds also have also been reported in Table 4.10. The experimental structures have an orthorhombic unit cell; however, the structures relaxed with VASP have not maintained the orthorhombic cell explicitly. However, the angles in the relaxed unit cells have not deviated too much from the orthorhombic value of  $90^\circ$ , thus the  $a$ ,  $b$ , and  $c$  parameters of the relaxed unit cells have been compared to the experimental lattice parameters. The volumes of the calculated and experimental unit cells have been plotted in Figure 4.50. A comparison of the  $a$ ,  $b$ , and  $c$  parameters have been plotted in Figures 4.51, 4.52, 4.53, respectively.

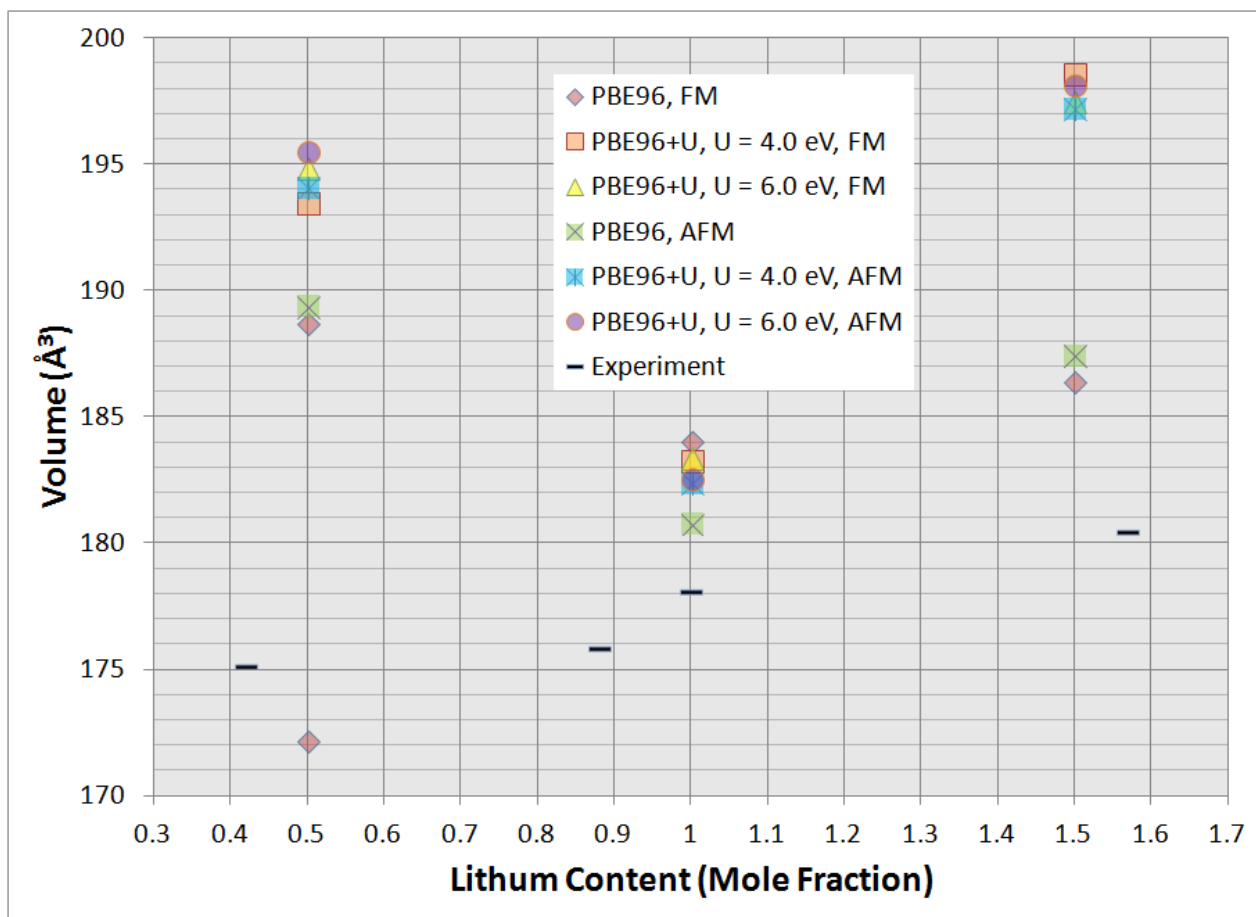
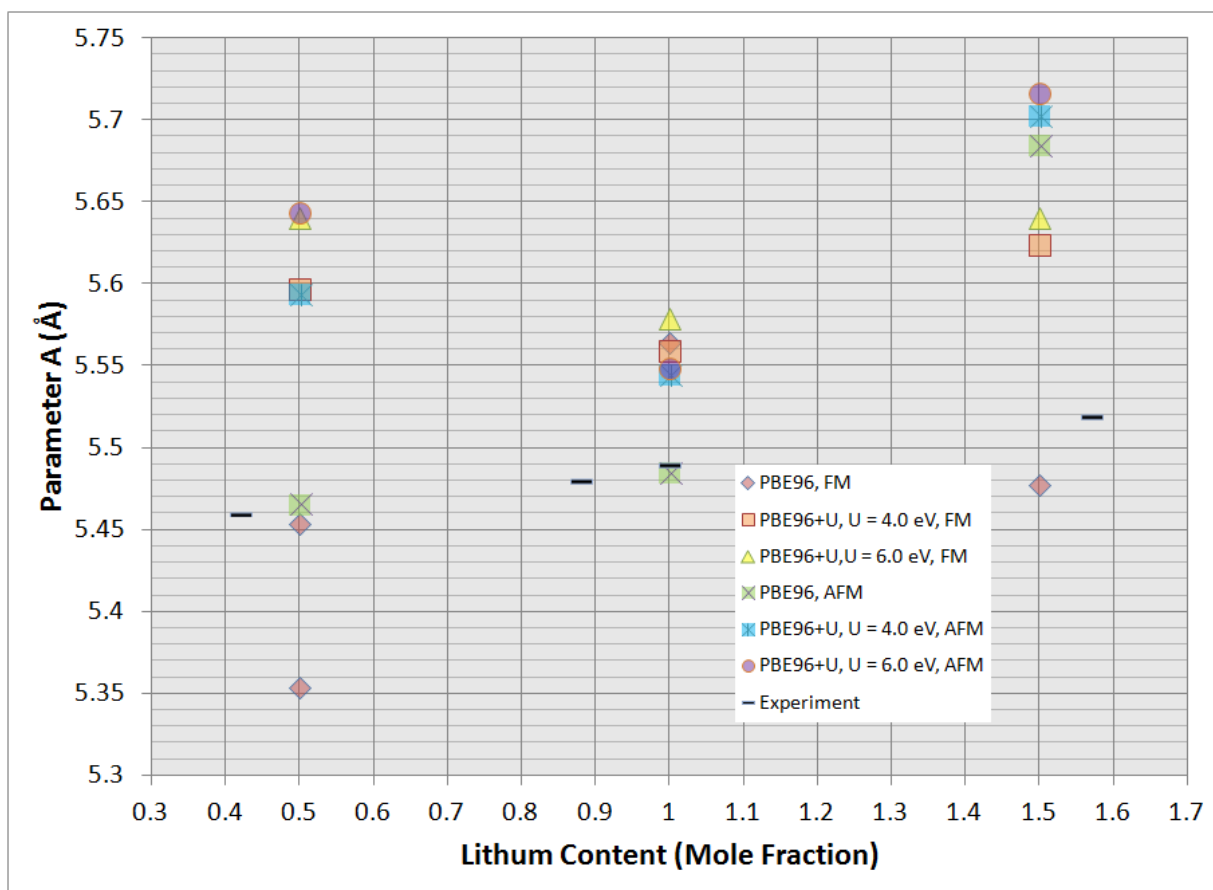


Figure 4.50: Comparison of different  $\text{T-Li}_x\text{FeO}_2$  unit cell volumes at different levels of electronic structure theory (PBE96, PBE96+U) and magnetic arrangement. (FM = ferromagnetic, AFM = antiferromagnetic)

The volumes calculated from the PBE96 and PBE96+U functional have been fairly close to experimental values for the T-LiFeO<sub>2</sub> structure in Figure 4.50. The error for the calculated volume was around 2.5 to 3.0% which has been reasonable. The volume error calculated for the C-type antiferromagnetic T-LiFeO<sub>2</sub> structure relaxed with the PBE96 functional was reported to be only 1.5% and the ferromagnetic T-LiFeO<sub>2</sub> relaxed with the PBE96 functional was reported to be as high as 3.3%. For the calculated volumes of The T-Li<sub>0.5</sub>FeO<sub>2</sub> and T-Li<sub>1.5</sub>FeO<sub>2</sub> structures, the values reported have been much higher in comparison to experiment than that of T-LiFeO<sub>2</sub>. The volumes reported for the T-Li<sub>0.5</sub>FeO<sub>2</sub> and T-Li<sub>1.5</sub>FeO<sub>2</sub> structures have grouped the values calculated from the PBE96 and PBE96+U functionals. The volumes reported for the T-Li<sub>0.5</sub>FeO<sub>2</sub> structures for the PBE96+U functional were only slightly higher than the values reported for the PBE96 functional while the volumes reported for the T-Li<sub>1.5</sub>FeO<sub>2</sub> structures have shown a larger difference between the volumes calculated for the PBE96 and PBE96+U functionals. The reported volumes for the T-Li<sub>0.5</sub>FeO<sub>2</sub> structures relaxed with the PBE96 functionals have about an 8% error compared to experiment while the error values reported for T-Li<sub>1.5</sub>FeO<sub>2</sub> structures relaxed with the PBE96 functional have been reported to be only about 3-4%. The volumes reported for the T-Li<sub>0.5</sub>FeO<sub>2</sub> and T-Li<sub>1.5</sub>FeO<sub>2</sub> structures relaxed with PBE96+U have reported errors as high as 10-11%. The exception to the reported volumes was for the low spin T-Li<sub>0.5</sub>FeO<sub>2</sub> structure which had a volumetric error of -1.7%.





**Figure 4.51: Comparison of the  $T\text{-Li}_x\text{FeO}_2$  unit cell parameters  $A$  at different levels of electronic structure theory (PBE96, PBE96+U) and magnetic arrangement. (FM = ferromagnetic, AFM = antiferromagnetic)**

The  $a$ ,  $b$ , and  $c$  parameters calculated for  $T\text{-Li}_{0.5}\text{FeO}_2$ ,  $T\text{-LiFeO}_2$ , and  $T\text{-Li}_{1.5}\text{FeO}_2$  have had more variation than the calculated volumes. For  $T\text{-Li}_{0.5}\text{FeO}_2$  structures at all levels of theory, the  $b$  and  $c$  parameters have been about 3% and 4.5% higher than experiment respectively. In Figure 4.51, the  $a$  parameter for the  $T\text{-Li}_{0.5}\text{FeO}_2$  structures relaxed with the PBE96 functional has been calculated at about -0.1% lower than experiment for the ferromagnetic arrangement and 0.1% higher for the C-type antiferromagnetic arrangement. The rest of the  $a$  parameters for the other  $T\text{-Li}_x\text{FeO}_2$  structures have been about 3% higher than experiment. The  $a$ ,  $b$ , and  $c$  parameters for the  $T\text{-LiFeO}_2$  structures have been consistently above experimental values with reported errors around 1 to 0.5%. The exception of the  $a$  parameter for  $T\text{-LiFeO}_2$  being lower for the antiferromagnetic structure relaxed with the PBE96 functional.

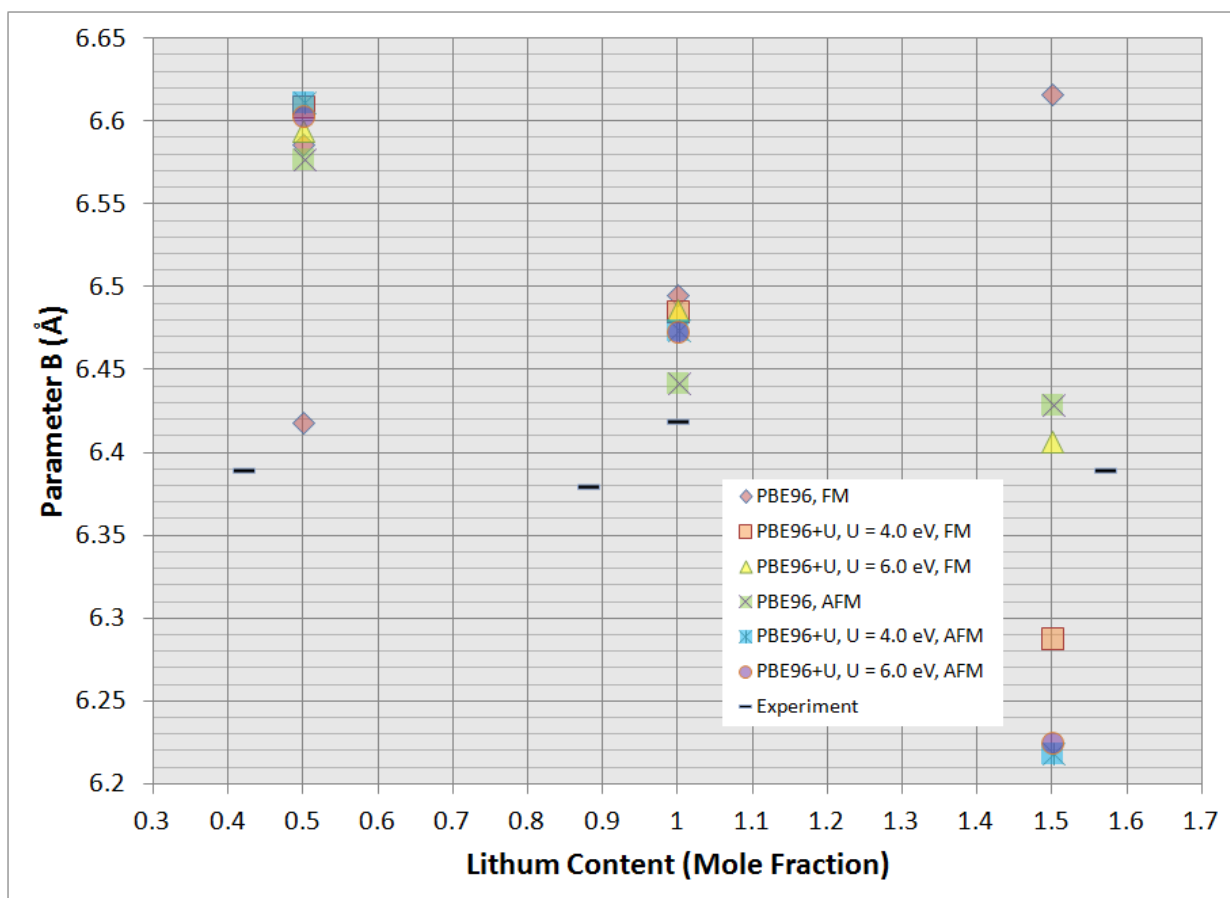


**Figure 4.52: Comparison of the  $T\text{-Li}_x\text{FeO}_2$  unit cell parameters B at different levels of electronic structure theory (PBE96, PBE96+U) and magnetic arrangement. (FM = ferromagnetic, AFM = antiferromagnetic)**

The reported unit cell parameters for  $T\text{-Li}_{1.5}\text{FeO}_2$  were not consistently grouped together except for the c parameter of the ferromagnetic and antiferromagnetic structures relaxed with the PBE96 functional. The deviation of the calculated unit cell angles from experiment have been more pronounced for the  $T\text{-Li}_{1.5}\text{FeO}_2$  structures which could have lead to a larger variation of the a, b, and c unit cell parameters.

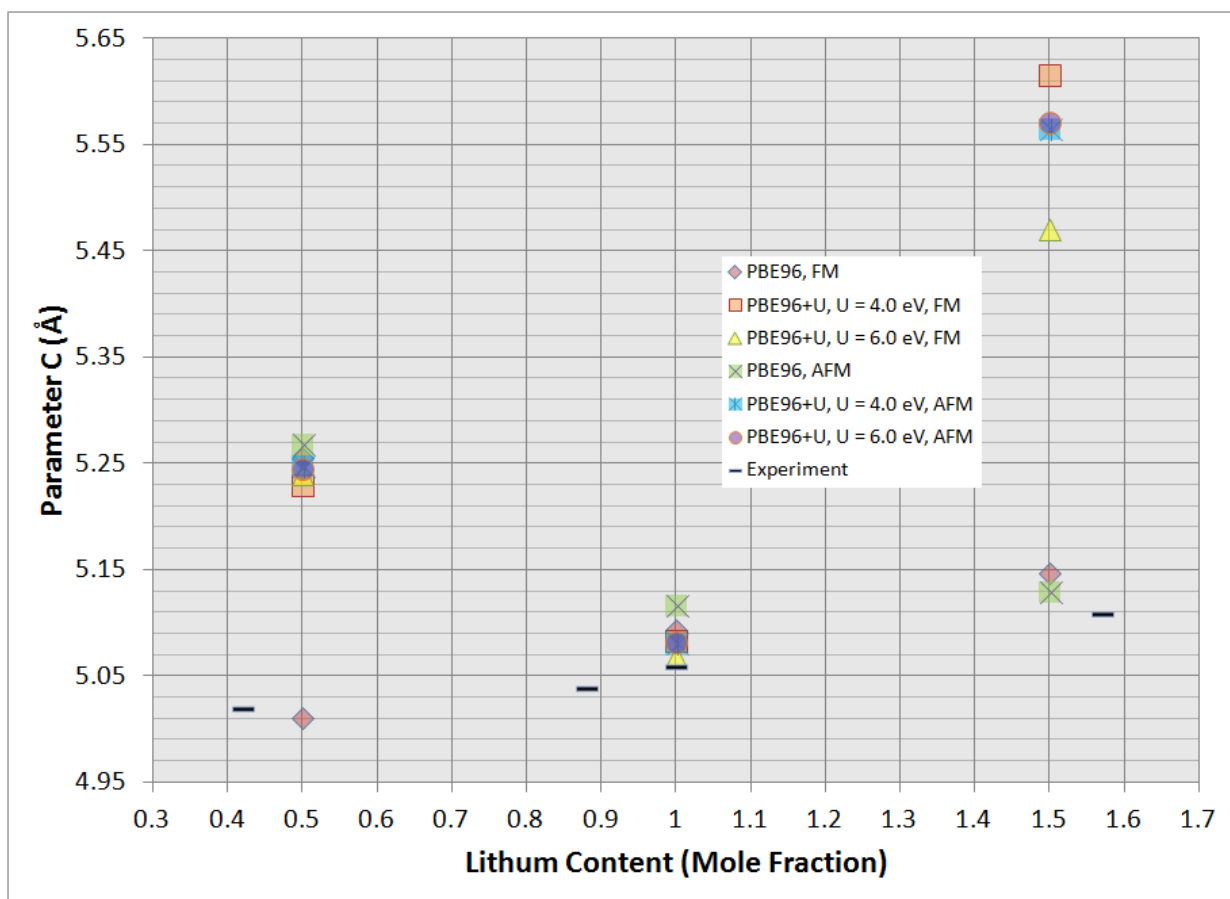


**Figure 4.53: Comparison of the  $T\text{-Li}_x\text{FeO}_2$  unit cell parameters C at different levels of electronic structure theory (PBE96, PBE96+U) and magnetic arrangement. (FM = ferromagnetic, AFM = antiferromagnetic)**

The discussion of unit cell lattice parameters and volumes have been generalized. The fully calculated error values have been reported in Table 4.11. Overall, the volumes and the unit cell parameters calculated from the C-type antiferromagnetic structures relaxed with the PBE96 functional have been the best reported, and in general the structures relaxed with the PBE96 functional have agreed better with experiment compared to structures relaxed with the PBE96+U functional.

**Table 4.11: Calculated Percent errors for the unit cell parameters and volumes for the T-Li<sub>x</sub>FeO<sub>2</sub> structures at various levels of theory.**

		Percent error of parameter a	Percent error of parameter b	Percent error of parameter c	Percent error of the volume
PBE96 FM	T-Li <sub>0.5</sub> FeO <sub>2</sub>	-0.122161172	3.0657277	4.678286853	7.740637132
	T-LiFeO <sub>2</sub>	1.352459016	1.167445483	0.651581028	3.339172422
	T-Li <sub>1.5</sub> FeO <sub>2</sub>	-0.765398551	3.543974961	0.719569472	3.276509695
	T-Li <sub>0.5</sub> FeO <sub>2</sub> (low spin)	-1.943956044	0.439593114	-0.186055777	-1.705126741
PBE96+U, U <sub>eff</sub> = 4.0 eV FM	T-Li <sub>0.5</sub> FeO <sub>2</sub>	2.511538462	3.432707355	4.17250996	10.44099166
	T-LiFeO <sub>2</sub>	1.262295082	1.020560748	0.448023715	2.889042165
	T-Li <sub>1.5</sub> FeO <sub>2</sub>	1.883695652	-1.589045383	9.890802348	10.00704266
PBE96+U, U <sub>eff</sub> = 6.0 eV FM	T-Li <sub>0.5</sub> FeO <sub>2</sub>	3.294139194	3.202190923	4.394023904	11.27099623
	T-LiFeO <sub>2</sub>	1.612750455	1.032398754	0.170355731	2.971679861
	T-Li <sub>1.5</sub> FeO <sub>2</sub>	2.177355072	0.269170579	7.070645793	9.424588366
PBE96 AFM	T-Li <sub>0.5</sub> FeO <sub>2</sub>	0.109523810	2.935367762	4.939840637	8.123250742
	T-LiFeO <sub>2</sub>	-0.093806922	0.347196262	1.113438735	1.502397395
	T-Li <sub>1.5</sub> FeO <sub>2</sub>	2.988949275	0.612519562	0.36888454	3.841112465
PBE96+U U <sub>eff</sub> = 4.0 eV AFM	T-Li <sub>0.5</sub> FeO <sub>2</sub>	2.457692308	3.469796557	4.528286853	10.80143412
	T-LiFeO <sub>2</sub>	1.001821494	0.846417445	0.412648221	2.41123856
	T-Li <sub>1.5</sub> FeO <sub>2</sub>	3.314492754	-2.682942097	8.900391389	9.261529086
PBE96+U U <sub>eff</sub> = 6.0 eV AFM	T-Li <sub>0.5</sub> FeO <sub>2</sub>	3.377838828	3.335524257	4.506374502	11.6285813
	T-LiFeO <sub>2</sub>	1.075045537	0.823208723	0.439328063	2.489138734
	T-Li <sub>1.5</sub> FeO <sub>2</sub>	3.567572464	-2.576995305	9.034833659	9.782307479

#### 4.6.4 Calculated Density of States for the T-Li<sub>x</sub>FeO<sub>2</sub> Structures with a Hubbard U<sub>eff</sub> of 4.0 eV

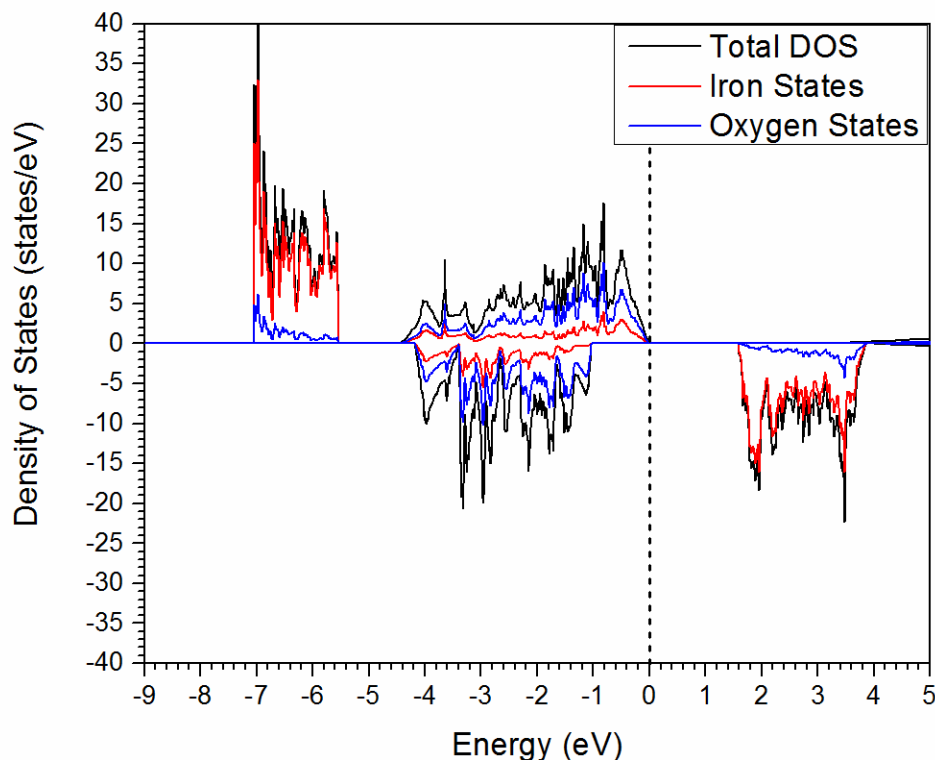


**Figure 4.54: Density of states for the ferromagnetic T-LiFeO<sub>2</sub> structure calculated with the PBE96+U functional after being relaxed with the PBE96 functional for a U<sub>eff</sub> value of 4.0 eV.**

The density of states for the T-Li<sub>0.5</sub>FeO<sub>2</sub>, T-LiFeO<sub>2</sub>, and T-Li<sub>1.5</sub>FeO<sub>2</sub> structures has been calculated at various levels of DFT and arrangements of magnetic moments. Figure 4.54 has shown the density of states calculated with the PBE96+U functional with a Hubbard U<sub>eff</sub> value of 4.0 eV after it had been relaxed with the PBE96 functional. The density of states has been calculated with the PBE96 functional, but has erroneously produced a non gapped metallic compound. The experimental compound has a reddish color which has suggested an electronically gapped compound. Much of the calculated density of states for the T-Li<sub>0.5</sub>FeO<sub>2</sub>, T-LiFeO<sub>2</sub>, and T-Li<sub>1.5</sub>FeO<sub>2</sub> structures have similar electronic. There have been some differences at the Fermi level which has depended on the lithium ion content, but the overall energetic order of the states has remained constant. The valence band in the density of states for the

T-LiFeO<sub>2</sub> structures has primarily been a wide set of oxygen p-states in Figures 4.54, 4.55, and 4.56. The conduction band has usually been consistent of unoccupied iron d-states. Figures 4.54, 4.55, and 4.56 have also shown a set of occupied iron d-states than the group of oxygen p-states. There have been two sets of iron bands/states because of the PBE96+U theory. The occupied states were lowered in energy below the oxygen p-states, and the unfilled iron d-states were pushed above the oxygen p-states. Because of the ferromagnetic arrangement used to calculate the density of states for the T-LiFeO<sub>2</sub> structures in Figures 4.54 and 4.55, the spin up state have moved below the Fermi level and the spin down states have moved above the Fermi level.

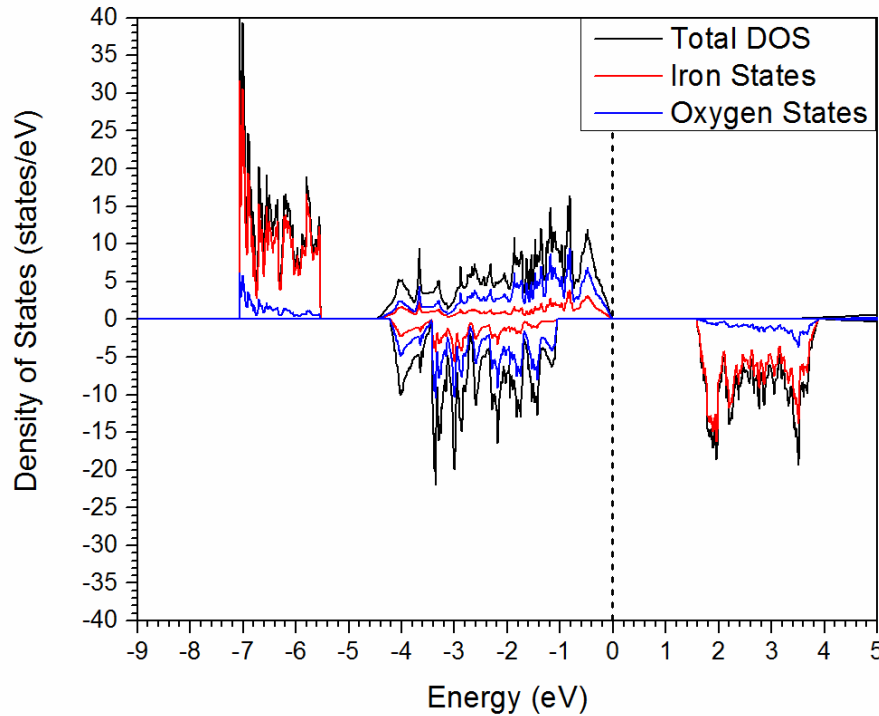


**Figure 4.55: Density of states for ferromagnetic T-LiFeO<sub>2</sub> structure calculated with the PBE96+U functional after being relaxed with the PBE96+U functional for a  $U_{\text{eff}}$  value of 4.0 eV.**

Figure 4.55 has shown the density of stats for the T-LiFeO<sub>2</sub> structure calculated with the PBE96+U functional after the structure had been relaxed with the PBE96+U functional for a  $U_{\text{eff}}$  value of 4.0 eV. The similarity of Figure 4.54 and Figure 4.55 has not been surprising due to the similar unit cell

parameters calculated for the T-LiFeO<sub>2</sub> structure after being relaxed with the PBE96+U and PBE96 functionals.

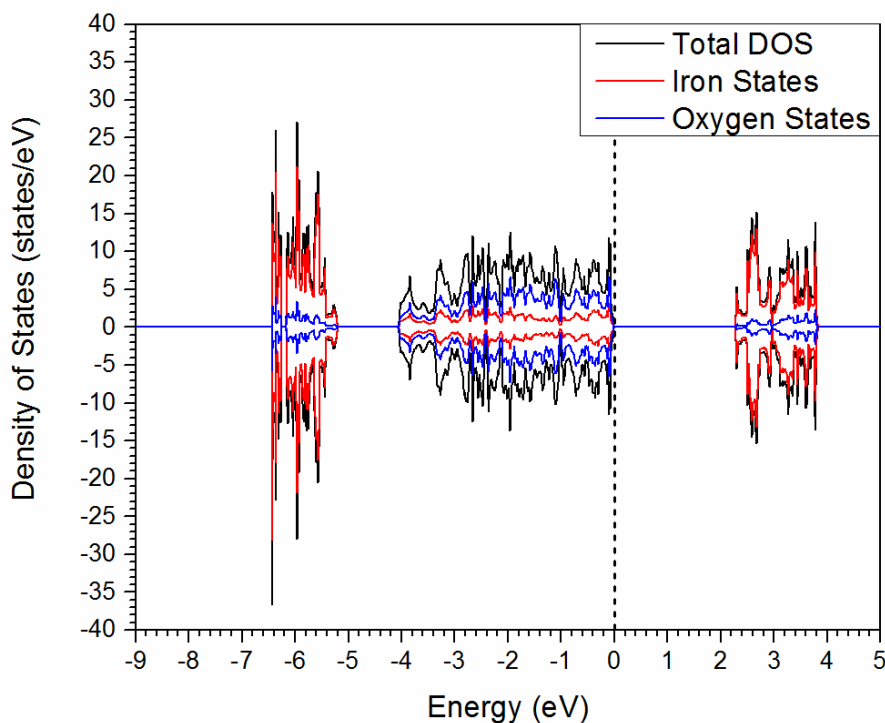


**Figure 4.56: Density of states for C-type antiferromagnetic T-LiFeO<sub>2</sub> structure calculated with the PBE96+U functional after being relaxed with the PBE96+U functional for a  $U_{\text{eff}}$  value of 4.0 eV.**

Figure 4.56 has shown the density of states for C-type antiferromagnetic T-LiFeO<sub>2</sub> structure calculated with the PBE96+U functional after the structure had been relaxed with the PBE96+U functional for a  $U_{\text{eff}}$  value of 4.0 eV. The only real differences in comparing the Figures 4.56 and 4.55 has been that the band gap was slightly larger for the antiferromagnetic structure compared to the ferromagnetic structure. Spin up and down iron states have been reported in the conduction band in Figure 4.56, as well.

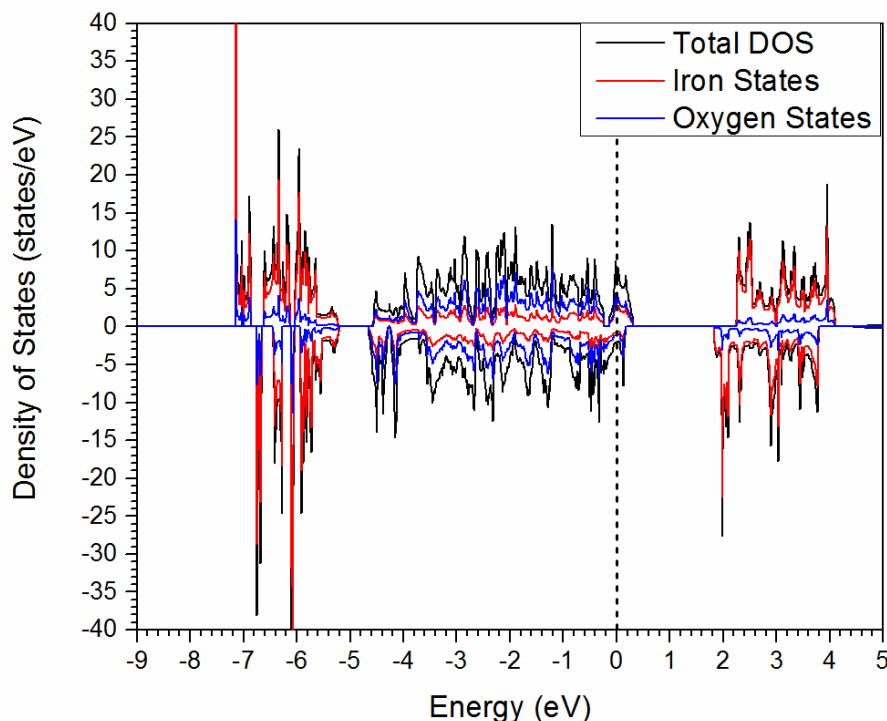
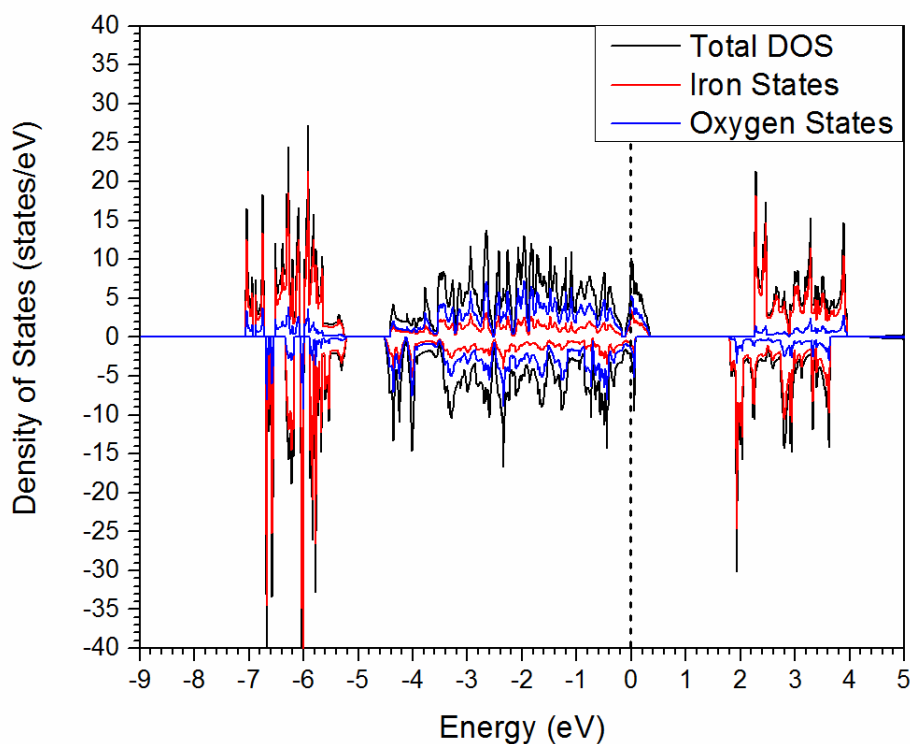


**Figure 4.57: Density of states for the initially ferromagnetic T-Li<sub>0.5</sub>FeO<sub>2</sub> structure calculated with the PBE96+U functional after being relaxed with the PBE96 functional for a  $U_{\text{eff}}$  value of 4.0 V.**

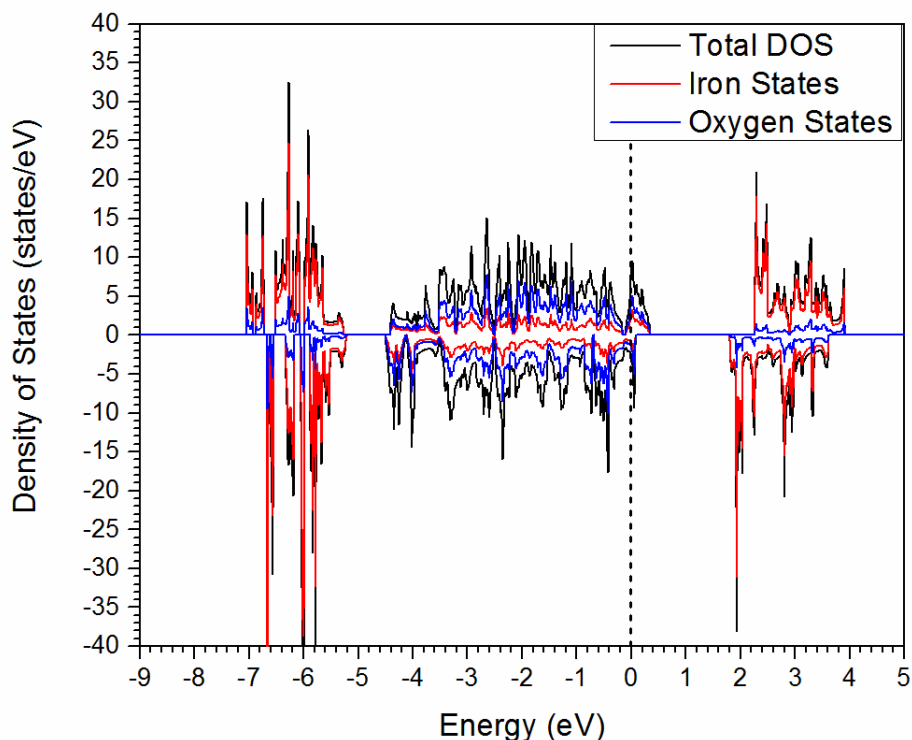
Figures 4.57, 4.58, and 4.59 have shown the density of states for T-Li<sub>0.5</sub>FeO<sub>2</sub> calculated with the PBE96+U functional from the ferromagnetic structure relaxed with the PBE96 functional, from the ferromagnetic structure relaxed with the PBE96+U functional, and from the C-type antiferromagnetic structure relaxed with the PBE96+U functional. The starting magnetic structure had no affect as each structure relaxed to a C-type antiferromagnetic structure. Between Figures 4.57, 4.58, and 4.59, they have shown a similar plot of the density of states for the T-Li<sub>0.5</sub>FeO<sub>2</sub> structures. Because the valance states in the T-LiFeO<sub>2</sub> structure primarily have oxygen character, the density of states for the T-Li<sub>0.5</sub>FeO<sub>2</sub> structures has shown the Fermi level crossing into the valance oxygen p-states. Ideally, the T-Li<sub>0.5</sub>FeO<sub>2</sub> structure should represent the T-LiFeO<sub>2</sub> compound as it has been oxidized from the iron III state to the iron IV state; however, the density of states has not matched experimental descriptions entirely. The T-Li<sub>0.42</sub>FeO<sub>2</sub> compound has been reported to have a reddish color meaning it should have an electronic



band gap. The calculated density of states for the  $\text{T-Li}_{0.5}\text{FeO}_2$  structures has aided in describing other experimental observations for an oxidized  $\text{T-LiFeO}_2$  structure.<sup>157</sup> This chapter and previous accounts have not shown the  $\text{T-LiFeO}_2$  compound to cycle the iron III/IV redox couple.<sup>157</sup> The density of states for the  $\text{T-Li}_{0.5}\text{FeO}_2$  structure has suggested that the attempted electrochemical cycling of the iron III/IV redox couple has been accessing oxygen p-states to produce oxygen vacancies and unstable peroxide states.<sup>51</sup> It has also been reported that the  $\text{T-LiFeO}_2$  structure has formed oxygen vacancies when oxidized.<sup>157,277</sup>

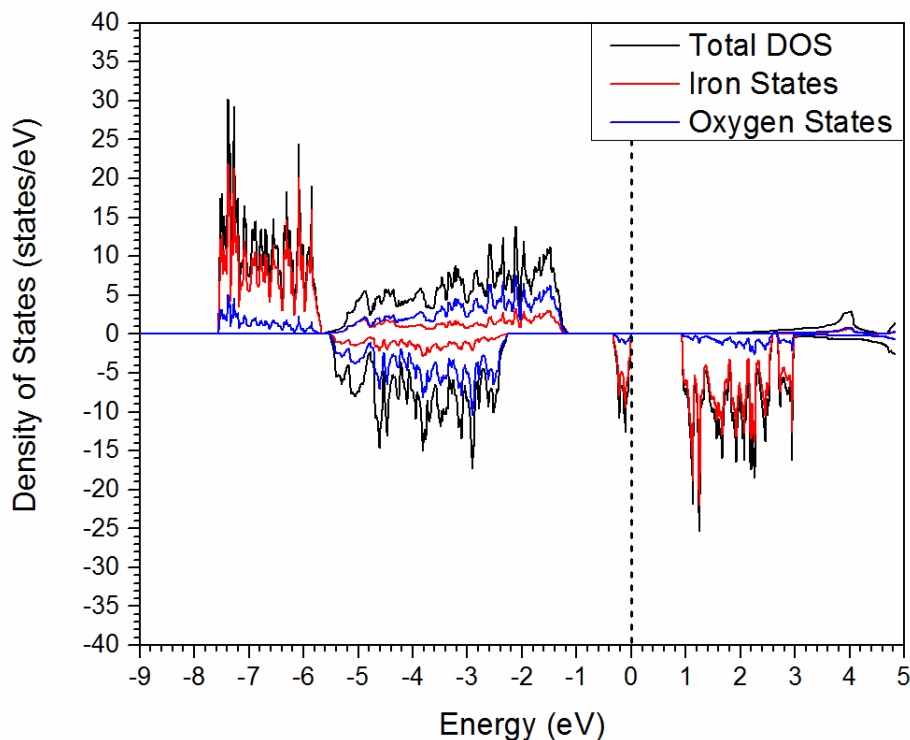


**Figure 4.58:** Density of states for the initially ferromagnetic  $\text{T-Li}_{0.5}\text{FeO}_2$  structure calculated with the PBE96+U functional after being relaxed with the PBE96+U functional for a  $U_{\text{eff}}$  value of 4.0 eV.



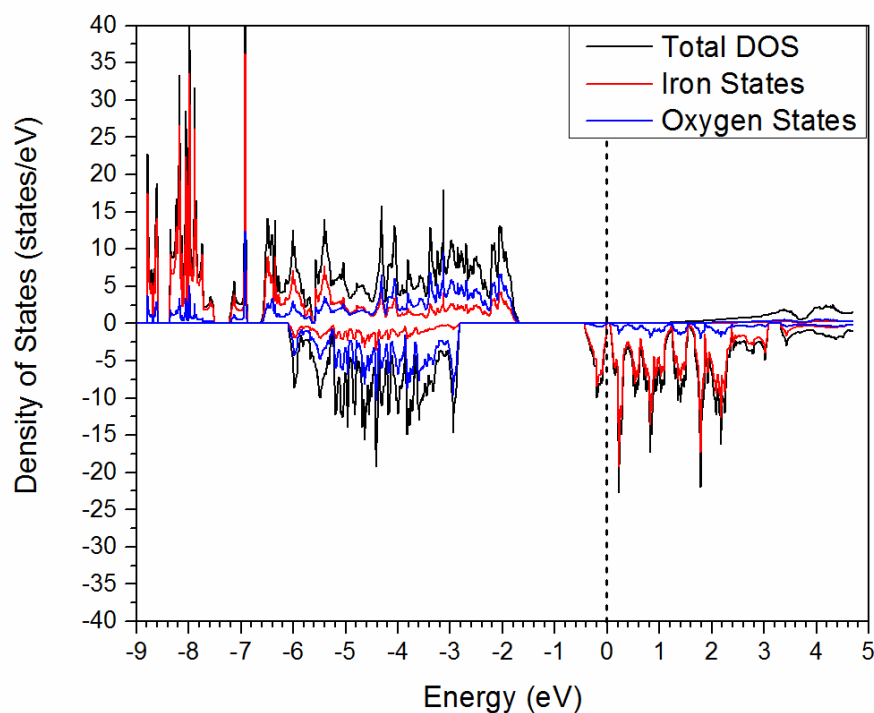
**Figure 4.59: Density of states for the C-type antiferromagnetic  $\text{T-Li}_{0.5}\text{FeO}_2$  structure calculated with the PBE96+U functional after being relaxed with the PBE96+U functional for a  $U_{\text{eff}}$  value of 4.0 eV.**

Figures 4.62, 4.63, and 4.64 have shown the density of states for the  $\text{T-Li}_{1.5}\text{FeO}_2$  structure calculated with the PBE96+U functional from a ferromagnetic structure relaxed with the PBE96 functional, from a ferromagnetic structure relaxed with PBE96+U, and from an C-type antiferromagnetic structure relaxed with the PBE96+U functional. Unlike Figures 4.56 to 4.61, the density of states for  $\text{T-Li}_{1.5}\text{FeO}_2$  has shown the formation of iron states at the top of the oxygen states at the Fermi level. The  $\text{T-Li}_{1.5}\text{FeO}_2$  structure should represent the reduced  $\text{T-LiFeO}_2$  compound for the access to the iron II/III redox couple. In Figures 4.62, 4.63, and 4.64, they have shown a portion of the iron conduction states having been lowered to the top valance oxygen states because of the added occupation of electrons.



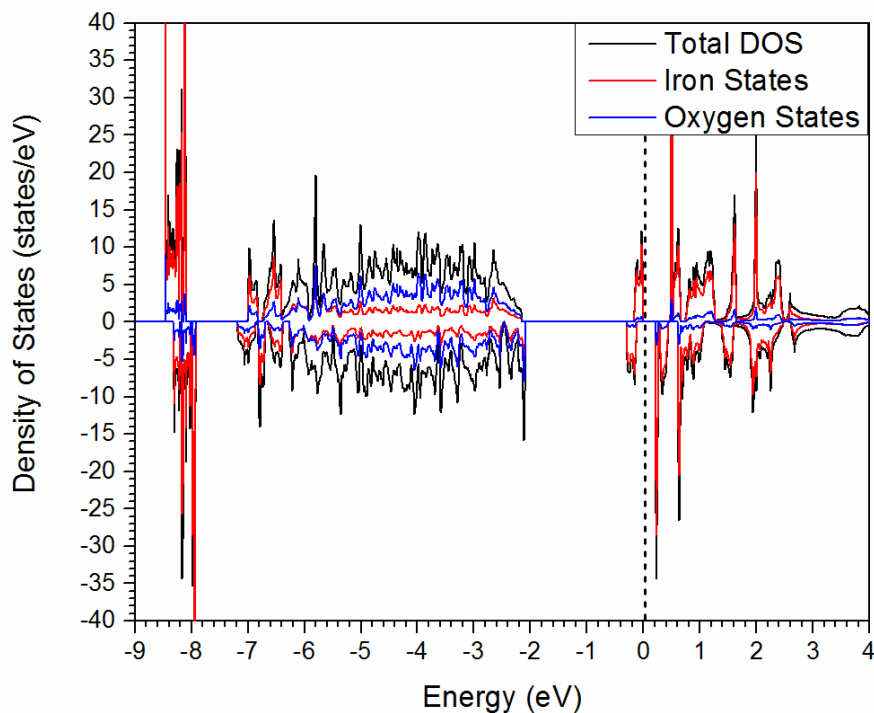
**Figure 4.60: Density of states for ferromagnetic T-Li<sub>1.5</sub>FeO<sub>2</sub> structure calculated with the PBE96+U functional after being relaxed with the PBE96 functional for a  $U_{\text{eff}}$  value of 4.0 eV.**

Figure 4.60 has shown a large band gap between the unoccupied conduction iron states and the occupied iron valance states. Figures 4.61 and 4.62 have shown that the relaxation of the T-Li<sub>1.5</sub>FeO<sub>2</sub> structures with the PBE96+U functional has decreased this gap significantly. Density functional theory has been defined as a ground state theory so it cannot always accurately predict band gaps and excited electronic states, even with corrective theory such as the DFT+U method.<sup>193,264,317,318</sup> However, Figure 4.62 has shown the band gap as slightly larger than Figure 4.61. The T-Li<sub>1.5</sub>FeO<sub>2</sub> compound should be a electronically gapped compound similar to the T-LiFeO<sub>2</sub> compound, thus Figure 4.62 has shown the most correct density of states for the T-Li<sub>1.5</sub>FeO<sub>2</sub> structure because it has an antiferromagnetic arrangement.<sup>157</sup> However, lattice parameters for the T-Li<sub>1.5</sub>FeO<sub>2</sub> structure relaxed with the PBE96 functional have shown to have shown slightly better experimental agreement when looking back at Figure 4.60.



**Figure 4.61: Density of states for the ferromagnetic T-Li<sub>1.5</sub>FeO<sub>2</sub> structure calculated with the PBE96+U functional after being relaxed with the PBE96+U functional for a  $U_{\text{eff}}$  value of 4.0 eV.**

Regardless of the level of theory, all of the plotted density of states for the T-Li<sub>1.5</sub>FeO<sub>2</sub> compounds has shown a correctly formed iron valance states at the Fermi level. Experimentally, only the iron II/III redox couple has been electrochemically accessed.<sup>157</sup> the iron states would have to be at the Fermi level to be electrochemically accessible.<sup>51</sup>



**Figure 4.62: Density of states for the C-type antiferromagnetic T-Li<sub>1.5</sub>FeO<sub>2</sub> structure calculated with the PBE96+U functional with the PBE96+U functional for a  $U_{\text{eff}}$  value of 4.0 eV.**

The density of states for the T-LiFeO<sub>2</sub>, T-Li<sub>0.5</sub>FeO<sub>2</sub> and T-Li<sub>1.5</sub>FeO<sub>2</sub> structures had been calculated for a Hubbard  $U_{\text{eff}}$  value of 6.0 eV, as well, but there has been little difference to discuss. The only major differences have been the increase band gaps between the valence and conduction bands and a slightly lower set of occupied iron d-states in the T-Li<sub>0.5</sub>FeO<sub>2</sub> and T-LiFeO<sub>2</sub> structures. Much of the energetic ordering of the states has been the same. The widening of the electronic band gaps has not been unexpected as higher a Hubbard  $U_{\text{eff}}$  value would have increased the energetic difference between occupied and unoccupied states.

#### 4.6.5 Calculated Density of States for the T-Li<sub>x</sub>FeO<sub>2</sub> Structures with the HSE06 Hybrid Functional

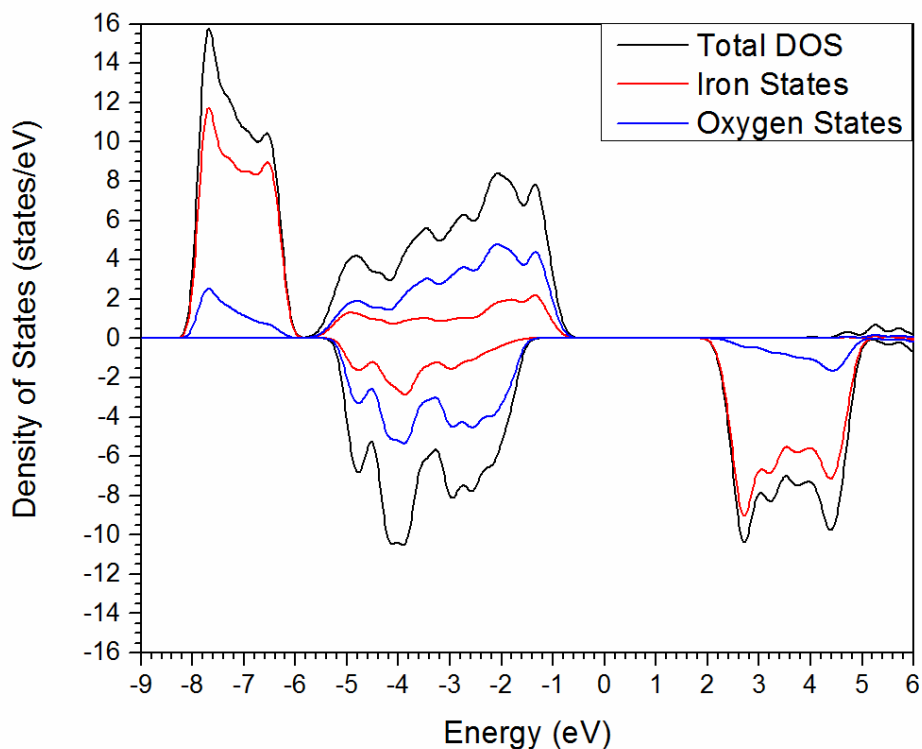


**Figure 4.63: Density of States for the ferromagnetic T-LiFeO<sub>2</sub> structure calculated with the HSE06 hybrid functional after being relaxed with the PBE96 functional.**

The density of states for the ferromagnetic T-LiFeO<sub>2</sub>, T-Li<sub>0.5</sub>FeO<sub>2</sub> and T-Li<sub>1.5</sub>FeO<sub>2</sub> structures has been calculated with the HSE06 hybrid functional after having been relaxed with the PBE96 functional. The density of states for T-LiFeO<sub>2</sub> structure calculated with the HSE06 functional has been shown in Figure 4.63. The density of states for T-Li<sub>0.5</sub>FeO<sub>2</sub> structure calculated with the HSE06 functional has been shown in Figure 4.64, and the density of states for the T-Li<sub>1.5</sub>FeO<sub>2</sub> structure has been shown in Figure 4.65. The densities of states for the HSE06 functional have been noticeably broader and less sharp. This has been due to the lower amount of k-points used (~200 k-points). The HSE06 functional has been a reportedly expensive method, and the more k-points use, the more expensive the simulation can be.<sup>149</sup> Figure 4.65 has shown similar energetic order of the density of states to that of the PBE96+U functional.

The valance states have been primarily of oxygen character while the conduction band has been primarily iron character. The HSE06 functional has calculated a higher band gap due to the added exact exchange.

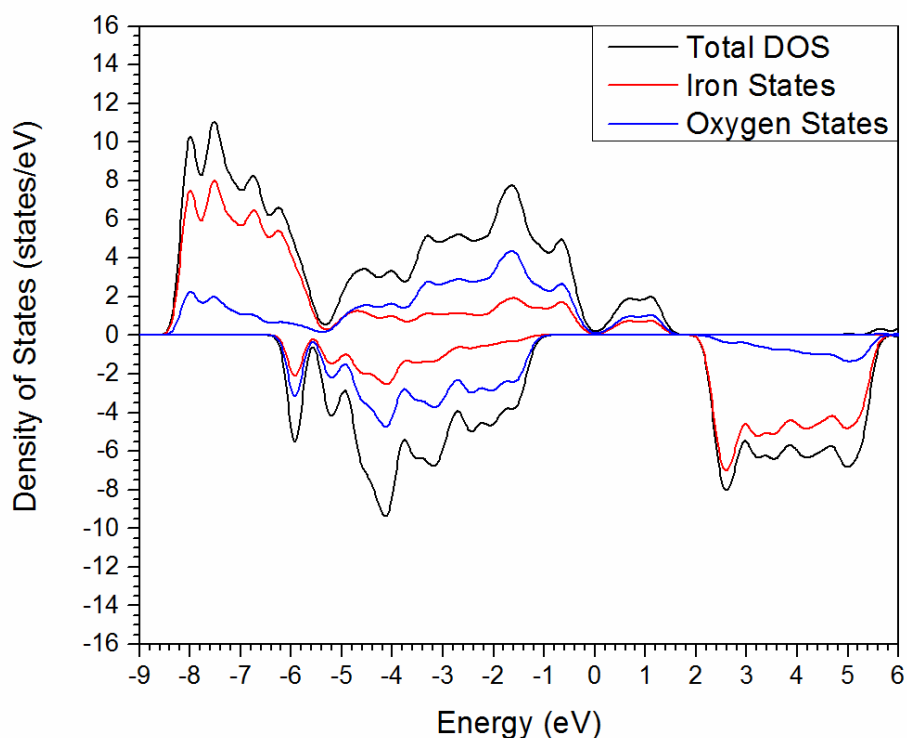


**Figure 4.64: Density of states for the ferromagnetic T-Li<sub>0.5</sub>FeO<sub>2</sub> structure calculated with the PBE96 function after being relaxed with the PBE96 functional.**

One of the more interesting things shown in Figure 4.64 has been the Fermi level has moving into the oxygen states for the T-Li<sub>0.5</sub>FeO<sub>2</sub> structure where the states have been split into occupied and unoccupied states. This has also supported the inaccessibility of the iron III/IV redox couple in the T-Li<sub>x</sub>FeO<sub>2</sub> structures and the formation of oxygen vacancies. There has been more mixing between the lower occupied iron states and the valance oxygen states with the HSE06 functional.

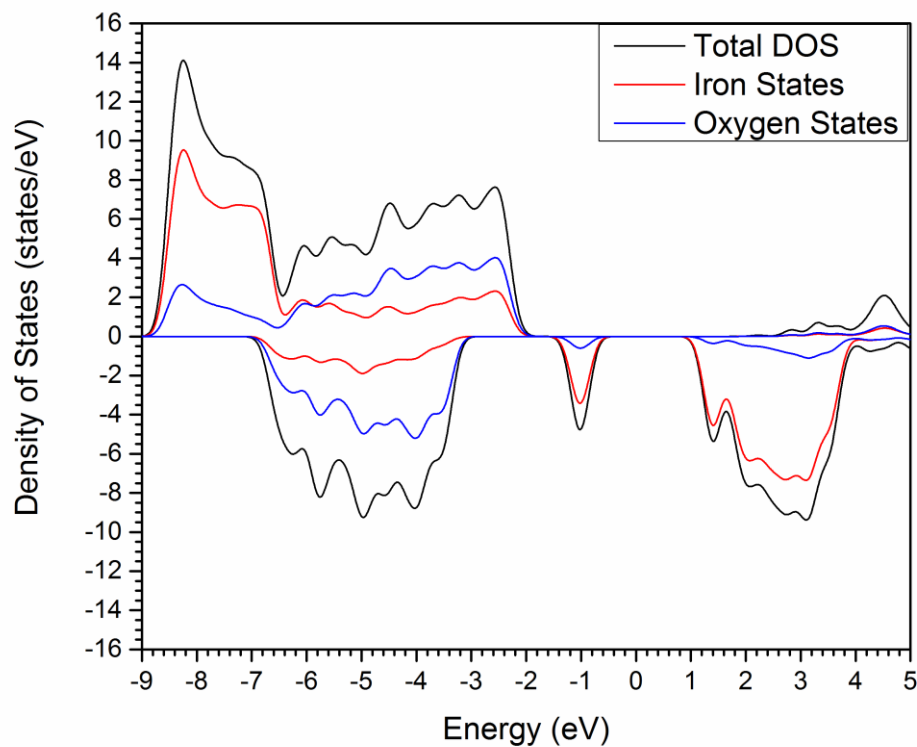


**Figure 4.65: Density of states for the ferromagnetic T-Li<sub>1.5</sub>FeO<sub>2</sub> structure calculated with the HSE06 functional after being relaxed with the PBE96 functional.**

Figure 4.65 has shown to be similar to previous calculated density of states for the T-Li<sub>1.5</sub>FeO<sub>2</sub> structure as the formation of iron valences states has occurred. This has supported the electrochemical stability of the iron II/III redox couple. The band gap for the HSE06 functional for the T-Li<sub>1.5</sub>FeO<sub>2</sub> structure has been very similar to that of PBE96+U functional.



#### 4.6.6 Calculated Magnetic Structures for T-LiFeO<sub>2</sub> and $\beta$ -NaFeO<sub>2</sub> with the PBE96 functional

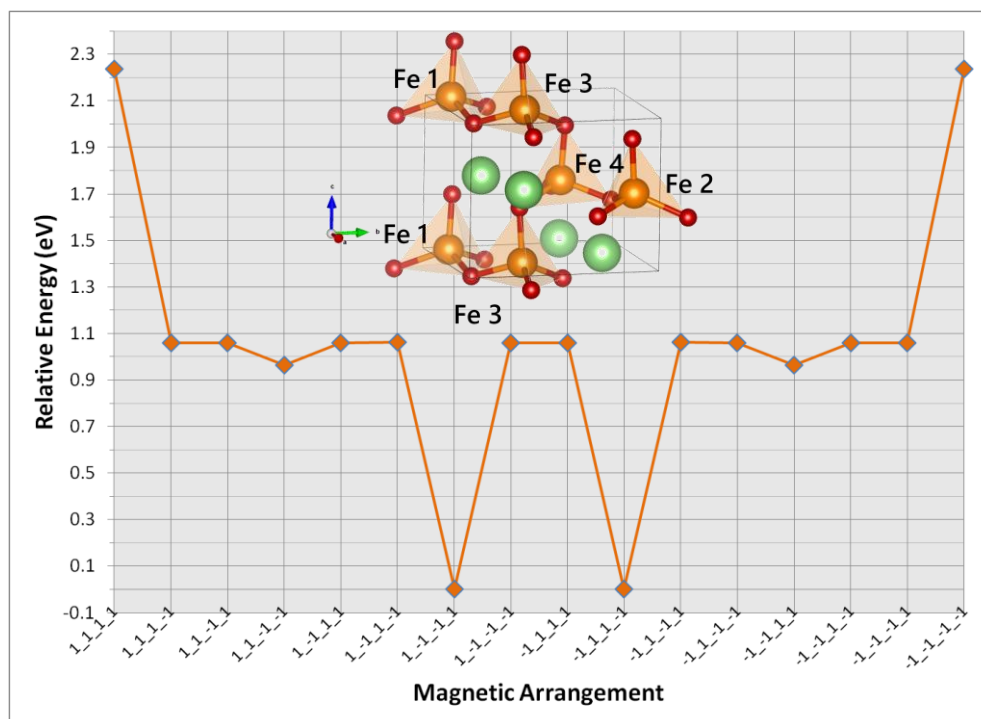


**Figure 4.66:** Relative energies of different magnetic unit cells of T-LiFeO<sub>2</sub> relaxed with the PBE96 functional. The designation -1 stands for spin down and the designation 1 stand for spin up. The unit cell is shown with the labeled iron positions. Green is the lithium ion positions and red is the oxygen ion positions.

The T-LiFeO<sub>2</sub> structure has been relaxed with respect to the magnetic moment in Figure 4.66. The two highest energy structures plotted have been for the completely ferromagnetic structure which also had the largest cell volume. The two lowest energy values have been for the completely antiferromagnetic structure (G type). In each of the unit cells, the FeO<sub>4</sub> tetrahedra have been connected through corner sharing. For the completely antiferromagnetic structure each interaction between the iron-oxygen-iron bonds had an antiferromagnetic coupling. The other structures with an energetic value of about 1.1 eV have contained at least contain at least one spin moment opposite to the rest of the spin moments. These structures have varying amounts of antiferromagnetic and ferromagnetic coupling. The complete antiferromagnetic structure had the smallest volume. The structure labeled “1\_1\_-1\_-1” has the same magnetic arrangement as the C-type antiferromagnetic T-Li<sub>x</sub>FeO<sub>2</sub> structures calculated before.

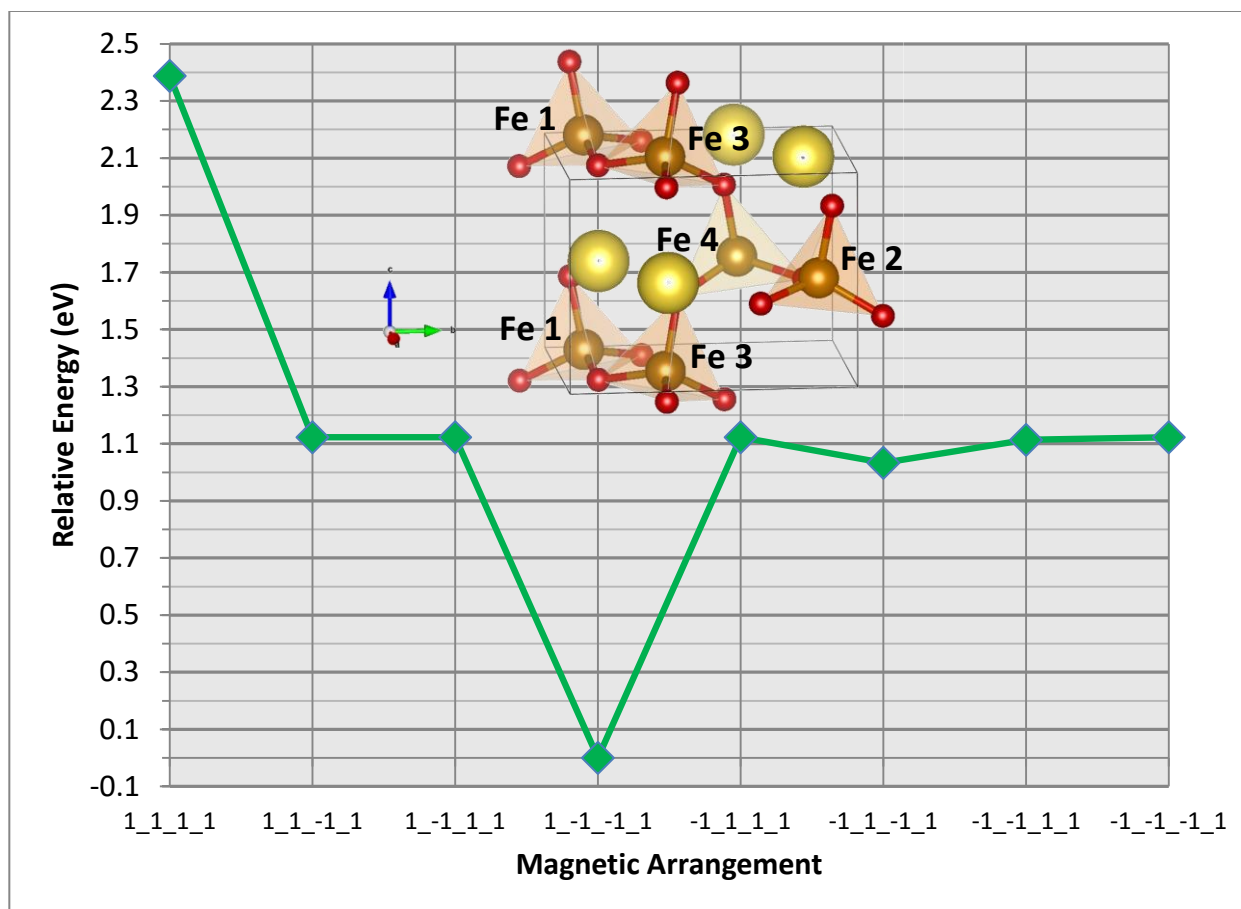


Figure 4.67: Relative energies of different magnetic unit cells for  $\beta$ -NaFeO<sub>2</sub> relaxed with the PBE96 functional. The designation -1 stands for spin down and the designation 1 stand for spin up. The unit cell is shown with labeled iron positions. Yellow is the lithium ion positions and red is the oxygen ion positions.

Figure 4.67 has shown the relaxation of the  $\beta$ -NaFeO<sub>2</sub> structure with respect to magnetic moment. For the sake of unnecessary redundancy, the forth iron position has remained as spin up. Repeatedly, the highest energetic value has been the complete ferromagnetic structure, while the lowest energetic value has been for the completely antiferromagnetic structure. The middle energetic values, again have a mixture of ferromagnetic and antiferromagnetic second order couplings. Both Figures 4.66 and 4.67 have shown a large energetic disparity between the varying magnetic structures with energetic differences larger than the values reported in Table 4.8. However, the structures in Figure 4.66 and 4.67 were only calculated with the PBE96 functional. The PBE96 functional has been known to be more diffusing and that and added Hubbard  $U_{\text{eff}}$  value would shrink the d orbital to mimic the effects

of correlated localized electrons. The wide energetic disparity of the magnetic states in Figures 4.66 and 4.67 have been due to the large orbital overlap between adjacent states which has been a consequence of the large diffusion of the PBE96 functional.<sup>264,265,319</sup>

#### 4.6.7 Calculation of the Hubbard $U_{\text{eff}}$ through the Linear Response Approach

The Hubbard  $U_{\text{eff}}$  value for the T-LiFeO<sub>2</sub> structure was calculated with the linear response approach.<sup>191</sup> The values used for  $\alpha$  for the linear response approach have been -0.25, -0.15, -0.10, -0.05, 0, 0.05, 0.10, 0.15, and 0.25. First, it had been calculated from a 2 by 2 response matrix that encompassed only one iron oxygen bond in the completely antiferromagnetic structure reported in Figure 4.66. It had also been calculated from a 5 by 5 response matrix consisting of the bonds in a single tetrahedron for the completely antiferromagnetic structure calculated in Figure 4.66. The 2 by 2 matrix had calculated a Hubbard  $U_{\text{eff}}$  value of 4.5 eV while the 5 by 5 matrix had calculated a Hubbard  $U_{\text{eff}}$  of 5.9 eV. The calculations had been performed to give a general confirmation of the Hubbard  $U_{\text{eff}}$  values used in the previous calculations. In many cases of iron oxides, a Hubbard  $U_{\text{eff}}$  of 4 eV has been used, but a Hubbard  $U_{\text{eff}}$  value of 6.0 has also been used sometimes.<sup>297,320–323</sup> Typically when calculating the Hubbard  $U_{\text{eff}}$  values by the linear response approach, the larger the matrix used, the better the calculation of the  $U_{\text{eff}}$  value. It could have been suggested that the calculated Hubbard  $U_{\text{eff}}$  of 6 eV would have been an more acceptable  $U_{\text{eff}}$  value for the T-Li<sub>x</sub>FeO<sub>2</sub> structures, even though a Hubbard  $U_{\text{eff}}$  value of 4 eV has been more typical.

### **4.7 Conclusion**

Even through the use of cobalt doping, it has been shown that the iron III/IV redox couple has not been electrochemically accessible. Electrochemical cycling of the T-LiFeO<sub>2</sub> structure has been only moderately effective for the iron II/III redox couple. Chromium, nickel, and vanadium doping of the  $\beta$ -NaFeO<sub>2</sub> structure has proven ineffective, although the interesting Na<sub>3</sub>Fe<sub>5</sub>O<sub>9</sub> phase had been forming for each attempted dopant after high temperatures and long reaction times. This has suggested that the

$\text{Na}_3\text{Fe}_5\text{O}_9$  compound should be the preferred thermodynamic product. The  $\text{Na}_3\text{Fe}_5\text{O}_9$  compound has an interesting structure for further research. The compound has large one dimension cavities for the sodium ions and both tetrahedral and octahedral iron coordination centers. Due to the large cavities, the sodium ions could potentially be exchanged for the smaller lithium ions as another prospective multi-redox battery material. Because chromium and vanadium have a preference for an octahedral coordination center, it could be suggested that dopant would take the octahedral coordination position in the compound. The  $\text{Na}_3\text{Fe}_5\text{O}_9$  structure has long corner shared chains made by the octahedra in the structure. Analysis of a band structure of the  $\text{Na}_3\text{Fe}_5\text{O}_9$  compound could be analyzed to deduce if the states from the octahedra chain formed frontier states. The frontier states could then be doped for increased conductivity as well as identifying a high symmetry electron pathway. The long chains of octahedra would be interesting because the structure would have a built in “alley way” for electronic conduction in addition to the large ionic cavities.

Most importantly, it has been clear from the density of states of the  $\text{T-Li}_x\text{FeO}_2$  structures that the iron III/IV redox couple has been electrochemically inaccessible. It has been shown that oxygen valance states have lead to an undesirable oxygen reactivity and formed holes instead of probing the desired iron states. The Fermi level of  $\text{T-Li}_{0.5}\text{FeO}_2$  structure has crossed into electrochemically undesirable oxygen states while the valance states for the  $\text{T-Li}_{1.5}\text{FeO}_2$  structure have electrochemically active iron states. The  $\text{T-LiFeO}_2$  compound has shown to have oxygen valance states while iron conduction states, as well. This electronic ordering of states has been found to occur in other polymorphs of the structure.<sup>313</sup> It may be futile to attempt to access the iron III/IV redox couple in any of the other  $\text{LiFeO}_2$  structures.

Although the material  $\text{T-LiFeO}_2$  has been shown to be electrochemically inactive, The recent Mössbauer measurements have shown a local magnetic moment for the experimental  $\text{T-Li}_{0.42}\text{FeO}_2$ ,  $\text{T-LiFeO}_2$ , and  $\text{T-Li}_{1.5}\text{FeO}_2$  structures. The Mössbauer data for  $\text{T-Li}_{0.42}\text{FeO}_2$  has also shown that the

compound has some type of iron IV state.<sup>157</sup> Magnetic calculations have suggested that the T-LiFeO<sub>2</sub> structure has a strong antiferromagnetic interaction similar to the magnetic structure calculated for the  $\beta$ -NaFeO<sub>2</sub> structure. The magnetic structure calculated for the  $\beta$ -NaFeO<sub>2</sub> compound has been confirmed by experiment with a Neel temperature of 450 K. The  $\beta$ -NaFeO<sub>2</sub> compound has also been investigated as multiferroic material (coupling between ferroelectric and magnetic interactions) for spintronic memory storage.<sup>324</sup> While the compound was found to have a G-type antiferromagnetic structure by neutron diffraction, it has been reported to have a small non-zero magnetic interaction due to spin canting. The T-Li<sub>0.42</sub>FeO<sub>2</sub> compound has been found to have a strong magnetic attraction to a table top neodymium magnet which suggests a ferrimagnetic interaction, derivative of the completely antiferromagnetic behavior found in pure T-LiFeO<sub>2</sub>. The T-LiFeO<sub>2</sub> and  $\beta$ -NaFeO<sub>2</sub> structures have been shown to maintain structure when chemically oxidized to deintercalate lithium and sodium.<sup>157</sup> It has been suggestive through calculations that the magnetic behavior of T-LiFeO<sub>2</sub> would be similar that of  $\beta$ -NaFeO<sub>2</sub> and vice versa.

Magnetic studies could be performed between the T-LiFeO<sub>2</sub> and  $\beta$ -NaFeO<sub>2</sub> structures as a comparison of the different alkali metals. A comparison of alkali metal size would quantify the how cell size and bond length could affect the magnetic interaction of a tetrahedral iron oxide. It could also be hypothesized that a decrease of the alkali metal content in the T-LiFeO<sub>2</sub> and  $\beta$ -NaFeO<sub>2</sub> structures could increase the non-zero magnetic moment of both compounds based on a ferrimagnetic interaction. It would, thus increase the multiferroic response.<sup>324</sup> One of the caveats to consider has been a decreased mechanical strength in the deintercalated structure due to ionic vacancies.<sup>157</sup> Also, both the T-LiFeO<sub>2</sub> and  $\beta$ -NaFeO<sub>2</sub> compounds have shown to be highly moisture sensitive, a factor that would increase with more alkali deintercalation. Investigating of the magnetic properties of the  $\beta$ -NaFeO<sub>2</sub> and T-LiFeO<sub>2</sub> structures would lead a better understanding how to improve the  $\beta$ -NaFeO<sub>2</sub> compound as a multiferroic, as well as allow for a decent study on a model iron oxide tetrahedral system. Fundamentally systems

that have a purely octahedral system will not work as a ferroelectric system (and therefore a multiferroic system) because it does not have an inversion center. Thus systems that naturally lack an inversion center should be explored more for applications similar to ferroelectricity and multiferroicity.<sup>66</sup>

## 5 Magnesium-ion Conductor $Mg_{0.5}B_5C$

### 5.1 Introduction

High ionic conductivity has been required for intercalation cathode and anode batteries materials, as well as for solid electrolytes used in batteries, fuel cells, and sensors. Significant efforts have been devoted to developing lithium-ion batteries with a lithium metal anode and a solid electrolyte, which should result in higher energy density.<sup>325</sup> Alternatively, due to high cost and scarcity of lithium, materials with  $Mg^{2+}$  ionic conductivity has been investigated for cathode and solid electrolyte applications in lithium-free batteries.<sup>326–329</sup> However, the activation energy for the solid state diffusion of multivalent cations has been substantially higher than that for  $Li^{1+}$ .<sup>330</sup> There has been a critical need for new compounds with high magnesium-ion mobility. In this chapter, there has been a new class of a magnesium-ion solid electrolytes reported, the  $Mg_{0.5}B_5C$  carbaboride, with a low  $Mg^{2+}$  diffusion barrier determined by first-principles calculations.

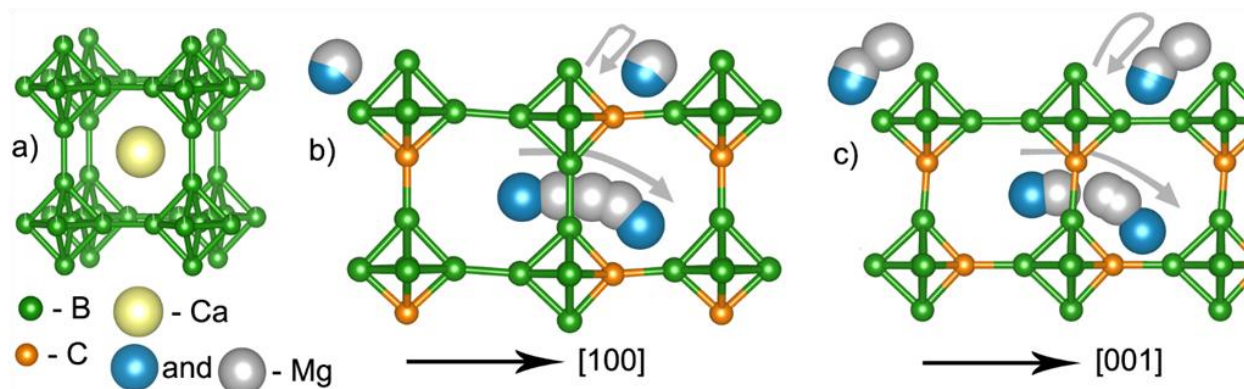


**Figure 5.1:** Crystal structure models of (a) calcium hexaboride,  $CaB_6$ , and (b-c)  $Mg_{0.5}B_5C$  for Mg ion diffusion in  $[100]$  and  $[00\bar{1}]$ . Mg ions in the initial and the final positions are shown as blue spheres, while grey spheres represent Mg atoms in the intermediate positions. Grey arrows indicate ion movements during the diffusion process.

A candidate compound with high magnesium-ion diffusion was found by focusing on structures containing only light and abundant elements, framework crystal structures with large openings between  $Mg^{2+}$  sites, and structures with a large number of  $Mg^{2+}$  vacancies. The metal hexaborides,  $MB_6$  ( $M =$

alkaline earth or rare earth elements), has attracted attention due to the simplicity of their chemical compositions, low formula weights, as well as due to peculiarities of the crystal and electronic structures.<sup>331,332</sup> The metal hexaboride crystal structure has consisted of a three-dimensional framework of linked B<sub>6</sub> octahedra (Figure 5.1a). The *M* ions would have a 24-fold coordination by boron atoms in eight different octahedra. The hexaboride structure could be described with the CsCl-type structure with the B<sub>6</sub> units in the Cl positions.<sup>333,334</sup> The bonding in hexaborides could also be understood using a molecular orbital theory description of the B<sub>6</sub> octahedra.<sup>335,336</sup> When examining the molecular orbitals of the structure, the lowest in energy would be the seven bonding orbitals filled with 14 electrons shared between all 6 boron atoms in an octahedron. Significant electronic density has been delocalized in B<sub>6</sub> units, which has been considered to be beneficial for facile ionic diffusion due to lower electronic density along the cation diffusion pathway. There have been also six outward pointing orbitals reported in the molecular orbital diagram at higher energies, which have been localized between each B<sub>6</sub> octahedra. These orbitals form 2c-2e (2-center-2-electron) bonds with other boron octahedra.<sup>335,336</sup> Thus, taking into consideration framework crystal structure and delocalized electronic density of the anionic part, metal hexaborides look promising for *M* ionic conductivity to occur. However, all *M* positions have been occupied in many MB<sub>6</sub> compounds; thus, no ionic conductivity by a vacancy mechanism has been expected.

Therefore, NaB<sub>5</sub>C carbaboride was considered as a possible parent phase for the Mg<sub>0.5</sub>B<sub>5</sub>C compound with half of the cation positions vacant. The compound NaB<sub>5</sub>C has been reported to be isostructural with hexaborides with carbon and boron atoms sharing the same crystallographic position.<sup>337</sup> The proposed Mg<sub>0.5</sub>B<sub>5</sub>C compound would be isoelectronic with NaB<sub>5</sub>C and could be potentially be prepared by aliovalent ion exchange of Mg<sup>2+</sup> for 2 Na<sup>1+</sup> ions. Such aliovalent exchange reactions, would result in cation vacancy formation, as demonstrated for layered transition metal oxides.<sup>156,338</sup> Partial topochemical lithium deintercalation from Li<sub>2</sub>B<sub>6</sub> has been reported,<sup>339</sup> indicating the



viability of soft chemistry approaches for hexaborides and the possibility of  $\text{Mg}_{0.5}\text{B}_5\text{C}$  synthesis. Thus, a density functional theory (DFT) investigation of cationic mobility in  $\text{Mg}_{0.5}\text{B}_5\text{C}$  has been performed.

## **5.2 Computational Methods**

Density functional theory calculations were used to determine activation barriers for  $\text{Mg}^{2+}$  diffusion in  $\text{Mg}_{0.5}\text{B}_5\text{C}$ . Initially, total energies for  $\text{NaB}_5\text{C}$  structures with different carbon and boron ordering patterns were calculated, the structural parameters of a supposed  $\text{Mg}_{0.5}\text{B}_5\text{C}$  structure was then established, and in the last step, activation barriers for  $\text{Mg}^{2+}$  diffusion in different crystallographic directions were calculated. Some calculations were performed with the Perdew-Wang 91 GGA functional as implemented in the Vienna Ab-initio Simulation Package (VASP) 5.2.12,<sup>177,182,183,186,257,258,299</sup> as well as the Perdew-Burke-Ernzerhof '96 functional using Quantum Espresso 5.1.<sup>175,182,183,185,196–199,256,340</sup> The nudged elastic band method was used to establish activation energy of  $\text{Mg}^{2+}$  diffusion.<sup>200,203,341</sup>

The boron/carbon ordered  $\text{NaB}_5\text{C}$  structures were calculated using a double volume unit cell ( $\text{Na}_2\text{B}_{10}\text{C}_2$ ), which was necessary to accommodate a large amount of possible anion ordering patterns. Crystal structures with the corresponding  $\text{B}_5\text{C}$  orientations have been shown in Figure 5.2 with the atomic positions provided in Table A.14-A.23. The experimental lattice parameters were used as the starting point. All Vienna Ab-initio Simulation Package (VASP) 5.2.12 calculations were spin-polarized and calculated with the projected augmented wave method, an energy cut-off of 400 eV, and the Perdew-Wang '91 functional.<sup>177,182,183,186,257,258,299</sup> The single point energy of each double unit was first calculated with an automatic mesh of 7000 k-points followed by a geometry optimization with an automatic mesh of 200 k-points using the conjugant gradient method.<sup>195</sup> A final single point calculation of each optimized structure was made with a 7500 automatic k-point mesh. In Quantum Espresso 5.1 the structures were relaxed with the BFGS algorithm, a wave-function cut-off of 50 Ry, and a k-point mesh of 4 x 8 x 8, and the Perdew-Burke-Ernzerhof '96 functional.<sup>175,182,183,185,196–199,256</sup>

The structural parameters for  $\text{Mg}_{0.5}\text{B}_5\text{C}$  were constructed by an analogous procedure utilizing data for calculated for the  $\text{NaB}_5\text{C}$  structures with a particular boron/carbon ordering with the sodium atoms removed and half of the sodium positions occupied by magnesium in a checkerboard pattern (Figure 5.1 b and c, Appendix Tables A.24-27). A super cell of the  $\text{Mg}_4\text{B}_{40}\text{C}_8$  composition was used for the calculations. For calculations of the band structure and density of states for  $\text{Mg}_{0.5}\text{B}_5\text{C}$ , the unit cell was relaxed with a wave-function cut-off of 60 Ry, a density cut-off of 240 Ry, a k-point mesh of  $5 \times 5 \times 5$ , 115 bands, and the PBE96 functional in Quantum Espresso 5.1.<sup>175,185,256</sup> The band structure was calculated with 100 k-points along the shown path.

The nudged elastic band (NEB) approach was used for calculating the activation energy of  $\text{Mg}^{2+}$  diffusion in the structure. With Quantum Espresso 5.1, the beginning and the end points of each nudged elastic band calculation were relaxed with a wave-function cut-off of 60 Ry and a density cut-off of 240 Ry at the gamma point only. For the nudged elastic band method the [100] and [001] directions and a total of 5 images were used. The band in the [001]-direction was converged to a value of 0.01 eV/atom and the band in the [100]-direction was converged to a value of 0.05 eV/atom. The functional used was the PBE96 functional,<sup>200,203,341,342</sup> and the band was optimized with the Broyden's method.<sup>201</sup>

For the  $\text{Mg}_8\text{B}_{40}\text{C}_8$  super cell calculations of the electronic structure, the unit cell was relaxed with a wave-function cut-off of 60 Ry, a density cut-off of 240 Ry, a k-point mesh of  $5 \times 5 \times 5$ , and the PBE96 functional in Quantum Espresso 5.1. A magnesium unit cell of 2 atoms was calculated with a wave-function cut-off of 180 Ry, a density cut-off of 720 Ry, and Gaussian smearing of 0.002 Ry. The intercalation voltage was calculated based on the relation of  $V = \Delta G / nF$ , where  $V$  is the voltage,  $\Delta G$  is the free energy of the reaction,  $n$  is the number of electrons exchanged in the reaction and  $F$  is Faraday's constant.

### 5.3 Results & Discussion

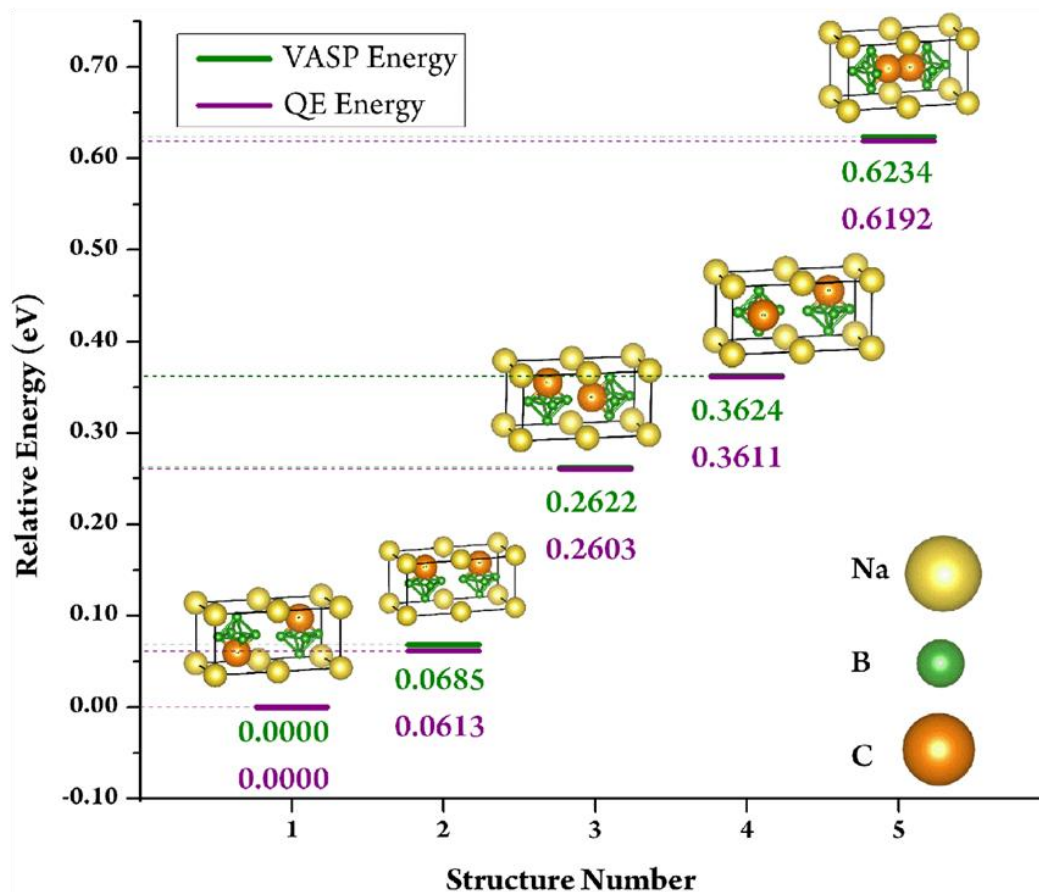


**Figure 5.2: Relative energies for  $\text{NaB}_5\text{C}$  structures with different boron and carbon ordering patterns. Carbon atoms are oversized for clarity.**

The  $\text{NaB}_5\text{C}$  structures with different boron/carbon ordering patterns and corresponding total energies have been displayed in Figure 5.2. The point of the different double unit cells was to investigate how different carbon ordering patterns could affect the relative energy of the structures. In the boron/carbon ordering pattern represented by the structure **1** (Figure 5.2) the vertex with carbon atoms of the  $\text{B}_5\text{C}$  units point in opposite directions, maximized the carbon-carbon distance. Smaller carbon-carbon separation in the structures **2**, **3** and **4** (Figure 5.2) lead to higher energies. The structure **5**, with a direct carbon-carbon bond was the highest in energy.

A comparison of the experimental and calculated cell parameters for  $\text{NaB}_5\text{C}$  has been presented in Table 5.1. The lattice parameters were determined by two DFT codes (VASP and Quantum Espresso)

which gave similar results. While the structures **1** and **2** were the lowest in energy, the *c* cell parameter differed by more than 4% with the experimental data. For the structure **3** the deviations of the calculated cell parameters to the experimental parameters were less than 1.6%. Thus, the boron/carbon ordering pattern shown in structure **3** was used as the starting model for  $\text{Mg}_{0.5}\text{B}_5\text{C}$ .

**Table 5.1: Unit cell parameters and volumes for the  $\text{NaB}_5\text{C}$  structures with different carbon/boron ordering patterns after the structure relaxations with Quantum Espresso or VASP.**

Software Used		Structure 1		Structure 2		Structure 3		Structure 4		Structure 5	
		Value ( $\text{\AA}$ or $\text{\AA}^3$ )	Change (%)	Value ( $\text{\AA}$ or $\text{\AA}^3$ )	Change (%)	Value ( $\text{\AA}$ or $\text{\AA}^3$ )	Change (%)	Value ( $\text{\AA}$ or $\text{\AA}^3$ )	Change (%)	Value ( $\text{\AA}$ or $\text{\AA}^3$ )	Change (%)
Quantum Espresso	<i>a</i>	4.1474	1.3427	4.1547	1.5223	4.0300	-1.5260	4.1549	1.5272	3.9232	-4.1357
	<i>b</i>	4.1570	1.5785	4.1570	1.5785	4.1567	1.5712	4.0264	-1.6127	4.1525	1.4686
	<i>c</i>	3.9048	-4.5841	3.9044	-4.5939	4.0268	-1.6030	4.0264	-1.6127	4.1525	1.4686
	Vol.	67.320	-1.7765	67.4332	-1.6125	67.4541	-1.5821	67.3588	-1.7211	67.6479	-1.2994
VASP	<i>a</i>	4.1523	1.4629	4.1604	1.6614	4.0338	-1.4322	4.1596	1.6430	3.9281	-4.0150
	<i>b</i>	4.1622	1.7051	4.1604	1.6614	4.1627	1.7186	4.0315	-1.4884	4.1580	1.6027
	<i>c</i>	3.9088	-4.4866	3.9091	-4.4790	4.0314	-1.4899	4.0315	-1.4884	4.1580	1.6027
	Vol.	67.553	-1.4368	67.6621	-1.2786	67.6941	-1.2320	67.6062	-1.3602	67.9123	-0.9136

*\*Lattice parameters *b* and *c* were taken from the relaxed structures directly while the shown *a* lattice parameters are half of that of the super cells used for the calculations. Percent change are given relatively to the cell parameter determined experimentally for  $\text{NaB}_5\text{C}$  (4.0925  $\text{\AA}$ ).<sup>343</sup>*

The initial  $\text{Mg}_{0.5}\text{B}_5\text{C}$  structure was created from four repeated units of  $\text{NaB}_5\text{C}$  with magnesium located in half of sodium positions in a checkerboard pattern. The magnesium ion should be smaller than the sodium ion. Therefore, it would not be surprising that the volume per formula unit has been smaller for the magnesium compound in comparison with that of the  $\text{NaB}_5\text{C}$  compound (Table A.21 and A.25). Additionally, magnesium ions have moved off the idealized corner positions during the structure relaxation.

The activation energies for  $\text{Mg}^{2+}$  diffusion in the  $[100]$  and in the  $[00\bar{1}]$  directions were smaller than 1 eV as shown in Figure 5.3. Activation energy values have reached a maximum of 0.92 eV for a jump in the  $[100]$  direction. However, the value for the activation energy for the ionic diffusion in the  $[00\bar{1}]$  direction has been reported with a low value of just 0.39 eV. The important question to ask would be what has caused such a large difference in activation energies. During the jump, the  $\text{Mg}^{2+}$  ion has

passed through an opening formed by four B<sub>5</sub>C octahedra. In the case of the jump in the [100] direction, the Mg<sup>2+</sup> ion has moved through a ring entirely made out of boron atoms (Figure 5.1b, 5.1c and 5.4 a); however, the movement in the [001] direction has corresponded to a movement through an inner ring containing two carbon and six boron atoms.

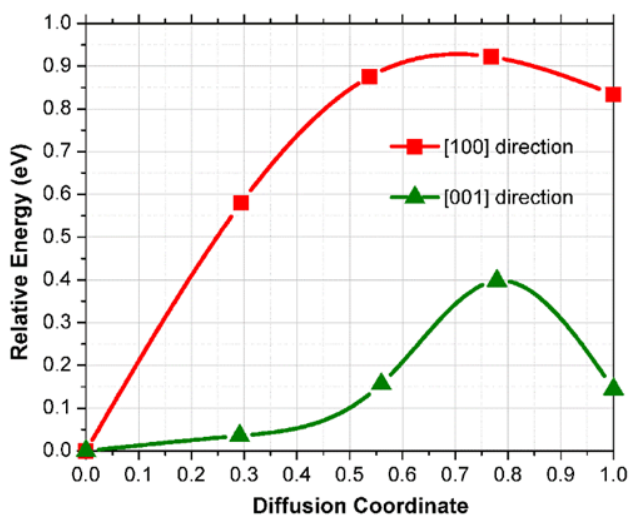


**Figure 5.3: Energy barriers for magnesium ion diffusion in the [100] and [001] direction for Mg<sub>0.5</sub>B<sub>5</sub>C.**

Considering the sections of the electronic density in Mg<sub>0.5</sub>B<sub>5</sub>C, as shown in Figures 5.4 and 5.5, localization of the electron density on the carbon atoms has been more pronounced. While this effect has some undesirability at a first glance, the presence of carbon atoms along the diffusion pathway has led to a lower activation energy for the diffusion pathway. In the transition state, the magnesium carbon interaction distance was 2.5 Å, which has been comparable to magnesium carbon bonding in Grignard reagents (2.3 Å).<sup>344</sup> Therefore, it has been reasonable to assume that an extra electron density around the carbon atoms have facilitated the movement of the magnesium ions through a temporary weak bonding interactions. Interestingly, The Mg<sup>2+</sup> jump initially has initially caused the nearest magnesium ion to move up 1.4 Å out its position and then to return, which probably minimized the coulomb repulsion between the ions during the transition state to some small extent (Figure 5.1b and c). On the other hand, the boron/carbon framework would stay essentially unchanged during the Mg<sup>2+</sup> jump, with boron/carbon atoms moving less than 0.1 Å.

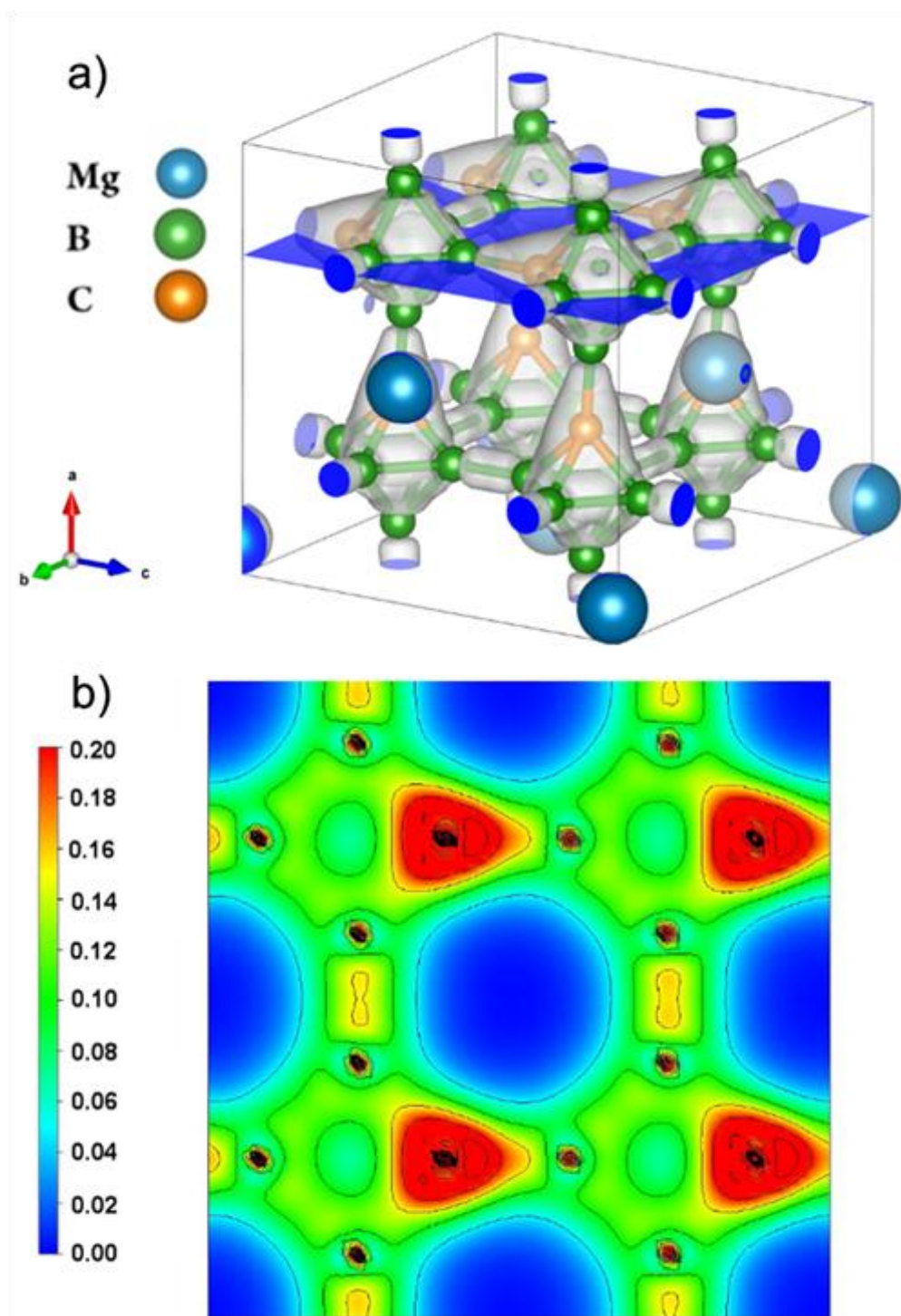
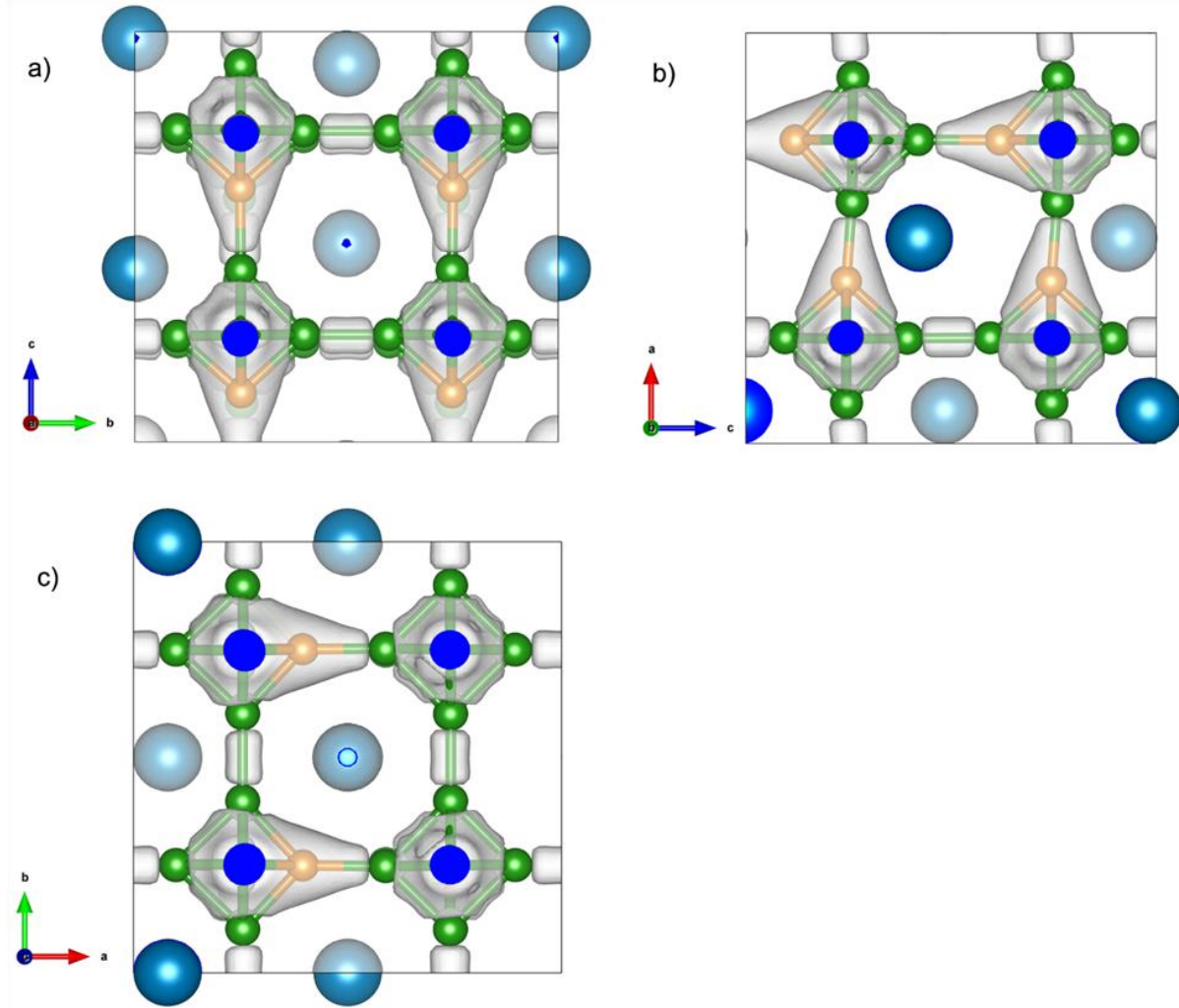


Figure 5.4: The charge density isosurfaces for  $\text{MgB}_5\text{C}$ : (a) a 3D view of the isosurface at  $0.115 \text{ e}/\text{\AA}^3$ , (b) the charge density section along the plane shown in (a) in values of  $\text{e}/\text{\AA}^3$ .



**Figure 5.5:** Electron density isosurface ( $0.115 \text{ e}/\text{\AA}^3$ ) of the optimized  $\text{Mg}_{0.5}\text{B}_5\text{C}$  structure. Section (a) is a view in the  $[\bar{1}00]$  direction; (b) is a view in the  $[0\bar{1}0]$  direction; (c) is a view in the  $[00\bar{1}]$  direction. Magnesium, boron and carbon atoms have been represented by blue, green, and orange spheres, respectively.

Based on the equations stated by Wilkinson<sup>345</sup>, Mehrer<sup>346</sup>, and Cussler<sup>347</sup> and explored by Park<sup>65</sup>, the connection between the ionic hopping activation energy, mass diffusivity, and ionic conductivity can be illustrated by equations 5.1, 5.2 and 5.3. While Park has used these equations to review lithium-ion conduction, the equations can universally describe conduction phenomenon in many ionic conduction materials.

$$\Gamma = \nu^0 \exp\left(-\frac{\Delta G}{k_B T}\right) \quad (5.1)$$

$$D_i = a_i^2 \Gamma \quad (5.2)$$

$$\sigma = \frac{q_i^2 c_i}{k_B T} D_i \quad (5.3)$$

In equation 5.1,  $v^0$  is the attempt frequency,  $\Delta G$  is the activation energy for ionic hopping,  $k_B$  is the Boltzmann constant, and  $T$  is temperature. In equation 5.2,  $a_i$  is the hopping length for ion  $i$  and  $D_i$  has typically been typically described as mass diffusivity of ion  $i$ . Equation 5.3 describes the direct correlation between mass diffusivity and ionic conductivity;  $q_i$  is the charge of ion  $i$  and  $c_i$  is the concentration of the ion  $i$  in the material.

The attempt frequency,  $v^0$ , has typically been calculated as a ratio of the product of the ground state normal modes to the product of the transition state normal modes.<sup>348,349</sup> However, instead of calculating the attempt frequency, the values have been taken from other sources for magnesium and lithium.<sup>52,350,351</sup> Values for lithium were used because lithium and magnesium have similar size and reactivity.<sup>36,352</sup> The attempt frequency values used for analysis were 1 THz<sup>52</sup>, 10 THz<sup>350</sup>, 16THz, and 18.99 THz.<sup>351</sup> From the NEB calculations of  $Mg_{0.5}B_5C$  in the  $[100]$  and  $[00\bar{1}]$  directions, the respective magnesium ionic hopping activation energies of 922 meV and 398 meV were used for further approximations of the ionic conductivity. The hoping distance and the concentration of ionic carriers were taken from structures used in the  $[100]$  and the  $[00\bar{1}]$  direction NEB calculations. The concentration of the ionic carriers was found based on the ratio of the number of magnesium ions in the cell per the volume of the unit cell. With the hopping activation energies, the hoping distance, the concentration of ionic carriers, and the attempt frequency taken from literature, the mass diffusivity and the ionic conduction of  $Mg_{0.5}B_5C$  were calculated at temperatures of 100K and 300K with equations 5.1, 5.2, and 5.3. They values has been displayed in Table 5.2. The mass diffusivity and ionic conduction values were comparable to conduction and diffusivity in many lithium-ion battery materials at 300k. Even with values calculated from magnesium-ion attempt frequencies, the mass diffusivity and ionic



conduction were agreeable.

It has been important to remember while diffusivity and conduction can be described similarly, they are not equal statement. Diffusivity has been defined as a constant that relates diffusion flux across a conduction gradient for changing concentrations, thus it can only relate to how fast an ion can hop on its own.<sup>353</sup> Ionic conductivity has related more to the number of ions that can be conducted per length of material which has included the information of vacancy concentration and mass diffusivity<sup>150</sup>. Ionic conductivity could be described as more encompassing value. Considering the low value of 0.39 eV for the activation energy of the ionic diffusion, high ionic conductivity can be expected for  $Mg^{2+}$  in the  $Mg_{0.5}B_5C$  compound.<sup>37</sup> For comparison, the ionic diffusion activation energy for  $Mg^{2+}$  was 1.31 eV in  $Mg(BH_4)(NH_2)$ ,<sup>327</sup> and 0.7 eV in  $MgVPO_4F$ .<sup>326</sup> The ionic diffusion activation energy in  $Mg_{0.5}B_5C$  was reported in the range typical for lithium ion conductors, such as  $Li_3OCl$  with an ionic diffusion energy of 0.36 eV.<sup>35438</sup>

**Table 5.2: Calculated mass diffusivity and ionic conduction of  $Mg_{0.5}B_5C$**

[100]- direction Diffusivity ( $m^2/s$ )			[001]-direction Diffusivity ( $m^2/s$ )		
	Temperature (K)			Temperature (K)	
Attempt Frequency (THz)	100	300	Attempt Frequency (THz)	100	300
1	$3.38818 \times 10^{-54}$	$3.17834 \times 10^{-23}$	1	$9.09953 \times 10^{-28}$	$2.08593 \times 10^{-14}$
10	$3.38818 \times 10^{-53}$	$3.17834 \times 10^{-22}$	10	$9.09953 \times 10^{-27}$	$2.08593 \times 10^{-13}$
16	$5.4211 \times 10^{-53}$	$5.08535 \times 10^{-22}$	16	$1.45593 \times 10^{-26}$	$3.33749 \times 10^{-13}$
18.99	$6.43416 \times 10^{-53}$	$6.03567 \times 10^{-22}$	18.99	$1.728 \times 10^{-26}$	$3.96118 \times 10^{-13}$
[100]-direction Ionic Conductivity (S/cm)			[001]-direction Ionic Conductivity (S/cm)		
	Temperature (K)			Temperature (K)	
Attempt Frequency (THz)	100	300	Attempt Frequency (THz)	100	300
1	$1.84723 \times 10^{-44}$	$5.77607 \times 10^{-14}$	1	$4.961 \times 10^{-18}$	$3.79078 \times 10^{-5}$
10	$1.84723 \times 10^{-43}$	$5.77607 \times 10^{-13}$	10	$4.961 \times 10^{-17}$	$3.79078 \times 10^{-4}$
16	$2.95556 \times 10^{-43}$	$9.24171 \times 10^{-13}$	16	$7.9376 \times 10^{-17}$	$6.06525 \times 10^{-4}$
18.99	$3.50788 \times 10^{-43}$	$1.09688 \times 10^{-12}$	18.99	$9.42094 \times 10^{-17}$	$7.19869 \times 10^{-4}$

The  $Mg_{0.5}B_5C$  electronic band structure calculated using the PBE96 functional has been shown in Figure 5.6. The material has a direct band gap of about 1.0 eV at the gamma point for this functional.<sup>355</sup>

However, It has been known that band gaps have been strongly underestimated in DFT calculations.<sup>356</sup> Therefore, in order to get a better evaluation of the band gap value for  $\text{Mg}_{0.5}\text{B}_5\text{C}$ , a calculation with the hybrid functional, HSE06 was performed.<sup>187–189</sup> The hybrid functional calculation produced a band gap value of 1.98 eV, which would sufficiently large for utilization of the  $\text{Mg}_{0.5}\text{B}_5\text{C}$  structure as a solid electrolyte with several well studied cathodes, such as the  $\text{Mo}_6\text{S}_8$  Chevrel phase, the Prussian blue analogs and the  $\text{MoS}_2$  structure.<sup>357</sup>

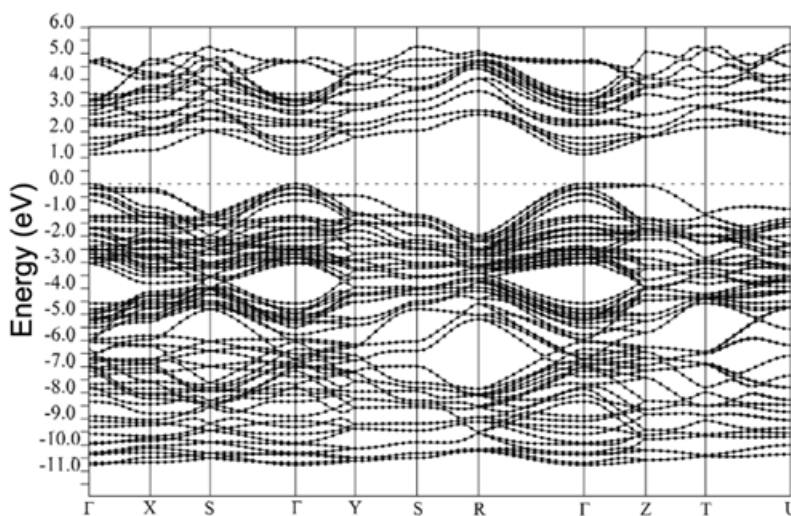


**Figure 5.6: Calculated electronic band structure for the  $\text{Mg}_{0.5}\text{B}_5\text{C}$  structure. K-points have been given for an orthorhombic symmetry of the Brillion zone. The Fermi energy has been set to an energy of zero.**

Thus, the calculated band gap value and low diffusion activation energy have been favorable for the  $\text{Mg}_{0.5}\text{B}_5\text{C}$  structure as a solid electrolyte. However, since  $\text{Mg}_{0.5}\text{B}_5\text{C}$  would be a potential solid electrolyte to be utilized with a magnesium metal anode, stability toward  $\text{Mg}^{2+}$  intercalation needs to be verified, as well. This would be especially important since half of cationic positions in the  $\text{Mg}_{0.5}\text{B}_5\text{C}$  structure would be vacant. The calculated potential for the reaction ( $0.5 \text{ Mg} + \text{Mg}_{0.5}\text{B}_5\text{C} \rightarrow \text{Mg}_1\text{B}_5\text{C}$ ) has been calculated with a value of -0.84 V, i.e. the reaction would not be spontaneous. Therefore,  $\text{Mg}_{0.5}\text{B}_5\text{C}$  should be stable against  $\text{Mg}^{2+}$  intercalation and could be utilized as a magnesium-ion solid electrolyte in batteries with a magnesium metal anode. However, the potential for ( $0.5 \text{ Mg} + \text{B}_5\text{C} \rightarrow \text{Mg}_{0.5}\text{B}_5\text{C}$ ) was found to be 1.56V which could lead to issues with a magnesium-ion cathode. This reported value could

also lead to applications as a cathode material, but the material may need to be engineered for increased electrical conductivity.

## **5.4 Conclusion**

In conclusion,  $\text{Mg}_{0.5}\text{B}_5\text{C}$  has been proposed as a new class of magnesium-ion conductor with low activation energy of  $\text{Mg}^{2+}$  diffusion, a large number of vacancies for the cation position, and a stability against  $\text{Mg}^{2+}$  intercalation, when used with a magnesium metal anode. The  $\text{Mg}_{0.5}\text{B}_5\text{C}$  compound has only contained light and abundant elements, which has been favorable for lower cost and higher gravimetric specific energy of a battery. The presence of carbon atoms along the  $\text{Mg}^{2+}$  diffusion pathway has facilitated diffusion by stabilizing the activation state of magnesium ion diffusion. Additionally, the results provoke interest in ionic conductivity of other related compounds with the hexaboride crystal structure and monovalent cations such as  $\text{Li}_2\text{B}_6$  and  $\text{NaB}_5\text{C}$  for potential battery materials, as well.

## APPENDIX

# APPENDIX

**Table A.1: Muffin tin sphere orbital occupations for the ordered PBE96 SrFeO<sub>2</sub>F ferromagnetic structure. The muffin-tin size is listed next to each atomic symbol in atomic units.**

Sr:2.00	S	P	D	F	PX	PY	PZ	D-Z2	D-X2Y2	D-XY	D-XZ	D-YZ	VALANCE	TOTAL
UP	0.9116	2.4152	0.0407	0.0024	0.8037	0.8037	0.8077	0.0061	0.0067	0.0074	0.01	0.01	3.37	17.36936
DOWN	0.9113	2.4139	0.0391	0.0023	0.8036	0.8036	0.8071	0.0054	0.0068	0.0065	0.0103	0.0103	3.367	17.36648
TOTAL	1.8229	4.8291	0.0798	0.0047	1.6073	1.6073	1.6148	0.0115	0.0135	0.0139	0.0203	0.0203	6.737	34.73584
Fe-1:1.90	S	P	D	F	PZ	PXY	D-Z2	D-XY	D-X2Y2	D-XZ,YZ	VALANCE	TOTAL		
UP	0.081	3.063	4.1727	0.0157	1.0089	2.054	0.8926	0.582	0.909	1.7893	7.336	13.3315		
DOWN	0.067	3.052	1.2746	0.0148	1.0048	2.0471	0.1052	0.238	0.2012	0.7306	4.4119	10.40702		
TOTAL	0.148	6.115	5.4473	0.0305	2.0137	4.1011	0.9978	0.82	1.1102	2.5199	11.7479	23.73852		
Fe-2:1.90	S	P	D	F	PZ	PXY	D-Z2	D-XY	D-X2Y2	D-XZ,YZ	VALANCE	TOTAL		
UP	0.081	3.063	4.1727	0.0157	1.0089	2.054	0.8926	0.582	0.909	1.7893	7.336	13.3315		
DOWN	0.067	3.052	1.2746	0.0148	1.0048	2.0471	0.1052	0.238	0.2012	0.7306	4.4119	10.40702		
TOTAL	0.148	6.115	5.4473	0.0305	2.0137	4.1011	0.9978	0.82	1.1102	2.5199	11.7479	23.73852		
Fe-3:1.90	S	P	D	F	PZ	PXY	D-Z2	D-XY	D-X2Y2	D-XZ,YZ	VALANCE	TOTAL		
UP	0.081	3.063	4.1727	0.0157	1.0089	2.054	0.8926	0.582	0.909	1.7893	7.336	13.3315		
DOWN	0.067	3.052	1.2746	0.0148	1.0048	2.0471	0.1052	0.238	0.2012	0.7306	4.4119	10.40702		
TOTAL	0.148	6.115	5.4473	0.0305	2.0137	4.1011	0.9978	0.82	1.1102	2.5199	11.7479	23.73852		
Fe-4:1.90	S	P	D	F	PZ	PXY	D-Z2	D-XY	D-X2Y2	D-XZ,YZ	VALANCE	TOTAL		
UP	0.081	3.063	4.1727	0.0157	1.0089	2.054	0.8926	0.582	0.909	1.7893	7.336	13.3315		
DOWN	0.067	3.052	1.2746	0.0148	1.0048	2.0471	0.1052	0.238	0.2012	0.7306	4.4119	10.40702		
TOTAL	0.148	6.115	5.4473	0.0305	2.0137	4.1011	0.9978	0.82	1.1102	2.5199	11.7479	23.73852		
O-1:1.64	S	P	D	F	PX	PY	PZ	D-Z2	D-X2Y2	D-XY	D-XZ	D-YZ	VALANCE	TOTAL
UP	0.8114	1.8979	0.0099	0.0023	0.6556	0.6768	0.5654	0.004	0	0	0.0028	0.0026	2.722	3.722039
DOWN	0.8026	1.7597	0.0061	0.0012	0.5629	0.6057	0.5913	0.0013	0	0	0.0024	0.0019	2.5702	3.570238
TOTAL	1.614	3.6576	0.016	0.0035	1.2185	1.2825	1.1567	0.0053	0	0	0.0052	0.0045	5.2922	7.292277
O-2:1.64	S	P	D	F	PX	PY	PZ	D-Z2	D-X2Y2	D-XY	D-XZ	D-YZ	VALANCE	TOTAL
UP	0.8114	1.8979	0.0099	0.0023	0.6556	0.6768	0.5654	0.004	0	0	0.0028	0.0026	2.722	3.722039
DOWN	0.8026	1.7597	0.0061	0.0012	0.5629	0.6057	0.5913	0.0013	0	0	0.0024	0.0019	2.5702	3.570238
TOTAL	1.614	3.6576	0.016	0.0035	1.2185	1.2825	1.1567	0.0053	0	0	0.0052	0.0045	5.2922	7.292277
F-1:1.84	S	P	D	F	PZ	PXY	D-Z2	D-XY	D-X2Y2	D-XZ,YZ	VALANCE	TOTAL		
UP	0.942	2.4946	0.012	0.0029	0.8336	1.661	0.0057	0.0006	0.0007	0.0052	3.4523	4.452325		
DOWN	0.9318	2.4326	0.007	0.0017	0.7802	1.6525	0.0007	0.0006	0.0007	0.0049	3.3731	4.373146		
TOTAL	1.8738	4.9272	0.019	0.0046	1.6138	3.3135	0.0064	0.0012	0.0014	0.0101	6.8254	8.825471		
F-2:1.84	S	P	D	F	PZ	PXY	D-Z2	D-XY	D-X2Y2	D-XZ,YZ	VALANCE	TOTAL		
UP	0.942	2.4946	0.012	0.0029	0.8336	1.661	0.0057	0.0006	0.0007	0.0052	3.4523	4.452327		
DOWN	0.9318	2.4326	0.007	0.0017	0.7802	1.6525	0.0007	0.0006	0.0007	0.0049	3.3731	4.373145		
TOTAL	1.8738	4.9272	0.019	0.0046	1.6138	3.3135	0.0064	0.0012	0.0014	0.0101	6.8254	8.825471		

**Table A.2: Muffin tin sphere orbital occupations for the ordered PBE96 SrFeO<sub>2</sub>F antiferromagnetic column structure. The muffin-tin size is listed next to each atomic symbol in atomic units.**

Sr:2.00	S	P	D	F	PX	PY	PZ	D-Z2	D-X2Y2	D-XY	D-XZ	D-YZ	VALANCE	TOTAL
UP	0.9116	2.4144	0.0403	0.0024	0.8036	0.8036	0.8074	0.006	0.0066	0.007	0.01	0.0105	3.3689	17.36826
DOWN	0.9116	2.4144	0.0403	0.0024	0.8036	0.8036	0.8074	0.006	0.0066	0.007	0.0105	0.01	3.3689	17.36826
TOTAL	1.8232	4.8288	0.0806	0.0048	1.6072	1.6072	1.6148	0.012	0.0132	0.014	0.0205	0.0205	6.7378	34.73653
Fe-1:1.90	S	P	D	F	PZ	PXY	D-Z2	D-XY	D-X2Y2	D-XZ,YZ	VALANCE	TOTAL		
UP	0.0842	3.0647	4.3524	0.0153	1.0093	2.0553	0.9181	0.7688	0.8996	1.7659	7.5202	13.51561		
DOWN	0.0689	3.0548	1.0603	0.0154	1.0055	2.0494	0.1904	0.3229	0.1378	0.4094	4.2031	10.19836		
TOTAL	0.1531	6.1195	5.4127	0.0307	2.0148	4.1047	1.1085	1.0917	1.0374	2.1753	11.7233	23.71397		
Fe-2:1.90	S	P	D	F	PZ	PXY	D-Z2	D-XY	D-X2Y2	D-XZ,YZ	VALANCE	TOTAL		
UP	0.0689	3.0548	1.0604	0.0154	1.0055	2.0494	0.1904	0.3229	0.1378	0.4095	4.2035	10.19837		
DOWN	0.0842	3.0647	4.3524	0.0153	1.0093	2.0553	0.9181	0.7688	0.8996	1.7659	7.5202	13.5156		
TOTAL	0.1531	6.1195	5.4128	0.0307	2.0148	4.1047	1.1085	1.0917	1.0374	2.1754	11.7237	23.71397		
Fe-3:1.90	S	P	D	F	PZ	PXY	D-Z2	D-XY	D-X2Y2	D-XZ,YZ	VALANCE	TOTAL		
UP	0.0842	3.0647	4.3523	0.0153	1.0093	2.0553	0.9181	0.7688	0.8996	1.7659	7.5202	13.5156		
DOWN	0.0689	3.0548	1.0602	0.0154	1.0055	2.0494	0.1904	0.3229	0.1378	0.4093	4.2031	10.19836		
TOTAL	0.1531	6.1195	5.4125	0.0307	2.0148	4.1047	1.1085	1.0917	1.0374	2.1752	11.7233	23.71397		
Fe-4:1.90	S	P	D	F	PZ	PXY	D-Z2	D-XY	D-X2Y2	D-XZ,YZ	VALANCE	TOTAL		
UP	0.0689	3.0548	1.0603	0.0154	1.0055	2.0494	0.1904	0.3229	0.1378	0.4093	4.2032	10.19839		
DOWN	0.0842	3.0647	4.3523	0.0153	1.0093	2.0553	0.9181	0.7688	0.8996	1.7659	7.5202	13.51559		
TOTAL	0.1531	6.1195	5.4126	0.0307	2.0148	4.1047	1.1085	1.0917	1.0374	2.1752	11.7234	23.71398		
O-1:1.64	S	P	D	F	PX	PY	PZ	D-Z2	D-X2Y2	D-XY	D-XZ	D-YZ	VALANCE	TOTAL
UP	0.8096	1.8317	0.0085	0.0017	0.5967	0.6394	0.5954	0.0037	0	0	0.002	0.0019	2.652	3.651957
DOWN	0.8096	1.8317	0.0085	0.0017	0.5967	0.6394	0.5954	0.0037	0	0	0.002	0.0019	2.652	3.651957
TOTAL	1.6192	3.6634	0.017	0.0034	1.1934	1.2788	1.1908	0.0074	0	0	0.004	0.0038	5.304	7.303914
O-2:1.64	S	P	D	F	PX	PY	PZ	D-Z2	D-X2Y2	D-XY	D-XZ	D-YZ	VALANCE	TOTAL
UP	0.8096	1.8317	0.0085	0.0017	0.5967	0.6394	0.5954	0.0037	0	0	0.002	0.0019	2.652	3.651958
DOWN	0.8096	1.8317	0.0085	0.0017	0.5967	0.6394	0.5954	0.0037	0	0	0.002	0.0019	2.652	3.651955
TOTAL	1.6192	3.6634	0.017	0.0034	1.1934	1.2788	1.1908	0.0074	0	0	0.004	0.0038	5.304	7.303913
F-1:1.84	S	P	D	F	PZ	PXY	D-Z2	D-XY	D-X2Y2	D-XZ,YZ	VALANCE	TOTAL		
UP	0.9424	2.5025	0.012	0.0029	0.8414	1.661	0.006	0.0006	0.0007	0.0051	3.4607	4.460601		
DOWN	0.9326	2.4277	0.0064	0.0013	0.7803	1.6475	0.0011	0.0007	0.0007	0.0043	3.3684	4.368404		
TOTAL	1.875	4.9302	0.0184	0.0042	1.6217	3.3085	0.0071	0.0013	0.0014	0.0094	6.8291	8.829006		
F-2:1.84	S	P	D	F	PZ	PXY	D-Z2	D-XY	D-X2Y2	D-XZ,YZ	VALANCE	TOTAL		
UP	0.9326	2.4277	0.0064	0.0013	0.7803	1.6475	0.0011	0.0007	0.0007	0.0043	3.3684	4.368404		
DOWN	0.9424	2.5025	0.012	0.0029	0.8414	1.661	0.006	0.0006	0.0007	0.0051	3.4607	4.460601		
TOTAL	1.875	4.9302	0.0184	0.0042	1.6217	3.3085	0.0071	0.0013	0.0014	0.0094	6.8291	8.829006		

**Table A.3: Muffin tin sphere orbital occupations for the ordered PBE96 SrFeO<sub>2</sub>F antiferromagnetic sheet structure. The muffin-tin size is listed next to each atomic symbol in atomic units.**

Sr:2.00	S	P	D	F	PX	PY	PZ	D-Z2	D-X2Y2	D-XY	D-XZ	D-YZ	VALANCE	TOTAL
UP	0.9116	2.4145	0.0398	0.0023	0.8037	0.8037	0.8072	0.006	0.0068	0.0071	0.0101	0.0101	3.3686	17.36793
DOWN	0.9116	2.4145	0.0398	0.0023	0.8037	0.8037	0.8072	0.006	0.0068	0.0071	0.0101	0.0101	3.3686	17.36793
TOTAL	1.8232	4.829	0.0796	0.0046	1.6074	1.6074	1.6144	0.012	0.0136	0.0142	0.0202	0.0202	6.7372	34.73586
Fe-1:1.90	S	P	D	F	PZ	PXY	D-Z2	D-XY	D-X2Y2	D-XZ,YZ	VALANCE	TOTAL		
UP	0.0805	3.0618	4.1585	0.0154	1.0079	2.0537	0.8811	0.5796	0.9089	1.7888	7.3198	13.31525		
DOWN	0.0684	3.0527	1.2916	0.0149	1.0059	2.0468	0.1342	0.238	0.1988	0.7207	4.4311	10.42621		
TOTAL	0.1489	6.1145	5.4501	0.0303	2.0138	4.1005	1.0153	0.8176	1.1077	2.5095	11.7509	23.74145		
Fe-2:1.90	S	P	D	F	PZ	PXY	D-Z2	D-XY	D-X2Y2	D-XZ,YZ	VALANCE	TOTAL		
UP	0.0805	3.0618	4.1584	0.0154	1.0079	2.0537	0.8811	0.5796	0.9089	1.7888	7.3198	13.31523		
DOWN	0.0684	3.0527	1.2916	0.0149	1.0059	2.0468	0.1342	0.238	0.1988	0.7207	4.4311	10.42623		
TOTAL	0.1489	6.1145	5.45	0.0303	2.0138	4.1005	1.0153	0.8176	1.1077	2.5095	11.7509	23.74146		
Fe-3:1.90	S	P	D	F	PZ	PXY	D-Z2	D-XY	D-X2Y2	D-XZ,YZ	VALANCE	TOTAL		
UP	0.0684	3.0527	1.2915	0.0149	1.0059	2.0468	0.1342	0.238	0.1988	0.7207	4.4311	10.4262		
DOWN	0.0805	3.0618	4.1585	0.0154	1.0079	2.0537	0.8811	0.5796	0.9089	1.7888	7.3198	13.31525		
TOTAL	0.1489	6.1145	5.45	0.0303	2.0138	4.1005	1.0153	0.8176	1.1077	2.5095	11.7509	23.74145		
Fe-4:1.90	S	P	D	F	PZ	PXY	D-Z2	D-XY	D-X2Y2	D-XZ,YZ	VALANCE	TOTAL		
UP	0.0684	3.0527	1.2916	0.0149	1.0059	2.0468	0.1342	0.238	0.1988	0.7207	4.4311	10.42624		
DOWN	0.0805	3.0618	4.1584	0.0154	1.0079	2.0537	0.8811	0.5796	0.9089	1.7888	7.3198	13.31523		
TOTAL	0.1489	6.1145	5.45	0.0303	2.0138	4.1005	1.0153	0.8176	1.1077	2.5095	11.7509	23.74146		
O-1:1.64	S	P	D	F	PX	PY	PZ	D-Z2	D-X2Y2	D-XY	D-XZ	D-YZ	VALANCE	TOTAL
UP	0.8106	1.897	0.0098	0.0023	0.6545	0.6768	0.5656	0.0039	0	0	0.0028	0.0026	2.7209	3.720721
DOWN	0.8027	1.7602	0.0061	0.0012	0.5631	0.606	0.591	0.0013	0	0	0.0024	0.0019	2.5706	3.570867
TOTAL	1.6133	3.6572	0.0159	0.0035	1.2176	1.2828	1.1566	0.0052	0	0	0.0052	0.0045	5.2915	7.291588
O-2:1.64	S	P	D	F	PX	PY	PZ	D-Z2	D-X2Y2	D-XY	D-XZ	D-YZ	VALANCE	TOTAL
UP	0.8027	1.7602	0.0061	0.0012	0.5631	0.606	0.591	0.0013	0	0	0.0024	0.0019	2.5706	3.570867
DOWN	0.8106	1.897	0.0098	0.0023	0.6545	0.6768	0.5656	0.0039	0	0	0.0028	0.0026	2.7209	3.720721
TOTAL	1.6133	3.6572	0.0159	0.0035	1.2176	1.2828	1.1566	0.0052	0	0	0.0052	0.0045	5.2915	7.291588
F-1:1.84	S	P	D	F	PZ	PXY	D-Z2	D-XY	D-X2Y2	D-XZ,YZ	VALANCE	TOTAL		
UP	0.9385	2.4595	0.0098	0.0019	0.8012	1.6582	0.0036	0.0006	0.0007	0.0049	3.4108	4.410707		
DOWN	0.9385	2.4595	0.0098	0.0019	0.8012	1.6582	0.0036	0.0006	0.0007	0.0049	3.4108	4.410707		
TOTAL	1.877	4.919	0.0196	0.0038	1.6024	3.3164	0.0072	0.0012	0.0014	0.0098	6.8216	8.821415		
F-2:1.84	S	P	D	F	PZ	PXY	D-Z2	D-XY	D-X2Y2	D-XZ,YZ	VALANCE	TOTAL		
UP	0.9385	2.4595	0.0098	0.0019	0.8012	1.6582	0.0036	0.0006	0.0007	0.0049	3.4108	4.410707		
DOWN	0.9385	2.4595	0.0098	0.0019	0.8012	1.6582	0.0036	0.0006	0.0007	0.0049	3.4108	4.410707		
TOTAL	1.877	4.919	0.0196	0.0038	1.6024	3.3164	0.0072	0.0012	0.0014	0.0098	6.8216	8.821414		

**Table A.4: Muffin tin sphere orbital occupations for the ordered PBE96 SrFeO<sub>2</sub>F total antiferromagnetic structure. The muffin-tin size is listed next to each atomic symbol in atomic units.**

Sr:2.00	S	P	D	F	PX	PY	PZ	D-Z2	D-X2Y2	D-XY	D-XZ	D-YZ	VALANCE	TOTAL
UP	0.9116	2.4145	0.0401	0.0024	0.8037	0.8037	0.8074	0.006	0.0065	0.007	0.0104	0.0104	3.3688	17.36827
DOWN	0.9116	2.4145	0.0401	0.0024	0.8037	0.8037	0.8074	0.006	0.0065	0.007	0.0104	0.0104	3.3688	17.36827
TOTAL	1.8232	4.829	0.0802	0.0048	1.6074	1.6074	1.6148	0.012	0.013	0.014	0.0208	0.0208	6.7376	34.73655
Fe-1:1.90	S	P	D	F	PZ	PXY	D-Z2	D-XY	D-X2Y2	D-XZ,YZ	VALANCE	TOTAL		
UP	0.0841	3.0635	4.3282	0.0153	1.0085	2.055	0.9001	0.7647	0.8992	1.7642	7.4944	13.48995		
DOWN	0.0705	3.0554	1.0883	0.0154	1.0062	2.0491	0.2066	0.3215	0.1371	0.4232	4.2334	10.22847		
TOTAL	0.1546	6.1189	5.4165	0.0307	2.0147	4.1041	1.1067	1.0862	1.0363	2.1874	11.7278	23.71842		
Fe-2:1.90	S	P	D	F	PZ	PXY	D-Z2	D-XY	D-X2Y2	D-XZ,YZ	VALANCE	TOTAL		
UP	0.0705	3.0554	1.0883	0.0154	1.0062	2.0491	0.2066	0.3215	0.1371	0.4232	4.2334	10.22846		
DOWN	0.0841	3.0635	4.3282	0.0153	1.0085	2.055	0.9001	0.7647	0.8992	1.7642	7.4944	13.48996		
TOTAL	0.1546	6.1189	5.4165	0.0307	2.0147	4.1041	1.1067	1.0862	1.0363	2.1874	11.7278	23.71842		
Fe-3:1.90	S	P	D	F	PZ	PXY	D-Z2	D-XY	D-X2Y2	D-XZ,YZ	VALANCE	TOTAL		
UP	0.0705	3.0554	1.0884	0.0154	1.0062	2.0491	0.2066	0.3215	0.1371	0.4232	4.2334	10.22846		
DOWN	0.0841	3.0635	4.3282	0.0153	1.0085	2.055	0.9001	0.7647	0.8992	1.7642	7.4944	13.48996		
TOTAL	0.1546	6.1189	5.4166	0.0307	2.0147	4.1041	1.1067	1.0862	1.0363	2.1874	11.7278	23.71842		
Fe-4:1.90	S	P	D	F	PZ	PXY	D-Z2	D-XY	D-X2Y2	D-XZ,YZ	VALANCE	TOTAL		
UP	0.0841	3.0635	4.3282	0.0153	1.0085	2.055	0.9001	0.7647	0.8992	1.7642	7.4944	13.48994		
DOWN	0.0705	3.0554	1.0883	0.0154	1.0062	2.0491	0.2066	0.3215	0.1371	0.4232	4.2333	10.22848		
TOTAL	0.1546	6.1189	5.4165	0.0307	2.0147	4.1041	1.1067	1.0862	1.0363	2.1874	11.7277	23.71842		
O-1:1.64	S	P	D	F	PX	PY	PZ	D-Z2	D-X2Y2	D-XY	D-XZ	D-YZ	VALANCE	TOTAL
UP	0.8095	1.8309	0.0085	0.0018	0.5966	0.6397	0.5945	0.0037	0	0	0.002	0.0019	2.651	3.651206
DOWN	0.8095	1.8309	0.0085	0.0018	0.5966	0.6397	0.5945	0.0037	0	0	0.002	0.0019	2.651	3.651205
TOTAL	1.619	3.6618	0.017	0.0036	1.1932	1.2794	1.189	0.0074	0	0	0.004	0.0038	5.302	7.302411
O-2:1.64	S	P	D	F	PX	PY	PZ	D-Z2	D-X2Y2	D-XY	D-XZ	D-YZ	VALANCE	TOTAL
UP	0.8095	1.8309	0.0085	0.0018	0.5966	0.6397	0.5945	0.0037	0	0	0.002	0.0019	2.651	3.651204
DOWN	0.8095	1.8309	0.0085	0.0018	0.5966	0.6397	0.5945	0.0037	0	0	0.002	0.0019	2.651	3.651207
TOTAL	1.619	3.6618	0.017	0.0036	1.1932	1.2794	1.189	0.0074	0	0	0.004	0.0038	5.302	7.302411
F-1:1.84	S	P	D	F	PZ	PXY	D-Z2	D-XY	D-X2Y2	D-XZ,YZ	VALANCE	TOTAL		
UP	0.939	2.4604	0.0098	0.002	0.8041	1.6564	0.0039	0.0006	0.0007	0.0046	3.4119	4.41198		
DOWN	0.939	2.4604	0.0098	0.002	0.8041	1.6564	0.0039	0.0006	0.0007	0.0046	3.4119	4.41198		
TOTAL	1.878	4.9208	0.0196	0.004	1.6082	3.3128	0.0078	0.0012	0.0014	0.0092	6.8238	8.82396		
F-2:1.84	S	P	D	F	PZ	PXY	D-Z2	D-XY	D-X2Y2	D-XZ,YZ	VALANCE	TOTAL		
UP	0.939	2.4604	0.0098	0.002	0.8041	1.6564	0.0039	0.0006	0.0007	0.0046	3.4119	4.41198		
DOWN	0.939	2.4604	0.0098	0.002	0.8041	1.6564	0.0039	0.0006	0.0007	0.0046	3.4119	4.41198		
TOTAL	1.878	4.9208	0.0196	0.004	1.6082	3.3128	0.0078	0.0012	0.0014	0.0092	6.8238	8.82396		



**Table A.5: Muffin tin sphere orbital occupations for the ordered PBE96+U SrFeO<sub>2</sub>F ferromagnetic structure. The muffin-tin size is listed next to each atomic symbol in atomic units.**

Sr:2.00	S	P	D	F	PX	PY	PZ	D-Z2	D-X2Y2	D-XY	D-XZ	D-YZ	VALANCE	TOTAL
UP	0.9119	2.4146	0.0412	0.0024	0.8036	0.8036	0.8079	0.0061	0.0062	0.0077	0.0106	0.0106	3.3705	17.37
DOWN	0.9116	2.4139	0.0408	0.0023	0.8032	0.8032	0.8076	0.0058	0.0064	0.007	0.011	0.011	3.369	17.36855
TOTAL	1.8235	4.8285	0.082	0.0047	1.6068	1.6068	1.6155	0.0119	0.0126	0.0147	0.0216	0.0216	6.7395	34.73854
Fe-1:1.90	S	P	D	F	PZ	PXY	D-Z2	D-XY	D-X2Y2	D-XZ,YZ	VALANCE	TOTAL		
UP	0.0948	3.0746	4.5794	0.0165	1.0107	2.0638	0.9369	0.8877	0.9237	1.831	7.7687	13.76433		
DOWN	0.0702	3.0559	0.7231	0.0153	1.0058	2.0501	0.0923	0.2078	0.1021	0.321	3.868	9.863068		
TOTAL	0.165	6.1305	5.3025	0.0318	2.0165	4.1139	1.0292	1.0955	1.0258	2.152	11.6367	23.6274		
Fe-2:1.90	S	P	D	F	PZ	PXY	D-Z2	D-XY	D-X2Y2	D-XZ,YZ	VALANCE	TOTAL		
UP	0.0948	3.0746	4.5794	0.0165	1.0107	2.0638	0.9369	0.8877	0.9237	1.831	7.7687	13.76433		
DOWN	0.0702	3.0559	0.7231	0.0153	1.0058	2.0501	0.0923	0.2078	0.1021	0.3209	3.8679	9.86307		
TOTAL	0.165	6.1305	5.3025	0.0318	2.0165	4.1139	1.0292	1.0955	1.0258	2.1519	11.6366	23.6274		
Fe-3:1.90	S	P	D	F	PZ	PXY	D-Z2	D-XY	D-X2Y2	D-XZ,YZ	VALANCE	TOTAL		
UP	0.0948	3.0746	4.5794	0.0165	1.0107	2.0638	0.9369	0.8877	0.9237	1.831	7.7687	13.76438		
DOWN	0.0702	3.0559	0.7229	0.0153	1.0058	2.0501	0.0923	0.2078	0.1021	0.3206	3.8678	9.863		
TOTAL	0.165	6.1305	5.3023	0.0318	2.0165	4.1139	1.0292	1.0955	1.0258	2.1516	11.6365	23.62738		
Fe-4:1.90	S	P	D	F	PZ	PXY	D-Z2	D-XY	D-X2Y2	D-XZ,YZ	VALANCE	TOTAL		
UP	0.0948	3.0746	4.5795	0.0165	1.0107	2.0638	0.9369	0.8877	0.9237	1.831	7.7687	13.7644		
DOWN	0.0702	3.0559	0.7229	0.0153	1.0058	2.0501	0.0923	0.2078	0.1021	0.3206	3.8678	9.862958		
TOTAL	0.165	6.1305	5.3024	0.0318	2.0165	4.1139	1.0292	1.0955	1.0258	2.1516	11.6365	23.62736		
O-1:1.64	S	P	D	F	PX	PY	PZ	D-Z2	D-X2Y2	D-XY	D-XZ	D-YZ	VALANCE	TOTAL
UP	0.8144	1.9314	0.0095	0.0023	0.6434	0.6714	0.6165	0.0049	0	0	0.0019	0.0021	2.7586	3.758466
DOWN	0.7997	1.7671	0.0041	0.0012	0.5598	0.6112	0.5961	0.0012	0	0	0.0011	0.0013	2.5723	3.572367
TOTAL	1.6141	3.6985	0.0136	0.0035	1.2032	1.2826	1.2126	0.0061	0	0	0.003	0.0034	5.3309	7.330833
O-2:1.64	S	P	D	F	PX	PY	PZ	D-Z2	D-X2Y2	D-XY	D-XZ	D-YZ	VALANCE	TOTAL
UP	0.8144	1.9314	0.0095	0.0023	0.6434	0.6714	0.6165	0.0049	0	0	0.0019	0.0021	2.7586	3.758494
DOWN	0.7997	1.7671	0.0041	0.0012	0.5598	0.6112	0.5961	0.0012	0	0	0.0011	0.0013	2.5723	3.572344
TOTAL	1.6141	3.6985	0.0136	0.0035	1.2032	1.2826	1.2126	0.0061	0	0	0.003	0.0034	5.3309	7.330838
F-1:1.84	S	P	D	F	PZ	PXY	D-Z2	D-XY	D-X2Y2	D-XZ,YZ	VALANCE	TOTAL		
UP	0.9416	2.5071	0.0109	0.0029	0.8437	1.6635	0.0053	0.0006	0.0007	0.0043	3.4634	4.463351		
DOWN	0.9319	2.4321	0.0062	0.0012	0.7873	1.6447	0.0008	0.0006	0.0007	0.0043	3.3718	4.371758		
TOTAL	1.8735	4.9392	0.0171	0.0041	1.631	3.3082	0.0061	0.0012	0.0014	0.0086	6.8352	8.835108		
F-2:1.84	S	P	D	F	PZ	PXY	D-Z2	D-XY	D-X2Y2	D-XZ,YZ	VALANCE	TOTAL		
UP	0.9416	2.5071	0.0109	0.0029	0.8437	1.6635	0.0053	0.0006	0.0007	0.0043	3.4634	4.46335		
DOWN	0.9319	2.4321	0.0062	0.0012	0.7873	1.6447	0.0008	0.0006	0.0007	0.0043	3.3717	4.371759		
TOTAL	1.8735	4.9392	0.0171	0.0041	1.631	3.3082	0.0061	0.0012	0.0014	0.0086	6.8351	8.83511		

**Table A.6: Muffin tin sphere orbital occupations for the ordered PBE96+U SrFeO<sub>2</sub>F antiferromagnetic column structure. The muffin-tin size is listed next to each atomic symbol in atomic units.**

Sr:2.00	S	P	D	F	PX	PY	PZ	D-Z2	D-X2Y2	D-XY	D-XZ	D-YZ	VALANCE	TOTAL
UP	0.9118	2.4144	0.0412	0.0024	0.803	0.8035	0.808	0.006	0.006	0.0076	0.0105	0.0112	3.37	17.36945
DOWN	0.9118	2.4144	0.0412	0.0024	0.8035	0.803	0.808	0.006	0.006	0.0076	0.0112	0.0105	3.37	17.36945
TOTAL	1.8236	4.8288	0.0824	0.0048	1.6065	1.6065	1.616	0.012	0.012	0.0152	0.0217	0.0217	6.74	34.73891
Fe-1:1.90	S	P	D	F	PZ	PXY	D-Z2	D-XY	D-X2Y2	D-XZ,YZ	VALANCE	TOTAL		
UP	0.0888	3.0703	4.632	0.0155	1.0107	2.0598	0.9371	0.9471	0.9216	1.8265	7.8104	13.80598		
DOWN	0.074	3.0621	0.6554	0.0163	1.0062	2.0558	0.1191	0.2716	0.1023	0.1627	3.8115	9.806594		
TOTAL	0.1628	6.1324	5.2874	0.0318	2.0169	4.1156	1.0562	1.2187	1.0239	1.9892	11.6219	23.61258		
Fe-2:1.90	S	P	D	F	PZ	PXY	D-Z2	D-XY	D-X2Y2	D-XZ,YZ	VALANCE	TOTAL		
UP	0.074	3.0621	0.6554	0.0163	1.0062	2.0558	0.1191	0.2716	0.1023	0.1627	3.8115	9.806595		
DOWN	0.0888	3.0703	4.632	0.0155	1.0107	2.0598	0.9371	0.9471	0.9216	1.8265	7.8104	13.80598		
TOTAL	0.1628	6.1324	5.2874	0.0318	2.0169	4.1156	1.0562	1.2187	1.0239	1.9892	11.6219	23.61258		
Fe-3:1.90	S	P	D	F	PZ	PXY	D-Z2	D-XY	D-X2Y2	D-XZ,YZ	VALANCE	TOTAL		
UP	0.0888	3.0703	4.632	0.0155	1.0107	2.0598	0.9371	0.9471	0.9216	1.8265	7.8104	13.80598		
DOWN	0.074	3.0621	0.6554	0.0163	1.0062	2.0558	0.1191	0.2716	0.1023	0.1627	3.8115	9.806594		
TOTAL	0.1628	6.1324	5.2874	0.0318	2.0169	4.1156	1.0562	1.2187	1.0239	1.9892	11.6219	23.61258		
Fe-4:1.90	S	P	D	F	PZ	PXY	D-Z2	D-XY	D-X2Y2	D-XZ,YZ	VALANCE	TOTAL		
UP	0.074	3.0621	0.6554	0.0163	1.0062	2.0558	0.1191	0.2716	0.1023	0.1627	3.8115	9.806595		
DOWN	0.0888	3.0703	4.632	0.0155	1.0107	2.0598	0.9371	0.9471	0.9216	1.8265	7.8104	13.80598		
TOTAL	0.1628	6.1324	5.2874	0.0318	2.0169	4.1156	1.0562	1.2187	1.0239	1.9892	11.6219	23.61258		
O-1:1.64	S	P	D	F	PX	PY	PZ	D-Z2	D-X2Y2	D-XY	D-XZ	D-YZ	VALANCE	TOTAL
UP	0.8077	1.8521	0.0072	0.0017	0.595	0.6399	0.6172	0.0035	0	0	0.0014	0.0016	2.6692	3.669263
DOWN	0.8077	1.8521	0.0072	0.0017	0.595	0.6399	0.6172	0.0035	0	0	0.0014	0.0016	2.6692	3.669263
TOTAL	1.6154	3.7042	0.0144	0.0034	1.19	1.2798	1.2344	0.007	0	0	0.0028	0.0032	5.3384	7.338525
O-2:1.64	S	P	D	F	PX	PY	PZ	D-Z2	D-X2Y2	D-XY	D-XZ	D-YZ	VALANCE	TOTAL
UP	0.8077	1.8521	0.0072	0.0017	0.595	0.6399	0.6172	0.0035	0	0	0.0014	0.0016	2.6692	3.669263
DOWN	0.8077	1.8521	0.0072	0.0017	0.595	0.6399	0.6172	0.0035	0	0	0.0014	0.0016	2.6692	3.669263
TOTAL	1.6154	3.7042	0.0144	0.0034	1.19	1.2798	1.2344	0.007	0	0	0.0028	0.0032	5.3384	7.338525
F-1:1.84	S	P	D	F	PZ	PXY	D-Z2	D-XY	D-X2Y2	D-XZ,YZ	VALANCE	TOTAL		
UP	0.9408	2.5026	0.0106	0.0028	0.8396	1.6628	0.0052	0.0006	0.0007	0.0042	3.4578	4.457502		
DOWN	0.9325	2.4386	0.0053	0.0012	0.7874	1.6508	0.0008	0.0008	0.0007	0.0036	3.378	4.377853		
TOTAL	1.8733	4.9412	0.0159	0.004	1.627	3.3136	0.006	0.0014	0.0014	0.0078	6.8358	8.835355		
F-2:1.84	S	P	D	F	PZ	PXY	D-Z2	D-XY	D-X2Y2	D-XZ,YZ	VALANCE	TOTAL		
UP	0.9325	2.4386	0.0053	0.0012	0.7874	1.6508	0.0008	0.0008	0.0007	0.0036	3.378	4.377853		
DOWN	0.9408	2.5026	0.0106	0.0028	0.8396	1.6628	0.0052	0.0006	0.0007	0.0042	3.4578	4.457502		
TOTAL	1.8733	4.9412	0.0159	0.004	1.627	3.3136	0.006	0.0014	0.0014	0.0078	6.8358	8.835355		

**Table A.7: Muffin tin sphere orbital occupations for the ordered PBE96+U SrFeO<sub>2</sub>F antiferromagnetic sheet structure. The muffin-tin size is listed next to each atomic symbol in atomic units.**

Sr:2.00	S	P	D	F	PX	PY	PZ	D-Z2	D-X2Y2	D-XY	D-XZ	D-YZ	VALANCE	TOTAL
UP	0.9118	2.4145	0.0413	0.0024	0.8035	0.8035	0.8079	0.006	0.0064	0.0073	0.0107	0.0107	3.3698	17.36931
DOWN	0.9118	2.4145	0.0413	0.0024	0.8035	0.8035	0.8079	0.006	0.0064	0.0073	0.0107	0.0107	3.3698	17.36931
TOTAL	1.8236	4.829	0.0826	0.0048	1.607	1.607	1.6158	0.012	0.0128	0.0146	0.0214	0.0214	6.7396	34.73862
Fe-1:1.90	S	P	D	F	PZ	PXY	D-Z2	D-XY	D-X2Y2	D-XZ,YZ	VALANCE	TOTAL		
UP	0.095	3.074	4.5832	0.0165	1.0098	2.064	0.9315	0.8966	0.9238	1.8313	7.772	13.76766		
DOWN	0.0711	3.0566	0.7176	0.0153	1.0066	2.0501	0.1063	0.2076	0.1021	0.3022	3.8642	9.859366		
TOTAL	0.1661	6.1306	5.3008	0.0318	2.0164	4.1141	1.0378	1.1042	1.0259	2.1335	11.6362	23.62703		
Fe-2:1.90	S	P	D	F	PZ	PXY	D-Z2	D-XY	D-X2Y2	D-XZ,YZ	VALANCE	TOTAL		
UP	0.095	3.074	4.5832	0.0165	1.0098	2.064	0.9315	0.8966	0.9238	1.8313	7.772	13.76766		
DOWN	0.0711	3.0566	0.7176	0.0153	1.0066	2.0501	0.1063	0.2076	0.1021	0.3022	3.8642	9.859367		
TOTAL	0.1661	6.1306	5.3008	0.0318	2.0164	4.1141	1.0378	1.1042	1.0259	2.1335	11.6362	23.62703		
Fe-3:1.90	S	P	D	F	PZ	PXY	D-Z2	D-XY	D-X2Y2	D-XZ,YZ	VALANCE	TOTAL		
UP	0.0711	3.0566	0.7177	0.0153	1.0066	2.0501	0.1063	0.2076	0.1021	0.3023	3.8642	9.859372		
DOWN	0.095	3.074	4.5832	0.0165	1.0098	2.064	0.9315	0.8966	0.9238	1.8313	7.772	13.76766		
TOTAL	0.1661	6.1306	5.3009	0.0318	2.0164	4.1141	1.0378	1.1042	1.0259	2.1336	11.6362	23.62703		
Fe-4:1.90	S	P	D	F	PZ	PXY	D-Z2	D-XY	D-X2Y2	D-XZ,YZ	VALANCE	TOTAL		
UP	0.0711	3.0566	0.7177	0.0153	1.0066	2.0501	0.1063	0.2076	0.1021	0.3023	3.8642	9.859377		
DOWN	0.095	3.074	4.5832	0.0165	1.0098	2.064	0.9315	0.8966	0.9238	1.8313	7.772	13.76766		
TOTAL	0.1661	6.1306	5.3009	0.0318	2.0164	4.1141	1.0378	1.1042	1.0259	2.1336	11.6362	23.62703		
O-1:1.64	S	P	D	F	PX	PY	PZ	D-Z2	D-X2Y2	D-XY	D-XZ	D-YZ	VALANCE	TOTAL
UP	0.8143	1.932	0.0095	0.0023	0.6415	0.671	0.6194	0.0049	0	0	0.0019	0.0021	2.759	3.759154
DOWN	0.7997	1.7673	0.004	0.0012	0.5606	0.6112	0.5957	0.0012	0	0	0.0011	0.0013	2.5727	3.572625
TOTAL	1.614	3.6993	0.0135	0.0035	1.2021	1.2822	1.2151	0.0061	0	0	0.003	0.0034	5.3317	7.331778
O-2:1.64	S	P	D	F	PX	PY	PZ	D-Z2	D-X2Y2	D-XY	D-XZ	D-YZ	VALANCE	TOTAL
UP	0.7997	1.7673	0.004	0.0012	0.5606	0.6112	0.5957	0.0012	0	0	0.0011	0.0013	2.5727	3.572626
DOWN	0.8143	1.932	0.0095	0.0023	0.6415	0.671	0.6194	0.0049	0	0	0.0019	0.0021	2.759	3.759153
TOTAL	1.614	3.6993	0.0135	0.0035	1.2021	1.2822	1.2151	0.0061	0	0	0.003	0.0034	5.3317	7.331779
F-1:1.84	S	P	D	F	PZ	PXY	D-Z2	D-XY	D-X2Y2	D-XZ,YZ	VALANCE	TOTAL		
UP	0.9377	2.4674	0.0087	0.0018	0.8108	1.6565	0.0034	0.0006	0.0007	0.004	3.4165	4.41627		
DOWN	0.9377	2.4674	0.0087	0.0018	0.8108	1.6565	0.0034	0.0006	0.0007	0.004	3.4165	4.41627		
TOTAL	1.8754	4.9348	0.0174	0.0036	1.6216	3.313	0.0068	0.0012	0.0014	0.008	6.833	8.83254		
F-2:1.84	S	P	D	F	PZ	PXY	D-Z2	D-XY	D-X2Y2	D-XZ,YZ	VALANCE	TOTAL		
UP	0.9377	2.4674	0.0087	0.0018	0.8108	1.6565	0.0034	0.0006	0.0007	0.004	3.4165	4.41627		
DOWN	0.9377	2.4674	0.0087	0.0018	0.8108	1.6565	0.0034	0.0006	0.0007	0.004	3.4165	4.416269		
TOTAL	1.8754	4.9348	0.0174	0.0036	1.6216	3.313	0.0068	0.0012	0.0014	0.008	6.833	8.832539		

**Table A.8: Muffin tin sphere orbital occupations tables for the ordered PBE96+U SrFeO<sub>2</sub>F total antiferromagnetic sheet structure. The muffin-tin size is listed next to each atomic symbol in atomic units.**

Sr:2.00	S	P	D	F	PX	PY	PZ	D-Z2	D-X2Y2	D-XY	D-XZ	D-YZ	VALANCE	TOTAL
UP	0.9118	2.4144	0.0412	0.0024	0.8031	0.8031	0.808	0.006	0.006	0.0076	0.0109	0.0109	3.37	17.36946
DOWN	0.9118	2.4144	0.0412	0.0024	0.8031	0.8031	0.808	0.006	0.006	0.0076	0.0109	0.0109	3.37	17.36946
TOTAL	1.8236	4.8288	0.0824	0.0048	1.6062	1.6062	1.616	0.012	0.012	0.0152	0.0218	0.0218	6.74	34.73892
Fe-1:1.90	S	P	D	F	PZ	PXY	D-Z2	D-XY	D-X2Y2	D-XZ,YZ	VALANCE	TOTAL		
UP	0.0887	3.0695	4.6261	0.0154	1.0096	2.0598	0.9316	0.9466	0.9214	1.8264	7.8034	13.79888		
DOWN	0.0746	3.0626	0.664	0.0163	1.0068	2.0556	0.1314	0.2703	0.102	0.1605	3.8212	9.816398		
TOTAL	0.1633	6.1321	5.2901	0.0317	2.0164	4.1154	1.063	1.2169	1.0234	1.9869	11.6246	23.61528		
Fe-2:1.90	S	P	D	F	PZ	PXY	D-Z2	D-XY	D-X2Y2	D-XZ,YZ	VALANCE	TOTAL		
UP	0.0746	3.0626	0.664	0.0163	1.0068	2.0556	0.1314	0.2703	0.102	0.1605	3.8212	9.816398		
DOWN	0.0887	3.0695	4.6261	0.0154	1.0096	2.0598	0.9316	0.9466	0.9214	1.8264	7.8034	13.79888		
TOTAL	0.1633	6.1321	5.2901	0.0317	2.0164	4.1154	1.063	1.2169	1.0234	1.9869	11.6246	23.61528		
Fe-3:1.90	S	P	D	F	PZ	PXY	D-Z2	D-XY	D-X2Y2	D-XZ,YZ	VALANCE	TOTAL		
UP	0.0746	3.0626	0.664	0.0163	1.0068	2.0556	0.1314	0.2703	0.102	0.1605	3.8212	9.816398		
DOWN	0.0887	3.0695	4.6261	0.0154	1.0096	2.0598	0.9316	0.9466	0.9214	1.8264	7.8034	13.79888		
TOTAL	0.1633	6.1321	5.2901	0.0317	2.0164	4.1154	1.063	1.2169	1.0234	1.9869	11.6246	23.61528		
Fe-4:1.90	S	P	D	F	PZ	PXY	D-Z2	D-XY	D-X2Y2	D-XZ,YZ	VALANCE	TOTAL		
UP	0.0887	3.0695	4.6261	0.0154	1.0096	2.0598	0.9316	0.9466	0.9214	1.8264	7.8034	13.79888		
DOWN	0.0746	3.0626	0.664	0.0163	1.0068	2.0556	0.1314	0.2703	0.102	0.1605	3.8212	9.816398		
TOTAL	0.1633	6.1321	5.2901	0.0317	2.0164	4.1154	1.063	1.2169	1.0234	1.9869	11.6246	23.61528		
O-1:1.64	S	P	D	F	PX	PY	PZ	D-Z2	D-X2Y2	D-XY	D-XZ	D-YZ	VALANCE	TOTAL
UP	0.8076	1.8521	0.0072	0.0017	0.5956	0.6401	0.6166	0.0035	0	0	0.0014	0.0016	2.6692	3.669093
DOWN	0.8076	1.8521	0.0072	0.0017	0.5956	0.6401	0.6166	0.0035	0	0	0.0014	0.0016	2.6692	3.669093
TOTAL	1.6152	3.7042	0.0144	0.0034	1.1912	1.2802	1.2332	0.007	0	0	0.0028	0.0032	5.3384	7.338187
O-2:1.64	S	P	D	F	PX	PY	PZ	D-Z2	D-X2Y2	D-XY	D-XZ	D-YZ	VALANCE	TOTAL
UP	0.8076	1.8521	0.0072	0.0017	0.5956	0.6401	0.6166	0.0035	0	0	0.0014	0.0016	2.6692	3.669093
DOWN	0.8076	1.8521	0.0072	0.0017	0.5956	0.6401	0.6166	0.0035	0	0	0.0014	0.0016	2.6692	3.669093
TOTAL	1.6152	3.7042	0.0144	0.0034	1.1912	1.2802	1.2332	0.007	0	0	0.0028	0.0032	5.3384	7.338187
F-1:1.84	S	P	D	F	PZ	PXY	D-Z2	D-XY	D-X2Y2	D-XZ,YZ	VALANCE	TOTAL		
UP	0.9375	2.4678	0.0083	0.0018	0.8099	1.6581	0.0032	0.0006	0.0007	0.0037	3.4162	4.41613		
DOWN	0.9375	2.4678	0.0083	0.0018	0.8099	1.6581	0.0032	0.0006	0.0007	0.0037	3.4162	4.41613		
TOTAL	1.875	4.9356	0.0166	0.0036	1.6198	3.3162	0.0064	0.0012	0.0014	0.0074	6.8324	8.832259		
F-2:1.84	S	P	D	F	PZ	PXY	D-Z2	D-XY	D-X2Y2	D-XZ,YZ	VALANCE	TOTAL		
UP	0.9375	2.4678	0.0083	0.0018	0.8099	1.6581	0.0032	0.0006	0.0007	0.0037	3.4162	4.41613		
DOWN	0.9375	2.4678	0.0083	0.0018	0.8099	1.6581	0.0032	0.0006	0.0007	0.0037	3.4162	4.41613		
TOTAL	1.875	4.9356	0.0166	0.0036	1.6198	3.3162	0.0064	0.0012	0.0014	0.0074	6.8324	8.832259		

**Table A.9: Muffin tin sphere orbital occupations for the disordered PBE96 SrFeO<sub>2</sub>F total antiferromagnetic structure. The muffin-tin size is listed next to each atomic symbol in atomic units.**

Sr-1:2.10	S	P	D	F	PX	PY	PZ	D-22	D-X2Y2	D-XY	D-XZ	D-YZ	VALENCE	TOTAL
UP	0.9367	2.5262	0.0504	0.0035	0.8409	0.8409	0.8441	0.0103	0.0113	0.0066	0.0113	0.011	3.5175	17.51712
DOWN	0.9367	2.5259	0.0504	0.0034	0.8409	0.8409	0.8441	0.0101	0.0111	0.0066	0.0107	0.0116	3.517	17.51667
TOTAL	1.8734	5.0521	0.1008	0.0069	1.6818	1.6818	1.6882	0.0204	0.0224	0.0132	0.022	0.0226	7.0345	35.03378
Sr-2:2.10	S	P	D	F	PX	PY	PZ	D-22	D-X2Y2	D-XY	D-XZ	D-YZ	VALENCE	TOTAL
UP	0.9368	2.5256	0.0503	0.0031	0.8404	0.8411	0.8436	0.0095	0.0099	0.0071	0.0118	0.0121	3.5162	17.51586
DOWN	0.9368	2.5253	0.0502	0.003	0.8404	0.8409	0.8436	0.0095	0.0099	0.007	0.0118	0.0119	3.5158	17.51543
TOTAL	1.8736	5.0509	0.1005	0.0061	1.6808	1.682	1.6872	0.019	0.0198	0.0141	0.0236	0.024	7.032	35.03129
Fe-1:1.88	S	P	D	F	PX	PY	PZ	D-22	D-X2Y2	D-XY	D-XZ	D-YZ	VALENCE	TOTAL
UP	0.0745	3.0423	4.44	0.0099	1.0096	1.0129	1.0197	0.8659	0.8922	0.8911	0.8955	0.8953	7.5688	13.56397
DOWN	0.0613	3.0357	0.8981	0.0106	1.0072	1.0114	1.0175	0.2505	0.1663	0.1741	0.1554	0.152	4.0081	10.00287
TOTAL	0.1358	6.078	5.3381	0.0205	2.0168	2.0243	2.0372	1.1164	1.0585	1.0652	1.0509	1.0473	11.5769	23.56684
Fe-2:1.88	S	P	D	F	PX	PY	PZ	D-22	D-X2Y2	D-XY	D-XZ	D-YZ	VALENCE	TOTAL
UP	0.0653	3.0321	0.9242	0.0098	1.0096	1.0077	1.0147	0.258	0.1648	0.2081	0.1348	0.1584	4.0336	10.02819
DOWN	0.071	3.0431	4.4123	0.0094	1.013	1.0125	1.0177	0.8577	0.8887	0.8827	0.8913	0.8918	7.5378	13.53283
TOTAL	0.1363	6.0752	5.3365	0.0192	2.0226	2.0202	2.0324	1.1157	1.0535	1.0908	1.0261	1.0502	11.5714	23.56102
Fe-3:1.88	S	P	D	F	PX	PY	PZ	D-22	D-X2Y2	D-XY	D-XZ	D-YZ	VALENCE	TOTAL
UP	0.0611	3.0323	0.8855	0.0106	1.0086	1.0042	1.0195	0.2526	0.1934	0.1378	0.1537	0.148	3.9919	9.986551
DOWN	0.0739	3.0418	4.4633	0.01	1.0132	1.0074	1.0215	0.8804	0.8924	0.9016	0.8935	0.8953	7.5916	13.58653
TOTAL	0.135	6.0741	5.3488	0.0206	2.0218	2.0116	2.041	1.133	1.0858	1.0394	1.0472	1.0433	11.5835	23.57308
Fe-4:1.88	S	P	D	F	PX	PY	PZ	D-22	D-X2Y2	D-XY	D-XZ	D-YZ	VALENCE	TOTAL
UP	0.0709	3.0421	4.4416	0.0099	1.0096	1.016	1.0167	0.8828	0.8893	0.8847	0.8922	0.8924	7.5664	13.56148
DOWN	0.0642	3.0317	0.8903	0.0099	1.0064	1.0107	1.0145	0.2545	0.1908	0.1935	0.1304	0.1214	3.9985	9.993338
TOTAL	0.1351	6.0738	5.3319	0.0198	2.016	2.0267	2.0312	1.1373	1.0801	1.0782	1.0226	1.0138	11.5649	23.55482
O-1:1.62	S	P	D	F	PX	PY	PZ	D-22	D-X2Y2	D-XY	D-XZ	D-YZ	VALENCE	TOTAL
UP	0.8016	1.8108	0.0053	0.001	0.5925	0.5867	0.6314	0.001	0.001	0.002	0.001	0.001	2.6191	3.619094
DOWN	0.8011	1.7814	0.005	0.001	0.5678	0.5897	0.6236	0.001	0.001	0.002	0.001	0.001	2.5889	3.588924
TOTAL	1.6027	3.5922	0.0103	0.002	1.1603	1.1764	1.255	0.002	0.002	0.004	0.002	0.002	5.208	7.208018
O-2:1.62	S	P	D	F	PX	PY	PZ	D-22	D-X2Y2	D-XY	D-XZ	D-YZ	VALENCE	TOTAL
UP	0.8013	1.8026	0.0059	0.001	0.6146	0.6123	0.5754	0.0028	0	0	0.001	0.001	2.6112	3.611034
DOWN	0.8007	1.7859	0.0059	0.001	0.5984	0.6054	0.5823	0.002	0	0	0.001	0.001	2.5937	3.593686
TOTAL	1.602	3.5885	0.0118	0.002	1.213	1.2177	1.1577	0.0048	0	0	0.002	0.002	5.2049	7.20472
O-3:1.62	S	P	D	F	PX	PY	PZ	D-22	D-X2Y2	D-XY	D-XZ	D-YZ	VALENCE	TOTAL
UP	0.8004	1.8101	0.005	0.001	0.587	0.5939	0.6294	0.001	0.001	0.002	0.001	0.001	2.6166	3.616572
DOWN	0.8002	1.7792	0.0044	0.001	0.5743	0.5837	0.6214	0.001	0.001	0.002	0.001	0.001	2.5851	3.585041
TOTAL	1.6006	3.5893	0.0094	0.002	1.1613	1.1776	1.2508	0.002	0.002	0.004	0.002	0.002	5.2017	7.201614
O-4:1.62	S	P	D	F	PX	PY	PZ	D-22	D-X2Y2	D-XY	D-XZ	D-YZ	VALENCE	TOTAL
UP	0.8034	1.787	0.0087	0.002	0.5934	0.5647	0.629	0.001	0.002	0.0029	0.001	0.001	2.6012	3.60121
DOWN	0.8043	1.8183	0.0082	0.002	0.5924	0.5985	0.6275	0.001	0.002	0.0029	0.001	0.001	2.6332	3.63328
TOTAL	1.6077	3.6053	0.0169	0.004	1.1858	1.1632	1.2565	0.002	0.004	0.0058	0.002	0.002	5.2344	7.23449
O-5:1.62	S	P	D	F	PX	PY	PZ	D-22	D-X2Y2	D-XY	D-XZ	D-YZ	VALENCE	TOTAL
UP	0.8006	1.7644	0.005	0.001	0.6005	0.5816	0.5822	0.002	0	0	0.001	0.001	2.5713	3.571305
DOWN	0.8005	1.8047	0.005	0.001	0.6083	0.6156	0.581	0.0021	0	0	0.001	0.001	2.612	3.612025
TOTAL	1.6011	3.5691	0.01	0.002	1.2088	1.1972	1.1632	0.0041	0	0	0.002	0.002	5.1833	7.18333
O-6:1.62	S	P	D	F	PX	PY	PZ	D-22	D-X2Y2	D-XY	D-XZ	D-YZ	VALENCE	TOTAL
UP	0.8017	1.8013	0.0068	0.001	0.6	0.5878	0.6137	0.001	0.0015	0.002	0.001	0.001	2.6112	3.611291
DOWN	0.8017	1.8014	0.0069	0.001	0.5931	0.5859	0.6221	0.001	0.0019	0.002	0.001	0.001	2.612	3.611823
TOTAL	1.6034	3.6027	0.0137	0.002	1.1931	1.1737	1.2358	0.002	0.0034	0.004	0.002	0.002	5.2232	7.223114
F-1:1.62	S	P	D	F	PX	PY	PZ	D-22	D-X2Y2	D-XY	D-XZ	D-YZ	VALENCE	TOTAL
UP	0.9379	2.4563	0.0055	0.001	0.8069	0.8155	0.8338	0.001	0.001	0.002	0.001	0.001	3.401	4.401088
DOWN	0.9379	2.4549	0.0056	0.001	0.8126	0.8095	0.833	0.001	0.001	0.002	0.001	0.001	3.4	4.399983
TOTAL	1.8758	4.9112	0.0111	0.002	1.6195	1.625	1.6668	0.002	0.002	0.004	0.002	0.002	6.801	8.801072
F-2:1.62	S	P	D	F	PX	PY	PZ	D-22	D-X2Y2	D-XY	D-XZ	D-YZ	VALENCE	TOTAL
UP	0.9386	2.4534	0.0069	0.001	0.8203	0.8012	0.8315	0.001	0.001	0.002	0.001	0.001	3.4006	4.400578
DOWN	0.9389	2.4678	0.0079	0.002	0.8116	0.8215	0.8348	0.001	0.002	0.002	0.001	0.001	3.4169	4.416813
TOTAL	1.8775	4.9212	0.0148	0.003	1.6319	1.6227	1.6663	0.002	0.003	0.004	0.002	0.002	6.8175	8.817391
F-3:1.62	S	P	D	F	PX	PY	PZ	D-22	D-X2Y2	D-XY	D-XZ	D-YZ	VALENCE	TOTAL
UP	0.939	2.4597	0.0079	0.0019	0.8123	0.8136	0.8337	0.001	0.0019	0.0028	0.001	0.001	3.409	4.409049
DOWN	0.9388	2.4588	0.0079	0.0019	0.8072	0.8214	0.8302	0.001	0.0019	0.0028	0.001	0.001	3.4074	4.407349
TOTAL	1.8778	4.9185	0.0158	0.0038	1.6195	1.635	1.6639	0.002	0.0038	0.0056	0.002	0.002	6.8164	8.816398
F-4:1.62	S	P	D	F	PX	PY	PZ	D-22	D-X2Y2	D-XY	D-XZ	D-YZ	VALENCE	TOTAL
UP	0.9378	2.4602	0.0049	0.001	0.819	0.8139	0.8276	0.001	0.001	0.001	0.001	0.001	3.4042	4.404227
DOWN	0.937	2.4459	0.004	0.001	0.8054	0.8155	0.8252	0.001	0.001	0.001	0.001	0.001	3.3883	4.38824
TOTAL	1.8748	4.9061	0.0089	0.002	1.6244	1.6294	1.6528	0.002	0.002	0.002	0.002	0.002	6.7925	8.792467

**Table A.10: Muffin tin sphere orbital occupations for the disordered PBE96+U SrFeO2F total antiferromagnetic structure. The muffin-tin size is listed next to each atomic symbol in atomic units.**

Sr-1:2.10	S	P	D	F	PX	PY	PZ	D-22	D-X2Y2	D-XY	D-XZ	D-YZ	VALENCE	TOTAL
UP	0.9372	2.526	0.0514	0.0035	0.8409	0.8409	0.8441	0.0105	0.0117	0.0067	0.0114	0.0112	3.5187	17.51833
DOWN	0.937	2.5259	0.0514	0.0035	0.8409	0.841	0.844	0.0105	0.0117	0.0067	0.0109	0.0116	3.5184	17.51804
TOTAL	1.8742	5.0519	0.1028	0.007	1.6818	1.6819	1.6881	0.021	0.0234	0.0134	0.0223	0.0228	7.0371	35.03637
Sr-2:2.10	S	P	D	F	PX	PY	PZ	D-22	D-X2Y2	D-XY	D-XZ	D-YZ	VALENCE	TOTAL
UP	0.9369	2.5256	0.0513	0.0031	0.8404	0.8413	0.8436	0.0096	0.0106	0.0071	0.0119	0.0121	3.5172	17.517
DOWN	0.9369	2.5254	0.0512	0.0031	0.8404	0.841	0.8436	0.0097	0.0106	0.0071	0.0119	0.0121	3.517	17.51665
TOTAL	1.8738	5.051	0.1025	0.0062	1.6808	1.6823	1.6872	0.0193	0.0212	0.0142	0.0238	0.0242	7.0342	35.03365
Fe-1:1.88	S	P	D	F	PX	PY	PZ	D-22	D-X2Y2	D-XY	D-XZ	D-YZ	VALENCE	TOTAL
UP	0.0786	3.0475	4.6055	0.0104	1.0111	1.0147	1.0217	0.9339	0.9135	0.9276	0.9149	0.9154	7.7443	13.73955
DOWN	0.0649	3.0397	4.6298	0.0107	1.0082	1.0125	1.0194	0.2133	0.0932	0.137	0.092	0.0943	3.7475	9.742171
TOTAL	0.1435	6.0872	5.2353	0.0211	2.0193	2.0272	2.0411	1.1472	1.0067	1.0646	1.0069	1.0097	11.4918	23.48172
Fe-2:1.88	S	P	D	F	PX	PY	PZ	D-22	D-X2Y2	D-XY	D-XZ	D-YZ	VALENCE	TOTAL
UP	0.0679	3.0366	4.6403	0.0099	1.011	1.0089	1.0166	0.2095	0.0921	0.1644	0.0831	0.0913	3.7567	9.751633
DOWN	0.0754	3.0481	4.5951	0.0099	1.0147	1.0142	1.0196	0.9291	0.9138	0.9242	0.9138	0.9142	7.7303	13.7256
TOTAL	0.1433	6.0847	5.2354	0.0198	2.0257	2.0231	2.0362	1.1386	1.0059	1.0886	0.9969	1.0055	11.487	23.47723
Fe-3:1.88	S	P	D	F	PX	PY	PZ	D-22	D-X2Y2	D-XY	D-XZ	D-YZ	VALENCE	TOTAL
UP	0.0645	3.0359	4.6403	0.0108	1.0097	1.0047	1.0213	0.2147	0.0922	0.1105	0.114	0.1084	3.754	9.748742
DOWN	0.078	3.0477	4.6058	0.0108	1.0154	1.0087	1.0237	0.931	0.9152	0.9275	0.9167	0.9153	7.7446	13.73979
TOTAL	0.1425	6.0836	5.2461	0.0216	2.0251	2.0134	2.045	1.1457	1.0074	1.038	1.0307	1.0237	11.4986	23.48853
Fe-4:1.88	S	P	D	F	PX	PY	PZ	D-22	D-X2Y2	D-XY	D-XZ	D-YZ	VALENCE	TOTAL
UP	0.0749	3.0479	4.6034	0.0099	1.0114	1.0184	1.0182	0.9331	0.9148	0.9265	0.9142	0.9153	7.7386	13.73379
DOWN	0.0673	3.0351	4.631	0.0105	1.0074	1.0123	1.0156	0.2061	0.1017	0.1528	0.0865	0.0837	3.7459	9.740698
TOTAL	0.1422	6.083	5.2344	0.0204	2.0188	2.0307	2.0338	1.1392	1.0165	1.0793	1.0007	0.999	11.4845	23.47449
O-1:1.62	S	P	D	F	PX	PY	PZ	D-22	D-X2Y2	D-XY	D-XZ	D-YZ	VALENCE	TOTAL
UP	0.7993	1.8241	0.005	0.001	0.5927	0.6003	0.6313	0.001	0.001	0.002	0.001	0.001	2.6293	3.629247
DOWN	0.7989	1.7993	0.0042	0.001	0.5847	0.5905	0.6245	0.001	0.001	0.001	0.001	0.001	2.6038	3.603744
TOTAL	1.5982	3.6234	0.0092	0.002	1.1774	1.1908	1.2558	0.002	0.002	0.003	0.002	0.002	5.2331	7.232991
O-2:1.62	S	P	D	F	PX	PY	PZ	D-22	D-X2Y2	D-XY	D-XZ	D-YZ	VALENCE	TOTAL
UP	0.7988	1.8183	0.005	0.001	0.6151	0.612	0.5912	0.002	0	0	0.001	0.001	2.6232	3.623317
DOWN	0.7984	1.8032	0.005	0.001	0.6026	0.6088	0.5917	0.002	0	0	0.001	0.001	2.6078	3.607667
TOTAL	1.5972	3.6215	0.01	0.002	1.2177	1.2208	1.1829	0.004	0	0	0.002	0.002	5.231	7.230985
O-3:1.62	S	P	D	F	PX	PY	PZ	D-22	D-X2Y2	D-XY	D-XZ	D-YZ	VALENCE	TOTAL
UP	0.7985	1.8206	0.004	0.001	0.5928	0.598	0.6297	0.001	0.001	0.0014	0.001	0.001	2.6245	3.624522
DOWN	0.7982	1.7956	0.004	0.001	0.5835	0.5893	0.6229	0.001	0.001	0.001	0.001	0.001	2.5989	3.598822
TOTAL	1.5967	3.6162	0.008	0.002	1.1763	1.1873	1.2526	0.002	0.002	0.0024	0.002	0.002	5.2234	7.223344
O-4:1.62	S	P	D	F	PX	PY	PZ	D-22	D-X2Y2	D-XY	D-XZ	D-YZ	VALENCE	TOTAL
UP	0.8005	1.8117	0.0069	0.0019	0.5927	0.5915	0.6277	0.001	0.002	0.002	0.001	0.001	2.6215	3.62153
DOWN	0.801	1.837	0.0069	0.0019	0.609	0.5988	0.629	0.001	0.002	0.002	0.001	0.001	2.6472	3.64712
TOTAL	1.6015	3.6487	0.0138	0.0038	1.2017	1.1903	1.2567	0.002	0.004	0.004	0.002	0.002	5.2687	7.268651
O-5:1.62	S	P	D	F	PX	PY	PZ	D-22	D-X2Y2	D-XY	D-XZ	D-YZ	VALENCE	TOTAL
UP	0.7984	1.7823	0.004	0.001	0.6023	0.5894	0.5904	0.002	0	0	0.001	0.001	2.586	3.586134
DOWN	0.7981	1.8186	0.0049	0.001	0.6126	0.6163	0.5893	0.002	0	0	0.001	0.001	2.6225	3.622585
TOTAL	1.5965	3.6009	0.0089	0.002	1.2149	1.2057	1.1797	0.004	0	0	0.002	0.002	5.2085	7.208719
O-6:1.62	S	P	D	F	PX	PY	PZ	D-22	D-X2Y2	D-XY	D-XZ	D-YZ	VALENCE	TOTAL
UP	0.7991	1.817	0.0056	0.001	0.6076	0.5954	0.6139	0.001	0.001	0.002	0.001	0.001	2.6229	3.622885
DOWN	0.7993	1.8199	0.0059	0.001	0.6008	0.5948	0.6244	0.001	0.001	0.002	0.001	0.001	2.6268	3.626684
TOTAL	1.5984	3.6369	0.0115	0.002	1.2084	1.1902	1.2383	0.002	0.002	0.004	0.002	0.002	5.2497	7.249569
F-1:1.85	S	P	D	F	PX	PY	PZ	D-22	D-X2Y2	D-XY	D-XZ	D-YZ	VALENCE	TOTAL
UP	0.9374	2.4596	0.0052	0.001	0.8086	0.8164	0.8344	0.001	0.001	0.002	0.001	0.001	3.4037	4.403649
DOWN	0.9374	2.4603	0.0052	0.001	0.8144	0.8118	0.8338	0.001	0.001	0.0013	0.001	0.001	3.4044	4.404323
TOTAL	1.8748	4.9199	0.0104	0.002	1.623	1.6282	1.6682	0.002	0.002	0.0033	0.002	0.002	6.8081	8.807972
F-2:1.85	S	P	D	F	PX	PY	PZ	D-22	D-X2Y2	D-XY	D-XZ	D-YZ	VALENCE	TOTAL
UP	0.9378	2.46	0.006	0.001	0.8215	0.8063	0.8324	0.001	0.001	0.002	0.001	0.001	3.4057	4.405635
DOWN	0.9381	2.4728	0.0069	0.0019	0.8144	0.8234	0.8348	0.001	0.0019	0.002	0.001	0.001	3.42	4.420105
TOTAL	1.8759	4.9328	0.0129	0.0029	1.6359	1.6297	1.6672	0.002	0.0029	0.004	0.002	0.002	6.8257	8.825739
F-3:1.85	S	P	D	F	PX	PY	PZ	D-22	D-X2Y2	D-XY	D-XZ	D-YZ	VALENCE	TOTAL
UP	0.9383	2.4658	0.0069	0.0019	0.8148	0.8169	0.834	0.001	0.001	0.002	0.001	0.001	3.4133	4.413204
DOWN	0.9379	2.4653	0.0069	0.0018	0.8109	0.8235	0.8309	0.001	0.0013	0.002	0.001	0.001	3.4121	4.411973
TOTAL	1.8762	4.9311	0.0138	0.0037	1.6257	1.6404	1.6649	0.002	0.0023	0.004	0.002	0.002	6.8254	8.825177
F-4:1.85	S	P	D	F	PX	PY	PZ	D-22	D-X2Y2	D-XY	D-XZ	D-YZ	VALENCE	TOTAL
UP	0.9373	2.4628	0.0049	0.001	0.8199	0.8147	0.8282	0.001	0.001	0.001	0.001	0.001	3.4059	4.406056
DOWN	0.9365	2.45	0.004	0.001	0.8075	0.8162	0.8261	0.001	0.001	0.001	0.001	0.001	3.3913	4.391283
TOTAL	1.8738	4.9128	0.0089	0.002	1.6274	1.6309	1.6543	0.002	0.002	0.002	0.002	0.002	6.7972	8.797339

**TableA.11: Starting structure of ordered SrFeO<sub>2</sub>F relaxed in VASP**

a	b	C	$\alpha$	B	$\gamma$
5.3315	5.3315	8.239	90	90	90

Element	x/a	y/b	z/c
Sr	0.50	0.00	0.25
Sr	0.50	0.00	0.75
Sr	0.00	0.50	0.25
Sr	0.00	0.50	0.75
Fe	0.00	0.00	0.00
Fe	0.50	0.50	0.00
Fe	0.00	0.00	0.50
Fe	0.50	0.50	0.50
O	0.25	0.25	0.00
O	0.75	0.75	0.00
O	0.75	0.25	0.00
O	0.25	0.75	0.00
O	0.25	0.25	0.50
O	0.75	0.75	0.50
O	0.75	0.25	0.50
O	0.25	0.75	0.50
F	0.00	0.00	0.25
F	0.00	0.00	0.75
F	0.50	0.50	0.25
F	0.50	0.50	0.75

**Table A.12: Starting structure of disordered SrFeO<sub>2</sub>F relaxed in VASP**

a	b	c	alpha	Beta	gamma
5.3315	5.3315	8.239	90	90	90

element	x/a	y/b	z/c
Sr	0.00	0.50	0.25
Sr	0.50	0.00	0.25
Sr	0.00	0.50	0.75
Sr	0.50	0.00	0.75
Fe	0.00	0.00	0.00
Fe	0.50	0.50	0.00
Fe	0.00	0.00	0.50
Fe	0.50	0.50	0.50
O	0.25	0.25	0.00
O	0.25	0.75	0.00
O	0.75	0.25	0.00
O	0.75	0.75	0.00
O	0.25	0.25	0.50
O	0.25	0.75	0.50
O	0.75	0.25	0.50
O	0.50	0.50	0.75
F	0.75	0.75	0.50
F	0.00	0.00	0.25
F	0.00	0.00	0.75
F	0.50	0.50	0.25



**Table A.13: Relaxed structure of disordered SrFeO<sub>2</sub>F relaxed in VASP**

a	b	c	alpha	beta	gamma
5.52994	5.52994	8.29216	90.2857	90.2857	89.042

element	x/a	y/b	z/c
Sr	0.00185	0.49776	0.22911
Sr	0.49776	0.00185	0.22911
Sr	0.99024	0.50731	0.75616
Sr	0.50731	0.99024	0.75616
Fe	0.00080	0.00080	0.99796
Fe	0.49316	0.49316	0.97563
Fe	0.02544	0.02544	0.49524
Fe	0.47481	0.47481	0.51658
O	0.24513	0.24513	0.03595
O	0.24865	0.74876	0.01308
O	0.74876	0.24865	0.01308
O	0.75350	0.75350	0.95904
O	0.25288	0.25288	0.43512
O	0.24790	0.75585	0.50922
O	0.75585	0.24790	0.50922
O	0.45289	0.45289	0.74839
F	0.75277	0.75277	0.55470
F	0.94936	0.94936	0.25509
F	0.04585	0.04585	0.74922
F	0.55509	0.55509	0.26193

**Table A.14: Crystal coordinates for the  $\text{Na}_2\text{B}_{10}\text{C}_2$  super cell of  $\text{NaB}_5\text{C}$  for the B/C ordered structure 1 (Figure 5.2) optimized by VASP.**

$a$ (Å)	$b$ (Å)	$c$ (Å)	$\alpha$ (°)	$\beta$ (°)	$\gamma$ (°)
8.294684	4.156983	3.904789	90.00000	90.0000	90.00000

Element	$x/a$	$y/b$	$z/c$
Na	0.000000	0.000000	0.000000
Na	0.500000	0.000000	0.000000
B	0.250000	0.797136	0.477001
B	0.750000	0.797136	0.522999
B	0.250000	0.500000	0.161341
B	0.750000	0.500000	0.838659
B	0.250000	0.202864	0.477001
B	0.750000	0.202864	0.522999
B	0.101075	0.500000	0.476721
B	0.601075	0.500000	0.523279
B	0.398925	0.500000	0.476721
B	0.898925	0.500000	0.523279
C	0.250000	0.500000	0.759069
C	0.750000	0.500000	0.240931

**Table A.15: Crystal coordinates for the  $\text{Na}_2\text{B}_{10}\text{C}_2$  super cell of  $\text{NaB}_5\text{C}$  for the B/C ordered structure 2 (Figure 5.2) optimized by VASP.**

$a$ (Å)	$b$ (Å)	$c$ (Å)	$\alpha$ (°)	$\beta$ (°)	$\gamma$ (°)
8.309383	4.15498	3.904426	90.00000	90.00000	90.00000

Element	$x/a$	$y/b$	$z/c$
Na	0.000000	0.000000	0.996938
Na	0.500000	0.000000	0.996938
B	0.250000	0.797147	0.495366
B	0.750000	0.797147	0.495366
B	0.250000	0.500000	0.809916
B	0.750000	0.500000	0.809916
B	0.250000	0.202853	0.495366
B	0.750000	0.202853	0.495366
B	0.101423	0.500000	0.495368
B	0.601423	0.500000	0.495368
B	0.398577	0.500000	0.495368
B	0.898577	0.500000	0.495368
C	0.250000	0.500000	0.211679
C	0.750000	0.500000	0.211679

**Table A16: Crystal coordinates for the  $\text{Na}_2\text{B}_{10}\text{C}_2$  super cell of  $\text{NaB}_5\text{C}$  for the B/C ordered structure 3 (Figure 5.2) optimized by VASP.**

$a$ (Å)	$b$ (Å)	$c$ (Å)	$\alpha$ (°)	$\beta$ (°)	$\gamma$ (°)
8.059856	4.156672	4.026797	90.00000	89.98331	90.00000

Element	$x/a$	$y/b$	$z/c$
Na	0.015504	0.000000	0.992352
Na	0.491586	0.000000	0.993060
B	0.257675	0.797095	0.488828
B	0.743229	0.797384	0.508336
B	0.258864	0.500000	0.785544
B	0.742733	0.500000	0.822900
B	0.257675	0.202905	0.488828
B	0.743229	0.202616	0.508336
B	0.104095	0.500000	0.487572
B	0.591512	0.500000	0.510469
B	0.259220	0.500000	0.190051
B	0.895401	0.500000	0.508806
C	0.397136	0.500000	0.487931
C	0.742141	0.500000	0.226987

**Table A17: Crystal coordinates for the  $\text{Na}_2\text{B}_{10}\text{C}_2$  super cell of  $\text{NaB}_5\text{C}$  for the B/C ordered structure 4 (Figure 5.2) optimized by VASP.**

$a$ (Å)	$b$ (Å)	$c$ (Å)	$\alpha$ (°)	$\beta$ (°)	$\gamma$ (°)
8.309772	4.026397	4.026397	90.00789	90.00000	90.00000

Element	$x/a$	$y/b$	$z/c$
Na	0.000000	0.006531	0.993469
Na	0.500000	0.006531	0.993469
B	0.250000	0.493955	0.190004
B	0.750000	0.809996	0.506045
B	0.250000	0.493812	0.786151
B	0.750000	0.511508	0.822081
B	0.250000	0.177919	0.488492
B	0.750000	0.213849	0.506188
B	0.100987	0.489131	0.488698
B	0.600987	0.511302	0.510869
B	0.399013	0.489131	0.488698
B	0.899013	0.511302	0.510869
C	0.250000	0.773452	0.488419
C	0.750000	0.511581	0.226548

**Table A18: Crystal coordinates for the  $\text{Na}_2\text{B}_{10}\text{C}_2$  super cell of  $\text{NaB}_5\text{C}$  for the B/C ordered structure 5 (Figure 5.2) optimized by VASP.**

$a$ (Å)	$b$ (Å)	$c$ (Å)	$\alpha$ (°)	$\beta$ (°)	$\gamma$ (°)
7.846282	4.152481	4.152481	90.00000	90.00000	90.00000

Element	$x/a$	$y/b$	$z/c$
Na	0.000000	0.000000	0.000000
Na	0.500000	0.000000	0.000000
B	0.264614	0.796975	0.500000
B	0.735386	0.796975	0.500000
B	0.264614	0.500000	0.796975
B	0.735386	0.500000	0.796975
B	0.264614	0.203025	0.500000
B	0.735386	0.203025	0.500000
B	0.107204	0.500000	0.500000
B	0.264614	0.500000	0.203025
B	0.735386	0.500000	0.203025
B	0.892796	0.500000	0.500000
C	0.594740	0.500000	0.500000
C	0.405260	0.500000	0.500000

**Table A.19: Crystal coordinates for the  $\text{Na}_2\text{B}_{10}\text{C}_2$  super cell of  $\text{NaB}_5\text{C}$  for the B/C ordered structure 1 (Figure 5.2) optimized by Quantum Espresso.**

$a$ (Å)	$b$ (Å)	$c$ (Å)	$\alpha$ (°)	$\beta$ (°)	$\gamma$ (°)
8.30453	4.16218	3.90879	90.00000	90.00000	90.00000

Element	$x/a$	$y/b$	$z/c$
Na	0.00000	0.0000	0.00000
Na	0.50000	0.0000	0.00000
B	0.25000	0.7969	0.47635
B	0.75000	0.7969	0.52365
B	0.25000	0.5000	0.16100
B	0.75000	0.5000	0.83900
B	0.25000	0.2031	0.47635
B	0.75000	0.2031	0.52365
B	0.10119	0.5000	0.47628
B	0.60119	0.5000	0.52372
B	0.39882	0.5000	0.47628
B	0.89882	0.5000	0.52372
C	0.25000	0.5000	0.75824
C	0.75000	0.5000	0.24176

**Table A.20: Crystal coordinates for the  $\text{Na}_2\text{B}_{10}\text{C}_2$  super cell of  $\text{NaB}_5\text{C}$  for the B/C ordered structure 2 (Figure 5.2) optimized by Quantum Espresso.**

$a$ (Å)	$b$ (Å)	$c$ (Å)	$\alpha$ (°)	$\beta$ (°)	$\gamma$ (°)
8.32078	4.16039	3.9091	90.00000	90.00000	90.00000

Element	$x/a$	$y/b$	$z/c$
Na	0.00000	0.00000	-0.01526
Na	0.50000	0.00000	-0.01526
B	0.25000	0.79688	0.49738
B	0.75000	0.79688	0.49738
B	0.25000	0.50000	0.81156
B	0.75000	0.50000	0.81156
B	0.25000	0.20313	0.49738
B	0.75000	0.20313	0.49738
B	0.10156	0.50000	0.49738
B	0.60156	0.50000	0.49738
B	0.39844	0.50000	0.49738
B	0.89844	0.50000	0.49738
C	0.25000	0.50000	0.21420
C	0.75000	0.50000	0.21420



**Table A.21: Crystal coordinates for the  $\text{Na}_2\text{B}_{10}\text{C}_2$  super cell of  $\text{NaB}_5\text{C}$  for the B/C ordered structure 3 (Figure 5.1) optimized by Quantum Espresso.**

$a$ (Å)	$b$ (Å)	$c$ (Å)	$\alpha$ (°)	$\beta$ (°)	$\gamma$ (°)
8.06757	4.16273	4.03142	90	90	90

Element	$x/a$	$y/b$	$z/c$
Na	0.01604	0.00000	-0.01430
Na	0.49316	0.00000	-0.00752
B	0.25757	0.79682	0.48685
B	0.74301	0.79715	0.51185
B	0.25882	0.50000	0.78369
B	0.74242	0.50000	0.82545
B	0.25757	0.20318	0.48685
B	0.74301	0.20285	0.51185
B	0.10405	0.50000	0.48668
B	0.59138	0.50000	0.51187
B	0.25918	0.50000	0.18877
B	0.89502	0.50000	0.51052
C	0.39688	0.50000	0.48734
C	0.74189	0.50000	0.23011

**Table A.22: Crystal coordinates for the  $\text{Na}_2\text{B}_{10}\text{C}_2$  super cell of  $\text{NaB}_5\text{C}$  for the B/C ordered structure 4 (Figure 5.2) optimized by Quantum Espresso.**

$a$ (Å)	$b$ (Å)	$c$ (Å)	$\alpha$ (°)	$\beta$ (°)	$\gamma$ (°)
8.31927	4.03149	4.03149	90	90	90

Element	$x/a$	$y/b$	$z/c$
Na	0	0.00751	-0.00751
Na	0.5	0.00751	-0.00751
B	0.25	0.49244	0.18982
B	0.75	0.81018	0.50756
B	0.25	0.49215	0.78539
B	0.75	0.51156	0.82266
B	0.25	0.17734	0.48844
B	0.75	0.21461	0.50786
B	0.10111	0.48924	0.48787
B	0.60111	0.51213	0.51076
B	0.39889	0.48924	0.48787
B	0.89889	0.51213	0.51076
C	0.25	0.77225	0.48829
C	0.75	0.51171	0.22775

**Table A.23: Crystal coordinates for the  $\text{Na}_2\text{B}_{10}\text{C}_2$  super cell of  $\text{NaB}_5\text{C}$  for the B/C ordered structure 5 (Figure 5.2) optimized by Quantum Espresso.**

$a$ (Å)	$b$ (Å)	$c$ (Å)	$\alpha$ (°)	$\beta$ (°)	$\gamma$ (°)
7.85618	4.15799	4.15799	90.00000	90.00000	90.00000

Element	$x/a$	$y/b$	$z/c$
Na	0.00000	0.00000	0.00000
Na	0.50000	0.00000	0.00000
B	0.26505	0.79682	0.50000
B	0.73495	0.79682	0.50000
B	0.26505	0.50000	0.79682
B	0.73495	0.50000	0.79682
B	0.26505	0.20318	0.50000
B	0.73495	0.20318	0.50000
B	0.10756	0.50000	0.50000
B	0.26505	0.50000	0.20318
B	0.73495	0.50000	0.20318
B	0.89244	0.50000	0.50000
C	0.59466	0.50000	0.50000
C	0.40534	0.50000	0.50000

**Table A.24: Crystal coordinates of the  $\text{Mg}_4\text{B}_{10}\text{C}_8$  super cell of  $\text{Mg}_{0.5}\text{B}_5\text{C}$  optimized by Quantum Espresso with the gamma point only. The structure was used as the starting point for the NEB calculations.**

$a$ (Å)	$b$ (Å)	$c$ (Å)	$\alpha$ (°)	$\beta$ (°)	$\gamma$ (°)
8.095122	8.337962106	8.082758029	90	90	90

Element	$x/a$	$y/b$	$z/c$
Mg	0.104392211	-0.000000307	-0.01021255
Mg	0.104389427	0.499999785	0.489788805
Mg	0.503510763	0.000000172	0.393839311
Mg	0.503513318	0.500000059	-0.10616536
B	0.25357042	0.396584642	0.243750454
B	0.253570397	0.603415292	0.243750462
B	0.253569593	0.896584698	0.743749664
B	0.253569563	0.103415281	0.743749701
B	0.25507731	0.396645937	0.74727406
B	0.2550773	0.603354041	0.747274028
B	0.255077376	0.896646047	0.247274329
B	0.255077351	0.103353889	0.247274321
B	0.739573819	0.398114825	0.264235686
B	0.739573815	0.60188523	0.264235703
B	0.739574184	0.898114913	0.764235408
B	0.739574183	0.10188517	0.764235392
B	0.740031443	0.39727154	0.756722772
B	0.740031472	0.602728541	0.756722791
B	0.740032117	0.89727183	0.256723422
B	0.740032158	0.102728225	0.256723404
B	0.255091607	0.248941065	0.393263095
B	0.255091507	0.75105884	0.393263099
B	0.255092215	0.748941444	0.893262975
B	0.255092112	0.251058493	0.893262989
B	0.738667691	0.249551413	0.419237087
B	0.738667767	0.750448643	0.419237107
B	0.738667603	0.749551996	0.919237143
B	0.738667649	0.250448065	0.919237124
B	0.099003798	0.247877034	0.247161351
B	0.099003788	0.752122954	0.247161266
B	0.099003719	0.747876714	0.747161484
B	0.099003712	0.25212331	0.747161407
B	0.589339785	0.253901807	0.2591973
B	0.589339763	0.746098245	0.259197381
B	0.589339756	0.753902433	0.759196839
B	0.589339742	0.246097639	0.759196898
B	0.256177852	0.251384026	0.097879274
B	0.256177949	0.74861587	0.097879261
B	0.256177595	0.751384274	0.597878973
B	0.256177705	0.248615665	0.597879004
B	0.888322948	0.248072038	0.261997356
B	0.888322944	0.751928021	0.261997298
B	0.888322856	0.74807148	0.761997477
B	0.888322838	0.251928621	0.761997387
C	0.39300051	0.251605912	0.245429393
C	0.393000514	0.748394064	0.245429477
C	0.393000392	0.751606258	0.745428831
C	0.393000379	0.248393746	0.745428931
C	0.73819114	0.252470825	0.122040367
C	0.738191093	0.747529227	0.122040382
C	0.738191466	0.752471294	0.622040126
C	0.738191386	0.247528773	0.622040109

**Table A.25: Crystal coordinates of the  $\text{Mg}_4\text{B}_{10}\text{C}_8$  super cell of  $\text{Mg}_{0.5}\text{B}_5\text{C}$  optimized by Quantum Espresso with 125  $k$ -points. The structure was used for electronic structure calculations.**

$a$ (Å)	$b$ (Å)	$c$ (Å)	$\alpha$ (°)	$\beta$ (°)	$\gamma$ (°)
8.02271	8.27501	8.01678	90	90	90

Element	$x/a$	$y/b$	$z/c$
Mg	0.07986	0	-0.01612
Mg	0.07985	0.5	0.48388
Mg	0.50041	0	0.42263
Mg	0.50041	0.5	-0.07738
B	0.25561	0.39852	0.24402
B	0.25561	0.60148	0.24402
B	0.25561	0.89853	0.74402
B	0.25561	0.10148	0.74402
B	0.25478	0.3982	0.74426
B	0.25478	0.6018	0.74426
B	0.25478	0.8982	0.24426
B	0.25478	0.1018	0.24426
B	0.73974	0.39939	0.2621
B	0.73974	0.60061	0.2621
B	0.73974	0.89939	0.7621
B	0.73974	0.10061	0.7621
B	0.74151	0.39869	0.7585
B	0.74151	0.60131	0.7585
B	0.74151	0.89869	0.2585
B	0.74151	0.10131	0.2585
B	0.25642	0.24771	0.39319
B	0.25642	0.75229	0.39319
B	0.25642	0.74771	0.89319
B	0.25642	0.25229	0.89319
B	0.73992	0.25051	0.41934
B	0.73992	0.74949	0.41934
B	0.73992	0.75051	0.91934
B	0.73992	0.24949	0.91934
B	0.09943	0.2492	0.24535
B	0.09943	0.7508	0.24535
B	0.09943	0.7492	0.74535
B	0.09943	0.2508	0.74535
B	0.58922	0.25267	0.25899
B	0.58922	0.74734	0.25899
B	0.58922	0.75267	0.75899
B	0.58922	0.24733	0.75899
B	0.2575	0.2526	0.0954
B	0.2575	0.7474	0.0954
B	0.2575	0.7526	0.5954
B	0.2575	0.2474	0.5954
B	0.89155	0.24942	0.26093
B	0.89155	0.75058	0.26093
B	0.89155	0.74942	0.76093
B	0.89155	0.25058	0.76093
C	0.39495	0.25108	0.24455
C	0.39495	0.74892	0.24455
C	0.39495	0.75108	0.74455
C	0.39495	0.24892	0.74455
C	0.73925	0.25121	0.12011
C	0.73925	0.74879	0.12011
C	0.73925	0.75121	0.62011
C	0.73925	0.24879	0.62011

**Table A.26: Crystal coordinates of  $\text{Mg}_4\text{B}_{10}\text{C}_8$  super cell of  $\text{Mg}_{0.5}\text{B}_5\text{C}$  for the endpoint of the NEB calculation for the  $\text{Mg}^{2+}$  diffusion in the [100] direction (optimized by Quantum Espresso with the gamma point only).**

$a$ (Å)	$b$ (Å)	$c$ (Å)	$\alpha$ (°)	$\beta$ (°)	$\gamma$ (°)
8.095122	8.337962	8.082758	90	90	90

Element	$x/a$	$y/b$	$z/c$
Mg	0.108518	-2.2E-08	-0.02596
Mg	0.479781	0.5	0.402302
Mg	0.478957	8.5E-08	0.413055
Mg	0.497512	0.5	-0.11446
B	0.246566	0.395882	0.245902
B	0.246566	0.604118	0.245902
B	0.264199	0.89684	0.743438
B	0.264199	0.10316	0.743438
B	0.259108	0.396179	0.739708
B	0.259108	0.603821	0.739708
B	0.247219	0.897005	0.24107
B	0.247219	0.102995	0.24107
B	0.732056	0.397281	0.269053
B	0.732056	0.602719	0.269053
B	0.745748	0.898485	0.770285
B	0.745748	0.101515	0.770285
B	0.746043	0.397046	0.765274
B	0.746043	0.602954	0.765274
B	0.733694	0.897715	0.269311
B	0.733694	0.102285	0.269311
B	0.252572	0.245934	0.391676
B	0.252572	0.754066	0.391676
B	0.260596	0.746601	0.89117
B	0.260596	0.253399	0.89117
B	0.740869	0.249418	0.427324
B	0.740869	0.750582	0.427324
B	0.742446	0.750893	0.924557
B	0.742446	0.249107	0.924557
B	0.095291	0.251581	0.250167
B	0.095291	0.748419	0.250167
B	0.106767	0.748532	0.744642
B	0.106767	0.251468	0.744642
B	0.583468	0.24819	0.257794
B	0.583468	0.75181	0.257794
B	0.595352	0.75489	0.764368
B	0.595352	0.24511	0.764368
B	0.254598	0.253553	0.095152
B	0.254598	0.746447	0.095152
B	0.261532	0.753368	0.596121
B	0.261532	0.246632	0.596121
B	0.884094	0.250827	0.266139
B	0.884094	0.749173	0.266139
B	0.895564	0.749229	0.765627
B	0.895564	0.250771	0.765627
C	0.388932	0.248075	0.240574
C	0.388932	0.751925	0.240574
C	0.40056	0.751842	0.746776
C	0.40056	0.248158	0.746776
C	0.7366	0.249995	0.12793
C	0.7366	0.750005	0.12793
C	0.743741	0.751584	0.628469
C	0.743741	0.248416	0.628469

**Table A.27: Crystal coordinates of the  $\text{Mg}_4\text{B}_{10}\text{C}_8$  super cell of  $\text{Mg}_{0.5}\text{B}_5\text{C}$  for the endpoint of the NEB calculation for the  $\text{Mg}^{2+}$  diffusion in the  $[00\bar{1}]$  direction (optimized by Quantum Espresso with the gamma point only).**

$a$ (Å)	$b$ (Å)	$c$ (Å)	$\alpha$ (°)	$\beta$ (°)	$\gamma$ (°)
8.095122	8.337962	8.082758	90	90	90

Element	$x/a$	$y/b$	$z/c$
Mg	0.110087	-1.3E-06	-0.02547
Mg	0.123379	0.499999	0.499976
Mg	0.479819	9E-07	0.408228
Mg	0.625173	0.500001	0.522257
B	0.245429	0.39644	0.240464
B	0.245429	0.60356	0.240464
B	0.258498	0.896793	0.738451
B	0.258498	0.103206	0.738452
B	0.259777	0.396888	0.745077
B	0.259777	0.603111	0.745076
B	0.247098	0.89704	0.243049
B	0.247098	0.10296	0.24305
B	0.734748	0.397141	0.266383
B	0.734748	0.60286	0.266383
B	0.740028	0.898077	0.767017
B	0.740028	0.101924	0.767017
B	0.740795	0.39681	0.766577
B	0.740795	0.60319	0.766577
B	0.728531	0.897428	0.262481
B	0.728531	0.102572	0.262481
B	0.253654	0.247439	0.389961
B	0.253653	0.752561	0.389961
B	0.252509	0.749198	0.889294
B	0.252508	0.2508	0.889294
B	0.735857	0.245445	0.421518
B	0.735857	0.754556	0.421518
B	0.737455	0.747339	0.919963
B	0.737455	0.252662	0.919963
B	0.092893	0.247352	0.248052
B	0.092893	0.752648	0.248052
B	0.101275	0.748702	0.740043
B	0.101275	0.251298	0.740042
B	0.580275	0.252825	0.253173
B	0.580275	0.747176	0.253174
B	0.589284	0.751495	0.766563
B	0.589283	0.248505	0.766563
B	0.24759	0.250778	0.094045
B	0.24759	0.749222	0.094045
B	0.260628	0.751969	0.594792
B	0.260629	0.24803	0.594792
B	0.882327	0.245948	0.262397
B	0.882327	0.754052	0.262397
B	0.890527	0.749797	0.758863
B	0.890527	0.250203	0.758862
C	0.385597	0.252074	0.238592
C	0.385596	0.747927	0.238593
C	0.394883	0.749914	0.748578
C	0.394883	0.250085	0.748578
C	0.73399	0.252993	0.12432
C	0.733989	0.747007	0.12432
C	0.737126	0.752671	0.62402
C	0.737125	0.247329	0.62402

ELSEVIER LICENSE  
TERMS AND CONDITIONS

Jul 20, 2016

This Agreement between Joshua D Davis ("You") and Elsevier ("Elsevier") consists of your license details and the terms and conditions provided by Elsevier and Copyright Clearance Center.

License Number	3913110183316
License date	Jul 20, 2016
Licensed Content Publisher	Elsevier
Licensed Content Publication	Journal of Fluorine Chemistry
Licensed Content Title	Multistep synthesis of the SrFeO <sub>2</sub> F perovskite oxyfluoride via the SrFeO <sub>2</sub> infinite-layer intermediate
Licensed Content Author	Colin K. Blakely, Joshua D. Davis, Shaun R. Bruno, Shannon K. Kraemer, Mengze Zhu, Xianglin Ke, Wenli Bi, E. Ercan Alp, Viktor V. Poltavets
Licensed Content Date	March 2014
Licensed Content Volume Number	159
Licensed Content Issue Number	n/a
Licensed Content Pages	7
Start Page	8
End Page	14
Type of Use	reuse in a thesis/dissertation
Intended publisher of new work	other
Portion	full article
Format	both print and electronic
Are you the author of this Elsevier article?	Yes
Will you be translating?	No
Order reference number	
Title of your thesis/dissertation	INTERPLAY OF CRYSTAL AND ELECTRONIC STRUCTURE IN BATTERY AND STRONGLY CORRELATED ELECTRON MATERIALS
Expected completion date	Aug 2016
Estimated size (number of pages)	243
Elsevier VAT number	GB 494 6272 12
Requestor Location	Joshua D Davis 1835 Nemoke Ct. Apt. 1  HASLETT, MI 48840 United States Attn: Joshua D Davis



**ELSEVIER LICENSE  
TERMS AND CONDITIONS**

Jul 20, 2016

This Agreement between Joshua D Davis ("You") and Elsevier ("Elsevier") consists of your license details and the terms and conditions provided by Elsevier and Copyright Clearance Center.

License Number	3913101392175
License date	Jul 20, 2016
Licensed Content Publisher	Elsevier
Licensed Content Publication	Journal of Power Sources
Licensed Content Title	Synthesis and electrochemical properties of novel $\text{LiFeTiO}_4$ and $\text{Li}_2\text{FeTiO}_4$ polymorphs with the $\text{CaFe}_2\text{O}_4$ -type structures
Licensed Content Author	Shaun R. Bruno, Colin K. Blakely, Jonathon B. Clapham, Joshua D. Davis, Wenli Bi, E. Ercan Alp, Viktor V. Poltavets
Licensed Content Date	1 January 2015
Licensed Content Volume Number	273
Licensed Content Issue Number	n/a
Licensed Content Pages	8
Start Page	396
End Page	403
Type of Use	reuse in a thesis/dissertation
Portion	full article
Format	both print and electronic
Are you the author of this Elsevier article?	Yes
Will you be translating?	No
Order reference number	
Title of your thesis/dissertation	INTERPLAY OF CRYSTAL AND ELECTRONIC STRUCTURE IN BATTERY AND STRONGLY CORRELATED ELECTRON MATERIALS
Expected completion date	Aug 2016
Estimated size (number of pages)	243
Elsevier VAT number	GB 494 6272 12
Requestor Location	Joshua D Davis 1835 Nemoke Ct. Apt. 1  HASLETT, MI 48840 United States Attn: Joshua D Davis
Total	0.00 USD
Terms and Conditions	

<https://is100.copyright.com/AppDispatchServlet>

1/6

## REFERENCES

## REFERENCES

- (1) *Climate Change Indicators in the United States, 2014: 3rd Edition*; 2014.
- (2) Yang, Z.; Zhang, J.; Kintner-Meyer, M. C. W.; Lu, X.; Choi, D.; Lemmon, J. P.; Liu, J. *Chem. Rev.* **2011**, *111* (5), 3577–3613.
- (3) Dunn, B.; Kamath, H.; Tarascon, J.-M. *Science* (80-. ). **2011**, *334* (6058), 928–935.
- (4) Rastler, D. *Electricity Energy Storage Technology Options (Report No. 1020676)*; Palo Alto, California, 2010.
- (5) Kulkarni, P.; Sayer, J. H.; Boyes, J. D.; Corey, G. P.; Peek, G. H. *Energy* **2005**, No. april, 31–39.
- (6) Doughty, D. H.; Butler, P. C.; Akhil, A. a; Clark, N. H.; Boyes, J. D. *Electrochem. Soc. Interface* **2010**, *19* (3), 49–53.
- (7) Chen, H.; Cong, T. N.; Yang, W.; Tan, C.; Li, Y.; Ding, Y. *Prog. Nat. Sci.* **2009**, *19* (3), 291–312.
- (8) Gyuk, I.; Johnson, M.; Vetrano, J.; Lynn, K.; Parks, W.; Handa, R.; Kannberg, L.; Hearne, S.; Waldrip, K.; Braccio, R. *Grid Energy Storage*; Washington, DC, 2013.
- (9) Goodenough, J. B.; Kim, Y. *Chem. Mater.* **2010**, *22* (3), 587–603.
- (10) Goodenough, J. B. *J. Solid State Electrochem.* **2012**, *16* (6), 2019–2029.
- (11) Goodenough, J. B. *Energy Environ. Sci.* **2014**, *7* (1), 14.
- (12) Fischer, B. How Much Energy a Smartphone Uses in a Year (And What it Means for Your Budget) <http://lifehacker.com/5948075/how-much-energy-a-smartphone-uses-in-a-year-and-what-it-means-for-your-budget> (accessed May 18, 2016).
- (13) How we use Energy, Transportation <http://needtoknow.nas.edu/energy/energy-use/transportation/> (accessed May 18, 2016).
- (14) Sarath, P.; Bonda, S.; Mohanty, S.; Nayak, S. K. *Waste Manag.* **2015**, *46*, 536–545.
- (15) *The Economist*. 2012, pp 1–5.
- (16) Mukhammadiev, M. M.; Dzhuraev, K. S.; Klychev, I. S. *Appl. Sol. Energy* **2013**, *49* (4), 267–271.
- (17) Robert, P. *Nature* **1991**, *351*, 509.
- (18) Young, H. D.; Freedman, R. A.; Ford, A. L. In *University Physics*; Black, A., Otway, M., Benson, C., Madhavan, C., Eds.; Pearson Addison-Wesley: San Francisco, CA, 2008; pp 815–845.
- (19) Muller, K. N. *Capacitors : Theory of Operation, Behavior and Safety Regulations.*; Nova Science Publishers, Inc, 2013.
- (20) Jansen, R. H.; McLallin, K. L. *G2 Flywheel Module Operated at 41,000 rpm*; 2004.

- (21) Pistoia, G. *Industrial Applications of Batteries*; Elsevier, 2007.
- (22) Zhang, Q. *Int. J. Electrochem. Sci.* **2013**, *8* (5), 6457–6466.
- (23) Kondoh, J. In *Industrial Applications of Batteries*; Broussely, M., Pistoia, G., Eds.; Elsevier B.V., 2007; pp 455–496.
- (24) Shukla, A. K.; Venugopalan, S.; Hariprakash, B. *J. Power Sources* **2001**, *100* (1-2), 125–148.
- (25) Godt, J.; Scheidig, F.; Grosse-Siestrup, C.; Esche, V.; Brandenburg, P.; Reich, A.; Groneberg, D. a. *J. Occup. Med. Toxicol.* **2006**, *1*, 22.
- (26) BU-203: Nickel-based Batteries  
[http://batteryuniversity.com/learn/article/nickel\\_based\\_batteries](http://batteryuniversity.com/learn/article/nickel_based_batteries) (accessed May 5, 2016).
- (27) Green, A. *Industrial Applications of Batteries*; Elsevier, 2007.
- (28) BU-107: Comparison Table of Secondary Batteries  
[http://batteryuniversity.com/learn/article/secondary\\_batteries](http://batteryuniversity.com/learn/article/secondary_batteries) (accessed May 20, 2016).
- (29) Armand, M.; Tarascon, J.-M. *Nature* **2008**, *451* (7179), 652–657.
- (30) Larcher, D.; Tarascon, J.-M. *Nat. Chem.* **2015**, *7* (1), 19–29.
- (31) Nitta, N.; Wu, F.; Lee, J. T.; Yushin, G. *Mater. Today* **2015**, *18* (5), 252–264.
- (32) Tesla Model S <https://www.teslamotors.com/models> (accessed Jul 7, 2016).
- (33) Han, M. H.; Gonzalo, E.; Singh, G.; Rojo, T. *Energy Environ. Sci.* **2014**, *8* (1), 81–102.
- (34) Yabuuchi, N.; Kubota, K.; Dahbi, M.; Komaba, S. *Chem. Rev.* **2014**, *114* (23), 11636–11682.
- (35) Ellis, B. L.; Nazar, L. F. *Curr. Opin. Solid State Mater. Sci.* **2012**, *16* (4), 168–177.
- (36) Shannon, R. D. *Acta Crystallogr. Sect. A* **1976**, *32* (5), 751–767.
- (37) Bucur, C. B.; Gregory, T.; Oliver, A. G.; Muldoon, J. J. *Phys. Chem. Lett.* **2015**, *6* (18), 3578–3591.
- (38) Shterenberg, I.; Salama, M.; Gofer, Y.; Levi, E.; Aurbach, D. *MRS Bull.* **2014**, *39* (05), 453–460.
- (39) Saha, P.; Datta, M. K.; Velikokhatnyi, O. I.; Manivannan, A.; Alman, D.; Kumta, P. N. *Prog. Mater. Sci.* **2014**, *66*, 1–86.
- (40) Weber, A. Z.; Mench, M. M.; Meyers, J. P.; Ross, P. N.; Gostick, J. T.; Liu, Q. *J. Appl. Electrochem.* **2011**, *41* (10), 1137–1164.
- (41) Modec Electric LCV  
<http://www.whatvan.co.uk/test-drives/first-drive/2008/modec-electric-lcv-%E2%80%94april-2007> (accessed May 23, 2016).
- (42) Linden, D.; Reddy, T. B. In *Linden's Handbook of Batteries, Fourth Edition*; Reddy, T. B., Ed.; McGraw Hill Professional, Access Engineering: New York, New York, 2011.

- (43) Luo, X.; Wang, J.; Dooner, M.; Clarke, J. *Appl. Energy* **2015**, *137*, 511–536.
- (44) Winter, M.; Brodd, R. J. *Chem. Rev.* **2004**, *104*, 4245–4269.
- (45) Zheng, G.; Lee, S. W.; Liang, Z.; Lee, H.-W.; Yan, K.; Yao, H.; Wang, H.; Li, W.; Chu, S.; Cui, Y. *Nat. Nanotechnol.* **2014**, *advance on* (8), 618–623.
- (46) Whittingham, M. S. *Chem. Rev.* **2004**, *104* (10), 4271–4301.
- (47) Jalkanen, K.; Karppinen, J.; Skogstrom, L.; Laurila, T.; Nisula, M.; Vuorilehto, K. *Appl. Energy* **2015**, *154*, 160–172.
- (48) Ohsaki, T.; Kishi, T.; Kuboki, T.; Takami, N.; Shimura, N.; Sato, Y.; Sekino, M.; Satoh, A. *J. Power Sources* **2005**, *146* (1-2), 97–100.
- (49) MacNeil, D. D.; Christensen, L.; Landucci, J.; Paulsen, J. M.; Dahn, J. R. *J. Electrochem. Soc.* **2000**, *147* (3), 970–979.
- (50) Myung, S.-T.; Hitoshi, Y.; Sun, Y.-K. *J. Mater. Chem.* **2011**, *21* (27), 9891.
- (51) Johannes, M. D.; Swider-Lyons, K.; Love, C. T. *Solid State Ionics* **2016**, *286*, 83–89.
- (52) Morgan, D.; Van der Ven, A.; Ceder, G. *Electrochem. Solid-State Lett.* **2004**, *7* (2), A30.
- (53) Ceder, G.; Aydinol, M.; Kohan, A. *Comput. Mater. Sci.* **1997**, *8* (1), 161–169.
- (54) Kang, K.; Meng, Y. S.; Bréger, J.; Grey, C. P.; Ceder, G. *Science* **2006**, *311* (5763), 977–980.
- (55) Aydinol, M.; Kohan, A.; Ceder, G.; Cho, K.; Joannopoulos, J. *Phys. Rev. B* **1997**, *56* (3), 1354–1365.
- (56) Chevrier, V. L.; Hautier, G.; Ong, S. P.; Doe, R. E.; Ceder, G. *Phys. Rev. B* **2013**, *87* (9), 094118.
- (57) Chen, H.; Hautier, G.; Jain, A.; Moore, C.; Kang, B.; Doe, R.; Wu, L.; Zhu, Y.; Tang, Y.; Ceder, G. *Chem. Mater.* **2012**, *24* (11), 2009–2016.
- (58) Xia, H.; Meng, Y. S.; Lu, L.; Ceder, G.; Alliance, S. *Scientific Commons*. 2010.
- (59) Li, L. F.; Lee, H. S.; Li, H.; Yang, X. Q.; Nam, K. W.; Yoon, W. S.; McBreen, J.; Huang, X. J. *J. Power Sources* **2008**, *184* (2), 517–521.
- (60) Du, W.; Xue, N.; Sastry, a. M.; Martins, J. R. R. a.; Shyy, W. *J. Electrochem. Soc.* **2013**, *160* (8), A1187–A1193.
- (61) Goodenough, J. B.; Park, K. S. *J. Am. Chem. Soc.* **2013**, *135* (4), 1167–1176.
- (62) Kim, J. G.; Son, B.; Mukherjee, S.; Schuppert, N.; Bates, A.; Kwon, O.; Choi, M. J.; Chung, H. Y.; Park, S. J. *J. Power Sources* **2015**, *282*, 299–322.
- (63) Islam, M. S.; Fisher, C. a J. *Chem. Soc. Rev.* **2014**, *43* (1), 185–204.
- (64) Tarascon, J. M.; Armand, M. *Nature* **2001**, *414* (6861), 359–367.

- (65) Park, M.; Zhang, X.; Chung, M.; Less, G. B.; Sastry, A. M. *J. Power Sources* **2010**, *195* (24), 7904–7929.
- (66) CLARK, J. B.; HASTIE, J. W.; KIHNBORG, L. H. E.; METSELAAR, R.; THACKERAY, M. M. *Pure Appl. Chem.* **1994**, *66* (3), 577–594.
- (67) Li, L.; Meng, F.; Jin, S. *Nano Lett.* **2012**, *12* (11), 6030–6037.
- (68) Wang, F.; Robert, R.; Chernova, N. a; Pereira, N.; Omenya, F.; Badway, F.; Hua, X.; Ruotolo, M.; Zhang, R.; Wu, L.; Volkov, V.; Su, D.; Whittingham, M. S.; Grey, C. P.; Amatucci, G. G.; Zhu, Y.; Graetz, J.; Omenya, F.; Bad-, F. *J. Am. Chem.Soc* **2011**, *133* (46), 18828–18836.
- (69) Cabana, J.; Monconduit, L.; Larcher, D.; Palacín, M. R. *Adv. Mater.* **2010**, *22* (35), 170–192.
- (70) ZEHNDER, D.; DESHPANDEY, C.; DUNN, B.; BUNSHAH, R. F. *Solid State Ionics* **2014**, *18 & 19*, 813–817.
- (71) Kukkonen, C. A.; Kaiser, W. J.; Logothetis, E. M.; Blumenstock, B. J.; Schroeder, P. A.; Faile, S. P.; Colella, R.; Gambold, J. *Phys. Rev. B* **1981**, *24* (4), 1691–1709.
- (72) Che, G.; Jirage, K. B.; Fisher, E. R.; Martin, C. R. *J. Electrochem. Soc.* **1997**, *144* (12), 4296.
- (73) Fletcher, S. In *Bottled Lightning: superbatteries, electric cars, and the new lithium economy*; Hill and Wang: New York, New York, 2011; p 51.
- (74) Newman, G. H.; Klemann, L. P. *J. Electrochem. Soc.* **1980**, *127* (10), 2097–2099.
- (75) Nagelberg, A. S.; Worrell, W. L. *J. Solid State Chem.* **1979**, *29* (3), 345–354.
- (76) Emly, A.; Van Der Ven, A. *Inorg. Chem.* **2015**, *54* (9), 4394–4402.
- (77) Mizushima, K.; Jones, P. C.; Wiseman, P. J.; Goodenough, J. B. *Mater. Res. Bull.* **1980**, *15* (6), 783–789.
- (78) Tan, G.; Wu, F.; Zhan, C.; Wang, J.; Mu, D.; Lu, J.; Amine, K. *Nano Lett.* **2016**, *acs.nanolett.5b05234*.
- (79) Gorman, J. Bigger, Cheaper, Safer Batteries: New material charges up lithium-ion battery work [http://www.sciencenews.org/view/generic/id/3159/title/Bigger,\\_Cheaper,\\_Safer\\_Batteries\\_New\\_material\\_charges\\_up\\_lithium-ion\\_battery\\_work](http://www.sciencenews.org/view/generic/id/3159/title/Bigger,_Cheaper,_Safer_Batteries_New_material_charges_up_lithium-ion_battery_work).
- (80) Jain, A.; Ong, S. P.; Hautier, G.; Chen, W.; Richards, W. D.; Dacek, S.; Cholia, S.; Gunter, D.; Skinner, D.; Ceder, G.; Persson, K. A. *APL Mater.* **2013**, *1* (1).
- (81) Thackeray, M. M.; Thomas, J. O.; Whittingham, M. S. *MRS Bull.* **2000**, *25* (3), 39–46.
- (82) Malik, R.; Abdellahi, A.; Ceder, G. *J. Electrochem. Soc.* **2013**, *160* (5), 3179–3197.
- (83) Sasaki, T.; Ukyo, Y.; Novak, P. *Nat Mater* **2013**, *12* (6), 569–575.
- (84) Masquelier, C.; Croguennec, L. *Chem. Rev.* **2013**, *113* (8), 6552–6591.
- (85) Lv, D.; Wen, W.; Huang, X.; Bai, J.; Mi, J.; Wu, S.; Yang, Y. *J. Mater. Chem.* **2011**, *21* (26), 9506.

- (86) Lv, D.; Bai, J.; Zhang, P.; Wu, S.; Li, Y.; Wen, W.; Jiang, Z.; Mi, J.; Zhu, Z.; Yang, Y. *Chem. Mater.* **2013**, 25 (10), 2014–2020.
- (87) Sobkowiak, A.; Roberts, M. R.; Younesi, R.; Ericsson, T.; Häggström, L.; Tai, C. W.; Andersson, A. M.; Edström, K.; Gustafsson, T.; Björefors, F. *Chem. Mater.* **2013**, 25 (15), 3020–3029.
- (88) Oku, M. *J. Solid State Chem.* **1978**, 23 (1-2), 177–185.
- (89) Hausbrand, R.; Cherkashinin, G.; Ehrenberg, H.; Gröting, M.; Albe, K.; Hess, C.; Jaegermann, W. *Mater. Sci. Eng. B Solid-State Mater. Adv. Technol.* **2015**, 192 (C), 3–25.
- (90) Dahn, J. R.; Fuller, E. W.; Obrovac, M.; von Sacken, U. *Solid State Ionics* **1994**, 69 (3-4), 265–270.
- (91) Nelson, P. A.; Gallagher, K. G.; Bloom, I.; Dees, D. W. *Modeling the Performance and Cost of Lithium-Ion Batteries for Electric-Drive Vehicles Chemical Sciences and Engineering Division*; Argonne, Illinois, 2012.
- (92) Omar, N.; Bossche, P. Van Den; Mulder, G.; Daowd, M.; Timmermans, J. M.; Mierlo, J. Van; Pauwels, S. *2011 IEEE Veh. Power Propuls. Conf.* **2011**, 1–7.
- (93) Kim, G.-Y.; Dahn, J. R. *J. Electrochem. Soc.* **2013**, 160 (8), A1108–A1111.
- (94) Park, Y.-U.; Seo, D.-H.; Kwon, H.-S.; Kim, B.; Kim, J.; Kim, H.; Kim, I.; Yoo, H.-I.; Kang, K. *J. Am. Chem. Soc.* **2013**, 135 (37), 13870–13878.
- (95) Li, X.; Ma, X.; Su, D.; Liu, L.; Chisnell, R.; Ong, S. P.; Chen, H.; Toumar, A.; Idrobo, J.; Lei, Y.; Bai, J.; Wang, F.; Lynn, J. W.; Lee, Y. S.; Ceder, G. *Nat. Mater.* **2014**, 13 (6), 586–592.
- (96) Yabuuchi, N.; Kajiyama, M.; Iwatate, J.; Nishikawa, H.; Hitomi, S.; Okuyama, R.; Usui, R.; Yamada, Y.; Komaba, S. *Nat. Mater.* **2012**, 11 (6), 512–517.
- (97) Padhi, A. K.; Nanjundaswamy, K. S.; Goodenough, J. B. *J. Electrochem. Soc.* **1997**, 144 (4), 1188–1194.
- (98) Yamada, A.; Chung, S. C.; Hinokuma, K. *J. Electrochem. Soc.* **2001**, 148 (3), A224.
- (99) Zhang, Y.; Wang, C. Y.; Tang, X. *J. Power Sources* **2011**, 196 (3), 1513–1520.
- (100) Niu, J.; Kushima, A.; Qian, X.; Qi, L.; Xiang, K.; Chiang, Y.-M.; Li, J. *Nano Lett.* **2014**, 14 (7), 4005–4010.
- (101) Tripathi, R.; Wood, S. M.; Islam, M. S.; Nazar, L. F. *Energy Environ. Sci.* **2013**, 6 (8), 2257–2264.
- (102) Thackeray, M. M.; David, W. I. F.; Bruce, P. G.; Goodenough, J. B. *Mater. Res. Bull.* **1983**, 18 (4), 461–472.
- (103) Lee, M.; Lee, S.; Oh, P.; Kim, Y.; Cho, J. *Nano Lett.* **2014**, 14, 993–999.
- (104) Thackeray, M. M.; Johnson, C. S.; Vaughey, J. T.; LiCurrent address: eVionyx Inc., Ha, N.; Hackney, S. A. *J. Mater. Chem.* **2005**, 15 (23), 2257.
- (105) Du Pasquier, A.; Blyr, A.; Courjal, P.; Larcher, D.; Amatucci, G.; Gérard, B.; Tarascon, J.-M. *J. Electrochem. Soc.* **1999**, 146 (2), 428–436.

- (106) Thackeray, M. M.; Johnson, P. J.; de Picciotto, L. A.; Bruce, P. G.; Goodenough, J. B. *Mater. Res. Bull.* **1984**, *19* (2), 179–187.
- (107) Ling, C.; Mizuno, F. *Chem. Mater.* **2013**, *25* (15), 3062–3071.
- (108) Kim, C.; Phillips, P. J.; Key, B.; Yi, T.; Nordlund, D.; Yu, Y. S.; Bayliss, R. D.; Han, S. D.; He, M.; Zhang, Z.; Burrell, A. K.; Klie, R. F.; Cabana, J. *Adv. Mater.* **2015**, *27* (22), 3377–3384.
- (109) Thackeray, M. M.; de Picciotto, L. A.; de Kock, A.; Johnson, P. J.; Nicholas, V. A.; Adendorff, K. T. *J. Power Sources* **1987**, *21* (1), 1–8.
- (110) Thackeray, M. M. *Prog. Solid State Chem.* **1997**, *25* (1-2), 1–71.
- (111) Thackeray, M. M. *J. Am. Ceram. Soc.* **1999**, *82*, 3347–3354.
- (112) Li, N.; Gong, H. X.; Qian, Y. T. *Chinese J. Chem. Phys.* **2013**, *26* (5), 597–600.
- (113) Moss, P. L.; Fu, R.; Au, G.; Plichta, E. J.; Xin, Y.; Zheng, J. P. *J. Power Sources* **2003**, *124* (1), 261–265.
- (114) Liu, P.; Zhang, J. G.; Turner, J. A.; Tracy, C. E.; Benson, D. K.; Bhattacharya, R. N. *Solid State Ionics* **1998**, *111* (1-2), 145–151.
- (115) Wang, Y. *Solid State Ionics* **2004**, *167* (3-4), 419–424.
- (116) He, X.; Ren, J.; Wang, L.; Pu, W.; Jiang, C.; Wan, C. *J. Power Sources* **2009**, *190* (1), 154–156.
- (117) Nazar, L. F.; Cuisinier, M.; Pang, Q. *MRS Bull.* **2014**, *39* (05), 436–442.
- (118) Wu, F.; Lee, J. T.; Fan, F.; Nitta, N.; Kim, H.; Zhu, T.; Yushin, G. *Adv. Mater.* **2015**, *27* (37), 5579–5586.
- (119) Wu, F.; Lee, J. T.; Nitta, N.; Kim, H.; Borodin, O.; Yushin, G. *Adv. Mater.* **2015**, *27* (1), 101–108.
- (120) Wu, F.; Lee, J. T.; Magasinski, A.; Kim, H.; Yushin, G. *Part. Part. Syst. Charact.* **2014**, *31* (6), 639–644.
- (121) Manthiram, A.; Fu, Y.; Chung, S.; Zu, C.; Su, Y. *Chem. Rev.* **2014**, *114*, 11751–11787.
- (122) Peng, H. J.; Huang, J. Q.; Zhao, M. Q.; Zhang, Q.; Cheng, X. B.; Liu, X. Y.; Qian, W. Z.; Wei, F. *Adv. Funct. Mater.* **2014**, *24* (19), 2772–2781.
- (123) He, B.; Li, W.-C.; Yang, C.; Wang, S.-Q.; Lu, A.-H. *ACS Nano* **2016**, acsnano.5b07340.
- (124) Zhao-Karger, Z.; Zhao, X.; Wang, D.; Diemant, T.; Behm, R. J.; Fichtner, M. *Adv. Energy Mater.* **2014**.
- (125) Riess, I. *Solid State Ionics* **2003**, *157*, 1–17.
- (126) Tuller, H. In *Springer Handbook of Electronic and Photonic Materials*; Kasap, S., Capper, P., Eds.; Springer US, 2007; pp 213–228.
- (127) Bandyopadhyay, D. *Eur. Phys. J. D* **2009**, *54* (3), 643–655.



- (128) Pugh, S. F. *Philos. Mag. Ser. 7* **1954**, 45 (367), 823–843.
- (129) Yamaki, J.; Tobishima, S. In *Handbook of Battery Materials*; Besenhard, J. O., Daniel, C., Eds.; Wiley-VCH: Weinheim, Germany, 2011; pp 377–404.
- (130) Xu, W.; Wang, J.; Ding, F.; Chen, X.; Nasybulin, E.; Zhang, Y.; Zhang, J.-G. *Energy Environ. Sci.* **2014**, 7 (2), 513–537.
- (131) Kuriyama, K.; Masaki, N. *Acta Crystallogr. Sect. B Struct. Crystallogr. Cryst. Chem.* **1975**, 31, 1793.
- (132) Huggins, R. A. In *Handbook of Battery Materials: Second Edition*; Besenhard, J. O., Daniel, C., Eds.; Wiley-VCH: Weinheim, Germany, 2011; pp 405–431.
- (133) Slater, M. D.; Kim, D.; Lee, E.; Johnson, C. S. *Adv. Funct. Mater.* **2013**, 23 (8), 947–958.
- (134) Winter, M.; Besenhard, J. O.; Spahr, M. E.; Novák, P. *Adv. Mater.* **1998**, 10 (10), 725–763.
- (135) Winter, M.; Besenhard, J. O. In *Handbook of Battery Materials: Second Edition*; Besenhard, J. O., Daniel, C., Eds.; Wiley-VCH: Weinheim, Germany, 2011; pp 433–478.
- (136) Stevens, D. a.; Dahn, J. R. *J. Electrochem. Soc.* **2000**, 147 (4), 1271.
- (137) Hatchard, T. D.; Dahn, J. R. *J. Electrochem. Soc.* **2004**, 151 (6), A838–A842.
- (138) Chan, M. K. Y.; Wolverton, C.; Greeley, J. P. *J. Am. Chem. Soc.* **2012**, 134 (35), 14362–14374.
- (139) Doughty, D.; Roth, E. P. *Electrochem. Soc. Interface* **2012**, 37–44.
- (140) Zaghib, K.; Dontigny, M.; Guerfi, A.; Charest, P.; Rodrigues, I.; Mauger, A.; Julien, C. M. *J. Power Sources* **2011**, 196 (8), 3949–3954.
- (141) Senguttuvan, P.; Rousse, G.; Seznec, V.; Tarascon, J. M.; Palac??n, M. R. *Chem. Mater.* **2011**, 23 (18), 4109–4111.
- (142) Rudola, A.; Saravanan, K.; Mason, C. W.; Balaya, P. *J. Mater. Chem. A* **2013**, 1 (7), 2653–2662.
- (143) Xu, K. *Chem. Rev.* **2004**, 104 (10), 4303–4417.
- (144) Xu, K. *Chem. Rev.* **2014**, 114 (23), 11503–11618.
- (145) Galinski, M.; Lewandowski, A.; Stepniak, I. *Electrochim. Acta* **2006**, 51 (26), 5567–5580.
- (146) Armand, M.; Endres, F.; MacFarlane, D. R.; Ohno, H.; Scrosati, B. *Nat. Mater.* **2009**, 8 (8), 621–629.
- (147) Anantharamulu, N.; Koteswara Rao, K.; Rambabu, G.; Vijaya Kumar, B.; Radha, V.; Vithal, M. *J. Mater. Sci.* **2011**, 46 (9), 2821–2837.
- (148) Kim, H.; Ding, Y.; Kohl, P. A. *J. Power Sources* **2012**, 198 (2012), 281–286.
- (149) Sholl, D. S.; Steckel, J. A. *Density Functional Theory: A Practical Introduction*, First.; John Wiley & Sons, Inc.: Hoboken, New Jersey, 2009.

- (150) West, A. R. *Basic Solid State Chemistry*, 2nd ed.; John Wiley & Sons, Inc.: West Sussex, 1999.
- (151) Urakaev, F. K. H.; Mulas, G.; Delogu, F.; Senna, M. *High-Energy Ball Milling*, First.; Sopicka-Lizer, M., Ed.; Woodhead Publishing Limited: Cambridge, 2010.
- (152) Phillips, G. C. *A Consise Introduction to Ceramics*, First.; Van Nostrand Reinhold: New York, New York, 1991.
- (153) Gopalakrishnan, J. *Chem. Mater.* **1995**, 7 (7), 1265–1275.
- (154) Tassel, C.; Kageyama, H. *Chem. Soc. Rev.* **2012**, 41 (6), 2025.
- (155) Blakely, C. K.; Bruno, S. R.; Davis, J. D.; Poltavets, V. V. *ECS Trans.* **2013**, 45 (29), 3–10.
- (156) Blakely, C. K.; Bruno, S. R.; Poltavets, V. V. *Chem. Commun.* **2014**, 50, 2797–2800.
- (157) Bruno, S. R. *Synthesis and Characterization of Novel Complex Iron Oxides With Layered and Tunnel Structures*, Michigan State University, 2014.
- (158) Greaves, C.; Francesconi, M. G. *Curr. Opin. Solid State Mater. Sci.* **1998**, 3 (2), 132–136.
- (159) McCabe, E. E.; Greaves, C. J. *Fluor. Chem.* **2007**, 128 (4), 448–458.
- (160) Rohrer, G. S. *Structure and Bonding in Crystalline Materials*; Cambridge University Press: Cambridge, 2001.
- (161) Pecharsky, V.; Zavalij, P.; Votano, J. R.; Parham, M.; Hall, L. H. *Fundamentals of Powder Diffraction and Structural Characterization of Materials*; 2009.
- (162) Woodward, P. M. X-ray Powder Diffraction II ray Powder Diffraction II Peak Intensities [https://chemistry.osu.edu/~woodward/ch754/lect2003/xrd\\_peakintensities.pdf](https://chemistry.osu.edu/~woodward/ch754/lect2003/xrd_peakintensities.pdf) (accessed Jan 1, 2016).
- (163) Kittel, C.; McEuen, P. *Introduction to Solid State Physics*, eighth.; John Wiley & Sons, Inc.: Hoboken, New Jersey, 2005.
- (164) Ashcroft, N. W.; Mermin, N. D. *Solid State Physics*; Haracourt College Publishers: Fort Worth, 1976.
- (165) Werner, P.-E. *Auto-indexing*; Oxford University Press: Oxford, 2002.
- (166) Flegler, S. L.; Heckman Jr., J. W.; Klomparens, K. L. *Scanning and Transmission Electron Microscopy An Introduction*; Oxford University Press: New York, New York, 1993.
- (167) Harris, D. C. *Quantitative Chemical Analysis*; Byrd, M. L., Ed.; W. H. Freeman Company: York, PA, 2007.
- (168) Stein, M.; Chen, C.-F.; Robles, D. J.; Rhodes, C.; Mukherjee, P. P. *J. Vis. Exp.* **2016**, No. 108, e53490.
- (169) Koch, W.; Holthausen, M. C. *Wolfram Koch , Max C. Holthausen A Chemist ' s Guide to Density Functional Theory*, 2nd ed.; Wiley-VCH Verlag GmbH: Federal Republic of Germany, 2001; Vol. 3.

- (170) Koch, W.; Holthausen, M. C. *A Chemist's Guide to Density Functional Theory*, Second.; Wiley-VCH Verlag GmbH: Weinheim, 2001.
- (171) Hohenberg, P.; Kohn, W. *Phys. Rev.* **1964**, *136* (3B), B864–B871.
- (172) Kohn, W.; Sham, L. J. *Phys. Rev.* **1965**, *140* (4A), A1133–A1138.
- (173) Hoffman, R. *Solids and Surfaces: A Chemist's View of Bonding in Extended Structures*; John Wiley & Sons, Inc.: New York, New York, 1989.
- (174) Blaha, P.; Schwarz, K.; Madsen, G. K. H.; Kvasnicka, D.; Luitz. (Karlheinz Schwarz, Techn. Universität Wien, Austria), 2001. ISBN 3-9501031-1-2 2001.
- (175) Giannozzi, P.; Baroni, S.; Bonini, N.; Calandra, M.; Car, R.; Cavazzoni, C.; Ceresoli, D.; Chiarotti, G. L.; Cococcioni, M.; Dabo, I.; Dal Corso, A.; de Gironcoli, S.; Fabris, S.; Fratesi, G.; Gebauer, R.; Gerstmann, U.; Gougoussis, C.; Kokalj, A.; Lazzeri, M.; Martin-Samos, L.; Marzari, N.; Mauri, F.; Mazzarello, R.; Paolini, S.; Pasquarello, A.; Paulatto, L.; Sbraccia, C.; Scandolo, S.; Sclauzero, G.; Seitsonen, A. P.; Smogunov, A.; Umari, P.; Wentzcovitch, R. M. *J. Phys. Condens. Matter* **2009**, *21*, 395502.
- (176) Kresse, G.; Hafner, J. *J. Phys. Condens. Matter* **1994**, *6*, 8245.
- (177) Kresse, G.; Furthmüller, J. *Comput. Mat. Sci.* **1996**, *6*, 15.
- (178) Francis, G. P.; Payne, M. C. *J. Phys. Condens. Matter* **1999**, *2* (19), 4395–4404.
- (179) Blöchl, P. E.; Kästner, J.; Först, C. J. In *Handbook of Materials Modeling*; Yip, S., Ed.; Springer, 2005; pp 93–119.
- (180) Blochl, P. E. *Phys. Rev. B* **1990**, *41* (8), 5414–5416.
- (181) Vanderbilt, D. *Phys. Rev. B* **1990**, *41* (11), 7892.
- (182) Kresse, G.; Joubert, D. *Phys. Rev. B* **1999**, *59* (3), 1758–1774.
- (183) Blochl, P. E.; Blöchl, P. E. *Phys. Rev. B* **1994**, *50* (24), 17953–17979.
- (184) Perdew, J.; Burke, K.; Wang, Y. *Phys. Rev. B* **1996**, *54* (23), 16533–16539.
- (185) Perdew, J. P.; Burke, K.; Ernzerhof, M. *Phys. Rev. Lett.* **1997**, *78* (7), 1396.
- (186) Perdew, J. P.; Chevary, J. A.; Vosko, S. H.; Jackson, K. A.; Pederson, M. R.; Singh, D. J.; Fiolhais, C.; Chevary, J. A.; Vosko, S. H.; Jackson, K. A.; Pederson, M. R.; Singh, D. J.; Fiolhais, C. *Phys. Rev. B* **1992**, *46* (11), 4978.
- (187) Krukau, A. V.; Vydrov, O. A.; Izmaylov, A. F.; Scuseria, G. E. *J. Chem. Phys.* **2006**, *125* (22).
- (188) Heyd, J.; Scuseria, G. E.; Ernzerhof, M. *J. Chem. Phys.* **2003**, *118* (18), 8207–8215.
- (189) Heyd, J.; Scuseria, G. E.; Ernzerhof, M. *J. Chem. Phys.* **2006**, *124*, 219906.
- (190) Gillan, M. J.; Alfe, D.; DeGironcoli, S.; Manby, F. R. *J. Comput. Chem.* **2008**, *29* (13), 2098–2106.

- (191) Cococcioni, M.; de Gironcoli, S. *Phys. Rev. B* **2004**, *71* (3), 035105.
- (192) Liechtenstein, a. I.; Anisimov, V. I.; Zaanen, J. *Phys. Rev. B* **1995**, *52* (AUGUST), 5467–5471.
- (193) Himmetoglu, B.; Floris, A.; De Gironcoli, S.; Cococcioni, M. *Int. J. Quantum Chem.* **2014**, *114* (1), 14–49.
- (194) Albers, R. C.; Christensen, N. E.; Svane, A. *J. Phys. Condens. Matter* **2009**, *21* (34), 343201.
- (195) Hestenes, M. R.; Stiefel, E. *Journal of Research of the National Bureau of Standards*. 1952, pp 409–436.
- (196) Goldfarb, D. *Math. Comput.* **1970**, *24*, 23–26.
- (197) Broyden, C. G. *Not. Amer. Math. Soc.* **1969**, *16*, 670.
- (198) Shanno, D. F. *Math. Comput.* **1970**, *24* (111), 647–647.
- (199) Fletcher, R. *Comput. J.* **1970**, *13*, 317–322.
- (200) Jonsson, H.; Mills, G.; Jacobsen, K. W. Berne, B. J., Ciccotti, G., Coker, D. F., Eds.; World Scientific: Singapore, 1998; p 385.
- (201) Broyden, C. G. *Math. Comput.* **1965**, *19*, 577.
- (202) Sheppard, D.; Terrell, R.; Henkelman, G. *J. Chem. Phys.* **2008**, *128* (13).
- (203) Henkelman, G.; Jónsson, H. *J. Chem. Phys.* **2000**, *113* (22), 9978–9985.
- (204) Tobias, G.; Armand, M.; Rousse, G.; Tarascon, J.-M.; Canadell, E.; Palacín, M. R.; Recham, N. *Solid State Sci.* **2014**, *38*, 55–61.
- (205) Blakely, C. K.; Bruno, S. R.; Davis, J. D.; Poltavets, V. V. In *ECS Transactions*; 2013; Vol. 45, pp 3–10.
- (206) Berry, F. J.; Ren, X.; Heap, R.; Slater, P.; Thomas, M. F. *Solid State Commun.* **2005**, *134* (9), 621–624.
- (207) Berry, F. J.; Heap, R.; Helgason, Ö.; Moore, E. A.; Shim, S.; Slater, P. R.; Thomas, M. F. *J. Phys. Condens. Matter* **2008**, *20* (21), 215207.
- (208) Alekseeva, A. .; Abakumov, A. .; Rozova, M. .; Antipov, E. .; Hadermann, J. J. *Solid State Chem.* **2004**, *177* (3), 731–738.
- (209) Isobe, M.; Li, J.-Q.; Matsui, Y.; Izumi, F.; Kanke, Y.; Takayama-Muromachi, E. *Phys. C Supercond.* **1996**, *269* (1-2), 5–14.
- (210) Troyanchuk, I. O.; Kasper, N. V.; Mantytskaya, O. S.; Shapovalova, E. F. *Mater. Res. Bull.* **1995**, *30* (4), 421–425.
- (211) Yoo, C. Y.; Kim, S. J. *J. Phys. Chem. Solids* **2008**, *69*, 1475–1478.
- (212) Leblanc, M.; Maisonneuve, V.; Tressaud, A. *Chem. Rev.* **2015**, *115*, 1191–1254.

- (213) Inaguma, Y.; Greneche, J. M.; Crosnier-Lopez, M. P.; Katsumata, T.; Calage, Y.; Fourquet, J. L. *Chem. Mater.* **2005**, *17* (6), 1386–1390.
- (214) Bednorz, J. G.; Muller, K. a. *Zeitschrift für Phys. B Condens. Matter* **1986**, *64*, 189–193.
- (215) Monthoux, P.; Balatsky, A. V. A. V.; Pines, D. *Phys. Rev. B. Condens. Matter* **1992**, *46* (22), 14803–14817.
- (216) Chakravarty, S.; Sudbø, A.; Anderson, P. W.; Strong, S. *Science (80- )*. **1993**, *261* (5119), 337–340.
- (217) Kirtley, J.; Tsuei, C.; Sun, J.; Chi, C. *Nature*. 1995, p 225.
- (218) Tsuei, C. C.; Kirtley, J. R.; Ren, Z. F.; Wang, J. H.; Raffy, H.; Li, Z. Z. *Nature*. 1997, p 481.
- (219) Keimer, B.; Kivelson, S. A.; Norman, M. R.; Uchida, S.; Zaanen, J. *Nature* **2015**, *518* (7538), 179–186.
- (220) Dagotto, E. *Rev. Mod. Phys.* **1994**, *66* (3), 763–840.
- (221) Bardeen, J.; Cooper, L. N.; Schrieffer, J. R. *Phys. Rev.* **1957**, *108* (5), 1175–1204.
- (222) Bardeen, J.; Cooper, L. N.; Schrieffer, J. R. *J. Chem. Inf. Model.* **1957**, *106* (1), 162–164.
- (223) Cooper, L. N. *Phys. Rev.* **1956**, *104* (4), 1189–1190.
- (224) Singh, J. In *Modern Physics for Engineers*; Wiley-VCH: Morlenbach, Germany, 2004; pp 122–123.
- (225) Bardeen, J. *Phys. Rev.* **1955**, *97* (6), 1724–1725.
- (226) Tipler, P. A.; Llewellyn, R. A. In *Modern Physics*; Fiorillo, J., Picerno, J., Calamari, S., Chan, J., Byrd, M. L., Szczepanski, T., Eds.; W. H. Freeman Company: New York, New York, 2008; pp 458–468.
- (227) Mansart, B.; Lorenzana, J.; Mann, A.; Odeh, A.; Scarongella, M.; Chergui, M.; Carbone, F. *Proc. Natl. Acad. Sci.* **2013**, *110* (12), 4539–4544.
- (228) Morosan, E.; Natelson, D.; Nevidomskyy, A. H.; Si, Q. *Adv. Mater.* **2012**, *24* (36), 4896–4923.
- (229) Anisimov, V. I.; Zaanen, J.; Andersen, O. K. *Phys. Rev. B* **1991**, *44* (3), 943–954.
- (230) Pereira, N.; Badway, F.; Wartelsky, M.; Gunn, S.; Amatucci, G. G. *J. Electrochem. Soc.* **2009**, *156* (6), A407–A416.
- (231) Kim, S.; Pereira, N.; Chernova, N. A.; Omenya, F.; Gao, P.; Whittingham, M. S.; Amatucci, G. G.; Su, D.; Wang, F.; Al, K. I. M. E. T. *ACS Nano* **2015**, *9* (Xx), 10076–10084.
- (232) Avdeev, M.; Ling, C. D.; Tan, T. T.; Li, S.; Oyama, G.; Yamada, A.; Barpanda, P. *Inorg. Chem.* **2014**, *53* (2), 682–684.
- (233) Kawabe, Y.; Yabuuchi, N.; Kajiyama, M.; Fukuhara, N.; Inamasu, T.; Okuyama, R.; Nakai, I.; Komaba, S. *Electrochem. commun.* **2011**, *13* (11), 1225–1228.
- (234) Barker, J.; Saidi, M. Y.; Swoyer, J. L. *Electrochem. Solid-State Lett.* **2003**, *6* (1), A1–A4.

- (235) Yonezawa, S.; Takashima, M. In *Fluorinated Materials for Energy Conversion*; Nakajima, T., Groult, H., Eds.; Elsevier Ltd: Kidlington, Oxford, 2005; pp 125–136.
- (236) Barpanda, P.; Ati, M.; Melot, B. C.; Rousse, G.; Chotard, J.-N.; Doublet, M.-L.; Sougrati, M. T.; Corr, S. a.; Jumas, J.-C.; Tarascon, J.-M. *Nat. Mater.* **2011**, *10* (10), 772–779.
- (237) Recham, N.; Chotard, J.-N.; Dupont, L.; Delacourt, C.; Walker, W.; Armand, M.; Tarascon, J.-M. *Nat. Mater.* **2010**, *9* (1), 68–74.
- (238) Ellis, B. L.; Makahnouk, W. R. M.; Makimura, Y.; Toghill, K.; Nazar, L. F. *Nat. Mater.* **2007**, *6* (10), 749–753.
- (239) Hautier, G.; Jain, A.; Mueller, T.; Moore, C.; Ong, S. P.; Ceder, G. *Chem. Mater.* **2013**, *25* (10), 2064–2074.
- (240) Avdeev, M.; Mohamed, Z.; Ling, C. D.; Lu, J.; Tamaru, M.; Yamada, A.; Barpanda, P. *Inorg. Chem.* **2013**, *52* (15), 8685–8693.
- (241) Kim, H. H.; Yu, I. H.; Kim, H. S.; Koo, H.-J.; Whangbo, M.-H. *Inorg. Chem.* **2015**, No. d, 150430103636009.
- (242) Wongittharom, N.; Lee, T.-C.; Wang, C.-H.; Wang, Y.-C.; Chang, J.-K. *J. Mater. Chem. A* **2014**, *2* (16), 5655.
- (243) Ateba Mba, J.-M.; Masquelier, C.; Suard, E.; Croguennec, L. *Chem. Mater.* **2012**, *24* (6), 1223–1234.
- (244) Barker, J.; Gover, R. K. B.; Burns, P.; Bryan, A.; Saidi, M. Y.; Swoyer, J. L. *J. Power Sources* **2005**, *146* (1-2), 516–520.
- (245) Al-Mamouri, M.; Edwards, P. P.; Greaves, C.; Slaski, M. *Lett. To Nat.* **1994**, *369* (2), 382–384.
- (246) Lee, S.; Apgar, B. A.; Martin, L. W. *Adv. Energy Mater.* **2013**, *3* (8), 1084–1090.
- (247) Sheng, Z. G.; Nakamura, M.; Koshibae, W.; Makino, T.; Tokura, Y.; Kawasaki, M. *Nat. Commun.* **2014**, *5*, 1–7.
- (248) Che, M.; Védrine, J. C. *Characterization of Solid Materials and Heterogeneous Catalysts: From Structure to Surface Reactivity, Volume 1&2*; Che, M., Védrine, J. C., Eds.; Wiley-VCH: Weinheim, Germany, 2012.
- (249) Sundarraj, P.; Maity, D.; Roy, S. S.; Taylor, R. A. *R. Soc. Chem. Adv.* **2014**, *4*, 46860–46874.
- (250) Wu, H.; Zheng, F.; Wu, D.; Ge, Z. H.; Liu, X.; He, J. *Nano Energy* **2015**, *13*, 626–650.
- (251) Momma, K.; Izumi, F. *J. Appl. Crystallogr.* **2011**, *44*, 1272–1276.
- (252) Tsujimoto, Y.; Tassel, C.; Hayashi, N.; Watanabe, T.; Kageyama, H.; Yoshimura, K.; Takano, M.; Ceretti, M.; Ritter, C.; Paulus, W. *Nature* **2007**, *450* (December), 1062–1065.
- (253) Inoue, S.; Kawai, M.; Shimakawa, Y.; Mizumaki, M.; Kawamura, N.; Watanabe, T.; Tsujimoto, Y.; Kageyama, H.; Yoshimura, K. *Appl. Phys. Lett.* **2008**, *92* (16), 161911–161911.

- (254) Chen, W. M.; Hong, W.; Geng, J. F.; Wu, X. S.; Ji, W.; Li, L. Y.; Qui, L.; Jin, X. *Phys. C Supercond.* **1996**, 270 (3-4), 349–353.
- (255) Anisimov, V. I.; Solovyev, I. V.; Korotin, M. A.; Czyzyk, M. T.; Sawatzky, G. A. *Phys. Rev. B* **1993**, 48 (23), 16929–16934.
- (256) Perdew, J. P.; Burke, K.; Ernzerhof, M. *Phys. Rev. Lett.* **1996**, 77 (18), 3865–3868.
- (257) Kresse, G.; Hafner, J.; Physik, T.; Wien, T. U.; Hauptstrasse, W. *Phys. Rev. B* **1993**, 47 (1), 558.
- (258) Kresse, G.; Furthmüller, J. *Phys. Rev. B* **1996**, 54, 11169.
- (259) Shi, J. M.; Peeters, F. M.; Hai, G. Q.; Devreese, J. T. *Phys. Rev. B* **1991**, 44 (11), 5692–5702.
- (260) Schmidt, M. J. *Phys. Chem. Solids* **2000**, 61 (8), 1363–1365.
- (261) Berry, F. J.; Heap, R.; Helgason, Ö.; Moore, E. A.; Shim, S.; Slater, P. R.; Thomas, M. F. *J. Phys. Condens. Matter* **2008**, 20 (21), 215207.
- (262) Blakely, C. K.; Davis, J. D.; Bruno, S. R.; Kraemer, S. K.; Zhu, M.; Ke, X.; Bi, W.; Alp, E. E.; Poltavets, V. V. *J. Fluor. Chem.* **2014**, 159, 8–14.
- (263) Ong, S. P.; Chevrier, V. L.; Hautier, G.; Jain, A.; Moore, C.; Kim, S.; Ma, X.; Ceder, G. *Energy Environ. Sci.* **2011**, 4 (9), 3680.
- (264) Cohen, A. J.; Mori-Sánchez, P.; Yang, W. *Chem. Rev.* **2012**, 112 (1), 289–320.
- (265) Cohen, A. J.; Mori-Sánchez, P.; Yang, W. *Science* (80-. ). **2008**, 321, 792–794.
- (266) Koller, D.; Tran, F.; Blaha, P. *Phys. Rev. B - Condens. Matter Mater. Phys.* **2012**, 85 (15), 1–8.
- (267) Koller, D.; Tran, F.; Blaha, P. *Phys. Rev. B* **2011**, 83 (19), 195134.
- (268) Camargo-Martinez, J. A.; Baquero, R. *Phys. Rev. B* **2012**, 86 (2), 195106.
- (269) Blaha, P. *J. Phys. Conf. Ser.* **2010**, 217, 012009.
- (270) Dufek, P.; Blaha, P.; Schwarz, K. *Phys. Rev. Lett.* **1995**, 75 (19), 3545–3548.
- (271) Vanko, G. J. *Chem. Theory Comput.* **2013**, 9, 5004–5020.
- (272) Petrilli, H.; Blöchl, P.; Blaha, P.; Schwarz, K. *Phys. Rev. B* **1998**, 57 (23), 14690–14697.
- (273) Gütlich, P.; Bill, E.; Trautwein, A. X. *Mössbauer Spectroscopy and Transition Metal Chemistry*, 1st ed.; Springer: London, NY, 2011; Vol. 49.
- (274) Thompson, C. M.; Blakely, C. K.; Flacau, R.; Greedan, J. E.; Poltavets, V. V. *J. Solid State Chem.* **2014**, 219, 173–178.
- (275) Li, J.; Li, J.; Luo, J.; Wang, L.; He, X. *Int. J. Electrochem. Sci.* **2011**, 6, 1550–1561.
- (276) Zhang, Z. J.; Wang, J. Z.; Chou, S. L.; Liu, H. K.; Ozawa, K.; Li, H. J. *Electrochim. Acta* **2013**, 108, 820–826.

- (277) Armstrong, A. R.; Tee, D. W.; La Mantia, F.; Novák, P.; Bruce, P. G. *J. Am. Chem. Soc.* **2008**, *130* (11), 3554–3559.
- (278) Kanno, R.; Shirane, T.; Inaba, Y.; Kawamoto, Y. *J. Power Sources* **1997**, *68* (1), 145–152.
- (279) Kanno, R.; Shirane, T.; Kawamoto, Y. *J. Electrochem. Soc.* **1996**, *143* (8), 2435–2442.
- (280) Shirane, T.; Kanno, R.; Kawamoto, Y.; Takeda, Y.; Takano, M.; Kamiyama, T.; Izumi, F. *Solid State Ionics* **1995**, *79*, 227–233.
- (281) Lee, Y. S.; Yoon, C. S.; Sun, Y. K.; Kobayakawa, K.; Sato, Y. *Electrochem. commun.* **2002**, *4* (9), 727–731.
- (282) Sakurai, Y.; Arai, H.; Okada, S.; Yamaki, J. *J. Power Sources* **1997**, *68* (2), 711–715.
- (283) Brec, R.; Guenne, L. B.; Deniard, P.; Lecerf, A.; Biensan, P.; Siret, C.; Fourne, L. *J. Mater. Chem.* **1999**, *5* (Table 1), 1127–1134.
- (284) Tabuchi, M.; Ado, K.; Sakaebe, H.; Masquelier, C.; Kageyama, H.; Nakamura, O. *Solid State Ionics* **1995**, *79*, 220–226.
- (285) Lee, Y. S.; Sato, S.; Sun, Y. K.; Kobayakawa, K.; Sato, Y. *Electrochem. commun.* **2003**, *5* (4), 359–364.
- (286) Morales, J.; Santos-Peña, J. *Electrochem. commun.* **2007**, *9* (8), 2116–2120.
- (287) Wang, X.; Gao, L.; Zhou, F.; Zhang, Z.; Ji, M.; Tang, C.; Shen, T.; Zheng, H. *J. Cryst. Growth* **2004**, *265* (1-2), 220–223.
- (288) Wu, S. H.; Liu, H. Y. *J. Power Sources* **2007**, *174* (2), 789–794.
- (289) Sakurai, Y. *Solid State Ionics* **1998**, *113-115* (1-2), 29–34.
- (290) West, A. R. *Lett. To Nat.* **1974**, *249*, 245–246.
- (291) Clemens, O.; Berry, F. J.; Wright, A. J.; Knight, K. S.; Perez-Mato, J. M.; Igartua, J. M.; Slater, P. R. *J. Solid State Chem.* **2013**, *206*, 158–169.
- (292) Garcia, B.; Lavallée, S.; Perron, G.; Michot, C.; Armand, M. *Electrochim. Acta* **2004**, *49* (26), 4583–4588.
- (293) Lahiri, A.; Schubert, T. J.; Iliev, B.; Endres, F. *Phys. Chem. Chem. Phys.* **2015**, *17*, 11161–11164.
- (294) Brown, I. D.; Altermatt, D. *Acta Crystallogr. Sect. B Struct. Crystallogr. Cryst. Chem.* **1985**, *B41*, 244–247.
- (295) Adams, S. J. *Power Sources* **2006**, *159* (1 SPEC. ISS.), 200–204.
- (296) Bruno, S. R.; Blakely, C. K.; Clapham, J. B.; Davis, J. D.; Bi, W.; Alp, E. E.; Poltavets, V. V. *J. Power Sources* **2015**, *273*, 396–403.
- (297) Eom, T.; Lim, H. K.; Goddard, W. A.; Kim, H. *J. Phys. Chem. C* **2015**, *119* (1), 556–562.



- (298) Dyer, M. 2013.
- (299) Kresse, G.; Hafner, J. *Phys. Rev. B* **1994**, *49*, 14251.
- (300) Dudarev, S. L.; Savrasov, S. Y.; Humphreys, C. J.; Sutton, P. A. *Phys. Rev. B* **1998**, *57* (3), 1505–1509.
- (301) Ravindran, P. Spin Ordering <http://folk.uio.no/ravi/activity/ordering/spinordering.html> (accessed Jan 1, 2016).
- (302) The pseudopotentials used were Na.pbe-spn-kjpaw\_psl.0.2.UPF, Fe.pbe-spn-kjpaw\_psl.0.2.1.UPF, O.pbe-n-kjpaw\_psl.0.1.UPF, and L.pbe-s-kjpaw\_psl.0.2.1.U. from <http://www.quantum-espresso.org>
- (303) Hoffmann, M. R.; Martin, S. T.; Choi, W.; Bahnemannt, D. W. *Chem. Rev.* **1995**, *95*, 69–96.
- (304) Altomare, A.; Cuocci, C.; Giacovazzo, C.; Moliterni, A.; Rizzi, R.; Corriero, N.; Falcicchio, A. *J. Appl. Crystallogr.* **2013**, *46*, 1231–1235.
- (305) Matsumoto, K.; Inoue, K.; Nakahara, K.; Yuge, R.; Noguchi, T.; Utsugi, K. *J. Power Sources* **2013**, *231*, 234–238.
- (306) Pauling, L. *The nature of the chemical bond, and the structure of molecules and crystals; an introduction to modern structural chemistry*, 3rd ed.; Cornell University Press: Ithaca, N. Y., 1960.
- (307) Toofan, J. *J. Chem. Educ.* **1994**, *71* (2), 147.
- (308) Miessler, G. L.; Tarr, D. A. *Inorganic Chemistry*, 4th ed.; Folchetti, N., DuPont, C., Neumann, J., Eds.; Pearson Education, Inc.: Boston, 2011.
- (309) Romers, C.; Rooymans, C. J. M.; de Graaf, R. A. G. *Acta Crystallogr.* **1967**, *22* (6), 766–771.
- (310) Bruker: Brisbane, Australia 2016.
- (311) Bruno, S. R.; Blakely, C. K.; Poltavets, V. V. *J. Solid State Chem.* **2012**, *192* (July 2016), 68–74.
- (312) Brown, D. I. *The chemical bond in inorganic chemistry : the bond valence model*; Oxford University Press: Oxford; New York, 2002.
- (313) Boufelfel, A. *J. Magn. Magn. Mater.* **2013**, *343*, 92–98.
- (314) Chen, Z.; Zhang, C.; Zhang, Z.; Li, J. *Phys. Chem. Chem. Phys.* **2014**, *16* (26), 13255.
- (315) Wang, L.; Maxisch, T.; Ceder, G. *Phys. Rev. B* **2006**, *73* (19), 195107.
- (316) Dagotto, E.; Moreo, A.; Nicholson, A.; Luo, Q.; Liang, S.; Zhang, X. *Front. Phys.* **2011**, *6* (4), 379–397.
- (317) Leiria Campo Jr, V.; Cococcioni, M. *J. Phys. Condens. Matter* **2010**, *22* (5), 055602.
- (318) Kim, M. C.; Sim, E.; Burke, K. *Phys. Rev. Lett.* **2013**, *111* (7), 1–5.

- (319) Christensen, R.; Hummelshøj, J. S.; Hansen, H. a.; Vegge, T. *J. Phys. Chem. C* **2015**, *119* (31), 17596–17601.
- (320) Forti, M.; Alonso, P.; Gargano, P.; Rubiolo, G. *Procedia Mater. Sci.* **2012**, *1*, 230–234.
- (321) Rollmann, G.; Rohrbach, A.; Entel, P.; Hafner, J. *Phys. Rev. B - Condens. Matter Mater. Phys.* **2004**, *69* (16), 1–12.
- (322) Anisimov, V. I.; Gunnarsson, O. *Phys. Rev. B* **1991**, *43* (10), 7570–7574.
- (323) Pou, P.; Flores, F.; Ortega, J.; Perez, R.; Yeyati, A. L. *J. Phys. Condens. MATTER* **2001**, *14* (1), 4.
- (324) Viret, M.; Rubi, D.; Colson, D.; Lebeugle, D.; Forget, A.; Bonville, P.; Dhalenne, G.; Saint-Martin, R.; André, G.; Ott, F. *Mater. Res. Bull.* **2012**, *47* (9), 2294–2298.
- (325) Thompson, T.; Sharafi, A.; Johannes, M. D.; Huq, A.; Allen, J. L.; Wolfenstine, J.; Sakamoto, J. *Adv. Energy Mater.* **2015**, *5* (11), 1–9.
- (326) Wu, J.; Gao, G.; Wu, G.; Liu, B.; Yang, H.; Zhou, X.; Wang, J. *RSC Adv.* **2014**, *4* (29), 15014–15017.
- (327) Higashi, S.; Miwa, K.; Aoki, M.; Takechi, K. *Chem. Commun. (Camb).* **2014**, *50* (11), 1320–1322.
- (328) Liu, C.; Rong, Z.; Malik, R.; Canepa, P.; Jain, A.; Ceder, G.; Persson, K. A.; Liu, M. *Energy Environ. Sci* **2015**, *8* (3), 964–974.
- (329) Pontiroli, D.; Aramini, M.; Gaboardi, M.; Mazzani, M.; Gorreri, A.; Ricci, M.; Margiolaki, I.; Sheptyakov, D.; Riccò, M.; Margiolaki, I.; Sheptyakov, D. *Carbon N. Y.* **2013**, *51* (1), 143–147.
- (330) Rong, Z.; Malik, R.; Canepa, P.; Sai Gautam, G.; Liu, M.; Jain, A.; Persson, K.; Ceder, G. *Chem. Mater.* **2015**, *27* (17), 6016–6021.
- (331) Etourneau, J.; Hagenmuller, P. *Philos. Mag. Part B* **1985**, *52* (3), 589–610.
- (332) Yahia, Z.; Turrell, S.; Turrell, G.; Mercurio, J. P. *J. Mol. Struct.* **1990**, *224* (C), 303–312.
- (333) Lin, Z.; Smith, M. E.; Sowrey, F. E.; Newport, R. J. *Phys. Rev. B - Condens. Matter Mater. Phys.* **2004**, *69* (22), 1–7.
- (334) Wei, X. S.; Cun, L. S.; Sheng, Z. Z.; Qing, Y. J.; Bo, X.; Jun, T. Y.; Li, Y. D. *Sci. China Physics, Mech. Astron.* **2011**, *54* (10), 1791–1795.
- (335) Albert, B. *Eur. J. Inorg. Chem.* **2000**, *2000*, 1679–1685.
- (336) Schmitt, K.; Stückl, C.; Ripplinger, H.; Albert, B. *Solid State Sci.* **2001**, *3* (3), 321–327.
- (337) Albert, B.; Schmitt, K.; Chemie, A. *Chem. Commun.* **1998**, 2373–2374.
- (338) Cushing, B. L.; Wiley, J. B. *J. Solid State Chem.* **1998**, *141* (2), 385–391.
- (339) Mair, G.; Schnering, H. G. von; Worle, M.; Nesper, R. *Zeitschrift Fur Anorg. Und Allg. Chemie* **1999**, *625*, 1207–1211.

- (340) The used the pseudopotentials were Na.pbe-spn-kjpaw\_psl.0.2.UPF, B.pbe-n-kjpaw\_psl.0.1.UPF, C.pbe-n-kjpaw\_psl.0.1.UPF, and M. pbe-nsp-bpaw. U. from <http://www.quantum-espresso.org>
- (341) Mills, G.; Jónsson, H. *Phys. Rev. Lett.* **1994**, 72 (7), 1124–1127.
- (342) Mills, G.; Jónsson, H.; Schenter, G. *Surf. Sci.* **1995**, 324, 305–337.
- (343) Albert, B.; Schmitt, K. *Chem. Mater.* **1999**, 11 (11), 3406–3409.
- (344) Silverman, G. S.; Rakita, P. E. *Handbook of Grignard Reagents*; 2015.
- (345) Wilkinson, D. S. *Mass Transport in Solids and Fluids*, illustrate.; Cambridge Solid State Science Series; Cambridge University Press, 2000.
- (346) Mehrer, H. In *Diffusion in Solids: Fundamentals, Methods, Materials, Diffusion-Controlled Processes*; Springer Berlin Heidelberg: Berlin, Heidelberg, 2007; pp 27–36.
- (347) Cussler, E. L. *Diffusion: Mass Transfer in Fluid Systems*, Third.; Cambridge Series in Chemical Engineering; Cambridge University Press, 2009.
- (348) Vogelsang, R.; Hoheisel, C. *Theor. Chim. Acta* **1986**, 69 (5-6), 475–489.
- (349) Vineyard, G. H. *J. Phys. Chem. Solids* **1957**, 3 (1-2), 121–127.
- (350) Kang, K.; Morgan, D.; Ceder, G. *Phys. Rev. B* **2009**, 79 (1), 014305.
- (351) Vočadlo, L.; Wall, A.; Parker, S. C.; Price, G. D. *Phys. Earth Planet. Inter.* **1995**, 88 (3-4), 193–210.
- (352) Daintith, J. *A dictionary of chemistry*, Sixth.; Daintith, J., Ed.; Oxford University Press: New York, New York, 2008.
- (353) Callister Jr., W. D. In *Materials Science and Engineering: An Introduction*; John Wiley & Sons, Inc.: New York, New York, 1997; pp 92–94.
- (354) Lü, X.; Wu, G.; Howard, J. W.; Chen, A.; Zhao, Y.; Daemen, L. L.; Jia, Q. *Chem. Commun.* **2014**, 50 (78), 11520–11522.
- (355) Ivanovskii, A. L.; Okatov, S. V. *Mendeleev Commun.* **2001**, 11 (1), 8–9.
- (356) Van Schilfgaarde, M.; Kotani, T.; Faleev, S. *Phys. Rev. Lett.* **2006**, 96 (22), 1–4.
- (357) Huie, M. M.; Bock, D. C.; Takeuchi, E. S.; Marschilok, A. C.; Takeuchi, K. J. *Coord. Chem. Rev.* **2015**, 287, 15–27.